Modelling the survival of meteoritic material exchanged between planetary bodies: scientific and commercial implications

Birkbeck, University of London

Thesis for the project:

Modelling the survival of meteoritic material exchanged between planetary bodies: scientific and commercial implications

Author:
Samuel H. Halim

Primary Supervisor:
Ian Crawford - Birkbeck, University of London

Secondary Supervisors:
Gareth Collins - Imperial College
Katherine Joy - University of Manchester

Submitted to the

Department of Earth and Planetary Sciences

for the degree of

Doctor of Philosophy

2022

Abstract

Impacts are the most ubiquitous process across the Solar System, with every solid planetary surface we see marked by evidence of this process in some regard. Some impacts provide enough energy for the transfer of material between planetary bodies. Using the iSALE shock physics code, the survival of projectile material after impact with the Moon is investigated. The work within this thesis also explores the transfer of ejecta from Earth to the Moon, as well as investigating the survival of a particular set of larger asteroids (carbonaceous chondrites) that impact the lunar surface.

This thesis investigates the potential for terrestrial material (i.e., terrestrial meteorites) to be transferred to the Moon by a large impact on Earth and subsequently survive impact with the lunar surface. Three-dimensional impact simulations show that a typical basin-forming impact on Earth can eject solid fragments at speeds sufficient to transfer them from Earth to the Moon. The importance of considering temperature when assessing the survival of biomarkers within the projectile is shown with the inclusion of a strength model that can resolve both shock and shear heating. This work shows that, assuming survival after launch from Earth, some biomarker molecules within terrestrial meteorites are likely to survive impact with the Moon, especially at the lower end of the range of typical impact velocities for terrestrial meteorites (2.5 km s^{-1}). Long-term survival of biomarkers depends heavily upon where the projectile material lands, whether it is buried or remains on the surface, and the related cooling timescales.

Carbonaceous chondrites contain relatively large quantities of carbon and nitrogen, two elements that are particularly depleted in the lunar crust. This work assesses the viability of surviving carbon and nitrogen within the impacted asteroids at a range of impact angles and velocities. At impact velocities of 5 km s^{-1}, up to 86% of the impactor remains solid with the potential to retain carbon- and nitrogen-based compounds. Highly oblique impacts (15°) lead to material concentrating out of the crater rim, downrange in the direction of impact. Increasing impact velocity and angle decreases the proportion of surviving solid material. However, less oblique impacts concentrate surviving material within or close to the crater rim, which may be beneficial for resource utilisation.

Acknowledgements

I would like to begin by thanking Ian Crawford, my primary supervisor, for his guidance and mentorship throughout this process. I could not have asked for a more supportive person to help me through the ups and downs of these past four years. Making time both in-person and online to discuss projects, open to ideas and opportunities beyond the PhD work itself and encouraging engagement with the scientific community on a regular basis. The same thanks can be extended to my secondary supervisors, Gareth Collins and Katherine Joy. I thank you both for the insightful and thought-provoking input into the work, as well as all of the support through meetings and discussions. I also thank Tom Davison (Imperial College), alongside Gareth Collins, for all of their tutelage in the use of iSALE, computing requirements, and post-processing script writing, without which I would not have a thesis to present. Lastly, I would like to thank Adrian Jones (UCL) for his support and for sponsoring my access to the UCL high-powered computing clusters.

A huge thank you to all of the people I have met as a result of this PhD. From the friends made in the Birkbeck office, the researchers met and collaborated with at conferences, to the planetary science community as a whole. A special thanks to David Kring and the team at LPI for the opportunity to work on such an amazing project during the CLSE internship. The experiences I had and people I met, worked, and lived with during that time will be remembered for the rest of my life.

To my family and friends, thank you for the unconditional love and support you have given me throughout this time. To my parents specifically, even if you can't quite explain to your friends exactly what it is I have been doing for the past four years of my life, it makes me unbelievably happy that you take pride in what I have chosen to do and the accomplishments and achievements that have come with it. I can never repay the kindness or support that I have been given by you all.

The biggest thanks go to my beautiful wife, Lizzie. You are my best friend and the person I depend on in the best and worst of times, both of which we have probably experienced during my time working on this. It is not an over-exaggeration to say that I would not have been able to do this without you. Lastly, thank you for putting up with me constantly being at home for the past two years, taking over part of the lounge, whilst I watched you leave to work through a global crisis.

Finally, I thank my cats, Simba and Nala, for keeping me sane. Working from home since 2020 would have probably been the loneliest experience of my life, had it not been for my two furry companions.

Contents

Abstract 1

Acknowledgements 2

List of tables 6

List of figures 8

Glossary 12

Acronyms 13

Symbols for equations 14

1 Introduction 18

1.1 Aim and objectives of the PhD thesis 18

1.2 Approach and method 19

1.3 Outline of thesis 19

1.4 Conference attendance 21

1.5 Publications 22

1.6 Statement of originality 23

2 Literature review 24

2.1 Lunar geology 24

2.1.1 The lunar surface – a brief overview 24

2.1.2 Potential resources native to the lunar surface 25

2.1.3 Carbon and nitrogen on the Moon 27

2.2 Impacts physics and crater formation 30

2.3 Meteorite production and the survivability of meteoritic material impacting planetary surfaces 34

2.3.1 Ejection processes and the production of meteorites from planetary bodies 35

2.3.2 Meteorite survival during hypervelocity impacts 38

2.3.3 Biological material within ejecta 40

2.4 Carbonaceous chondrites 41

2.4.1 Properties of the carbonaceous chondrite groups 42

2.4.2 Parent asteroid properties 45

2.4.3 ISRU of materials in carbonaceous chondrites 47

2.5 Summary 49

3 Methods 50

3.1 Numerical shocks physics code modelling 50

3.2 iSALE 53

3.2.1 Fundamental equations to solve 54
3.2.2 Mesh geometry 55
3.2.3 Equations of state 57
3.2.4 Constitutive (strength) model parameters 59
3.2.5 Limitations and areas of uncertainty within the model parameters 62
3.3 Processing numerical simulation outputs 64
3.4 Summary 66

4 Modelling the impact ejection of low-pressure material from Earth to the Moon* 67
4.1 Introduction 67
4.2 Methods 69
4.3 Results 73
4.3.1 Two dimensional simulations 73
4.3.2 Three dimensional simulations 77
4.3.3 Temperature regimes in low-pressure ejecta 86
4.4 Discussion 89
4.5 Conclusions 93

5 Assessing the survivability of biomarkers within terrestrial material impacting the lunar surface* 94
5.1 Introduction 94
5.2 Methods 97
5.2.1 iSALE modelling of terrestrial meteorite impacts on the Moon 97
5.2.2 Material strength and shear heating in the projectile 101
5.2.3 Biomarker selection 102
5.3 Results 106
5.3.1 The influence of material strength 106
5.3.2 Influence of impactor velocity, shape, porosity, and composition 108
5.3.3 Sandstone projectiles – molecule biomarker survival 117
5.3.4 Sandstone projectiles - fossil biomarker survival 122
5.4 Discussion 123
5.4.1 External factors influencing biomarker survival 123
5.4.2 Detecting terrestrial material on the lunar surface 125
5.4.3 Comparing Earth–Moon to Mars–Phobos material transfer 128
5.5 Conclusions 129

6 Survival of carbonaceous chondrites impacting lunar surface and their use as future resources 131
6.1 Introduction 131
6.2 Methods 135
6.2.1 Evaluating and selecting a projectile material model 136

6.2.2 Simulation set-up – 2D 141
6.2.3 Simulation set-up – 3D 144
6.2.4 Overcoming issues in 3D simulations 145
6.3 Results 148
6.3.1 Projectile survival – temperature and location 150
6.3.2 Nitrogen and carbon survival 159
6.4 Discussion 165
6.4.1 Probability estimates for CC impacts into the Moon 165
6.4.2 Detection of surviving CC meteoritic material 168
6.5 Conclusions 172

7 Discussion and conclusions 174
7.1 Scientific and commercial opportunities for meteoritic material on the Moon 174
7.2 Concluding remarks 176
7.3 Future work 178
7.3.1 Earth ejection simulations 179
7.3.2 Terrestrial meteorite simulations 180
7.3.3 Carbonaceous chondrite simulations 181
7.3.4 Comparative experimental, laboratory-based modelling 182

Bibliography 183

Appendix 218

List of tables

Table 4.1: Thermal, strength, and damage input parameters for the impactor and target material in the numerical modelling work for Chapter 4…….70

Table 5.1: Description of model set up parameters. The names given to the simulations indicate the material of the projectile, the extent to which the projectile and target are porous, and the impact velocity……99

Table 5.2: Thermal, strength, and damage input parameters for the impactor and target materials used in the numerical modelling work for Chapter 5……..100

Table 5.3: Examples of organic materials that may be contained within terrestrial rocks, with thermal degradation parameters and decomposition/vaporisation temperatures based upon published experimental results……103

Table 5.4: Fossil and microfossil biomarkers that may be contained within terrestrial rocks with minimum survival pressures and temperatures based upon examples found in metamorphosed Earth rock samples……105

Table 5.5: Mean peak pressure and temperature results for each of the simulation scenarios…...……..114

Table 6.1: Equations of state (EoS) available within the iSALE EoS library which were considered to represent CC-like material……...138

Table 6.2: Thermal, strength, and damage input parameters for the impactor and target materials used in the numerical modelling work for Chapter 6……..142

Table 6.3: Names assigned to each of the 12 different scenarios covered by this suite of simulations by varying impact velocity and angle……147

Table 6.4: Abundances of C-bearing materials found in a range of CM/CI meteorites (Murchison, Murray and Orgueil) and the average abundances of N-bearing molecules found in CM samples (Murchison and Murray). Associated vaporisation temperatures included for both C- and N-bearing molecules……...……...147

Table 6.5: Percentage of 40% porous CC projectile material that remains solid after impact, based upon peak temperatures reached within the projectile at any time during the simulation……...152

Table 6.6: Proportions of projectile volume in their respective final locations after impact for scenarios where solid material survived……...…156

Table 6.7: Estimated masses of projectile material in their respective final locations after impact for scenarios where solid material survived. Values for the molecule sources of nitrogen and carbon are taken from Table 6.3 and estimations for the maximum values are calculated using average values of C and N wt.% in CI meteorites (Pearson *et al.*, 2006)……..162

List of figures

Figure 2.1: Illustration showing the initial formation stages for a simple impact crater using an idealised spherical projectile travelling perpendicular to the target surface…….31

Figure 2.2: Illustration showing the excavation stage of the impact cratering process……...……...32

Figure 2.3: Illustration showing the modification stage and final simple crater formed by the impact cratering process.....33

Figure 2.4: Simplified, schematic cross-section highlighting the formation of a spallation zone during an oblique impact……....35

Figure 3.1: Examples of Lagrangian and Eulerian methods for a projectile impacting vertically into a target with identical simulation set-ups……. 51

Figure 3.2: A typical mesh geometry used for 2D and 3D simulations in iSALE……...……...56

Figure 3.3: An example Hugoniot curve for an equation of state representing a dunite material model…….…….58

Figure 3.4: Example of a typical impact scenario displayed in the interactive window available through pySALEPlot….65

Figure 4.1: Resolution test for the suite of two-dimensional models……..….73

Figure 4.2: The cumulative mass of target material ejected (M_{ej}) as fraction of impactor mass (M_i) shown as a function of shock pressure (P) for different impact velocities in 2D simulations with a resolution of 600 cppr……...74

Figure 4.3: Provenance plot of high-speed ejecta that experiences different peak shock pressures for a 2D simulation of a 50-km diameter impactor striking Earth a speed of 20 km $\mathbf{s^{-1}}$ and resolution 600 cppr……76

Figure 4.4: Resolution test for the suite of three-dimensional models…….…….78

Figure 4.5: Provenance plot of high-speed ejecta that experiences different peak shock pressures for a simulation of a 50-km diameter impactor striking Earth at 45° to the surface and a speed of 20 km $\mathbf{s^{-1}}$ with resolution 100 cppr……..…79

Figure 4.6: The cumulative mass of target material ejected (M_{ej}) as fraction of impactor mass (M_i) shown as a function of shock pressure for different impact angles (30°-60°) for impacts with velocity of 20 km $\mathbf{s^{-1}}$…….....81

Figure 4.7: The cumulative mass of target material ejected (M_{ej}) as fraction of impactor mass (M_i) shown as a function of shock pressure for different impact angles (30°-60°) for impacts with velocity of 30 km $\mathbf{s^{-1}}$…….83

Figure 4.8: The cumulative mass of target material ejected (M_{ej}) as fraction of impactor mass (M_i) shown as a function of shock pressure for different impact angles (30°-60°) for impacts with velocity of 55 km $\mathbf{s^{-1}}$…….83

Figure 4.9: Provenance plot of high-speed ejecta that experiences different peak shock pressures for a simulation of a 50-km diameter impactor striking Earth at 30° to the surface and with velocity of 20 km $\mathbf{s^{-1}}$ & resolution 100 cppr……..84

Figure 4.10: Provenance plot of high-speed ejecta that experiences different peak shock pressures for a simulation of a 50-km diameter impactor striking Earth at 30° to the surface and with velocity of 30 km $\mathbf{s^{-1}}$ & resolution 100 cppr…….....85

Figure 4.11: The cumulative mass of target material ejected (M_{ej}) as fraction of impactor mass (M_i) that experiences pressures <10 GPa, shown as a function of (a) peak-shock temperature and (b) temperature at the final timestep of simulation (15 s post-impact) for different impact velocities (20, 30, & 55 km $\mathbf{s^{-1}}$) at an impact angle of 30°……..…..88

Figure 5.1: Resolution study for simulation ID S_S_5, showing the volume (%) of the impactor which reaches a certain temperature and pressure at increasing amounts of cells per projectile radius (cppr)……...…100

Figure 5.2: Comparative contour maps of peak pressure and temperature for solid projectiles impacting a solid target with and without a strength model included……107

Figure 5.3: Contour plots of peak-shock pressures and peak-shock temperatures in a solid sandstone projectile after impacting a solid basalt target…….109

Figure 5.4: Contour plots of peak-shock pressures and peak-shock temperatures in a sandstone projectile with varying porosity (10-40%) after impacting a solid basalt target……...110

Figure 5.5: Contour plots of peak-shock pressures and peak-shock temperatures in a solid sandstone projectile after impacting a basalt target with varying porosity (30-70%)……...111

Figure 5.6: Contour plots of peak-shock pressures and peak-shock temperatures in a prolate, solid sandstone projectile after impacting a solid basalt target…….113

Figure 5.7: Contour plots of peak-shock pressures and peak-shock temperatures in an oblate, solid sandstone projectile after impacting a solid basalt target…….113

Figure 5.8: Contour plots of comparing pressure and temperature regimes in sandstone and limestone projectiles. Both sets of plots are the result of a solid projectile impacting a 70% porous target……116

Figure 5.9: Contour plots of comparing pressure and temperature regimes in sandstone and limestone projectiles. Both sets of plots are the result of a 40% porous projectile impacting a solid target……116

Figure 5.10: Survival of selected biomarkers for a tracer that reaches a post-shock temperature of 600 K in the main body of the sandstone projectile shown in Figure 5.8……...119

Figure 5.11: Survival of selected biomarkers for a tracer that reaches a post-shock temperature of 800 K in part of the sandstone projectile shown in Figure 5.9…….120

Figure 5.12: Survival of selected biomarkers for a tracer that reaches a post-shock temperature of 2000 K in the main body of the sandstone projectile shown in Figure 5.9……..…..121

Figure 5.13: Contour plots showing regions of the projectile where lycophyte megaspores are likely to survive after impact……..122

Figure 6.1: Schematic diagram showing the process of projectile decapitation after a highly oblique impact. Several snapshots in the cratering process are shown for an impact angle less than 15°……...134

Figure 6.2: A comparison of shock Hugoniot data for iSALE EoS data (dunite, serpentine, quartzite, granite, basalt, and CC material models) and experimental data for ordinary chondrites (Bruderheim) and CM carbonaceous chondrites (Murchison)……139

Figure 6.3: A comparison of shock Hugoniot data for iSALE EoS (serpentine and CC, both including 20% porosity) and experimental data for ordinary chondrites (Bruderheim) and CM carbonaceous chondrites (Murchison)……..140

Figure 6.4: Resolution study for the 2D, vertical impact described in the text, showing the volume (%) of the projectile which reaches a certain temperature (y-axis) at increasing amounts of cells per projectile radius (cppr)……..…143

Figure 6.5: Peak temperature and location plots for projectile material (initial porosity = 40%) landed on the lunar surface in scenarios (a) a15_v5, (b) a15_v10, and (c) a15_v15……153

Figure 6.6: Peak temperature and location plots for projectile material (initial porosity = 40%) landed on the lunar surface in scenarios (a) a30_v5, (b) a45_v5, and (c) a60_v5……155

Figure 6.7: Cross-section provenance plots for the area where projectile material is predicted to land by the end of the impact process for simulations (a) a15_v5, (b) a30_v5, (c) a45_v5, (d), a60_v5……..158

Figure 6.8: Total mass of the decapitated portion of the projectile highlighted in Figure 6.5a, simulation a15_v5, plotted against the peak temperature recorded for a given total mass……..160

Figure 6.9: Total mass of the projectile material landed directly downrange from simulation a15_v10 plotted against the peak temperature recorded for a given total mass. This plot represents material highlighted 20 km downrange and 3 km either side of the impact point in Figure 6.5b……...163

Figure 6.10: Total mass of the projectile material landed in the proximal ejecta and crater from simulation a30_v5 plotted against the peak temperature recorded for a given total mass. The proximal ejecta describes material highlighted 20 km downrange and 4 km either side of the impact point in Figure 6.6a……..163

Figure 6.11: Total mass of the projectile material landed in the proximal ejecta and crater from simulation a45_v5 plotted against the peak temperature recorded for a given total mass. The proximal ejecta describes material highlighted 7 km downrange and 4 km either side of the impact point in Figure 6.6b…….164

Figure 6.12: Total mass of the projectile material landed in the proximal ejecta and crater from simulation a60_v5 plotted against the peak temperature recorded for a given total mass. The proximal ejecta describes material highlighted 6 km downrange and 5 km either side of the impact point in Figure 6.6c……....164

Glossary

Asteroid	Rocky, iron or icy debris, too small to be classified as a planet, generally in orbit of the Sun.
Biomarker	Biological markers: preserved complex organic compounds that can be related to biological activity.
Eulerian	A description of the motion of a fluid. In terms of numerical modelling within a hydrodynamic simulation, variations in fluid flow are described at fixed points as a function of time.
Hydrocode	Computer program that models the behaviour of a continuous medium through the influence of external and internal forces on a predefined “mesh” of cells.
Impact gardening	The process where frequent small impacts stochastically churn the uppermost surface of a planetary body.
Jetting	Ejection at high velocities of shock-melted and vaporised materials at the initial interface between an impactor and a target.
Lagrangian	A description of the motion of a fluid. In terms of numerical modelling within a hydrodynamic simulation, individual particles are tracked as they move through the flow field.
Matplotlib	Comprehensive library for creating static, animated, and interactive visualisations in Python.
Primitive	When relating to meteorites, primitive describes a sample that is near unchanged since it formed with little to no alteration.
Python	**I**nterpreted, object-oriented, high-level programming language.
Spallation	Process in which fragments of material (spall) are ejected from the surface or near-surface of a body due to impact. Occurs when a dynamic compressive pressure wave meets a free surface and is reflected as a rarefaction wave. Typically produces relatively low-pressure, high-velocity ejecta.
Terrestrial meteorite	A piece of Earth ejected by an impact that subsequently lands on another planetary body.

Acronyms

ANEOS	semi-Analytical Equation of State
CC	Carbonaceous Chondrite
CPPR	Cells Per Projectile Radius
DHC	Dark-Haloed Crater
EoS	Equation of State
ESA	European Space Agency
GRAIL	Gravity Recovery and Interior Laboratory
HVM^3	The High-resolution Volatiles and Minerals Moon Mapper
iSALE	impact-Simplified Arbitrary Lagrangian Eulerian shock physics code
ISRU	*In-Situ* Resource Utilisation
KREEP	Potassium**,** Rare-Earth Elements, And Phosphorus
LADEE	Lunar Atmosphere and Dust Environment Explorer
LGG	Light Gas Gun
LMO	Lunar Magma Ocean
LTM	Lunar Thermal Mapper
ProSPA	PROSPECT Sample Processing and Analysis element
PSR	Permanently Shadowed Region
PROSPECT	Package for Resource Observation and *in-Situ* Prospecting for Exploration, Commercial exploitation and Transportation
VIR	Visible-Infrared spectrum
M^3	Moon Mineralogy Mapper

Symbols for equations

A	pre-exponential factor
A_c	cell area
a	Simon approximation constant
B	positive constant in the Ivanov damage model
c	Simon approximation constant
c_B	bulk sound speed
c_{so}	bulk sound speed of solid material at zero pressure
$c(\alpha)$	bulk sound speed of the porous material at zero pressure
D	scalar measure of damage (0 = intact, 1 = completely damaged)
dM	change in mass
dt	change in time
E	internal energy
E_a	activation energy of organic molecule
F_i	external body force per unit volume
M_{ej}	ejected mass
M_i	impactor mass
M_{or}	mass of organic material

P	pressure
p_c	pressure above which failure is assumed compressional
P_r	probability of a meteoroid impact at particular angle
q	artificial viscosity
R	gas constant
$T(t)$	time dependant temperature
T_m	melt temperature
T_{m0}	melt temperature at zero pressure
TrP	tracer peak pressure
TrT	tracer peak temperature
Tru	tracer velocity, x-component
Trv	tracer velocity, y-component
Trw	tracer velocity, z-component
V	volume
v_{ej}	ejection velocity
v_i	velocity
Y	yield strength
Y_d	yield strength of damaged material
Y_{d0}	cohesion of damaged material at zero pressure

Y_{dm}	limiting strength at high pressure for damaged material
Y_i	yield strength of intact material
Y_{i0}	cohesion of the intact material at zero pressure
Y_{im}	limiting strength at high pressure for intact material
Y_t	tensile strength after damage
Y_{to}	intact tensile strength
θ	impact angle
α	distension; related to porosity (ϕ)
α_0	initial porosity within a material
ϕ	porosity
ϵ_v	volumetric strain
ϵ_c	volumetric strain in the compression regime
ϵ_e	volumetric strain in the elastic compaction region
ϵ_x	volumetric strain in the exponential compaction region
ϵ_p	invariant measure of the accumulated total plastic strain
ϵ_f	plastic strain at failure
ϵ_{fb}	minimum failure strain for low pressure states
ϵ'_{ij}	deviatoric strain rate
κ	parameter accounting for variations in materials and types of porosity

ρ	material density
σ_{ij}	stress tensor
s_{ij}	deviatoric stress tensor
μ_d	coefficient of internal friction for damaged material
μ_i	coefficient of internal friction for intact material
$\nabla.u$	velocity divergence
λ_1, λ_2	constants for artificial viscosity

1 Introduction

Throughout the history of the Solar System, many thousands of asteroids and comets have struck planetary surfaces, including those of the Earth and Moon. Recently, growing evidence has suggested that some fraction of these projectiles can survive impact with a planetary surface, depending on the circumstances. In the case of the Moon, the heavily cratered surface we see today is a result of the rich history of impact bombardment and the lack of erosional processes to remove or obscure much of the evidence. If impactor material can be recovered from the Moon, it will yield valuable information about the composition of asteroids and comets passing through the inner Solar System (Joy *et al.et al.*, 2016). Material impacting the Moon is typically imagined as solely extra-terrestrial, by bodies originating from the depths of the wider Solar System. However, material ejected from the Earth after large impacts may travel to the lunar surface and possibly carry with it evidence of the early development of terrestrial biological activity (Armstrong *et al.*, 2002; Armstrong, 2010). Life itself is unlikely to survive the typically violent ejection, travel, and subsequent impact process into the lunar surface, but stronger, more resistant markers of biological activity may. These biological markers or "biomarkers" would be of key significance if discovered on the lunar surface, providing insight into the early Earth which has been lost to geological processes on Earth itself. The most effective biomarkers are organic compounds with specific biological sources, whose structures can be preserved through geologic time. The remains of impacted asteroids and comets may also provide local sources of raw materials which are naturally scarce on the Moon (e.g., native metals, carbon, nitrogen, organic molecules, and hydrated materials), but which will be very useful in the context of future human activities on the Moon. This work will aim to investigate the survival of projectiles and their key constituents during and post-impact, using numerical modelling. The following sections will introduce and provide details for the aims, objectives, approach, and outline of the content of this thesis.

1.1 Aim and objectives of the PhD thesis

This PhD project aims to address several questions relating to the survival of projectile material (and possible biomarkers contained within such material) after impact with the surfaces of planetary bodies. Additionally, a hypothesis that material can survive ejection from the surface of the Earth whilst remaining solid and experiencing pressures/temperatures conducive with biomarker survival is tested. A series of objectives are listed to achieve these aims:

1) Complete a series of simulations investigating the ejection of target material from terrestrial bodies (in particular, the Earth) and subsequent transfer of such material to the Moon.

2) Complete a series of simulations using numerical modelling to assess the survivability of terrestrial meteorites and their constituent biological-markers (biomarkers) impacting the lunar surface.

3) Complete a series of simulations investigating carbonaceous chondrites impacting into the lunar surface and estimate the fraction of impacts that are likely to retain a sufficient amount of impactor material to be useful as a potential resource. This includes assessing pressure and temperature regimes as well as predicting the location of surviving material post-impact.

4) Determine potential locations of such material in and around the resulting impact crater and access the methods that could be used to find such impact sites using remote sensing techniques.

5) Consider these results in terms of use for future lunar missions designed to make use of *in situ* materials, particularly using surviving impactor material on the Moon.

1.2 Approach and method

Objectives 1-4, set out in the previous section, will be achieved using the impact-Simplified Arbitrary Lagrangian Eulerian (iSALE) shock physics code (Amsden *et al.*, 1980; Collins *et al.*, 2004; Wünnemann *et al.*, 2006). A detailed description of the use and development of this numerical hydrocode is presented in Chapter 3. Both the two-dimensional and three-dimensional versions of the code have been used, based on the advantages each version provides for particular sets of data. Results from these simulations have then been combined with knowledge of remote sensing data from the lunar surface, upcoming missions to the lunar surface, and the practicalities of surface operations to address Objective 5.

1.3 Outline of thesis

Chapter 1 has introduced the topic and themes of the work carried out to produce this thesis. The aims and objectives have been set out and the approach to complete them have been described.

Chapter 2 reviews the current state of the scientific literature on the various topics covered in this thesis. These include lunar geology, an introduction to cratering and impact physics, survivability of projectiles impacting planetary surfaces, and a general overview of carbonaceous chondrites.

Chapter 3 describes the methodologies used in order to complete the research undertaken for the thesis. An

introduction to numerical modelling used for simulating impacts is followed by a detailed description of the specific hydrocode used for this project, the impact-Simplified Arbitrary Lagrangian Eulerian (iSALE) shock physics code. Finally, the post-processing techniques used to analyse the simulation results are described.

Chapter 4 is the first results chapter, describing the ejection and survival of material from terrestrial bodies. More specifically, this begins the investigation of material transfer from giant impacts on the early Earth to the lunar surface, addressing the question of whether biological markers (biomarkers) could survive the launch.

Chapter 5 continues this line of investigation at the end of the process. The chapter details the results of simulations modelling impacts of terrestrial material into the lunar surface. Survival of the terrestrial meteorites and the biomarkers within are accessed using the simulation results, alongside calculations of thermal degradation of organic material over time. The long-term survival of biomarkers is discussed over geological timescales and the techniques that could be used to find survived terrestrial material are explored.

Chapter 6 moves on to the survival of a different type of meteorite impacting the lunar surface, carbonaceous chondrites (CCs) and their source asteroid parent bodies. The survival of non-native elements (carbon and nitrogen in particular) in the lunar regolith and near-surface is investigated using three-dimensional numerical modelling. The chapter not only focuses on the scientific value of these surviving materials, but also the possible commercial value for long-term, sustainable resources for future operations on the lunar surface. Methods of detection and utilisation of such resources are discussed, and plans suggested for future missions.

Chapter 7 brings together all three of the results chapters (4, 5, and 6) and discusses the content as part of a broader picture. General discussion of how the work builds upon and progresses the current knowledge on the subject of projectile survival on terrestrial bodies is considered and the impact the work may have for future research and potential influence over future missions to the lunar surface is explored. The chapter ends with the outcomes and conclusions of the thesis, directly addressing the objectives set out in the introduction. A final comment is made upon what future work may look like relating to the conclusions of this project.

1.4 Conference attendance

Conferences where an abstract based on work in this PhD was submitted, accepted, and presented as either a talk or poster:

- 50th Lunar and Planetary Science Conference, 18th–22nd March 2019, The Woodlands, Texas, USA.
  Abstract: Survival of terrestrial material impacting the lunar surface. (Poster)

- 7th European Lunar Symposium, 21st–23rd May 2019, Manchester, UK.
  Abstract: Assessing the survivability of terrestrial material impacting the lunar surface. (Talk)

- 2nd British Planetary Science Conference, 13th–15th January 2020, Oxford, UK.
  Abstract: Assessing the survivability of biomarkers within terrestrial material impacting the lunar surface. (Talk)

- 8th European Lunar Symposium, 12th–14th May 2020, Virtual.
  Abstract: Assessing biomarker survival in terrestrial material impacting the lunar surface. (Talk)

- RAS Early Career Poster Exhibition, 14th September 2020, Virtual.
  Abstract: Assessing biomarker survival in terrestrial material impacting the lunar surface. (Poster)

- 43rd COSPAR Scientific Assembly, 28th–4th February 2021, Sydney, Australia/Virtual (attended virtually).
  Abstract: Assessing the survivability of biomarkers within terrestrial material impacting the lunar surface. (Talk)

- 52nd Lunar and Planetary Science Conference, 15th–19th March 2021, Virtual
  Abstract: Modelling the survival of carbonaceous chondrites impacting the lunar surface as a potential resource. (Poster)

- Space Resources Week, 19th–22nd April 2021, Luxembourg/Virtual (attended virtually).
  Abstract: Modelling carbonaceous chondrite survival for use as a potential lunar resource. (Poster)

- 12th Annual Lunar and Small Bodies Graduate Forum, 15th–16th July 2021, Virtual.
  Abstract: Modelling carbonaceous chondrite survival for use as a potential lunar resource. (Talk)

- Joint NASA Exploration Science Forum & European Lunar Symposium, 20th–23rd July 2021, Virtual.
  Abstract: Modelling carbonaceous chondrite survival: a potential resource cache on the lunar surface. (Talk)

- The Moon and Early Earth Conference, 29th–30th November 2021, Virtual.
  Abstract: Assessing the survivability of biomarkers within terrestrial material impacting the lunar surface. (Talk)

- 53rd Lunar and Planetary Science Conference, 7th–11th March 2022, The Woodlands, Texas, USA/Virtual (attended virtually).
  Abstract: Modelling the impact ejection of low-pressure material from Earth to the Moon. (Talk)

Additional contributions have been made as part of the Centre for Lunar Science & Exploration Internship (CLSE) attended from 25th May – 5th August 2019, at the Lunar and Planetary Institute in Houston, Texas, USA:

- 8th European Lunar Symposium, 12th–14th May 2020, Virtual.
  Abstract: Geological investigation of the lunar south pole: potential EVA targets and implications for Artemis 2024. (Poster)

- 43rd COSPAR Scientific Assembly, 28th–4th February 2021, Sydney, Australia/Virtual (attended virtually).
  Abstract: Geological investigation of the lunar south pole and identification of potential EVA targets. (Talk)

Travel grants received:

- **$1500**: 51st Lunar and Planetary Science Conference, 2020. Awarded by SSERVI-CLSE (unused due to COVID restrictions cancelling the conference).

- **£1000**: 43rd COSPAR Scientific Assembly, 2020. Awarded by the Royal Astronomical Society (unused due to COVID restrictions postponing the conference).

1.5 Publications

Resulting from work related to this PhD:

- **Halim, S.H.**, Crawford, I.A., Collins, G.S., Joy, K.H., Davison, T.M., 2021a. Assessing the Survivability of Biomarkers within Terrestrial Material Impacting the Lunar Surface. *Icarus 354*, 114026. https://doi.org/10.1016/j.icarus.2020.114026

- **Halim, S.H.,** Crawford, I.A., Collins, G.S., Joy, K.H., Davison, T.M., *In Prep*. Modelling the survival of carbonaceous chondrites impacting the lunar surface as a potential resource.

Resulting from the CLSE internship:

- Gawronska, A.J., Barrett, N., Boazman, S.J., Gilmour, C.M., **Halim, S.H.**, Harish, McCanaan, K., Satyakumar, A.V., Shah, J., Meyer, H.M., Kring, D.A., 2020. Geologic context and potential EVA targets at the lunar south pole. *Advances in Space Research 66,* 1247-1264. https://doi.org/10.1016/j.asr.2020.05.035

- **Halim, S.H.**, Barrett, N., Boazman, S.J., Gawronska, A.J., Gilmour, C.M., Harish, McCanaan, K., Satyakumar, A.V., Shah, J., Kring, D.A., 2021b. Numerical Modeling of the Formation of Shackleton Crater at the Lunar South Pole. *Icarus 354*, 113992. https://doi.org/10.1016/j.icarus.2020.113992

- Boazman, S.J., Shah, J., Harish, Gawronska, A.J., **Halim, S.H.**, Satyakumar, A.V., Gilmour, C.M., Bickel, V.T., Barrett, N., Kring, D.A., *Submitted.* The distribution and accessibility of geologic targets near the lunar south pole and potential Artemis Landing sites 001 and 004. *Planetary Science Journal*.

1.6 Statement of originality

The entirety of the work presented in this thesis has been carried out and written-up by myself during my PhD at Birkbeck, University of London, unless otherwise stated. Part of the work in this thesis has been submitted and published by as a peer-reviewed journal article (Halim *et al.*, 2021a) alongside my supervisors (Prof. Ian Crawford, Prof. Gareth Collins, Prof. Katherine Joy) and research fellow Dr Thomas Davison. My personal share of the investigation in this work includes the majority of the paper, aside from a portion of modelling work conducted by Thomas Davison. This work is included in Chapter 4, describing the ejection of material from Earth and includes the initial modelling phase (a resolution test for escaping masses of low-pressure material from Earth). The results for this modelling are shown in Figures 4.4 and 4.5. All other subsequent modelling work, analysation, and investigation was conducted by myself. All results were interpreted by myself, with assistance from my supervisors and Dr Thomas Davison.

Signed: Samuel H. Halim

2 Literature review

2.1 Lunar geology

The composition and geology of the lunar surface has been characterised by study of samples returned by the Apollo, Luna (e.g., Heiken *et al.*, 1991) and Chang'e-5 (Qian *et al.*, 2018; 2021) missions, lunar meteorite samples (e.g., Joy and Arai, 2013), and remote sensing techniques from orbit (e.g., Hodges, 1973; Feldman *et al.*, 1998; Ohtake *et al.*, 2008; Pieters *et al.*, 2009a; Colaprete *et al.*, 2010; Schultz *et al.*, 2010) and the surface of the Earth (Kuiper, 1960; Wilhelms and McCauley, 1971; Whitaker, 1999; Honniball *et al.*, 2021). The combination of analysing samples from the lunar surface and remote sensing has also allowed the calibration of remote sensing data which has greatly improved the accuracy and viability of analyses of the lunar surface from orbit. It is important to combine the efforts of laboratory work and remote sensing data to elucidate details of the compositional characteristics of lunar lithologies, but also be able to place these samples in the bigger picture of the lunar surface and its evolution. In the context of this thesis, defining the composition of the lunar surface, and near sub-surface, is important for at least two reasons. Firstly, in order to consider the survival of any projectile impacting the Moon, we need to have a good understanding of the physical properties of the target materials. Secondly, considering key elements that may be necessary for sustaining a future human presence on the Moon. Whilst there are a considerable number of lunar materials that are being actively investigated as potential resources (e.g., regolith for habitats or oxygen extraction, water-ice in craters, and extractable metals across the surface; Crawford, 2015), there are a number of important chemical elements that are not readily available in extractable quantities for use by future long-term, human based missions. These will be explored and discussed in the next section.

2.1.1 The lunar surface – a brief overview

The Moon can be divided into two distinct terrains: the heavily cratered, ancient highlands and the broadly smooth, lowland maria. The bright lunar highlands are thought to represent the original crust of the Moon and compose mainly of ferroan anorthositic rocks and a magnesium suite including dunites, troctolites, norites and gabbronorites. The dark mare plains are formed of younger basaltic volcanic rocks including lava flows and pyroclastic deposits. Mare basalts are more common on the lunar nearside. The four major mineral phases occurring in lunar lithologies are pyroxene, plagioclase feldspar, multiple oxides (ilmenite, spinel, and armalcolite), and olivine (Heiken *et al.*, 1991; Anand *et al.*, 2015). The

younger basaltic rocks of the lunar maria compose predominantly of plagioclase, clinopyroxene, orthopyroxene, olivine, and ilmenite, whilst the older highlands are rich in anorthositic rocks dominated by plagioclase feldspar. This leads to highland rocks being rich in calcium, aluminium, silicon, and oxygen but relatively depleted in magnesium and iron. Conversely, the mare basalts are relatively rich in iron, magnesium, and titanium, but poor in calcium and aluminium. Rocks across the lunar surface are generally significantly depleted in volatile elements, such as carbon, nitrogen, and sodium (Gibson, 1977).

The 4.5-billion-year impact history of the lunar surface has created a global, unconsolidated surface layer known as the lunar regolith (Hörz *et al.*, 1991; McKay *et al.*, 1991; Lucey *et al.*, 2006; Spray, 2016; Wieler, 2016). Whilst the first few centimetres may consist of a powdery, dust-like texture (extensively noted by Apollo astronauts walking on the surface), the deeper regolith compacts and quickly rises in density with depth. The porosity of the uppermost centimetre of regolith is likely to be up to 87%, based on both sample analysis (Ohtake *et al.*, 2010) and remote sensing techniques (Hapke and Sato, 2015). The build-up of regolith layers over time has led to the burial of ancient regolith layers, known as palaeoregoliths, and multiple regolith layers create a much deeper megaregolith in some regions. Crustal porosity has been estimated using high-resolution measurements from NASA's Gravity Recovery and Interior Laboratory (GRAIL). If the surface composition of the Moon is representative of the underlying crust, then the implied average porosity would be ~12%, varying regionally between 4–21% (Wieczorek *et al.*, 2013), with highland crust averaging a bulk density of 2550 kg m^{-3}. The relatively high porosity at the upper end of the expected range likely extends 10s of km into the crust (Besserer *et al.*, 2014; Milbury *et al.*, 2015).

2.1.2 Potential resources native to the lunar surface

The lunar surface may provide an abundance of available and relatively accessible resources that could be extracted to maintain long-term human exploration and habitation (see Crawford, 2015 for a comprehensive review). Materials that are readily accessible and extractable can be used for operations on the lunar surface and taking advantage of such *in-situ* resource utilisation (ISRU) opportunities will greatly improve the longevity of sustainable missions to the Moon.

Water is likely available as a viable lunar resource from at least two sources, including extraction from the lunar regolith and recovery from within permanently shadowed polar craters where temperatures are low enough for water-ice to remain stable over geological time (Arnold, 1979, Feldman *et al.*, 2001; Anand, 2010; Sargeant *et al.*, 2020). Renewed

interest in landing humans on the Moon has centred around the lunar south pole. The south pole is being targeted, in part, because it contains topographically high locations, which provide high proportions of illumination throughout the year needed for solar power (Mazarico *et al.*, 2011; Speyerer and Robinson, 2013; Gläser *et al.*, 2014). The south pole is also being targeted because it is home to many permanently shadowed regions (PSRs) that may contain volatiles in the form of ices suitable for ISRU (Fegley and Swindle, 1993; Duke *et al.*, 2003; Anand, 2010; Spudis and Lavoie, 2010; Anand *et al.*, 2012). Of course, this is also true of the lunar north pole, but no missions are currently scheduled or planned to explore this area of the Moon. Access to those volatiles could be vital for sustainable exploration of the surface and associated geologic samples will satisfy several scientific objectives as set out by the National Research Council (NRC, 2007). Additionally, water could be produced in high-Ti mare regions via hydrogen reduction of ilmenite (e.g., Schwandt *et al.*, 2012; Sargeant *et al.*, 2020). Whilst this technique has worked in a laboratory setting, it has yet to be reproduced on the lunar surface itself and on a large enough scale to be cost and energy efficient enough to be a viable production method. However, this will potentially change in future with an *in-situ* test of the ProSPA instrument, a miniature analytical laboratory, demonstrating the process on the lunar surface in a prospective, upcoming European Space Agency (ESA) mission called PROSPECT (Barber *et al.,* 2017). Not only will this provide water as a resource but also will release available oxygen from the regolith, another crucial component for sustaining a crewed lunar base. Another electrochemical process for the simultaneous extraction of oxygen and production of metal alloys from lunar regolith is based on the Metalysis-FFC (Fray, Farthing, Chen) process (Fray *et al.*, 1999). This process would not rely on ilmenite for the production of oxygen and therefore could be used in any location on the Moon where metal oxides are abundant. A proof-of-concept study has been conducted by Lomax *et al.* (2020) for the electro-deoxidation of a powdered solid-state lunar regolith simulant. During this study, 96% of the total oxygen was extracted to give a mixed metal alloy product and approximately a third of the total oxygen in the sample was detected in the gaseous products. The remaining oxygen was lost to corrosion of the reactor vessel, but this does offer a viable alternative to the reduction of ilmenite to produce oxygen on the lunar surface. Again, this has yet to be proven with *in situ* experimentation on the Moon and will require modification to the experimental set-up to become viable on a larger scale.

Much of the regolith contains significant masses of extractable metals (Duke *et al.*, 2006; Schwandt *et al.*, 2012), especially iron and aluminium. Whilst iron is abundant in lunar basalts, it will require energy intensive extraction techniques to release from the silicate minerals (e.g., olivine and pyroxene) or metal oxides (ilmenite) they are trapped within. Iron is available in lunar regolith in native form but in much lower abundances than those locked in minerals (~0.5

wt.% and ~14 wt.%, respectively; Crawford, 2015 and references therein). Similar to the mare basalts containing locked-up iron, highland regolith contains abundant masses of aluminium (~10–18 wt.%) contained within anorthositic plagioclase, a very useful metal for industrial purposes. Again, processes for extracting such metals will be energy intensive and require specialised equipment to do so (e.g., carbothermal reduction; Duke *et al.*, 2006, or molten salt electrochemical processing; Schwandt *et al.*, 2012).

The regolith itself has great potential as a viable construction material for lunar habitats, providing protection from harmful radiation and wildly fluctuating temperatures for humans living on the surface for prolonged periods of time. There is the potential for use of the regolith for protection in multiple ways, including unprocessed (Eckart, 1999), sintered into a more coherent habitat (e.g., Desai *et al.*, 1993; Taylor and Meek, 2005), or building components for a lunar outpost using 3D printing techniques (e.g., Cesaretti *et al.*, 2014).

Carbon and nitrogen are two elements that could be necessary for long-term crewed missions to the lunar surface to be successful, without dependence on costly resupply from Earth. As previously mentioned, the lunar surface is predominantly lacking in terms of volatile elements, including sources for carbon and nitrogen. The next section will focus on the limited resources available in terms of evidence for carbon and nitrogen abundance on the Moon.

2.1.3 Carbon and nitrogen on the Moon

The abundance of carbon and nitrogen on the Moon has been investigated through multiple analyses of sample returns using a variety of techniques and remote sensing (both from the Earth and from lunar orbiters e.g., Yokota *et al.*, 2020; Mandt *et al.*, 2022). The return of samples from the Apollo missions provided a wealth of information from a range of geological materials, including regolith, breccias, and basaltic rock samples. Bulk soil samples provided evidence for carbon concentrations between 2.5 ppm (Modzeleski *et al.*, 1972) and 280 ppm (Moore *et al.*, 1973), with a mean value of 124 ± 45 ppm across multiple studies (summarised by Fegley and Swindle, 1993). In general, bulk soil samples from multiple studies, analysing materials from each Apollo mission (Apollo 11, 12, 14, 15, 16, 17) produce median carbon abundances between 100 and 150 ppm (Epstein and Taylor, 1970; Chang *et al.*, 1970; Friedman *et al.*, 1971; Gibson and Moore, 1973; Moore *et al.*, 1973; DesMarais *et al.*, 1975; Moore and Lewis, 1975). More recent analyses of bulk soil samples recorded carbon concentrations of ~100 ppm (Haskin & Warren, 1991). The calculated median and mean values of the carbon content in lunar breccias and basaltic rocks are systemically lower than those found in bulk soils, however the variation between samples is considerable. Across multiple Apollo breccias, the calculated average mean equated to 93

± 73 ppm (Epstein and Taylor, 1970, 1972; Friedman *et al.*, 1972; Kaplan *et al.*, 1970, 1976; Moore *et al.*, 1970, 1971, 1972, 1973, 1974; Sakai *et al.*, 1972; Becker and Epstein; 1981); a maximum of 385 ppm carbon was recorded in a breccia by Becker and Epstein (1981) and is by far the highest recorded by any lunar sample. Basalts recorded lower mean abundances than both breccias and bulk soil, with a value of 26 ± 20 ppm (calculated from samples analysed by: Friedman *et al.*, 1970, 1972; Moore *et al.*, 1970, 1972, 1973, 1974; Kaplan and Petrowski, 1971; DesMarais 1978). Other samples from Apollo 11 released methane (CH_4, up to 6 ppm) and other hydrocarbons after treatment via acid hydrolysis (Abell *et al.*, 1970), however it was uncertain whether the methane was produced by the process or was present as methane in the original samples.

Solar wind implantation is the most likely source for a widespread, relatively uniform concentration of carbon across the surficial lunar regolith. Across the entirety of the accessible lunar surface regolith, there may be a mass amounting to $\sim 7\times10^{13}$ kg of carbon (Cannon, 2021). This value will vary spatially across the lunar surface, with different compositions and depths of regolith between the highlands and maria. The highlands generally consist of thicker, older material stemming from the increased generation of regolith from extensive impact gardening. Observations from the lunar orbiter KAGUYA (Ohtake *et al.*, 2008) identified the emission of carbon ions from the lunar surface, with estimated emission fluxes of $\sim 5\times10^{4}$ cm^{-2} s^{-1} (Yokota *et al.*, 2020). Calculations determined that this was greater than the possible supply of carbon via solar wind and micrometeorite bombardment and therefore implies the presence of indigenous carbon being emitted from the lunar surface or exosphere. Whilst the emissions were observed across the lunar surface (within the bound of the capabilities of KAGUYA), amounts did vary with respect to lunar geography. Areas associated with lunar magnetic anomalies effectively limited the emission of carbon ions.

Cold traps at the lunar poles are the most likely areas to find large quantities of solid CO_2, where sublimation rates may be low enough to allow for CO_2 ice to build up over time (Schorghofer *et al.*, 2021). The LCROSS (Lunar CRater Observation and Sensing Satellite) probe impact in Cabeus crater (Colaprete *et al.*, 2010; Marshall *et al.*, 2012) generated a plume of ejecta that was subsequently analysed by remote sensing. The proportion of CO_2 measured was significantly higher than that measured in Apollo samples and may be the result of impacting a cold trap containing solid CO_2. Carbon species included CO, C_2H_4, CO_2, CH_3OH, and CH_4, contributing to a total of ~5000 ppm C in the regolith at the impact site. Additionally in a separate study, the Lunar Atmosphere and Dust Environment Explorer (LADEE) spacecraft identified an active methane cycle involving the lunar exosphere, including surface adsorption and desorption (Hodges, 2016). However, the data from LADEE has not provided provenance of where methane was being adsorbed on the lunar

surface. According to the simplified Carbon Content of Ices model proposed by Cannon (2021), polar ice deposits may contain as much as 20 wt.% C in the coldest regions, but are more likely to range between ~0-3 wt.% C. The total abundance from all these polar deposits could add up to $\sim 1 \times 10^{11}$ kg (Cannon, 2021).

Nitrogen is believed to be even less prevalent on the lunar surface than carbon. Despite being one the of most abundant elements in the universe and the main component of our own atmosphere here on Earth, the Moon lacks any significant source of indigenous nitrogen. Apollo samples have provided a range of abundances for bulk molecular nitrogen, depending on the type of sample analysed. Samples analysed by Moore *et al.* (1970) from Apollo 11 determined weighted mean values of 100 ppm and 150 ppm nitrogen in two sets of fines (10086-A and 10086-B, respectively). Other samples analysed in the same study found a range of nitrogen abundances from 30 ppm in medium-grain rock to 125 ppm in fine breccia. A multitude of igneous Apollo samples from the surface of the Moon have provided evidence for nitrogen present in similar abundances on the order of ppm or lower (Funkhouser *et al.*, 1971; Becker *et al.*, 1976; Müller *et al.*, 1976; DesMarais, 1978; Mathew and Marti, 2001; Mortimer *et al.*, 2015). The origin of lunar nitrogen has been a topic of contention ever since samples were returned to Earth and studied in great detail. A significant proportion of lunar nitrogen is expected to be contributed by the solar wind, implanted within the lunar regolith over billions of years. However, analysis of ancient regolith has produced an anomalously high abundance of nitrogen (roughly an order of magnitude higher) when compared to the solar wind (Kerridge, 1975; Thiemens and Clayton, 1980). Additionally, $^{15}N/^{14}N$ ratios can vary from sample to sample by over 30% and the isotopic variation is potentially related to the time at which nitrogen was introduced to the Moon (Kerridge, 1993). These variations were believed to either reflect actual changes in the outer layers of the Sun over time or an addition of extra-solar nitrogen with different isotopic compositions than the solar wind. Noble gases in lunar soils are predominantly solar in origin and nitrogen is well correlated with these solar components. Therefore, ratios between noble gases and nitrogen can be used to determine the likely origin of nitrogen in a given sample. The analysis of multiple individual grains from lunar soils revealed wide variations in the ratio of $^{14}N/^{16}Ar$ from grain to grain, whereas the ratios of noble gases Ar/Kr and Kr/Xe remained constant (Wieler *et al.*, 1999). Additionally, bulk soil samples analysed by Mortimer *et al.* (2016) revealed significantly more enriched ^{15}N compared to the measured solar wind nitrogen value during high-resolution stepped combustion. Both Wieler and Mortimer concluded that up to 90% of the nitrogen in the samples was not delivered by the solar wind and had to be explained by extra-solar processes.

Three prospective sources of extra-solar nitrogen have been suggested: assimilation of nitrogen from chondritic meteorite impacts (Brilliant *et al.*, 1992; Füri & Marty, 2015), degassing from the lunar interior (Mortimer *et al.*, 2015), or

transfer to the lunar exosphere from the Earth via the loss of gasses from our atmosphere (Ozima *et al.*, 2005). Carbonaceous chondrite impacts during the early history of the Moon have been considered as a significant source for the accumulation of nitrogen (Brilliant *et al.*, 1992), especially in some mare basalts (Füri & Marty, 2015). Nitrogen delivered by the meteorites during the formation of the lunar magma ocean (LMO) was trapped within crystallising mafic minerals (e.g., olivine, garnet, pyroxene) during the reducing conditions. This chondritic reservoir supplied nitrogen in abundances of ppm to mare regions but left anorthositic highland rocks relatively free of nitrogen, apart from brecciated highland rocks which may have trapped chondritic melt after shock-induced melting.

A comprehensive summary of carbon and nitrogen abundances from Apollo samples can be found in Fegley and Swindle (1993).

2.2 Impacts physics and crater formation

Formed during the hypervelocity (>1 km s^{-1}) impact of a cosmic projectile into a target surface, impact craters are the most easily recognised, ubiquitous product across all solid, planetary surfaces in our Solar System. Conventionally there are three stages to the impact-cratering process: contact and compression, excavation, and modification or gravitational collapse. These stages are more of a continuum than individual and separate processes, however each stage is dominated by its own physical phenomenon that make it easier to describe and quantify in isolation.

Contact and compression: This stage starts the instant the projectile makes contact with the target surface and continues as it propagates into the target material (Figure 2.1a). In a typical, theoretical impact, the projectile will travel up to a depth of twice its own diameter in solid rock and even more if the target is unconsolidated or layered, within a fraction of a second, before it is stopped (Melosh, 1989). Of course, this is entirely dependent on the speed and size of the projectile, with faster/larger projectiles penetrating further. The kinetic energy of the projectile is converted into shock waves which travel through the target and the impactor, leading to very high pressures, up to hundreds of giga-Pascals (GPa), and temperatures (thousands of K) due to compression of the highly shocked materials (Collins *et al.*, 2012). Shortly after the shock compression, the shock wave reaches the back of the projectile and is reflected as a rarefaction wave (or "release wave") back into the projectile (Melosh, 1989). As this release wave passes through the projectile material, the projectile is unloaded from the high shock-pressure regime it previously experienced. This unloading results in melting and vaporisation of the projectile, depending on the pressures and temperatures experienced. Eventually the rarefaction wave reaches the front end of the projectile and also continues into the now-highly-compressed target, causing decompression. At this point, the contact and compression stage is said to be complete (Figure 2.1b). This first stage only lasts a few seconds for projectiles in the km-scale and in most smaller impacts (metre-scale projectiles), is over in much less than one second (Melosh, 1989; French, 1998).

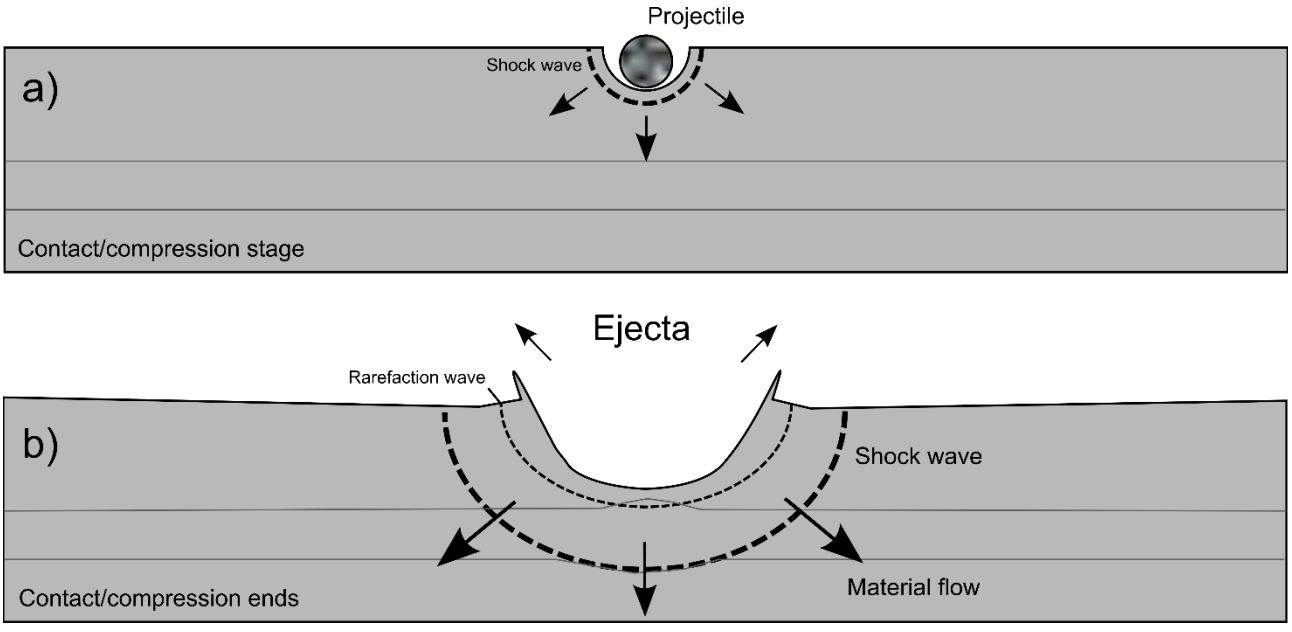

Figure 2.1: *Illustration showing the initial formation stages for a simple impact crater using an idealised spherical projectile travelling perpendicular to the target surface. Adapted from French, (1998).*

Excavation: The hemispherical shockwave travels away from the impact site, located beneath the original ground surface, and causes material in the upper layers to move upward and outward, whilst lower layers move downward and outward (Figure 2.2a). A bowl-shaped depression, called the transient cavity/crater, is produced (Melosh, 1989) and can be divided into approximately equal volume upper and lower zones. Highly oblique impacts (<15° to the horizontal) can lead to elongation of the crater in the direction of impact, however this can be obscured or overprinted by later increasing crater growth (Collins *et al.*, 2012). The upper zone is dominated by ejection of material at velocities as high as several kilometres per second which can travel far beyond the rim of the crater. The lower zone, sometimes called the displaced zone, is where material is excavated at lower velocities and fracturing is less pronounced, with excavated material unable to travel past the crater rim. Gravity is the most significant factor limiting crater growth for large impact events, with excavation stopping once the energy remaining cannot lift the target material against its own weight (Melosh, 1989; French, 1998; Bray, 2009). Once growth of the transient crater volume ceases the excavation stage comes to an end (Figure 2.2b). It is estimated that in multi-km-scale craters, this stage lasts seconds to minutes, and scales with the size of the event (Melosh, 1989).

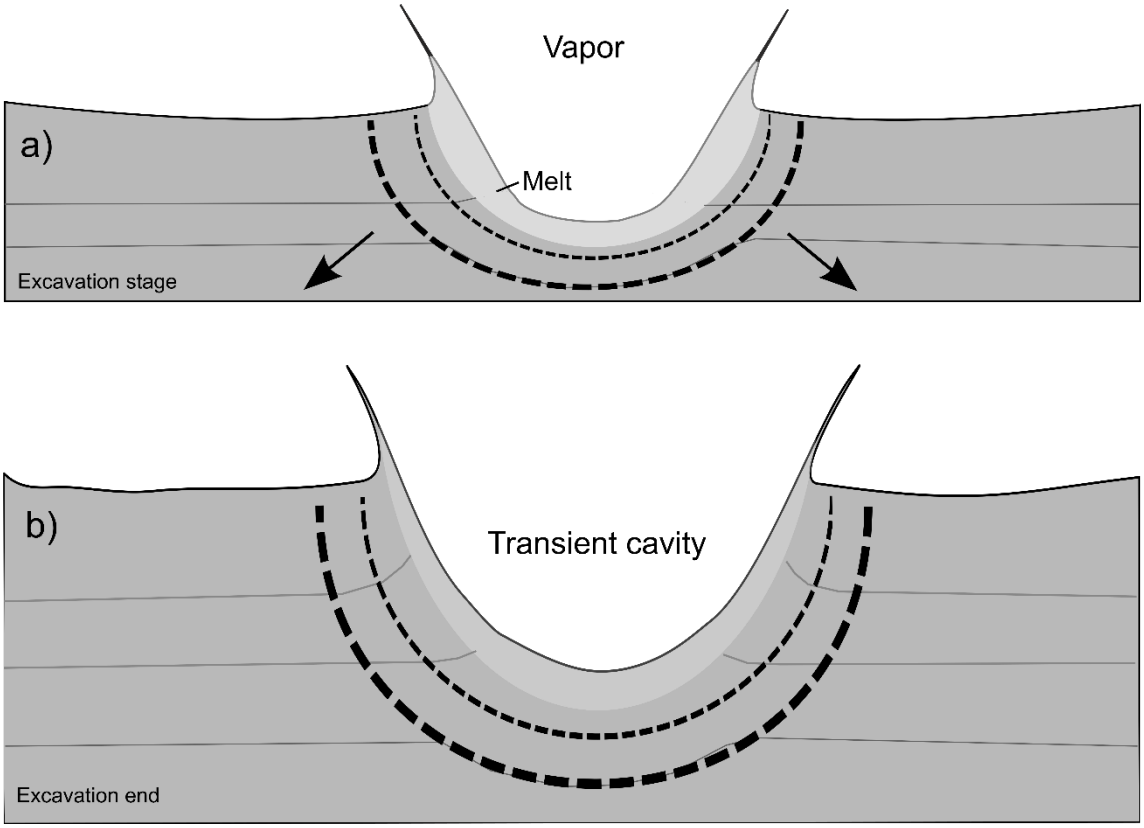

Figure 2.2: *Illustration showing the excavation stage of the impact cratering process. Adapted from French, (1998).*

Collapse and modification: The last stage of impact crater formation is driven by the gravitational modification of the transient crater and rock mechanics (Figure 2.3). The collapse stage does not have a clear end point and will simply continue until the gravity specific to the planetary surface ceases to have an influence on the movement of material. Major impact-related changes will last less than a minute for smaller craters, <4 km diameter, but can last many minutes for larger craters; 200-300 km diameter structures such as those in Vredefort (South Africa) are estimated to have taken around 15 minutes to form (Melosh, 1989). Modification extends beyond just gravitational collapse and into long term erosion of the crater. Initial erosion will preferentially remove near-surface ejecta deposits, as well as deeper erosion over longer periods of time which can ultimately remove evidence of the original crater entirely by geological processes, e.g., infilling and crater rim destruction. On Earth, erosional processes are responsible for much of the modification and destruction of impact structures. The hydrological cycle and atmospheric effects (e.g., high winds) displace, bury, and break-up impact structures

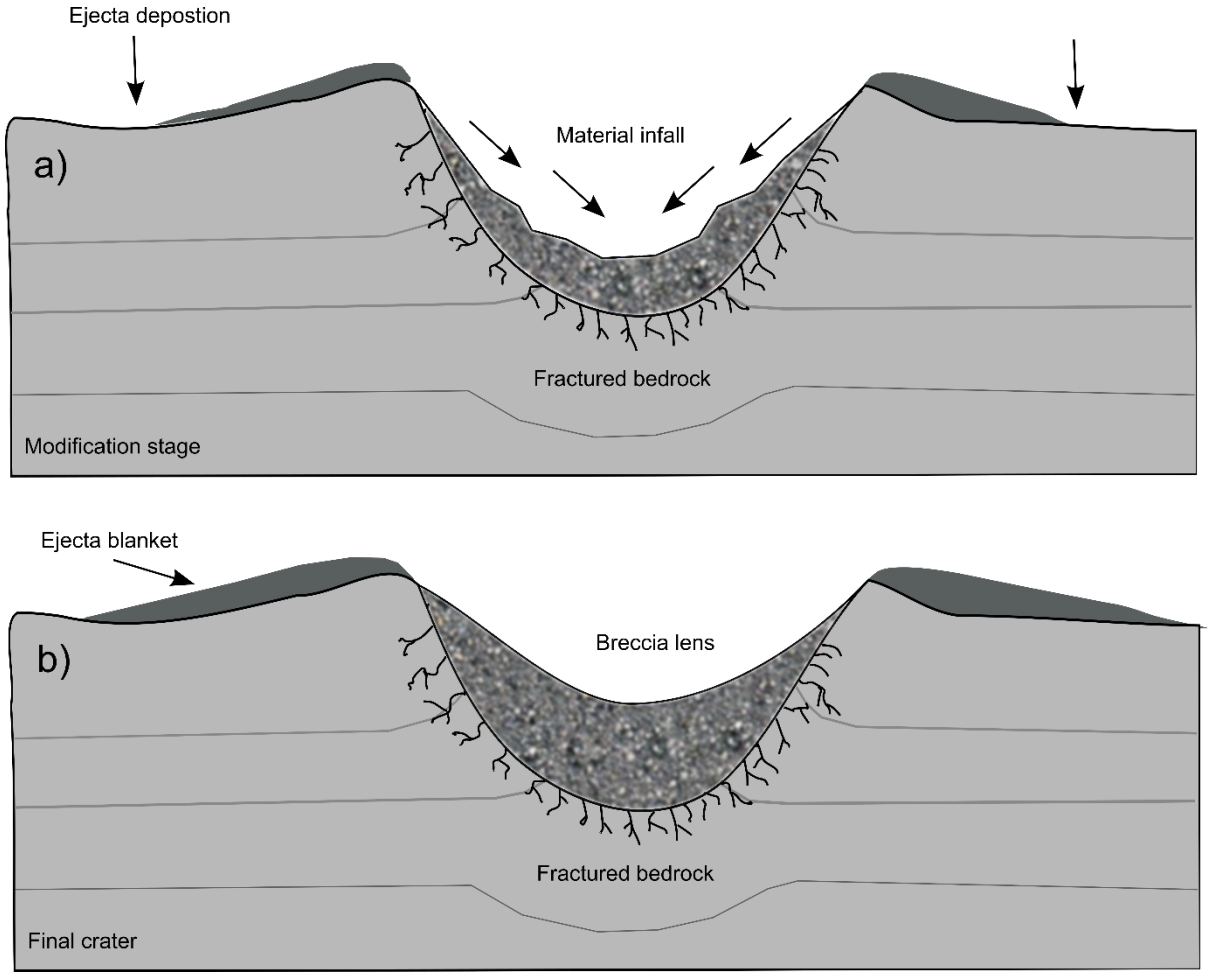

Figure 2.3: *Illustration showing the modification stage and final simple crater formed by the impact cratering process. Adapted from French, (1998).*

and the associated shocked material. Continuously active plate tectonism also contributes to much of the distortion of impact craters on Earth, leading to burial, horizontal compression, and displacement of shocked material (French, 1998).

Geological activity on the Moon is much less frequent and pronounced, lacking plate tectonics, a wide-scale hydrological cycle, and many erosional processes. Therefore, there is very little modification to many impact craters on the lunar surface, even over long geological timescales (millions to billions of years), making the Moon an incredibly detailed record of the bombardment history of the inner Solar System.

2.3 Meteorite production and the survivability of meteoritic material impacting planetary surfaces

The ejection of meteorites from planetary surfaces is a complex and sometimes controversial subject of investigation. Work in this project on the ejection of material focuses on ejection from Earth and the generation of so-called "terrestrial meteorites", an area where there has been a lack of investigation in previous studies. The production and survival of meteorites from the Moon, Mars, and many smaller bodies from the asteroid belt (e.g., Vesta) is undeniable, as we have examples of them in the Earth's meteorite collection. There is no such record of terrestrial meteorites being found on other planetary bodies, so it is much harder to prove that terrestrial meteorites can be produced. The ejection process stems from a hypervelocity impact into a target surface and so typically involves very high pressure and temperatures, not conducive to the survival of solid ejecta. Therefore, much investigation into the generation of solid ejecta after impacts has been focused on Mars, where 1) we already have evidence for the ejection of low-shock, solid material (i.e., Martian meteorites) and 2) the limiting threshold for material escaping the gravity of Mars (~5 km s^{-1}) is much lower than for Earth (~11.2 km s^{-1}). The following section (2.3.1) will review the current state of the literature regarding the mechanisms of impact ejection, focusing on the potential generation of meteorites from Earth.

The potential for a meteorite to survive after a hypervelocity impact depends on a number of factors. In terms of impacts on planetary surfaces other than the Earth, experimental and numerical modelling are the best tools to probe the fate of projectiles during and immediately after impact. Section 2.3.2 will provide a review of studies that have contributed to the investigation of projectile survival, with particular focus on the potential survival of material impacting the lunar surface.

2.3.1 Ejection processes and the production of meteorites from planetary bodies

The generation of potential meteorites requires the launch of material from a target surface during a hypervelocity impact. Much of the highest speed ejecta is produced very early in an impact event and at a point very close to the site of impact via a process known as "jetting". The convergence of a projectile and a target produces a concentration of energy at the site of collision, resulting in ejection velocities greater than the impact velocity (Kieffer, 1977; Melosh and Sonett, 1986; Vickery, 1994; Johnson *et al.*, 2014, 2015; Kurosawa *et al.*, 2015, 2018). However, with this material being so close to the impact site, the majority of the ejecta will experience pressures and temperatures high enough to melt or vaporise rock (potentially >50 GPa and many 1000s K). Jetted ejecta is not likely to produce the kind of meteoroids that could remain solid and retain biological evidence from the target they were ejected from. However, impact ejection can also produce lightly shocked, high-velocity ejecta by the process of "spallation". Spallation normally occurs after jetting and before normal excavation of a target, with different ejection velocities and peak pressures/temperatures relating to each process (Johnson *et al.*, 2014; Kurosawa *et al.*, 2015, 2017; Okatmoto *et al.*, 2020). This spalled material originates from a zone of the target closest to the free surface (Figure 2.4), where the dynamic compressive shock wave from the impact reflects as a rarefaction wave (Melosh, 1984). Associated tensile stress in the target can lead to complete detachment from

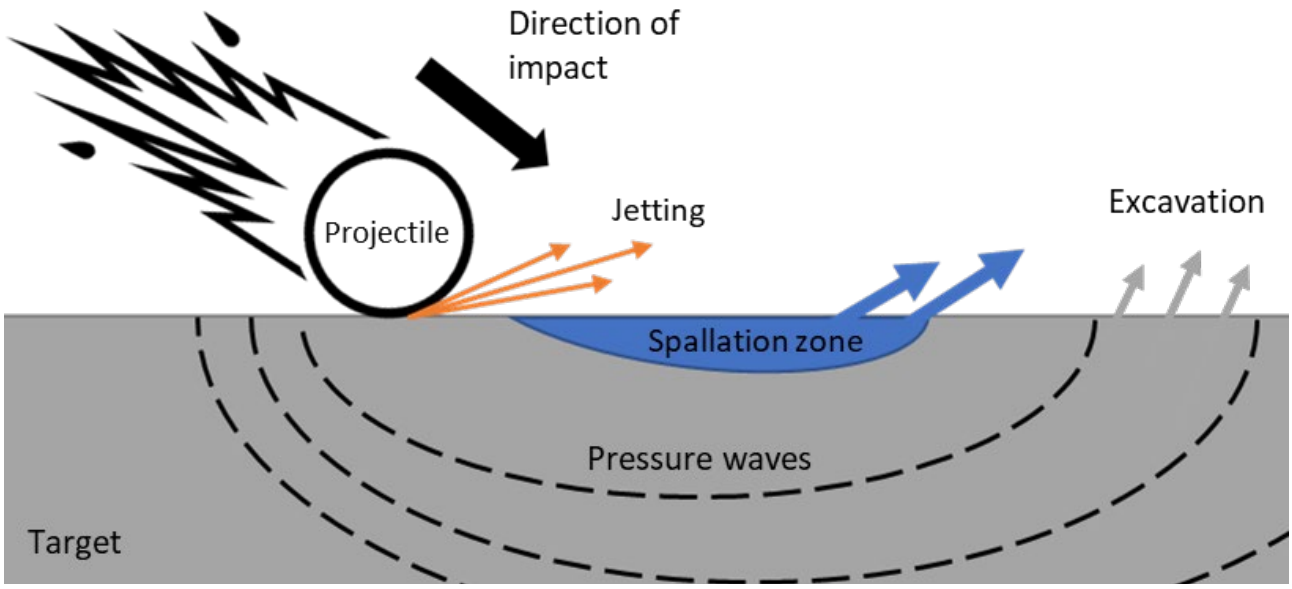

Figure 2.4: *Simplified, schematic cross-section highlighting the formation of a spallation zone during an oblique impact. Jetting occurs closest to the point of impact, followed by the spallation zone (in contact with the free surface), and finally a zone of normal excavation. Each zone represents a decrease in the velocity and pressures experienced by ejecta.*

the free-surface, with ejecta reaching high-velocities but escaping the high-pressures associated with the shock wave due to the complex interactions near the free-surface. Physical support for the spallation model has been confirmed in experimental work investigating spallation, targets fractures, and the associated spall velocities. The presence of a boundary where visible fractures were absent in the near-surface of the target but present below indicated that the near-surface material experienced lower shock conditions than the interior (Polanskey and Ahrens, 1990).

Published investigations of ejecting solid material from the surface of planetary bodies have generally focused on the production of Martian meteorites. Understanding where meteorites may have originated on Mars and an explanation for the relatively low shock pressures experienced by some Martian meteorites (Fritz *et al.*, 2002, 2004) are of interest. Initially, three types of meteorites were thought to have originated from Mars, the Shergottite, Nakhlite, and Chassigny (SNC) meteorites. These were later accompanied by Allan Hills 84001 and Polymict Regolith Breccia NWA 7034 and its associated pairs (Udry *et al.*, 2020). Originally, they were thought to have been generated by one very large impact (>100 km diameter), ~200 Myr ago (Vickery and Melosh, 1987), but later modelling work by Head *et al.* (2002) questioned these results and suggested an alternative production. High-speed ejection was suggested to be efficient for craters as small as ~3 km in diameter, ejecting material at the decimetre scale, depending on the composition of the target material. Both scenarios require the high-speed ejecta to surpass the escape velocity of Mars (~5 km s^{-1}), so the energy imparted by both small and large impactors must have been sufficient to propel target material beyond this threshold. Subsequent modelling work provided evidence that moderately oblique impacts (30°−40°) on Mars produce substantially more high-velocity, solid ejecta that than vertical or near-vertical impacts (Artemieva and Ivanov, 2004), all of which originated from the spallation zone in the near-surface. This reinforced the results from experimental work with impacts into regolith targets by Yamamoto (2002), albeit at relatively low impact velocities (maximum of ~0.27 km s^{-1}), where a higher proportion of high-speed ejecta was produced at progressively lower impact angles. Combining mineralogical observations of Martian meteorites with results from numerical modelling, Fritz *et al.* (2005) concluded that rocks launched from the Martian surface could experience pressures as low as 5 GPa and post-shock temperature increases as little as 10 °C. The relatively low pressure and temperature regimes allowed for the possibility of ejecting Martian rocks with potentially viable organisms within. Additionally, ultramafic rocks with low compressibility, low porosity (<10 %), and low pre-impact temperatures, such as those on the surface of Mars, can positively contribute to the enhanced survival of organisms in ejected material (Meyer *et al.*, 2011).

The process by which meteorites are ejected from Mars was challenged by De Carli *et al.* (2007) who argued that

the commonly accepted production via spallation was impossible due to violating conservation of momentum. The theoretical maximum particle velocity in the presence of a shock wave is approximately double the particle velocity of the shocked state (u_{pH}). This is known as the "velocity-doubling rule" when considered at the free surface of a target. De Carli *et al.* suggested that ejecting material at velocities >5 km s^{-1} whilst experiencing pressures <10 GPa violated Hugoniot relations, particularly the relationship between particle velocity and pressures defined by the equation of state of a material in numerical modelling. Essentially, it was suggested that the low pressures found near the free surface in simulations were artefacts of the numerical simulations and did not represent reality. De Carli further questioned the validity of spallation producing low-pressure, high-speed ejecta (De Carli, 2013), suggesting alternative mechanisms of ejection. The favoured mechanism was ejection via vapor acceleration, accredited to Wasson and Wetherill (according to a personal communication to De Carli in 2011). Comparable to a two-stage gas gun in a laboratory-based setting, compression of water in the near-surface via an impact (~12 km s^{-1} impact velocity for a rock-based impact on Mars) heats water to >15000 K, vaporises, and reaches an expansion velocity >5 km s^{-1}. Any escaping vapour through fissures in the sub-surface could release entrained rocks with little shock-based metamorphism and propel them beyond escape velocity. However, the mechanism neglects the contribution of the projectile motion on the target materials and does not consider any complications related to the expansion of the water vapour.

Additional mechanisms have been suggested to further explain the plausibility of spallation producing meteorites, especially for the production of Martian meteorites. Based on a vertical impact, the maximum ejection velocity would be reduced from the maximum particle velocity (u_{pH}) to $\sqrt{2}u_{pH}$ (Kurosawa *et al.*, 2018). However, this "maximum velocity" can be overcome by a process named "post-shock acceleration", described as a more gradual acceleration by the compressive nature of the ejection flow near the point of impact (Kurosawa *et al.*, 2018; Okamoto *et al.*, 2020). The pressure gradient is directed upward and outward, leading to efficient acceleration produced by sustained compression around the target surface. Oblique impacts are more efficient at accelerating material to high speeds than vertical impacts (Okamoto *et al.*, 2020) and so this mechanism can eject material within the spallation zone at both high-velocity and low-pressure, breaking no laws of conservation in the process.

If the possibility of hypothetical biological material escaping Mars is to translate to biological material escaping from Earth by the same mechanism, the ejecta will need to overcome a significantly higher escape velocity threshold (~11.2 km s^{-1}) whilst remaining solid. Whilst investigating the formation of the Cretaceous–Paleogene (K–Pg) boundary layer, several simulations of Chicxulub-scale impact scenarios were produced by Artemieva & Morgan (2009). Although their

simulations did not aim to investigate the production of low-shock ejecta, their results found no material ejected at escape velocity that was not shocked beyond the level likely to destroy entrained biomarkers (>50 GPa). However, these simulations used a relatively low spatial resolution of 12-15 cells per projectile radius, with the results for the mass of ejecta reaching a certain pressure and velocity threshold only being tabulated in fractions of 10^{-3} impactor masses. Theoretical estimates using extrapolation of an analytical model of spallation (Melosh, 1984, 1985) suggest that a mass of ejecta equivalent to as much as 10^{-5} to 10^{-2} of the original impactor's mass may escape Earth's gravity without exceeding a shock pressure of 10 GPa (Armstrong *et al.*, 2002; Armstrong, 2010). This leaves room for a small proportion of target material (equivalent to 10^{-4} to 10^{-5} impactor masses) to be ejected from the surface of Earth at low pressures.

2.3.2 Meteorite survival during hypervelocity impacts

The fate of the projectile in impacts has been previously assessed by multiple studies. Projectile survivability is influenced by multiple factors in the impact process including impact velocity (Melosh, 1989; Bland *et al.*, 2008, Kurosawa and Genda, 2018), projectile material (Crawford *et al.*, 2008; Daly and Schultz, 2013; Svetsov and Shuvalov, 2015; Wickham-Eade *et al.*, 2018), projectile porosity (Wünnemann *et al.*, 2008; Jutzi *et al.*, 2008; Güldemeister *et al.*, 2013), target porosity (Wünnemann *et al.*, 2006; Avdellidou *et al.*, 2016), target material (Christiansen *et al.*, 1993; Davison *et al.*, 2011; Burchell *et al.*, 2014a, 2014b), and angle of impact (Pierazzo and Melosh, 2000; Davison *et al.*, 2011; Potter and Collins, 2013; Nishida *et al.*, 2019). Numerically simulated hypervelocity impacts have indicated the survival of rocky projectiles impacting multiple planetary bodies including Earth (Pierazzo and Melosh, 2000; Wells *et al.*, 2003; Potter and Collins, 2013; Beech *et al.*, 2019), the Moon (Bland *et al.*, 2008; Yue *et al.*, 2013), Europa (Pierazzo and Chyba, 2002), and Vesta (Turrini *et al.*, 2014; Turrini *et al.*, 2016; Daly and Schultz, 2016). Some numerical models also indicate that volatiles and organic material within projectiles may survive impact with the Moon (e.g. Crawford *et al.*, 2008; Ong *et al.*, 2010; Svetsov and Shuvalov, 2015).

Projectiles in laboratory-scale experiments can survive hypervelocity impacts with a multitude of different target materials (Daly and Schultz, 2015; Wickham-Eade *et al.*, 2018). Examples of surviving asteroidal material have been found in lunar samples from Apollo 11 (Goldstein *et al.*, 1970; McKay *et al.*, 1970; Quaid and Bunch, 1970), Apollo 12 (Wood *et al.*, 1971; Zolensky *et al.*, 1996; Joy *et al.*, 2016, 2020), and Apollo 16 (Jolliff *et al.*, 1993). Fragments of surviving material have also been identified in lunar breccias, including a chondritic fragment within lunar meteorite Pecora Escarpment 02007 (Day *et al.*, 2006; Liu *et al.*, 2009; Joy *et al.*, 2012), and younger Apollo 16 regolith breccias (Joy *et al.*,

2012). More recently, discovery of a possible terrestrial clast in Apollo sample 14321 by Bellucci *et al.* (2019) may provide physical evidence for terrestrial material surviving impact with the lunar surface. However, there is currently an active debate over this interpretation and the provenance of the sample has now been questioned in more recent work (Warren and Rubin, 2020).

The median survival time for centimetre to meter scale rocky material on the surface of an airless body (like the Moon) has been estimated to be between 40 and 80 Ma, with some surviving up to 300 Ma, depending on the material (Basilevsky *et al.*, 2013, 2015). This implies that if projectile material is to survive over long periods of time (e.g., billions of years) after impact, then the material must be protected from destructive processes at the surface. Rapid burial of meteorites by crater and basin ejecta, and/or by mare basalt flows, could potentially provide protection for meteoritic material (e.g., Crawford and Joy, 2014; Joy *et al.*, 2016). The most likely form of protection will come from the lunar surface itself, more specifically, covering via the lunar regolith. This can occur during subsequent projectile impacts distal to the previous surviving meteorite so as to not significantly heat or alter it, but proximal enough that ejecta is thrown over it. Later, basalt lava flows could further protect the material by creating an insulating layer overtop the ejecta. In order to be used as resources or for samples with scientific value, these meteorites would need to be at least partially exhumed at a later date via impact gardening.

In terms of using surviving meteorites as resources for extended human activities on the lunar surface, the density and concentration of useful materials is of critical importance. If a large amount of meteoritic material is predicted to survive impact, but spreads over a large area of many 10s or 100s of kilometres, then the collection and processing of the material may not be economically viable. Preferably, material will be concentrated as a solid block of surviving material or spread in relatively rich "vein" of material, downrange from the impact site, perhaps after an oblique angle of approach. Whilst there has been plenty of investigation into the fragmentation of projectiles upon impact (e.g., Melosh *et al.*, 1992; Nagaoka *et al.*, 2013; Wickham-Eade, 2017; Nishida *et al.*, 2019), there is a lack of data on the concentration of surviving fragments proximal to the impact site. Work by Yue *et al.* (2013) suggests that projectile remnants may become concentrated in the central peaks of complex impact craters on the Moon, and Potter and Collins (2013) have investigated how large fragments of a meteorite have survived at the Morokweng crater on Earth. Iron rich meteorites which have partially survived collision with the lunar surface may provide high localised concentrations of native iron, and associated siderophile elements (Haskin *et al.*, 1993; Wingo, 2004). Additionally, Wieczorek *et al.* (2012) have interpreted prominent lunar magnetic anomalies as being due to surviving Fe-rich meteoritic debris. Further afield, Daly and Schultz (2016)

suggest that craters at or above the equilibrium crater diameter on Vesta are able to preserve localised deposits of carbonaceous impactor material. With a similar high porosity and low-density regolith as the Moon, it is reasonable to assume that the same could occur on the lunar surface when considering projectiles with relatively low impact velocities (<10 km s^{-1}).

The ejection of material from Mars may not only lead to the meteorites we find on Earth, but also to the presence of martian material on the moons Phobos and Deimos. It is expected that Phobos' regolith will contain, on average, 2 ppm of Martian surface material ejected within the past 10 Myr (Chappaz *et al.*, 2013). Over the last 500 Myr, Ramsley and Head (2013) predict much of the Martian ejecta could be concentrated preferentially in the uppermost 0.4–1.0 m of the regolith of Phobos. During the last 3.5 Gyr, a bulk concentration of ~250 ppm could potentially be found in the Phobos regolith. Basin forming events on Mars may have produced thick layers of ejecta with the potential reach Phobos in significant quantities over a very short period of time. If this ejecta was to reach Phobos, deposit in contiguous layers, and survive subsequent impact events, they may remain distinguishable within the deep Phobos regolith as recognisable and distinct events (Ramsley and Head, 2013).

2.3.3 Biological material within ejecta

The survival of solid rock post-ejection and subsequently after impact with another body is one thing, but the survival of biological material or the remnants of such are another entirely. Lithopanspermia is the theory hypothesising the spread of life in our Solar System via transfer of biological material between planetary bodies, entrained within ejected rock fragments. The theory requires life to survive the ejection from a planetary surface, the journey through space toward the prospective target surface, and the final impact with the new planetary body (e.g., Melosh, 1988; Mileikowsky *et al.*, 2000). By some, this process has been deemed too difficult a barrier for any life to survive alive or intact, whilst others consider the process viable for at least the evidence of life to survive as biological markers (biomarkers; e.g., Mimura and Toyama, 2005; Stöffler *et al.*, 2006; Parnell *et al.*, 2010; Meyer *et al.*, 2011; Burchell *et al.*, 2014a, 2014b, 2017; Matthewman *et al.*, 2015) Belief in such survival has led to multiple studies investigating the transfer of organic biomarker material (or evidence that there once was) entrained within rocks between multiple planetary bodies (Worth *et al.*, 2013), some in specific scenarios including Mars to Earth (Artemieva and Ivanov, 2004; Fritz *et al.*, 2005), Mars to Phobos (Fujita *et al.*, 2019), Earth to Mars (Beech *et al.*, 2019), Earth to the Moon (Armstrong *et al.*, 2002; Crawford *et al.*, 2008; Beech *et al.*, 2019; Halim *et al.*, 2021a) and Venus to the Moon (Cabot and Laughlin, 2020). The most effective biomarkers are

organic compounds with specific biological sources, whose structures can be preserved through geologic time. In the case of surviving biomarkers after an impact event, these compounds must not only survive geological time but also high pressures and temperatures.

The survival of hypothetical microbial life or biomarkers in Martian material and the subsequent transfer to Earth via Martian meteorites has been studied via numerical and experimental modelling. Mileikowsky *et al.* (2000) deemed adequate survival of microbial material ejected from Mars when the ejecta experienced pressures ~1 GPa. However, most evidence provided by SNC meteorite samples reveal pressures of at least 5 GPa, so this 1 GPa threshold is likely unrealistic for the potential survival of microbial material ejected from Mars. On the other hand, biomarkers can withstand much higher pressures and temperatures than the life that produces them. An experimental impact study investigating the survival of amino acids, many of which are produced by biotic processes, found that branched, alkyl side-chain amino acids could survive after experiencing pressures up to 28 GPa (Bertrand *et al.*, 2009).

The early Earth would have experienced many large impacts, potentially large enough to sterilise the planet of any early life (Moorbath, 2001; Schoenberg *et al.*, 2002; van Zuilen *et al.*, 2002). If ejecta from such an impact (e.g., 300 km diameter, 30 km s^{-1} velocity) were home to entrained *Bacillus subtilis* and *Deinococcus radiodurans* with initial cell population on the order ~10^5 cells kg^{-1}, there may be potential for some organisms to survive ejection and subsequent in fall back to the Earth after a period of 3000-5000 years (Wells *et al.*, 2003). Survival of life-saturated material into *cis*-lunar space and returning to Earth within a relatively short period of time may have allowed for a sterilised Earth to be reseeded with surviving life in the orbiting ejecta. However, this requires a significantly lower escape velocity than material reaching the Moon (~4-5 km s^{-1} versus ~11 km s^{-1}) and so represents a much higher volume of material likely to survive after ejection. Further discussion on the ejection and survival of organic material from Earth to the lunar surface can be found later in this work, specifically Chapters 4 and 5 in sections 4.1 and 5.1, respectively.

2.4 Carbonaceous chondrites

One of the reasons for investigating the survival of projectiles impacting planetary surfaces is to determine if they can be used as caches of materials for ISRU. This is most pertinent to the lunar surface, where there are already plans for crewed missions in the near-future (Bridenstine, 2019) and the potential to create a permanent and sustainable human presence on the Moon (NASA, 2020). It is therefore necessary to determine which materials/elements are needed to maintain a sustainable presence on the Moon, which of these materials are not native/abundant in the lunar crust (as

discussed in Section 2.1), and those which can be provided by projectiles that survive impacts. Carbon and nitrogen are two such elements that are uncommon in the lunar crust yet very important to the longevity of human missions to the lunar surface. The following section considers impactors which contain the highest proportions of these elements, carbonaceous chondrites, and describes the many variations in this suite of meteorites.

Meteorites can be rudimentarily and loosely classified by their appearance and relative composition to one another, such as iron, stony, and stony-iron. However, it is more appropriate to name meteorites based on their composition, resulting in the classifications of chondritic (undifferentiated) or achondritic (differentiated) meteorites. Chondrites are undifferentiated meteorites that can contain chondrules, however they are better described as meteorites that have solar-like compositions and are derived from asteroids that did not evolve enough to experience planetary differentiation (Weisberg *et al.*, 2006). They can be divided into three separate classes: ordinary, enstatite and carbonaceous. Carbonaceous chondrites are the most primitive of the three classes and can be further divided into nine groups, primarily based on the properties of the original meteorites used as type specimens, including bulk chemistry and mineralogy. These sub-classes include CI (Ivuna-like), CM (Mighei-like), CO (Ornans-like), CV (Vigarano-like), CK (Karoonda-like), CR (Renazzo-like), CB (Bencubbin-like), CH (high Fe; ALH 85085-like) and C UNGR (ungrouped samples exhibiting likenesses to many groups). The carbonaceous chondrite class is thought to be representative of the materials that formed the protoplanetary disk at the conception of the Solar System (Zolensky and McSween, 1988). The CI, CM and CR groups are the most hydrated, meaning that they have H_2O or OH trapped within the structure of minerals in the meteorite, such as phyllosilicates. Carbonaceous chondrites are characterised by whole chondrite (Mg-normalized) refractory-lithophile-element abundances ≥1 CI, and O-isotopic compositions that plot near or below the terrestrial fractionation (TF) line. They have a range of chondrule sizes, from the large rimmed chondrules in CV and CR chondrites to the small chondrules in CH chondrites and the lack of any chondrules in CI chondrites. Although many carbonaceous chondrites (e.g., CI, CM, CO, CV, CR) are matrix-rich, some (e.g., CH, CB) are matrix-poor (Weisberg *et al.*, 2006). A secondary classification can be applied which reflects the petrographic type of the meteorite (Type 1-6). This indicates the type and extent of alteration (both thermal and aqueous) that the particular sample has undergone on the asteroid parent body.

2.4.1 Properties of the carbonaceous chondrite groups

CI (Ivuna-like): Often considered the most primitive Solar System material we have on record, being similar in composition to the Sun's photosphere. Their mineralogy is dominated by phyllosilicates (serpentine, smectite, chlorite etc)

as well as some minor phases including olivine, pyroxene and carbonates (Busec and Hua, 1993). They contain the highest abundances of carbon (up to 6 wt.%) and nitrogen (up to 0.5 wt.%; Sephton, 2002). CI meteorites are almost 100% matrix, with no chondrules present (McSween, 1979), and are the most hydrated of all carbonaceous chondrites, with up to 20 wt.% H_2O content (Barnes *et al.*, 2016). All CI chondrites are of petrologic Type 1, indicating that they are heavily aqueously altered and have never been heated above 323K (50°C). They can be one of the most porous and least dense carbonaceous chondrite samples, with an average grain density of 2.27 g cm^{-3} and a range of porosities from 2-35% (Britt and Consolmagno, 2000).

CM (Mighei-like): The most abundant group of carbonaceous chondrites, characterised by very small (0.1-0.3 mm) chondrules in a matrix with volumes ranging from ~55-85% (McSween, 1979). They contain refractory elements such as calcium-aluminium inclusions (CAIs) and amoeboid olivine aggregates (AOAs) which have been partially or completely replaced by phyllosilicates (e.g. cronstedite, greenalite, antigorite, chrysolite; e.g., Weisberg *et al.*, 2006). These refractory elements are some of the most primitive materials we have in the Solar System, thought to have formed as independent objects in the protoplanetary disk by high-temperature processes that included condensation and evaporation. Minor phases include olivine, pyroxene and carbonaceous matter (Busec and Hua, 1993). CM chondrites contain a wealth of organic material, including over 90 amino acids in the Murchison meteorite (CM2) alone (Koga and Naraoka, 2017). Most are petrological Type 2, however aqueous alteration in CMs varies widely (Rubin *et al.*, 2007) and contain on average 11 wt.% water (Barnes *et al.*, 2016). They have porosities similar to that of CIs (3-30%) and average grain densities ~2.71 g cm^{-3} (Britt and Consolmagno, 2000).

CR (Renazzo-like): The third and final carbonaceous chondrite group that contains H_2O in its mineral structures, but is the least hydrated of the three groups at an average of 5 wt.% H_2O (Barnes *et al.*, 2016). Similar in composition to CMs in some respects (phyllosilicates and magnetite), however they differ in containing reduced metal (Ni-Fe and FeS) in black matrix and large olivine rich chondrules (which compose ~50% of the volume; Weisberg *et al.*, 2006). The mineralogy, petrology, and chemistry of CR chondrites and their components are described in detail in several papers (McSween, 1977; Bischoff *et al.*, 1993; Weisberg *et al.*, 1993, 2004; Kallemeyn *et al.*, 1994; Krot *et al.*, 2000, 2002; Aléon *et al.*, 2002). Due to the presence of denser elements and minerals (such as Ni-Fe and olivine), the average grain density is higher than CI and CM chondrites at 3.11 g cm^{-3} and also a lower porosity at just 2-11% (Britt and Consolmagno, 2000).

CO (Ornans-like): Major mineralogy of CO chondrites is olivine, contained within smaller (150 μm) chondrules surrounded by relatively high matrix abundances (35-50%; McSween, 1979). Minor phases can include Ca-rich and -poor clinopyroxene, kamacite, taenite, magnetite, maghemite, ferrihydrite, feroxyhyte, serpentine (Busec and Hua, 1993). Three characteristics have been used to link the CM and CO chondrites and support a CM-CO clan (Kallemeyn and Wasson, 1981, 1982): (1) chondrules are similar in size and anhydrous minerals have similar compositions; (2) refractory lithophile-element abundances are similar; and (3) O-isotopic compositions of high-temperature minerals are similar (Weisberg *et al.*, 2006). Unlike CMs, CO chondrites are anhydrous and so contain no phyllosilicates or aqueously altered minerals. They do however have a high average grain density (3.69 g cm^{-3}) and quite high porosities (4-35%; Britt and Consolmagno, 2000).

CV (Vigarano-like): Dominated by large olivine chondrules (1mm), a high percentage of matrix (35-50%) (McSween, 1979) and high abundance of CAIs and AOAs. They have a wide variety of compositions and can be divided into oxidised (CV_{oxA} and CV_{oxB}) and reduced (CV_{red}) (Weisberg *et al.*, 2006). Minor mineral phases include magnetite, Fe-Ni sulphides, enstatite, diopside, fassaite, andradite, chromite, spinel, anorthite, sodalite (Busec and Hua, 1993). The CV_{oxB} chondrites have experienced some aqueous alteration and can contain hydrous phyllosilicates. Porosity can vary from none at all up to 26%, with average grain densities of 3.51 g cm^{-1} (Britt and Consolmagno, 2000).

CK (Karoonda-like): A high abundance of matrix and large chondrules (700–1000 μm), most of which have porphyritic textures, are found in CK chondrites. Major mineralogy composes of olivine and plagioclase, whilst minor phases include pyroxene, magnetite, Fe-Ni sulphides and phosphates (Tomeoka *et al.*, 2005). They exhibit dark-grey/black colours due to high percentages of magnetite in the matrix and dark silicates (Fe-olivine and pyroxene). Most contains larger chondrules, CAIs and some shock veins. Thought to have formed under oxidising conditions yet no aqueous alteration seen, and oxygen signatures suggest a close relation to CO/CV (Kallemeyn *et al.*, 1991). Veins could indicate a history of impact and most CK chondrites are of high (4–6) petrologic type. From the few samples that have been analysed, porosity is lower at 22% and average grain density is similar to CO and CV at 3.58 g cm^{-3} (Consolmagno *et al.*, 2008).

CB (Bencubbin-like): A very rare group, with only a handful of samples ever recorded. They contain incredibly high percentages of metals (50-80 wt.%) with very little chondrule and matrix (<<1%) material (Weisberg *et al.*, 2006). Minor mineral phases include troilite, anorthite and chromite (Weisberg *et al.*, 2001). Porosities are low (2-6%) and average grain densities are very high, more than any other carbonaceous chondrite at 5.66 g cm^{-3} (Macke *et al.*, 2011).

CH (High metal): Characterized by small (<50–100 μm in diameter) chondrules, which are mostly cryptocrystalline in texture, and high abundance of Fe-Ni metal (up to 40 vol%; Weisberg *et al.*, 2006). Major phases include Fe-Ni metals, olivine, pyroxene, whilst minor phases are CAIs, sulphides (Scott, 1988). They are anhydrous with very little matrix (5%) and almost no porosity in most cases (Macke *et al.*, 2011). Their high metal content and low porosity gives them a higher-than-average density at 3.64 g cm^{-3} (Macke *et al.*, 2011).

C UNGR (ungrouped): This final group of carbonaceous chondrites can contain textures, mineralogy's, and other characteristics of any of the groups described. Sometimes they may display similarities to just a couple of groups, but others may even have multiple clasts of different groups in the same sample. This means that the meteorite cannot be placed into one single group and so must either be classes as a new group or be placed in the ungrouped category and be assessed later on. A good example of this group is the Tagish Lake meteorite, possibly one of the most diverse and interesting carbonaceous chondrites in the worldwide collection (Zolensky *et al.*, 2002; Herd *et al.*, 2011).

2.4.2 Parent asteroid properties

Carbonaceous chondrites found in the Earth's meteorite collection are small fragments of much larger parent asteroid bodies. These are the bodies that are of interest when considering the survival of carbonaceous material on the Moon, depositing large enough masses of carbon and nitrogen bearing compounds to act as a potentially significant resource cache. Therefore, it is important to understand the composition and nature of these parent bodies and not the meteorites we find on Earth, when considering which parameters to use for numerical modelling.

Visible and near-infrared reflectance spectra of C, G, B, F, and D-type asteroids have been compared with laboratory measurements of meteorite samples to link the mineralogical composition of asteroids and carbonaceous chondrites (Hiroi *et al.*, 1993, 2001; Luu *et al.*, 1994; Burbine, 1998; Botta *et al.*, 2002). Additionally, analyses of amino acids within the CI carbonaceous chondrites Orgueil and Ivuna provide a possible link of these meteorites to a cometary parent body (Ehrenfreund *et al.*, 2001). This suggests that the amino acids in CI chondrites Orgueil and Ivuna could have been synthesized in an early aqueous alteration phase on a parent body that was rich in cometary components such as water and ammonia. However, the capability for comets to contain liquid water needed for aqueous alteration at any point in their lifetime is controversial, with some models suggesting the circumstances required are unlikely to near-impossible (Podolak & Prialnik, 1997). Mass and volume estimates of many asteroids have been produced using a variety of remote sensing techniques. For mass, these include measuring effects of the motion on the orbit of natural satellites, perturbations on

spacecraft orbiting an asteroid body, and for large objects (specifically Ceres, Pallas, and Vesta), the perturbations on the orbit of Mars. Volume estimates for many asteroids can be made using an effective radius determined by the Infrared Astronomical Satellite (IRAS) Minor Planet Survey (Tedesco, 1992). For some others (e.g., Dunham *et al.*, 1990), asteroid shapes and therefore their volumes can be determined by occultation techniques. Shape modelling using photometric data from telescopic measurements can also be used to estimate the size and volume of asteroids (Hanuš *et al.*, 2017). Of course, the most accurate shape, volume, and mass estimates come from those bodies which have been directly orbited by spacecraft (e.g., Bennu, Ryugu, Vesta). The combination of mass and volume estimates can be used to indirectly measure the bulk densities and porosities of asteroids, which are critical for the parameters used in numerical modelling.

The bulk densities of multiple primitive asteroids (including C, F, and B-types) have been determined as systematically lower than other less primitive examples (1–2 g cm^{-3} and 2–3 g cm^{-3}, respectively) in a study of over 40 asteroid bodies (Hanuš *et al.*, 2017). The estimated macroporosity of an average C-type asteroid is ~30%, but individual asteroids can range between 5% and over 60%, depending heavily upon their assumed mineralogical composition. When considering total porosity, including macroporosity (large scale fractures and pore spaces) and microporosity (grain-scale porosity), the average increases to 35–40% (Britt *et al.*, 2002). For example, Mathilde (C-type asteroid) is likely to have a porosity of 40 ± 6% if composed of CI material, 51 ± 8% if composed of CM material, or 61 ± 9% if composed of CO/CV material (Veera *et al.*, 1999). Other C-types include Ryugu (50% porosity, Sugita *et al.*, 2019) and Ceres (5–15% porosity, Zolotov, 2009; Castillo-Rogez, 2011), however Ceres is a large (~950 km diameter) and likely differentiated body which explains a higher bulk density and lower porosity. Pallas is another large example (~530 km diameter), part of the B-type asteroids, but contrary to other primitive asteroids it appears to lack any significant macroporosity (Britt *et al.*, 2002). Asteroid macroporosity is estimated by taking the bulk porosity of an asteroid and subtracting the average porosity of a known asteroid meteorite analogue. The significance of any microporosity is assumed to be negligible and therefore this technique provides a direct estimation of the large-scale voids and fractures of a particular asteroid. However, a well-studied example of a porous B-type asteroid is that of Bennu, with an estimated 40 ± 10% porosity (Chesley *et al.*, 2014; Lauretta *et al.*, 2014). The largest Martian satellite, Phobos, exhibits many of the characteristics of D-type asteroids and has a potentially similar porosity to such primitive objects, estimated at 30 ± 5% (Andert *et al.*, 2010). Overall, primitive asteroids that have the potential to represent carbonaceous chondrite parent bodies are likely very porous and as a result have relatively low bulk densities. Many low-albedo, primitive asteroids can be described as loosely consolidated or

"rubble-pile" asteroids, where the bodies are highly fractured and may compose of a collection of smaller objects held together by gravity (Britt *et al.*, 2002; Richardson *et al.*, 2002).

2.4.3 ISRU of materials in carbonaceous chondrites

Whilst the lunar regolith and near surface materials may provide many elements that will be useful for future missions to the lunar surface, carbon and nitrogen have only been found in abundances of ppm or less (as detailed previously in this chapter). However, both of these elements are relatively abundant in a variety of forms within some types of carbonaceous chondrites (e.g., Sephton *et al.*, 2002; Pearson *et al.*, 2006; Chan *et al.*, 2016; Tartèse *et al.*, 2018; Parker *et al.*, 2022) and are therefore also likely found in the parent asteroids that may have impacted the Moon. The next subsection will detail ways in which these elements could be useful in terms of ISRU for humans visiting or living on the lunar surface.

Carbon can be used in a variety of scenarios related to human development on the Moon. In the near-term, many of the current and near-future options for spacecraft navigating to the lunar surface no longer use liquid oxygen and liquid hydrogen as fuel (LOX+LH2). Instead, transport systems such as the SpaceX Starship use a mixture of liquid oxygen and methane (CH_4). Refuelling an LOX+LH2 engine using ISRU on the Moon would require the presence on large volumes of H_2O, which has contributed to the interest in permanently shadowed regions at the lunar poles. In those regions, generally within craters, layers of frozen H_2O are thought to be present in quantities that may sustain the refuelling of rockets (Colaprete *et al.*, 2010). However, the requirement of methane for vehicles like Starship requires a source for carbon, which surviving carbonaceous chondrites may provide. Additionally, in the near- to mid-term, carbon in the form of silicon-carbide (SiC) may be of great interest when considering building permanent structures on the surface. Composite materials made from polypropylene resin reinforced with SiC provide greater protection from space radiation than conventional metal shielding (Naito *et al.*, 2020). The production of SiC on the lunar surface by carbothermal reduction of the regolith has been suggested (Samouhos *et al.*, 2022), however this requires solid carbon as a prerequisite and would have to be supplied from extra-lunar sources. Carbonaceous chondrites, however, can contain SiC in low but still significant masses when considering large impactors, up to 0.01 wt. % (Sephton, 2002), and may provide a source of SiC native to the lunar surface as they are particularly resistant to both high shock-pressures and temperatures. In the longer-term, carbon may be used as the basis for life support systems, agriculture for growing food (sequestering into lunar-based soils), and the production of steel for construction purposes.

Another consideration for sustained human-based missions in the future is for the availability of food. Transporting any material from Earth is costly and once the infrastructure is in place to allow humans to spend longer periods of time on the lunar surface, transporting large masses of food would become unsustainable. Similarly, transporting soil from Earth as a means to grow food on the Moon would also take a significantly amount of time, money, and resources to sustain. Therefore, the idea of lunar-based agriculture has been discussed for decades (Ming and Henninger, 1989). Lunar soils contain many of the necessary nutrients required for the successful growth of higher plants. Based on the composition of returned lunar soils and the dissolution properties of lunar dust (Keller and Huang, 1971), lunar soils may have the potential to be an effective medium for plant growth. Macronutrients including Mg, Ca, and S, as well as micronutrients Fe, Mn, and Zn, are readily available within lunar soil in quantities suitable for plant growth (Turkevich, 1973; Hossner and Allen, 1989). Limited success of plant growth in lunar regolith simulant JSC1-1A (McKay *et al.*, 1993; Sibille *et al.*, 2006) has shown that agricultural development using lunar soils may be possible (Wamelink *et al.*, 2014). However, in the lunar simulant many germinated plants died or stayed very small, with only one plant forming a flower butt. Additionally, growth within a simulant does not extend to growing plants in full lunar soil. More recent work has explored the growth of plants within lunar soils using samples from Apollo 11, 12, and 17 (Paul *et al.*, 2022). The terrestrial plant *Arabidopsis thaliana* was able to germinate and grow in the diverse lunar regoliths but struggled to develop and many presented severe indicators of stress. Plants grown in the more mature Apollo 11 regolith struggled the most, whilst the least mature Apollo 17 provided the best conditions for growth. Growing plants on the Moon itself comes with more obstacles to overcome, where the combination of available nutrients, including reactive nitrogen, and the influence of gravity would need to be explored further for *in situ* plant growth. The main nutrient missing from lunar soil in a form available to plants is a reactive form of nitrogen, crucial for effective plant growth. Carbonaceous chondrites can contain a variety of nitrogen bearing molecules, especially in the CI and CM groups (discussed earlier in this chapter), in proportions up to 0.5 wt.% (Sephton, 2002; Pearson *et al.*, 2006). These nitrogen bearing molecules could be used as the nitrogen source for lunar-based soil for agriculture, if they survive in significant quantities after a CI/CM-like impact on the Moon.

The need for sustainable ISRU practices will be paramount for the longevity of exploration on the Moon, especially for crewed missions and the long-term presence of humans. Even if landed carbonaceous chondrite material can be found, extracted, and utilised for prospective lunar industrial purposes, carbon and nitrogen will still remain a relatively scarce and finite resource. It has been suggested that typical hydrocarbon plastics should be replaced with silicone plastic

for production on the lunar surface for a multitude of reasons (Ellery, 2020), including: (i) hydrocarbon plastics requiring complex manufacturing reagents and processes; (ii) the alternating Si–O backbone of silicon oils (siloxanes) minimises the consumption of carbon-based volatiles which are incorporated into the side chains only; (iii) silicone plastic being resistant to UV-radiation; (iv) silicone plastic has higher operational temperature tolerance. Adopting this alternative polymer structure could increase the longevity of carbon reserves provided by carbonaceous chondrites and provide additional benefits for lunar operations. In this situation where carbonaceous chondrites provides a native source of carbon, all of the necessary constituents for producing silicon plastics (e.g., C, H, O, Si, Al, Ni) could be provided by the lunar surface, apart from a chlorine reagent needed for producing methlychloride. Carbon monoxide (CO) is also required as a reagent for the production of many metals, including Ni, Fe, and Co. One approach is the Mond process, named for Ludwig Mond, where heated CO is passed over metallic granular material at modestly high temperatures (~100° C) under pressures of up to 10 atmospheres. Interaction between a Fe-Ni metal and the heated gas forms iron and nickel carbonyls in vapour form, which can then be removed and condensed as metal films. Such a technique has been suggested for extraction of metals from NEAs using a spacecraft (SHEPHERD) to capture, process, and utilise resources from an asteroid in a gas-filled enclosure (Jenniskens *et al.*, 2015). The same process has been suggested for use on the lunar surface already, with Spudis (2014) recommending that “it makes sense to develop the technologies and operational procedure for remote mining on the Moon rather than on asteroids” in a piece for the Smithsonian Magazine.

2.5 Summary

This chapter began with a broad overview of the geology of the lunar surface, then detailed the current research on particular native elements and compounds that could be used for *ISRU* if extracted from the Moon in future missions. The lack of significant quantities of indigenous lunar carbon and nitrogen was then explored. Next, the physical and mechanical processes behind impacts and crater forming processes was described. This led to the discussion of the generation of meteoritic material after large impacts on planetary bodies and the fate of the meteorite projectiles after subsequent impact with a target. Additionally, previous work on the survival of biological material within meteorites is discussed. Lastly, carbonaceous chondrites are described in detail, specifically the various types and their compositions, and how the materials found within them could be used for *ISRU* on the lunar surface.

3 Methods

The main objective of this project is to investigate the survival of a variety of projectiles impacting the lunar surface. In principle, this objective might be met with either experimental or computational techniques. Impact experiments in a laboratory set-up (commonly using a light-gas gun) can be used to approximate the impact process, usually at scales much smaller than those investigated on planetary bodies (i.e., mm-scale vs. m to km-scale impactors; e.g. McDonnell, 2006; Patel *et al.*, 2010; Hibbert *et al.*, 2017). Whilst these practical experiments offer many benefits (e.g., control of and analysis of projectile constituents before and after impact), they are limited in scale and impact velocity (typically <8 km s^{-1}) and have no way to directly measure pressure and temperature within the materials during impact. On the other hand, numerical modelling allows for the simulation of impact processes at any scale required, along with the ability to calculate and record pressures and temperatures for any part of the projectile or target during the entire impact process. As projectile survival is the main focus of this work, accurate pressure and temperature data within the projectile is of critical importance: therefore, a series of numerical modelling experiments are used to achieve the aims and objectives of this PhD project. This chapter describes the numerical modelling techniques and the shock physics code itself that will be utilised in this work as well as the post-processing tools, which will allow for the analysis of raw data and the production of many figures to interpret this data.

3.1 Numerical shocks physics code modelling

A hydrocode is a computational tool used for modelling the behaviour of continuous media (Anderson, 1987). Modelling the formation of an impact crater requires sophisticated computer coding that can not only resolve the passage of a shockwave through a medium, but also the complicated behaviour of the geological material comprising that medium. Breaking down “hydrocode”, the term “hydro“ refers to the fluid nature of a material that experiences high shock pressures and “-code” refers to the numerical nature of the modelling process. When simulating impacts, it is more common to use the term “shock physics code” to emphasize the importance of shock and the behaviour of solid rock-like materials during physical deformation.

Shock physics codes solve multiple partial differential equations that describe the conservation of mass, momentum, and energy. In a three-dimensional hydrodynamic system, there are five equations (one mass, one energy and three components of momentum), with six unknown variables: pressure, energy, density, and three velocity components.

In the two-dimensional system, the three velocity components are reduced to two. A final equation is needed to close the system, which is the equation of state of the material being modelled. This equation of state relates pressure, energy, and density of the material. If the material also has strength, then there are additional stress terms in the energy and momentum equations and another separate equation (the constitutive equation) is required relating those stress terms to the other state variables. The differential equations also need to be discretised, which is often done by replacing the derivatives with finite difference approximations. Section 3.2.1 describes how these equations are solved and discretised within iSALE.

For a computer to interpret the dynamics of a continuous medium it must be divided into distinct "packets" of information via a process known as discretisation. This is normally performed by generating a "mesh" of cells which represent the volume being modelled and can be influenced by external and internal forces specified during the simulation. Time can also be discretised by specifying timesteps at which computational work is processed. During each of these timesteps, the code iterates through each cell in the mesh and updates the position of the materials within that mesh. There are generally three approaches to modelling a material in a hydrocode: Lagrangian and Eulerian (both grid-based methods), and Smooth Particle Hydrodynamics (SPH), a grid-less Lagrangian method (Gingold & Monaghan, 1977).

Lagrangian and Eulerian grid-based methods both use a mesh to determine how material moves during the simulation (Figure 3.1). The Lagrangian grid-based method works using a numerical mesh that moves and distorts with the physical material. Mass, momentum, and energy are transported by the material flow and the grid points in the mesh move

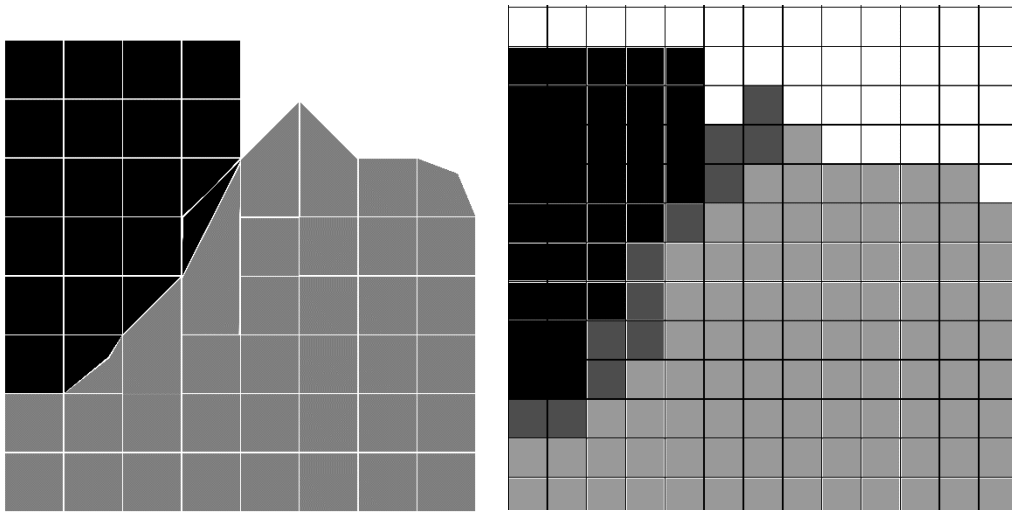

Figure 3.1: *Examples of Lagrangian (left) and Eulerian (right) methods for a projectile (black) impacting vertically into a target (grey) with identical simulation set-ups. In the Lagrangian method, cells move and distort throughout the simulation with material fixed in each cell. In the Eulerian method, material passes through the static mesh and cells may contain multiple materials (here shown in dark grey).*

relative to a fixed spatial coordinate system. Although this can produce problems due to the computational grid becoming overly distorted, it is well suited in describing solid behaviour during impact modelling for small deformations. In the Eulerian grid-based approach the mesh coordinates are fixed, and the material flows through the grid. Thus, mass, momentum, and energy must flow across cell boundaries. Unlike the Lagrangian grid-based method, this prevents extreme distortion of the mesh which can force timesteps to become so small that the calculation is effectively stopped. As material can flow from cell to cell, this can lead to mixing of materials within the same cell. Whilst this may be useful in terms of represented mixed materials that are found in actual impact events, this actually presents a disadvantage of Eulerian, as handling material mixtures is computationally challenging. Finally, the Lagrangian SPH method does not involve the generation of a mesh at all. Instead, the flow of material is described by the motion of a set of points or particles. The velocity and thermal energy of each point is computed along with an assigned mass. SPH functions in a similar way to the Lagrangian grid-based method, but with the added benefit of remaining stable when large displacements are involved, as none of the particles are explicitly connected.

Some of the elements from all of these methods can be used to complement one another in a single simulation, in order to maximise the effectiveness and resulting data of a simulation. When using a grid-based approach, the Eulerian method is the only option for simulating impacts as it can handle large deformations, simulating the dynamic nature of complex geological materials flowing through a defined mesh. SPH could also be used for studying large impact events, however, it tends to require a higher spatial resolution to achieve comparable results. Additionally, it is fundamentally three-dimensional in nature and so less efficiently models vertical impacts and it also does not handle material interfaces very well. Eulerian simulations do not naturally track the fate of a parcel of material in time, providing only information about what is happening at a fixed point in space as time proceeds. Lagrangian ‘tracers’ can be added at the beginning of a Eulerian simulation to track a set volume of material as it flows through the mesh. This provides a way to mitigate the limitation of the Eulerian method by approximately tracking the time evolution of a representative parcel of material. This tracer will record all of the parameters needed to approximately describe the journey of a volume of material through the multitude of pressure and temperature regimes over the course of an impact event.

The work in this thesis adopts the use of the Eulerian mode to solve the differential equations required to simulate impact events and therefore the following sections will describe the models only using this method (Section 3.2.1). The following subsection describes the specific shock physics code used during this project and an overview of the parameters

that are available to use as part of the code. The specific parameters used in the simulations completed for this thesis can be found in Chapter 4 (Section 4.2), Chapter 5 (Section 5.2), and Chapter 6 (Section 6.2).

3.2 iSALE

This work uses iSALE (impact-SALE), a well-established, multi-material, multi-rheology shock physics code (Wünnemann *et al.*, 2006) based on the SALE hydrocode (Amsden *et al.*, 1980). The Simplified Arbitrary Lagrangian Eulerian (SALE) hydrocode that iSALE is based on was developed by Amsden *et al.* (1980) to study fluid flow at all speeds. The SALE code is capable of solving fluid-flow problems using either, or a combination, of the two descriptions. It achieves this by solving a Lagrangian set of differential conservation equations and then, if the Eulerian description is desired, remapping the cell and vertex quantities back onto the original grid. The original SALE code was only capable of simulating a single material and Newtonian-fluid flow. Additions to the SALE code were made in the 1990s by Jay Melosh, Boris Ivanov and collaborators. These included an elasto-plastic constitutive model, fragmentation models, various equations of state (Melosh *et al.*, 1992), and multiple materials improvements to the solution algorithm and the incorporation of damage accumulation and strain-weakening, as well as the implementation of the semi-analytical equation of state (EoS; see Section 3.2.2), ANEOS (Thompson and Lauson, 1972). This resulted in the SALEB hydrocode (Ivanov *et al.*, 1997), capable of simulating impact events throughout the entire impact process.

The iSALE shock physics code extended the SALEB code further. Additional improvements include a modified strength model (Collins *et al.*, 2004), an epsilon-alpha (ε-α) porosity-compaction model (Wünnemann *et al.*, 2006; Collins *et al.*, 2011a), and a dilatancy model for including the effects of shear bulking during impacts (Collins, 2014). Shear bulking is the process of reducing the bulk density of geological materials that have been fractured and subsequently made more porous than their original form. These material models and the definition of their parameters are explained in detail in Sections 3.2.3 and 3.2.4.

iSALE has been benchmarked against other shock physics codes (Pierazzo *et al.*, 2008) and validated against experimental data from laboratory scale impacts (e.g., Pierazzo *et al.*, 2008; Davison *et al.*, 2011, Miljković *et al.*, 2012). Both two- and three-dimensional impacts are able to be computed using the relevant version of the code, iSALE2D or iSALE3D. The 3D code (Elbeshausen *et al.* 2009) includes an adaptive interface reconstruction algorithm (Elbeshausen and Wünnemann, 2011), creating sharp boundaries between material within one cell width. Simulations in 3D can also be parallelised by using Message Passing Interfaces (MPI). MPI parallelisation allows for the use multiple nodes at the same

time to reduce the time a simulation takes to run. The simulation is split into packets of information and each packet is given to a separate processor to handle, allowing for each packet of information to be processed simultaneously by each processor. For this to work within iSALE, the number of cells in the x-direction must be a multiple of the number of processors used so that the simulation is split into equal packets.

3.2.1 Fundamental equations to solve

The form of the differential equations solved by a computer code for modelling material dynamics depends on the frame of reference adopted. In the Eulerian description, the conservation equations take the form:

(3.1) Conservation of Mass $$\frac{\partial \rho}{\partial t} + v_i \frac{\partial \rho}{\partial x_i} = -\rho \frac{\partial v_i}{\partial x_i}$$

(3.2) Conservation of Momentum $$\frac{\partial \rho v_i}{\partial t} = F_i + \frac{\partial \sigma_{ij}}{\partial x_j}$$

(3.3) Conservation of Energy $$\frac{\partial \rho E}{\partial t} = -P \frac{\partial v_i}{\partial x_i} + s_{ij} \epsilon'_{ij}$$

where v_i is the velocity, ρ is the material density, x is the position in space, and t is time. In these equations, σ_{ij} is the stress tensor, composed of a hydrostatic part, the pressure P, and a deviatoric part, s_{ij}. F_i is the external body force per unit volume, and ϵ'_{ij} is the deviatoric strain rate. The subscripts represent standard tensorial notation for the coordinate directions and summation over repeated indices is implied. This means that in two-dimensions, these equations are expanded to include separate velocity components (*u, v*) and coordinate directions (*r, z*) in cylindrical geometry. In three-dimensions, these equations are further expanded to include third velocity components (*u, v, w*) and coordinate directions (*x, y, z*) in Cartesian geometry.

Pressure, P, is determined using an equation of state for the material being modelled and is additionally supported with an artificial viscous pressure (or the artificial viscosity, q). This is used to calculate the influence of shock waves through a material and is described by:

(3.4) $$q = \left(\lambda_1 c_B \rho \sqrt{A_c} + \lambda_2 \rho A \nabla . u\right) \min(0, \nabla . u)$$

where A_c is the cell area, c_B is the bulk sound speed, $\nabla.u$ is the velocity divergence, and λ_1, λ_2 are constants.

The set of partial differential conservation equations and the artificial viscosity are completed by the description of material behaviour under deformation during an impact event. This requires two more equations to be considered: the equation of state and a constitutive (strength) model. Both are described in the subsequent sections (Section 3.2.3 and 3.2.4, respectively). Whilst these equations describe the flow and deformation of a medium as a continuum, a computer has a finite memory allocation. Therefore, to apply the equations described above, a computer must divide the spatial domain into a set of nodes on a grid. This is process known as discretisation and splits the continuous media into one that can be interpreted by a computer with a limited, finite memory. In iSALE, the spatial domain is divided into rectangular cells, with 4 corners in 2D or 8 corners in 3D. Physical properties (like density, energy, or pressure) are known at the centre of each cell, whilst other parameters, such as velocity and position, are known at the cell vertices.

3.2.2 Mesh geometry

The geometry of the mesh generated depends on the style of required simulation. In three-dimensions, iSALE3D uses a regular cartesian grid that comprises a central high-resolution zone, where the cell height and width are constant, and optional extension zones below, above and to the left and right of the high-resolution zone. Cell height increases in a geometric progression away from the high-resolution zone in the extension zones above and below; cell width increases in the same manner away from the high-resolution zone in the extension zones to the left and right. The increase in cell size can be capped by a maximum allowable cell size in each dimension. The two-dimensional co-ordinate system employed can be set to standard cartesian co-ordinates or cylindrical co-ordinates. Typical impact simulations in two dimensions will employ cylindrical symmetry, with a high-resolution zone that encompasses the projectile and the portion of the mesh within which the crater is likely to fit. Extension zones to the right, top and bottom are used to displace the mesh boundaries far away from the cratering region, to minimise the adverse effects of reflections from the boundaries. In cylindrical symmetry geometry, no extension zone should be set on the left side of the mesh (Figure 3.2a). The left boundary is a rotational symmetry axis, reducing the problem from 3D to 2D. The whole mesh is assumed to rotate around this axis to create a hypothetical cylinder, with the impactor at the centre of the mesh. This requires just two dimensions to be considered in cylindrical co-ordinates: the height of the cylinder/mesh (z) and the radius of the cylinder/mesh (r).

Three-dimensional meshes are generated with a different assumption regarding symmetry. In 3D, the front face comprises a symmetry plane (not axis) where half of the simulation is generated and cut along an axis, usually parallel to the direction of impact (Figure 3.2b, 3.2c). The high-resolution and expansion zones are generated in three directions, x, y,

and z. Everything on one side of the boundary is assumed to reflect perfectly on the other side and so is not generated in the simulation. This assumption essentially halves the amount of material needed to be simulated and reduces computational time and power needed to run the simulation.

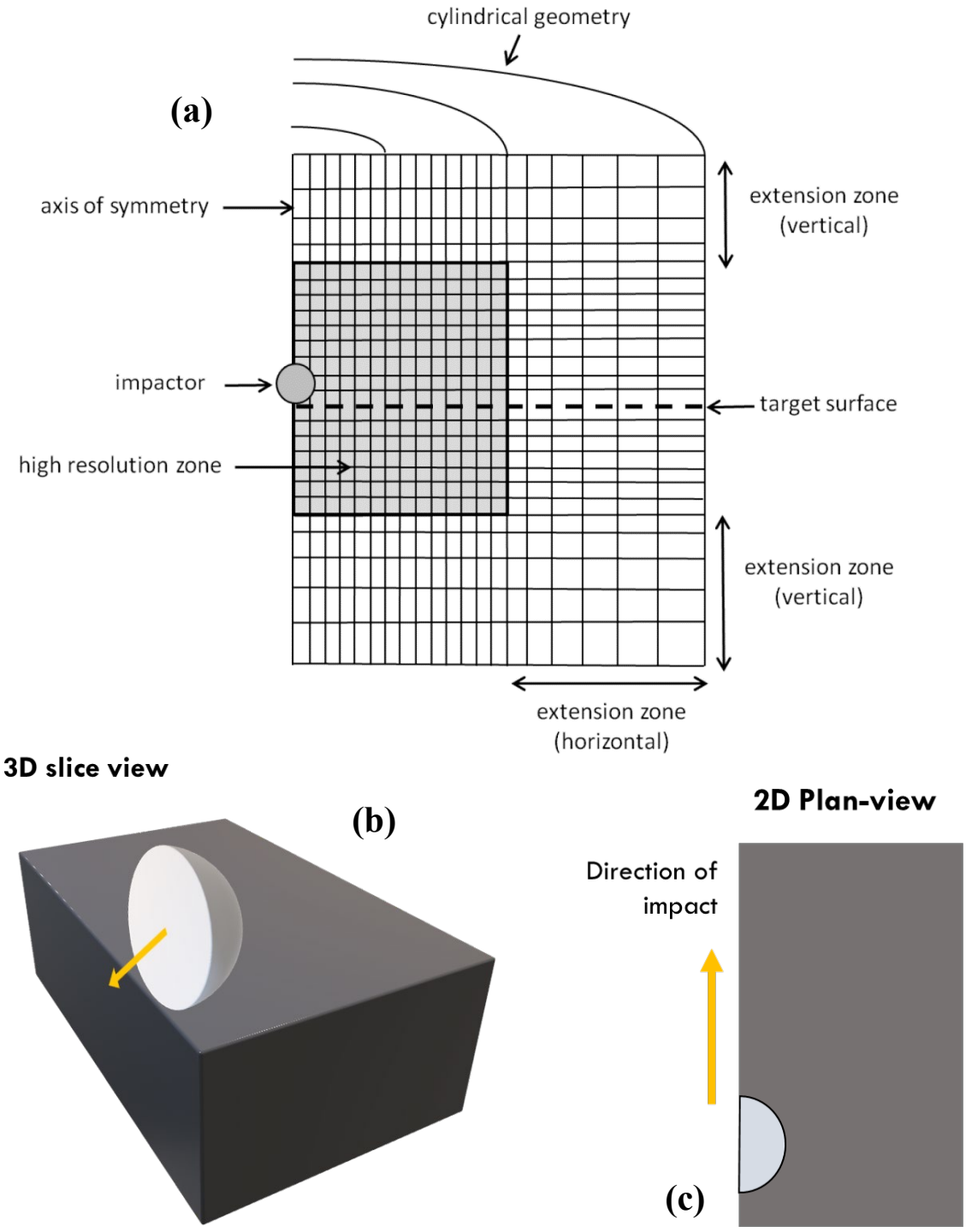

Figure 3.2: *A typical mesh geometry used for simulations in iSALE. (a) Two-dimensional (2D) mesh set-up in cylindrical geometry. (b) Three-dimensional (3D) set-up with typical symmetry along the y = 0 boundary. (c) A 2D illustration showing an overhead view of the 3D set-up shown in (c). Yellow arrow depicts the direction of impact into the target.*

3.2.3 Equations of state

An equation of state (EoS) describes the relationship between pressure, density, and internal energy of a particular material. Pressure (P) is related to deformation (or volume, V) and internal energy (E) by the equation:

$$P = P(V, E) \tag{3.5}$$

When coupled to the shock physics code, compressibility during impacts is accounted for within the EoS by calculating changes in density of the material and thermodynamic processes such as shock-heating can be simulated (Collins, 2002). The EoS for a particular material is typically found by planar shock experiments. There are many options available when choosing an EoS for a hypervelocity impact simulation. When an object is subject to a hypervelocity impact it can undergo significant changes in the thermodynamic state of the material within its volume. Impacts involve a wide range of pressures and temperatures, potentially reaching hundreds of giga-Pascals (GPa) and thousands of Kelvins (K). This means that regions within the material could be solid, liquid, vapour, or a mix of theses phases at any given time. Therefore, the ideal equation of state would describe material behaviour in all the states mentioned. However, there is usually a need for compromise between computational time and accuracy of an EoS.

A variety of materials from the semi-analytical equation of state library, ANEOS (Thompson and Lauson, 1972; Melosh, 2007), are used in the simulations presented in this thesis. In Chapter 4, the granite ANEOS table provided in the iSALE package was used for both impactor and target, using input parameters derived by Pierazzo *et al.* (1997). In Chapter 5, impactors were modelled using ANEOS tables for quartz and calcite, with parameters taken from Melosh (2007) and Pierazzo *et al.* (1998) to represent sandstone and limestone, respectively. The quartz equation of state table was modified for the simulations presented in Chapter 5 to remove the solid-solid phase transition, so that the high-pressure phase of quartz was not represented. This was done to remove spurious high temperatures recorded within the impactor and is further explained in Section 5.2.1. The target material was modelled using ANEOS tables for basalt, included within the iSALE EoS library. Input parameters for basalt were taken from Pierazzo *et al.* (2005) to represent the lunar surface. In Chapter 6, ANEOS tables for serpentine were used to represent the impactor in the final models, using parameters taken from Brookshaw (1998). The target was once again represented by the same ANEOS tables for basalt as those used in Chapter 5.

The state of the material lies along the curve known as the Hugoniot. The Rankine-Hugoniot equations for the shock jump conditions can be regarded as defining a relation between any pair of the variables ρ (density), P (pressure), e (energy), u_p (particle velocity), and u_s (shock velocity). For example, Figure 3.3 shows the Hugoniot curve for dunite, presenting the relationship between shock pressure and particle velocity. This curve can be used to determine the shock pressure experienced by the dunite material if it reaches a particular particle velocity, and vice versa. The same process can be applied to any of the variables listed above when compared to one another in a Hugoniot curve diagram.

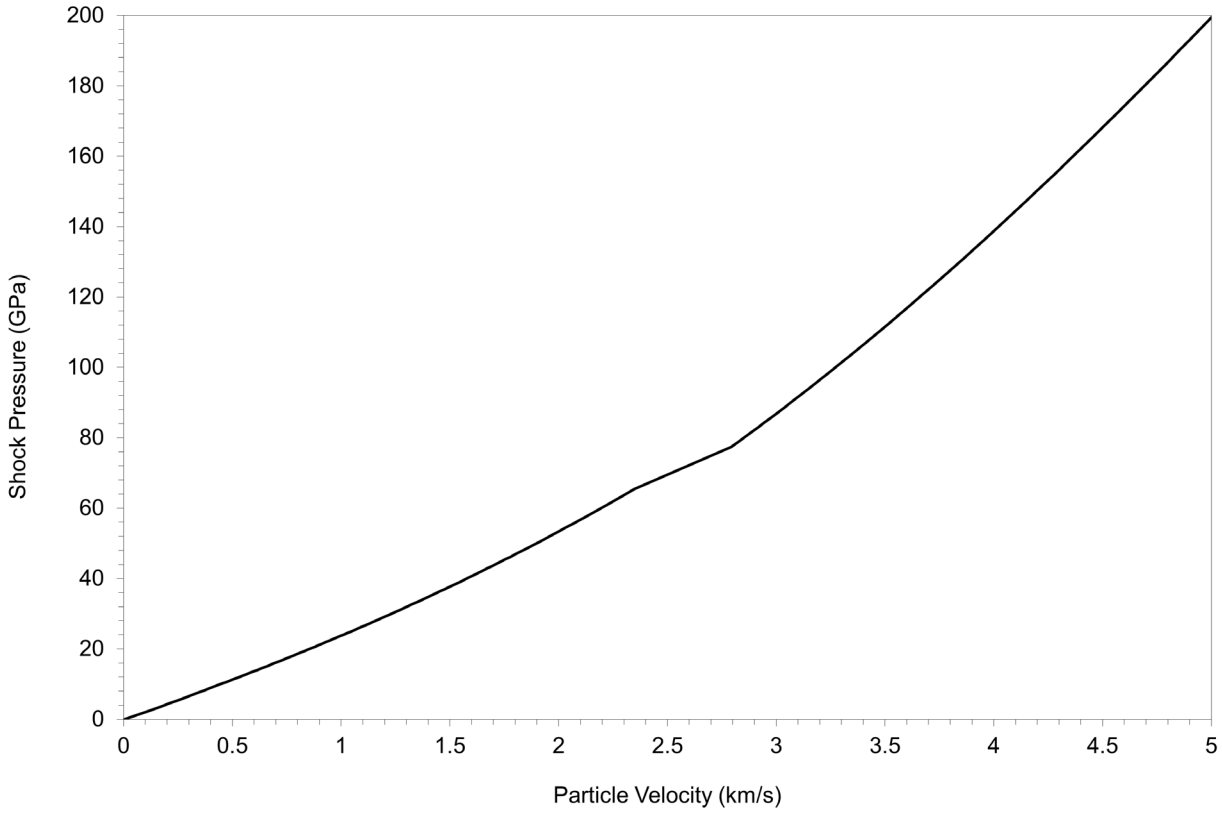

Figure 3.3: *An example Hugoniot curve for an equation of state representing a dunite material model. This particular curve describes the relationship between particle velocity (x-axis) and shock pressure (y-axis).*

3.2.4 Constitutive (strength) model parameters

In addition to the EoS of a given material, several strength models are included in iSALE, which can be selected along with the relevant parameters for each model, set in the input file. This allows for more complex geological materials to be modelled within the simulation. Constitutive equations for geological materials can be defined by taking known materials on Earth (e.g., basalt, granite, or quartz) and subjecting them to experimental tests relating to the pressures that the material can withstand before failure (e.g., Sekine *et al.*, 2017). The following section describes the models that were used in this work.

Rheologic model: iSALE allows four rheologic models: viscous, elastic, elastic-plastic, or viscos-elastic. The elastic-plastic model was used for the work in this thesis. Elastic-plastic models compute more complex solid, rheological materials. The model requires the definition of the poisson ratio, which depends on the shear modulus and bulk modulus. In iSALE, it is assumed to be independent of temperature and pressure during simulations.

Damage model: Three damage models are available in iSALE: Simple, Ivanov, and Collins. The Simple and Ivanov (Ivanov *et al.*, 1997) models both describe damage as a function of plastic strain; however, the Collins model computes damage from both tensile and shear failure (Collins *et al.*, 2004). Both the Ivanov and Collins damage models are used within the modelling work carried out for this thesis.

The Ivanov damage model prescribes damage D as a function of plastic strain:

$$D = \min\left(\frac{\epsilon_p}{\epsilon_f}, 1\right) \tag{3.6}$$

where ϵ_p is an invariant measure of the accumulated total plastic strain (always positive) and ϵ_f is the plastic strain at failure. In this model ϵ_f is an increasing function of pressure:

$$\epsilon_f = \max\left(\epsilon_{fb}, B(p - p_c)\right) \tag{3.7}$$

where ϵ_{fb} is a minimum failure strain for low pressure states, p_c is a pressure above which failure is assumed compressional and B is a positive constant.

The Collins damage model computes damage D resulting from tensile and shear failure, with the shear component to the damage as function of plastic strain. This uses the same formula as equation 3.1 but computes the plastic strain at

failure using three piecewise linear functions of pressure. This incorporates the brittle-ductile and brittle-plastic transition pressures. Tensile strength (Y_t) is also calculated and defined by:

$$Y_t = Y_{t0}(1 - D) \tag{3.8}$$

where D is the damage and Y_{to} is the intact tensile strength.

Strength model: The strength of geological materials is complex, with multiple factors (e.g., pressure, temperature, porosity) contributing to the onset of failure, surpassing the critical stress within a rock (yield strength). The strength of rocks can be modelled via the Rock (Collins *et al.*, 2004), Drucker-Prager (Drucker and Prager, 1952), Lundborg (LUNDD and LUNDI; Lundborg, 1968), von Mises (von Mises, 1913), and Johnson-Cook (Johnson and Cook, 1985) strength models. Each uses a combination of parameters, including cohesion, internal friction, and limiting strengths, as well as many others.

The Rock strength model was used in this work, a model that defines the yield strength Y as:

$$\mathrm{Y} = \mathrm{Y}_d\mathrm{D} + \mathrm{Y}_i(1 - \mathrm{D}) \tag{3.9}$$

where D is a scalar measure of damage (0 = intact; 1 = damaged) that is computed by the damage model. The damaged material strength, Y_d is defined by:

$$Y_d = min(Y_{d0} + \mu_d P, Y_{dm}) \tag{3.10}$$

where P is pressure. The intact material strength, Y_i is defined by:

$$Y_i = Y_{i0} + \frac{\mu_i P}{1 + \frac{\mu_i P}{Y_{im} - Y_{i0}}} \tag{3.11}$$

where Y_{i0} is the cohesion of the intact material, μ_i is the coefficient of internal friction for intact material, Y_{im} is the limiting strength at high pressure for intact material, Y_{d0} is the cohesion of damaged material, μ_d is the coefficient of internal friction for damaged material, and Y_{dm} is the limiting strength at high pressure for damaged material.

T**hermal softening model**: The temperature of rock materials influences phase changes and the shear strength of the material. Melt temperature is estimated as a function of pressure in iSALE using the Simon approximation, whilst the

reduction in shear strength with increasing temperature is approximated using the Ohnaka thermal softening model (Ohnaka, 1995). The Simon approximation calculates the melt temperature, T_m, of a material using the following equation:

$$T_m = T_{m0}\left(\frac{P}{a}+1\right)^{1/c} \quad (3.12)$$

where T_{m0} is the melt temperature at zero pressure, a and c are material constants.

Porosity model: iSALE is capable of incorporating porosity into any solid material within a simulation, employing the ε-α compaction model (Wünnemann *et al.*, 2006). This model describes how porous materials respond to compression using distension (α) instead of porosity directly, to represent the relative volume of pore space. Porosity (ϕ) is related to distension by $\alpha = 1/(1-\phi)$. iSALE calculates the thermodynamic state of a porous material by separating the compaction of pore space from the compression of the solid component (Herrmann, 1969). The model also considers the change in porosity during elastic loading and unloading, after improvements from Collins *et al.* (2011a). The full compaction model of Wünnemann *et al.* (2006) and Collins *et al.* (2011a) comprises four regimes that describe the compression of a pristine porous material up to, and beyond, the fully consolidated state: elastic compaction, exponential compaction, power-law compaction, and compression. These four components can be described using the following equations:

(3.13) Elastic compaction: $0 > \epsilon > \epsilon_e \qquad \alpha = \alpha_0$

(3.14) Exponential compaction: $\epsilon_e > \epsilon > \epsilon_x \qquad \alpha = \alpha_0 e^{\kappa(\epsilon-\epsilon_e)}$

(3.15) Power-law compaction: $\epsilon_e > \epsilon > \epsilon_c \qquad \alpha = 1 + (\alpha_x - 1)\left(\frac{\epsilon_c - \epsilon}{\epsilon_c - \epsilon_x}\right)^2$

(3.16) Compression: $\epsilon_c > \epsilon \qquad \alpha = 1$

where ϵ represents the volumetric strain, sub-scripts relating to each component. However, in iSALE the rate of compaction is computed instead of directly deriving α from equations 3.8–3.11 and then α is updated using the relationship:

$$\alpha_{n+1} = \alpha_n + \frac{d\alpha}{d\epsilon}\frac{d\epsilon}{dt}\Delta t \quad (3.17)$$

An update to the porosity model during elastic loading and unloading includes the definition of the elastic compaction rate described by Collins *et al.* (2011a):

$$\frac{d\alpha}{d\epsilon_v} = \alpha\left[1 - \left(\frac{c(\alpha)}{c_{s0}}\right)^2\right] \tag{3.18}$$

where c_{so} is the bulk sound speed of the solid material at zero pressure and $c(\alpha)$ is the bulk sound speed of the porous material at zero pressure.

The main portion of the compaction function is the exponential compaction regime, which occurs for volumetric strains between ϵ_e and ϵ_x. In this regime, the rate of compaction is:

$$\frac{d\alpha}{d\epsilon_v} = \kappa\alpha = \kappa\alpha_0 e^{\kappa(\epsilon_v - \epsilon_e)} \tag{3.19}$$

where κ is the parameter accounting for the different materials and types of porosity and α_0 is the initial porosity within the material. The idealized case where all pore space is crushed out before the matrix starts to compress would be where $\kappa = 1$. If matrix compression occurs concurrently with pore-space compaction, then $\kappa < 1$. For a large proportion of materials studied so far, κ is very close to 1, which is indirect support for this form of the compaction function.

When the compaction regime transitions from the exponential to the power-law regime, it does so at a volumetric strain of ϵ_x and a distension of α_x. The power-law regime exhibits less rapid compaction and eventually transitions to the final compression regime, where no porosity remains. This compaction rate is expressed as:

$$\frac{d\alpha}{d\epsilon_v} = 2(1 - \alpha_x)\frac{\epsilon_c - \epsilon}{(\epsilon_c - \epsilon_x)^2} \tag{3.20}$$

where ϵ_c is the volumetric strain in the compression regime, where all porosity has been compacted out of the material. In this regime, where $\epsilon_v \leq \epsilon_c$, the distension will be 1, with compaction rate and porosity being 0.

3.2.5 Limitations and areas of uncertainty within the model parameters

Representing geological materials in numerical modelling results in the simplification of some very complex materials. As mentioned previously, all of the methods typically used to represent complex geological materials are based on empirical observations. As such, there remains considerable uncertainty in the equations of state of geological materials,

especially when considering the range of high impact velocities for many bodies in our Solar System (typically many km s^{-1}). Whilst ANEOS has always included the ability to explicitly interpret the melt and vapour states of a material, the original version did have several limitations. Gaseous products were treated as monoatomic species, leading to an overestimation of the liquid-vapour phase curve and the critical point (a set of conditions where a liquid and associated vapour become identical and can coexist) of many complex materials. This particular issue has been addressed in an updated version of ANEOS, available in the current build of the iSALE package. The new version includes the specific treatment of bi- and tri-atomic molecular gases (Melosh, 2007), but cannot account for different, complex molecules present within the vapour phase.

The liquid solid phase transitions used within ANEOS can also be problematic when it comes to representing geological materials. Typically, the observed temperature dependence of solid-state phase boundaries in geological materials suggests that the pressure at which the phase transition occurs is heavily influenced by temperature. However, because high-pressure phase transitions in ANEOS are treated as a modification of just the cold fraction of the Helmholtz free energy (F_c), this leads to both the high- and low-pressure phases being dependent on temperature in identical ways (Thompson and Lauson, 1972). As such, the nearly fixed-pressure phase transition prevents ANEOS from locating the solid-liquid phase boundary with any real accuracy. This implies that the liquid and solid states in a material cannot be distinguished during high pressure events when a phase transformation is included and results in an omission in the calculation of the latent heat of melting. Since this process is problematic for ANEOS, iSALE uses a separate equation to determine the solidus of a material (and hence the melt temperature) as a function of pressure (described previously as the Simon approximation). The Simon approximation itself includes inherent assumptions and uncertainties, particularly that it assumes only material above the liquidus is molten. This leads to an underestimation of the total melt produced when compared to melt volumes if partially molten material was considered.

Fragmentation of ejecta during hypervelocity impacts is a process that is still relatively poorly understood. Due to numerical modelling principally considering the hydrodynamic behaviour of a material, fragmentation is difficult to calculate especially at high energies where multiple states of matter are likely to coexist. Additionally, explicitly estimating the size of fragments during ejection is limited by the resolution of the simulation itself, with cell sizes in the high-resolution zone becoming the lower limit on the estimation of the size of ejected blocks of material. This can have particularly detrimental effects on the impactor ejecta, as many simulations are limited to 10s of cells per projectile radius or less due to computational power or time. The Grady-Kipp fragmentation algorithm (Grady & Kipp, 1980) was included within a

previous version of iSALE that could calculate the propagation of fractures and some explosive fragmentation, but only when considering isotropic tensile fracture. This was only available in the Lagrangian version of the code and was later removed. More recently, an updated version of the Grady-Kipp fragmentation model has been reimplemented into a specific branch of the iSALE code (Wiggins *et al.*, 2019). This enables the tracking of fragment size within ejecta curtains and has been used in iSALE work investigating lunar craters (Wiggins and Johnson, 2021). However, these additions to the iSALE code are not yet available to be used beyond the scope of testing and so have not been included in this work.

3.3 Processing numerical simulation outputs

Once a simulation is complete, the data are stored in a single data file (*jdata.dat*). There are two main types of data: cell data and tracer data. Cell data describes the state of the material at fixed points in space during the simulation. Each cell will record a variety of variables, including the pressure, temperature, velocity, and type of material throughout the simulation. Tracer data records the state of a representative packet of material as it moves through the simulation domain in response to the impact. As this project is mostly concerned with the survival of impactor material and the fate of shallow target material, most of the work involved processing, analysing, and interpreting tracer data. Whilst tracers offer a method of tracking the state of the same material from the start to the end of simulation, their use does come with a set of limitations. Firstly, by representing the state of a particular volume of material (often large) with a single point, you lose fidelity relating to all material within that set volume. Variables recorded by the tracer are therefore averaged over that volume and applied to the whole packet when recorded as data. This results in a reliance on the resolution of the simulation to accurately represent the material at smaller scales. Higher resolution means smaller cell dimensions, smaller volumes of material tracked by a single tracer, and therefore less averaging of recorded variables over the simulation. Secondly, the movement of the tracer is based on a linearly interpolated velocity field, which means that the tracer can slowly "drift" away from the material it was supposed to represent originally. In some extreme cases, where velocities of the material being tracked are very high, this drifting can cause tracers so far out of the original material that they have to be removed from the simulation by the code itself. This can lead to a loss of tracer data over the course of the simulation and produces very large error files. Lastly, in large simulations the number of tracers can reach the millions, especially when modelling in three dimensions. This drastically increases the time it takes to run a simulation and creates very large data files upon completion. To mitigate this issue, "tracer zones" can be defined to contain tracers only in the areas of most importance for a particular simulation. For the particularly large 3D models in this work, tracer zones were restricted to the projectile

material when concerning the survival of carbonaceous chondrites and to the upper target surface when investigating the escape of material from Earth.

These data can be extracted and interpreted using a tool developed by Thomas Davison (a member of the iSALE development team at Imperial College, London), named pySALEPlot, which includes a library of functions for post-processing iSALE datasets. Using Python (the interpreted, object-oriented, high-level programming language) and Matplotlib (the comprehensive library for creating static, animated, and interactive visualisations in Python), pySALEPlot allows the user to extract multiple, discrete datasets recorded during the simulation and produce a multitude of plots describing the data. The data can also be accessed through an interactive module within pySALEPlot (Figure 3.4) or scripts can be written in the Python programming language to produce specific tables of data or plots for data interpretation (see projectile plots in Chapters 4, 5, and 6). Examples of the python scripts used to process the data files and produce some of the figures for this work can be found in Appendix A4–A6.

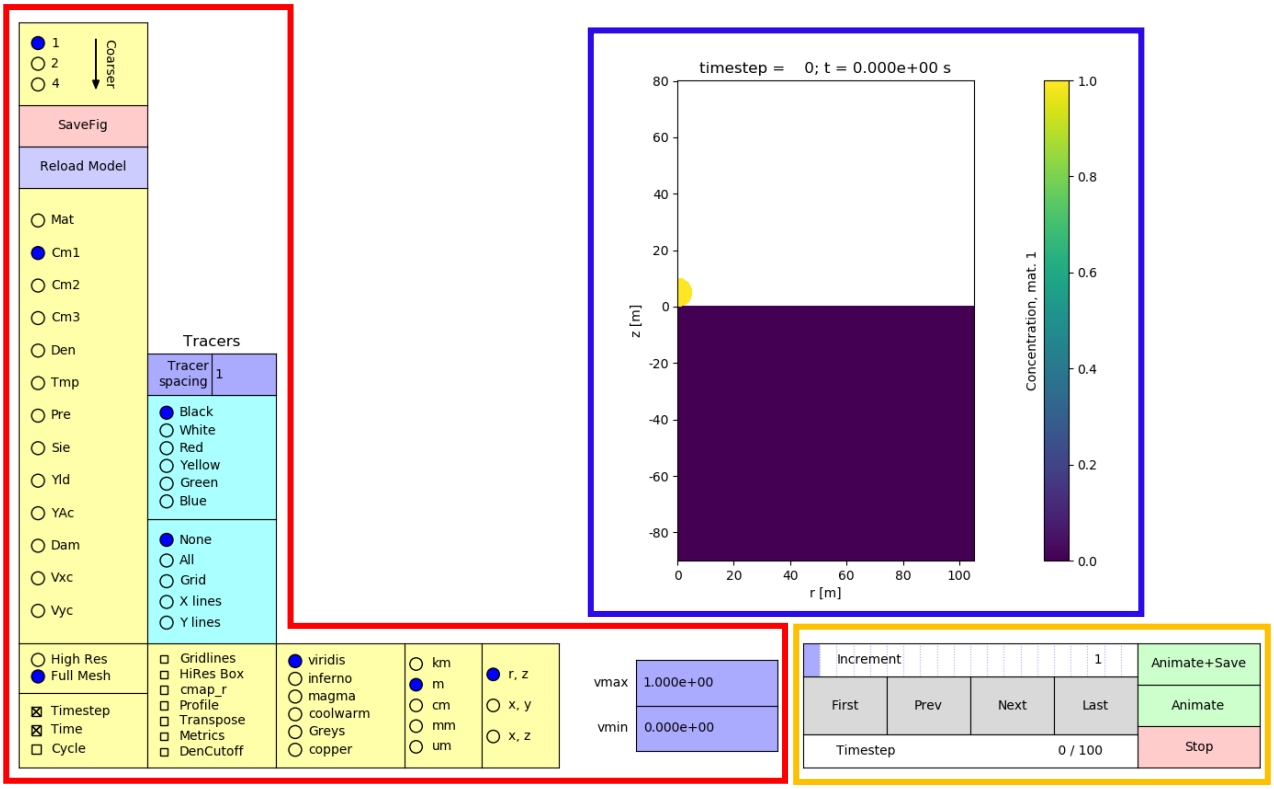

Figure 3.4: *Example of a typical impact scenario displayed in the interactive window available through pySALEPlot. Red box: Options available for dataset selection and visualisation. Orange box: Timestep selection and animation options. Blue box: Display of selected data. In this example, the yellow semi-circle represents the projectile and the blue square the target.*

3.4 Summary

Shock physics codes can be used to simulate the formation of impact craters throughout the entire impact process. iSALE is an example of a code specifically designed to investigate this process, including the relevant geological material models, equations of state, strength, damage, and porosity models to do so. To complete the work set out in this thesis, iSALE was used in both the 2D and 3D modes, utilising a variety of parameters to best represent the real-world geological materials required.

The programming language Python was used to investigate the data produced by the simulations, using Matplotlib and the iSALE dedicated code pySALEPlot to interpret and illustrate the final results. More detailed explanations of the methods used within iSALE for each specific simulation set up can be found in each of the relevant results Chapters (4, 5, and 6) as part of the Methods sub-sections.

4 Modelling the impact ejection of low-pressure material from Earth to the Moon*

**Part of this chapter is adapted from work published as a research paper:*
Halim, S. H., Crawford, I. A., Collins, G. S., Joy, K. H., Davison, T. M., 2021a. Assessing the survivability of biomarkers within terrestrial material impacting the lunar surface. Icarus, 354. doi:10.1016/j.icarus.2020.114026

4.1 Introduction

This chapter builds upon previous work involving the ejection of material from Earth and the subsequent transfer of that material to the Moon during giant, terrestrial impacts (e.g., Armstrong *et al.*, 2002; Artemieva and Morgan, 2009; Armstrong, 2010; Beech *et al.*, 2019; Cabot and Laughlin, 2020). Using high-resolution, 3D modelling, the work determines whether large impacts on Earth can accelerate ejecta to velocities greater than Earth's escape velocity whilst also remaining solid and, more importantly, experiencing shock-pressures lower than those capable of destroying entrained biomarkers (<10 GPa). Additionally, investigating the temperature of this ejected material is critical for determining the survival of biomarkers, some of which may be destroyed under prolonged high temperatures due to thermal degradation (discussed further in Chapter 5). This requires detailed investigation of the spallation zone of an impact, the area where ejected material can reach velocities high enough to escape the Earth's gravity but also low enough pressures to remain intact. The location of such ejecta in the target body will greatly depend on the parameters for the impacting body, especially the impact velocity and angle of impact relative to the target surface. The composition of the target will also play a key role in the production of the ejecta.

The ejection of material from planetary surfaces has been investigated using many different techniques and applied to a multitude of planetary bodies throughout the Solar System. Examples of generalised planetary ejection from no particular planetary surface include impacts into idealised targets during laboratory (e.g., Meyer *et al.*, 2011; Wünnemann *et al.*, 2016; Okamoto *et al.*, 2020) and numerical modelling (e.g., Melosh, 1984; Shuvalov, 2011; Kurosawa *et al.*, 2018; Luther *et al.*, 2018; Hyodo and Genda, 2020). These techniques have been used to study the effect of a range of parameters on the ejection efficiency during impact, including various resolutions, materials (both target and impact), porosity, impact angle, and velocity. Exploration of biomarkers escaping planetary bodies even extends beyond our own Solar System, potentially enabling the detection of dust ejected after large impacts on exoplanets inferred using current and future telescope technology (Cataldi *et al.*, 2017). The rich impact history of the Solar System has allowed for the transfer of

material between many planetary bodies via ejection after hypervelocity impacts. As discussed in Chapter 2 (Section 2.3), evidence for such transfers include Martian and lunar meteorites found on Earth, which point to the possibility of finding material from Earth on other planetary surfaces, most likely on our nearest celestial neighbour, the Moon. Basin-forming, hypervelocity impacts striking Earth (Marchi *et al.*, 2014) could potentially eject terrestrial material at velocities great enough to surpass escape velocity and take up Moon-crossing orbits (Armstrong *et al.*, 2002; Armstrong, 2010; Beech *et al.*, 2019). Theoretical estimates using extrapolation of an analytical model of spallation (Melosh, 1984; 1985) suggest that a mass of ejecta equivalent to as much as 10^{-5} to 10^{-2} of the original impactor's mass (M_i) may escape Earth's gravity without exceeding a shock pressure of 10 GPa (Armstrong *et al.*, 2002; Armstrong, 2010). On the other hand, shock physics simulations of several Chicxulub-scale impact scenarios did not resolve any material ejected at escape velocity that was not shocked beyond the level likely to destroy entrained biomarkers (i.e., >50 GPa: Artemieva & Morgan, 2009). However, these simulations used a relatively low spatial resolution of 12-15 cells per projectile radius (cppr), with the results only being tabulated in fractions of $\sim 10^{-3}$ M_i. Based on the assumptions and calculations by Armstrong *et al.* (2002) and Armstrong (2010), this leaves room for a small proportion of material (equivalent to 10^{-4} to 10^{-5} M_i) to be ejected from the surface of Earth at low pressures. Higher resolution simulations will allow for the resolution of smaller "packets" of material relative to the size of the impactor and the simulation as a whole. Higher resolution simulations (in terms of cells per projectile radius) can lead to the detection of smaller masses of material that experience lower pressures that may have otherwise been averaged over in lower resolution studies. However, these calculations come with the downside of requiring either substantially more computational time and/or higher computational power. Increasing resolution eventually yields diminishing returns in this respect and there comes a point where a simulation is considered to "converge", where increasing the resolution essentially provides negligible improvements to the accuracy of the simulation.

Multiple studies have been dedicated to exploring the launch of material from other planetary bodies, most frequently Mars (e.g., Artemieva and Ivanov, 2004; Fritz *et al.*, 2005; Chappaz *et al.*, 2013; De Carli, 2013; Bowling *et al.*, 2020; Elliot *et al.*, 2022), looking to explain the origins for Martian meteorites found in Earth's meteorite collection. The limitations for ejecting low-pressure material from the surface of Mars are less restrictive than those for the Earth, for a multitude of reasons. Firstly, at a very simple base level, we know that material can be ejected from Mars at low enough pressures to remain solid and retain organic molecules because we have evidence for them in our Martian meteorite collection. Currently, there is no conclusive evidence for any terrestrial material on other planetary bodies, let alone material containing ancient organic material or biomarkers. Tentatively, the potential discovery of a terrestrial clast in

Apollo sample 14321 by Bellucci *et al.* (2019) may provide the first physical evidence for terrestrial material surviving impact with the lunar surface. However, this interpretation is controversial and can also be attributed to an unusual geological history based solely on the Moon (e.g., Warren and Rubin, 2020). Hopefully, with an increasing number of sample return missions planned on multiple planetary surfaces, direct evidence of terrestrial ejecta may yet be obtained. Secondly, the escape velocity for Mars is ~5 km s^{-1}, less than half that of Earth (~11.2 km s^{-1}), which allows for a greater proportion of material to escape for identical impacts on both terrestrial bodies. Additionally, this allows for a greater range of impact scenarios to produce escaping ejecta as well as a greater mass of ejecta per impact. Lastly, the relative density of the Martian atmosphere has been less than that of Earth for most of its history, so there would be less atmospheric deceleration and heating of ejecta. For these reasons, ejecting solid material from Earth has been considered much less likely compared to Mars, where such ejection is known to occur. The generation of terrestrial meteorites has therefore seen less investigation than the origin of Martian meteorites.

Here, the results from high-resolution, 2D and 3D numerical simulations are presented, resolving the fraction of ejecta that experiences both high speed (> 11 km s^{-1}) and low pressure (<50 GPa for solid material, <10 GPa for surviving biological markers), to show that low-shock ejection is possible from Earth.

4.2 Methods

The shock physics code iSALE was used to simulate the high-speed ejection of terrestrial material via a basin-forming impact on Earth. Both the two-dimensional (Wünnemann *et al.*, 2006) and three-dimensional (Elbeshausen *et al.*, 2009; Elbeshausen and Wünnemann, 2011) versions of the code were used to investigate multiple components of the ejection process. The 2D simulations were limited to vertical impacts but allowed the resolution of the simulations to far exceed those capable in 3D simulations. The simulation of oblique impact is only possible with the 3D version of iSALE and was crucial for investigating the ejection of high-speed material at low pressure.

In the 3D simulations, a 50 km diameter projectile was simulated striking Earth at angles of 30°, 45°, and 60° to the surface (assumed to be horizontal) and at velocities of 20, 30, and 55 km s^{-1}. This impactor size is representative of basin-forming impacts on the Earth and Moon (Stöffler and Ryder, 2001; Le Feuvre and Wieczorek, 2011; Marchi *et al.*, 2014). Whilst the most common values for asteroid impacts on Earth are 20 km s^{-1} and 45° (Shoemaker, 1962; Le Feuvre and Wieczorek, 2011), impacts for faster projectiles, such as short and long-period comets with average velocities of 30

Table 4.1: Thermal, strength, and damage input parameters for the impactor and target material in this numerical modelling work. Taken from Collins et al., (2020), representing a Chicxulub-like impact of a giant asteroid striking Earth.

Parameter	Symbol (units)	Impactor and target (Granite EoS)
Thermal		
Thermal softening coefficient	ξ	1.2
Melt temperature (p = 0)	T_m (K)	1673
Strength		
Poisson's ratio	ν	0.3
Intact cohesive strength	Y_{i0} (MPa)	10
Intact friction coefficient	μ_i	2
Intact strength limit	Y_{lim} (GPa)	2.5
Damaged cohesive strength	Y_{d0} (MPa)	0.01
Damaged friction coefficient	μ_d	0.6

and 55 km s^{-1} respectively (Chyba *et al.*, 1994; Weissman, 1997), were also considered. Angles of impact were varied (30°, 45°, and 60°, relative to the horizontal) to investigate any change in the proportion and location of ejected material. At the time of starting these simulations, iSALE-3D was limited by the requirement for both the impactor and target to be composed of the same material. Therefore, the granite equation of state table provided in the iSALE package was used for both impactor and target. This was made using the analytical equation of state package (ANEOS; Thompson and Lauson, 1972) with input parameters derived by Pierazzo *et al.* (1997). The strength of the material was modelled using the Rock strength model (see Section 3.2.4 for details) described by Collins *et al.* (2004), with identical parameters to those used to represent the impactor and crust in iSALE-3D simulations of the Chicxulub impact (Table 4.1; Collins *et al.*, 2020). Both the impactor and target were modelled as entirely solid, therefore there is no porosity model included. The same material models were used in every scenario and ice was not used as the impactor material for the simulations with cometary-like velocities. The inclusion of an ice impactor would lead to a reduction in density, thereby reducing the impacting mass and resulting energy for the same sized projectile. The reduction in energy transferred into the target upon impact would likely lead to less target material being ejected at high velocity and therefore decrease the amount of target material reaching escape velocity. Additionally, ice is significantly weaker than granite and has a much lower melting temperature, making it likely that some of the energy during the impact would be dissipated in the compaction and melting of the weaker

impactor material, rather than efficiently transfer into the target to contribute to the ejection process. Therefore, it might be expected that despite having significantly higher average impact velocities, cometary impactors may not be as efficient at producing escaping ejecta. However, this has not been explored in this work and would be an interesting continuation of the modelling in future.

The pressure, temperature, and velocity of ejecta were recorded by tracer particles placed in each cell. Then, tracer data were analysed to measure the cumulative mass of material that was ejected from the target at speeds faster than the velocity required for material to escape and reach Moon crossing orbits (11 km s^{-1}). In order to accurately measure the launch speed of the target material, parameters for the three components (velocity vectors in the x, y, and z directions) of the tracer velocity were stored for every tracer placed. These saved tracer (Tr) values are stored in the corresponding data files named *Tru* (x velocity), *Trv* (y velocity), and *Trw* (z velocity), respectively. The total ejection velocity (v_{ej}) of each tracer was calculated for every timestep by combining the three vectors using the equation:

$$v_{ej} = \sqrt{Tru^2 + Trv^2 + Trw^2} \tag{4.1}$$

Data for v_{ej} was stored for each timestep and sorted into a series of arrays where each tracer had an assigned v_{ej}. These arrays were then compared to one another to find the maximum v_{ej} value for each tracer at any point in the simulation. Any material ejected at velocities greater than 11 km s^{-1} was investigated and processed further to identify the peak pressures (*TrP*) and temperatures (*TrT*) experienced by the material at any time during the simulation. The simulations were run long enough to measure peak pressures across the entirety of the target and ejection of all material reaching velocities greater than ~5 km s^{-1}. A series of simulations of the same impact scenario (20 km s^{-1} and 45° impact velocity and angle, respectively) but with different spatial resolutions, from 40 to 100 cells per projectile radius (cppr), was performed to test the robustness of the results.

For consistency, the 2D simulations used the same model parameters as the 3D simulations. These simulations were limited to a vertical impact (90° to the horizontal) and simulated in cylindrical geometry. The computational resources required for 2D simulations are significantly lower than those in 3D and, as a result, the resolutions of the 2D simulations can be pushed to much higher cells per projectile radius. Simulations in 2D were run with a maximum of 1000 cppr, with multiple simulations run at 100, 200, 300, 400, 600, 800, and 1000 cppr, testing whether the results converged with an impact velocity of 20 km s^{-1}. Once the resolution test was complete, a suitable resolution was chosen as the best

compromise between accuracy and computational time taken to compete (essentially where results began to converge). Then, for this given resolution, vertical impact velocities between 20 and 50 km s^{-1} were investigated to determine the effect on the mass of escaping ejecta. Maximum ejection velocities were calculated using a similar method to the 3D simulations (using equation 4.1), with the omission of the y component of the material velocity as only the x and z components exist in two dimensions. The maximum resolutions used for both the 2D (1000 cppr) and 3D (100 cppr) simulations may seem incongruous when considering the attempt to find convergence of the results. However, the number of cells represented in the projectiles is relatively similar when factoring in the extra dimension. The 1000 cppr in the two-dimensional half-space in cylindrical geometry used in iSALE represents a total of ~1.5 million cells in the projectile, whilst the 100 cppr in three-dimensional half-space represents ~2 million cells in the projectile.

The 50 km diameter impactor is significantly greater than Earth's atmospheric scale height (8.5 km) and, as a result, it is likely that the influence of the atmosphere on the impactor and high-speed ejecta is negligible as the large impactor drives a path through the atmosphere. Additionally, the ejecta fragments are likely to be large enough to be relatively unaffected by atmospheric drag. Therefore, no atmosphere was considered in any of the simulations. However, as this assumption is the best-case scenario for escaping ejecta, discussion in later sections addresses the possible influence of atmospheric effects. Example input files for the simulations can be found in Appendix A1 and A2.

4.3 Results

4.3.1 Two dimensional simulations

Despite the high resolution reached in the two-dimensional simulations, minimum pressures experienced by any ejecta fast enough to escape the Earth were too high for biomarker survival at any resolution or any impact velocity. The highest resolution (1000 cppr) 2D simulation resolved ~10^{-5} M_i of ejected material experiencing a minimum pressure of ~32 GPa, low enough to remain solid after ejection but too high to be considered "low-shock" material that could retain evidence of biomarkers. The results have started to converge by 600 cppr, experiencing minimum pressures of ~41 GPa in 10^{-5} M_i in escaping ejecta and experiencing almost identical pressures to those at 800 and 1000 cppr from pressures of 80 GPa and above (Figure 4.1). Simulations run at 100 and 200 cppr resolved no significant mass (>10^{-5} M_i) of material ejected at velocities >11 km s^{-1} and pressures <150 GPa, therefore they are not included in Figure 4.1. After determining that results

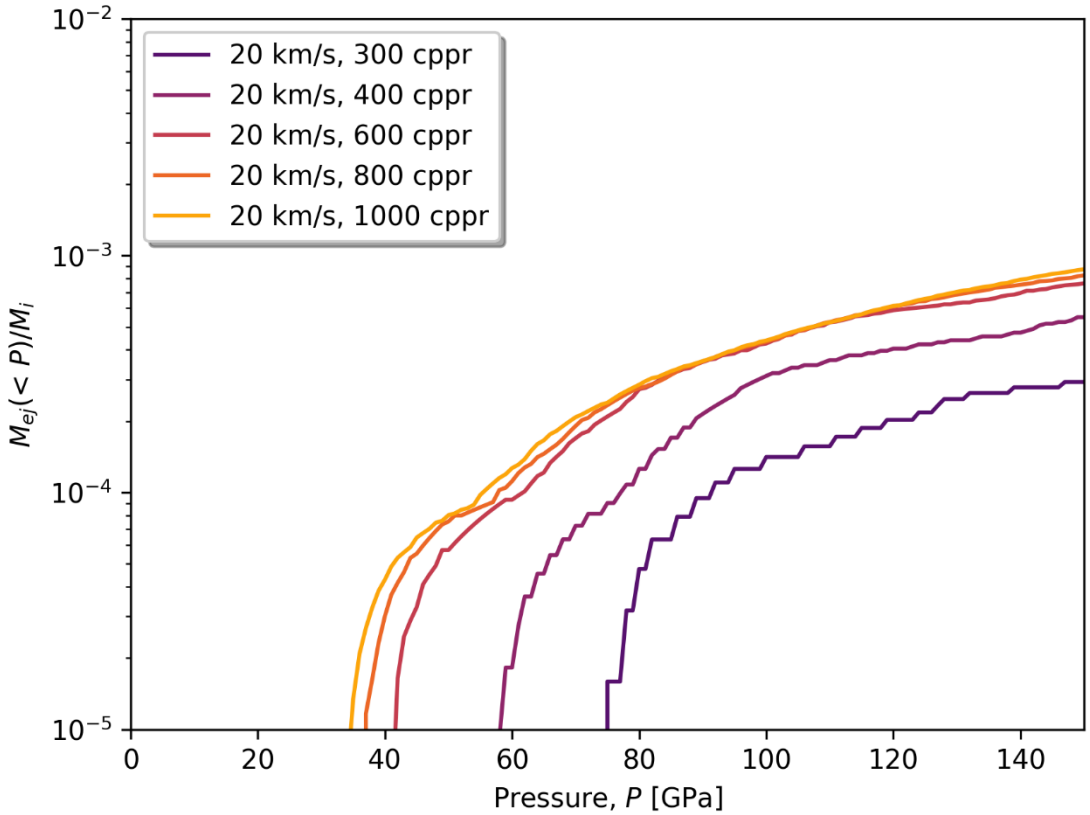

Figure 4.1: *Resolution test for the suite of two-dimensional models. The cumulative mass of target material ejected (M_{ej}) as fraction of impactor mass (M_i) shown as a function of shock pressure (P) for different resolutions (cppr). Simulations run at 100 and 200 cppr are excluded due to having no resolvable ejecta experiencing pressures less than 150 GPa.*

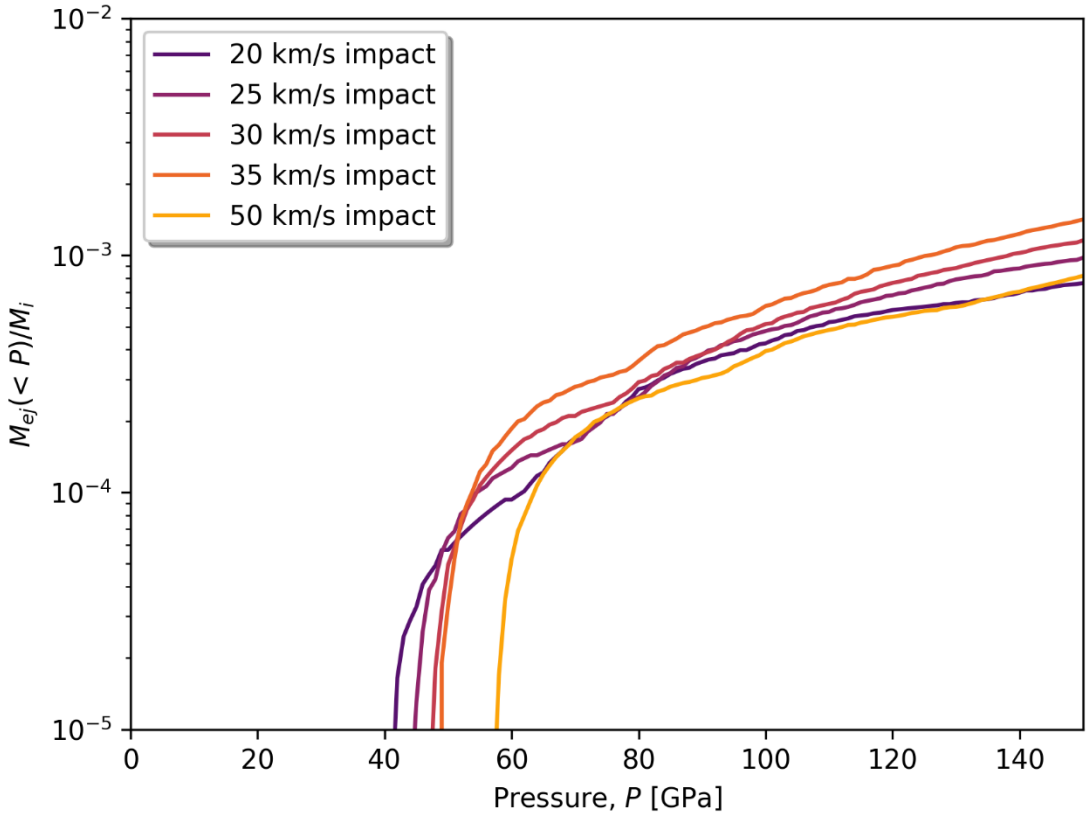

Figure 4.2: *The cumulative mass of target material ejected (M_{ej}) as fraction of impactor mass (M_i) shown as a function of shock pressure (P) for different impact velocities in 2D simulations with a resolution of 600 cppr.*

from 600 cppr simulations at 20 km s^{-1} impact velocity were comparable to higher resolution simulations, 600 cppr was used to simulate subsequent impacts at higher impact velocities. Increasing impact velocity from 20 km s^{-1} up to 35 km s^{-1} in 5 km s^{-1} increments increased the minimum pressure experienced by escaping ejecta (Figure 4.2). The minimum pressure of 10^{-5} M_i of escaping ejecta increased from 41 GPa at 20 km s^{-1} to 45 GPa at 25 km s^{-1}, 48 GPa at 30 km s^{-1}, and 50 GPa at 35 km s^{-1}. For these impact velocities, the total mass of ejected material at any pressure up to 150 GPa increased overall with increasing impact velocity, so faster projectiles produce more ejecta as expected. However, increasing impact velocity further to 50 km s^{-1} resulted in a marked increase in the minimum pressure for escaping material, up to ~58 GPa. The amount of material experiencing pressures <150 GPa decreased relative to the previous trend shown with the lower impact velocities. Figure 4.2 shows an accumulated mass of ejected material experiencing pressures <150 GPa similar to the 20 km s^{-1} scenario, ~7×10^{-4} M_i.

The source location of the high-speed ejecta is explored in the 20 km s^{-1} impact, the scenario with the lowest pressures experienced by escaping material. Figure 4.3 shows the peak pressures mapped over the original shapes of the target and projectile (Figure 4.3a), along with a zoomed-in plot highlighting the low-pressure, high-speed area of the target where material was ejected (Figure 4.3b). The proximity of the high-speed ejecta to the impact zone (Figure 4.3) meant

that a significant proportion of the ejected material underwent the process of "jetting" away from the impact site, rather than being spalled further from the point of impact. Jetting involves the "squeezing" of target material between the projectile and material immediately adjacent to the point of impact. Jetted material characteristically ejects at velocities faster than that of the impacting projectile and reaches high shock pressures, routinely melting and vaporising after ejection. Figure 4.3a shows high pressure material directly beneath the impact site, extending to ~22 km from the initial point of contact on the surface. The area of the target where material is ejected at velocities >11 km s^{-1} is highlighted in Figure 4.3b (dashed black line) and shows that the only material that is ejected at these high speeds is located close to the surface of target. The 11 km s^{-1} ejecta zone extends less than 300 m into the target, with the lowest peak pressures found in the area most distal to the point of impact. These figures showcase the need for the very high resolution of the simulations in order to resolve such small volumes of material that experience both high speed and pressures low enough to remain solid in these impacts. The vertical nature of these simulations heavily limits the amount of material that can experience velocities sufficient for material to escape the Earth and concentrates the material close to the contact zone. As the projectile motion has no horizontal component, there is a significant lack of horizontal motion of ejected material when compared to impacts with lower impact angles. Subsequently, the relatively small amount of material that does escape is forced out under more extreme conditions, with jetted material dominating over spalled. The next section introduces variable impact angles of the 3D simulations and provides evidence supporting the theory that oblique impacts produce more high-speed, low-pressure ejecta than their vertical counterparts.

Data tables for the 2D simulations can be found in the electronic appendix, under the filename "Ch4_2D_earth_esc_vel_resolution_tables".

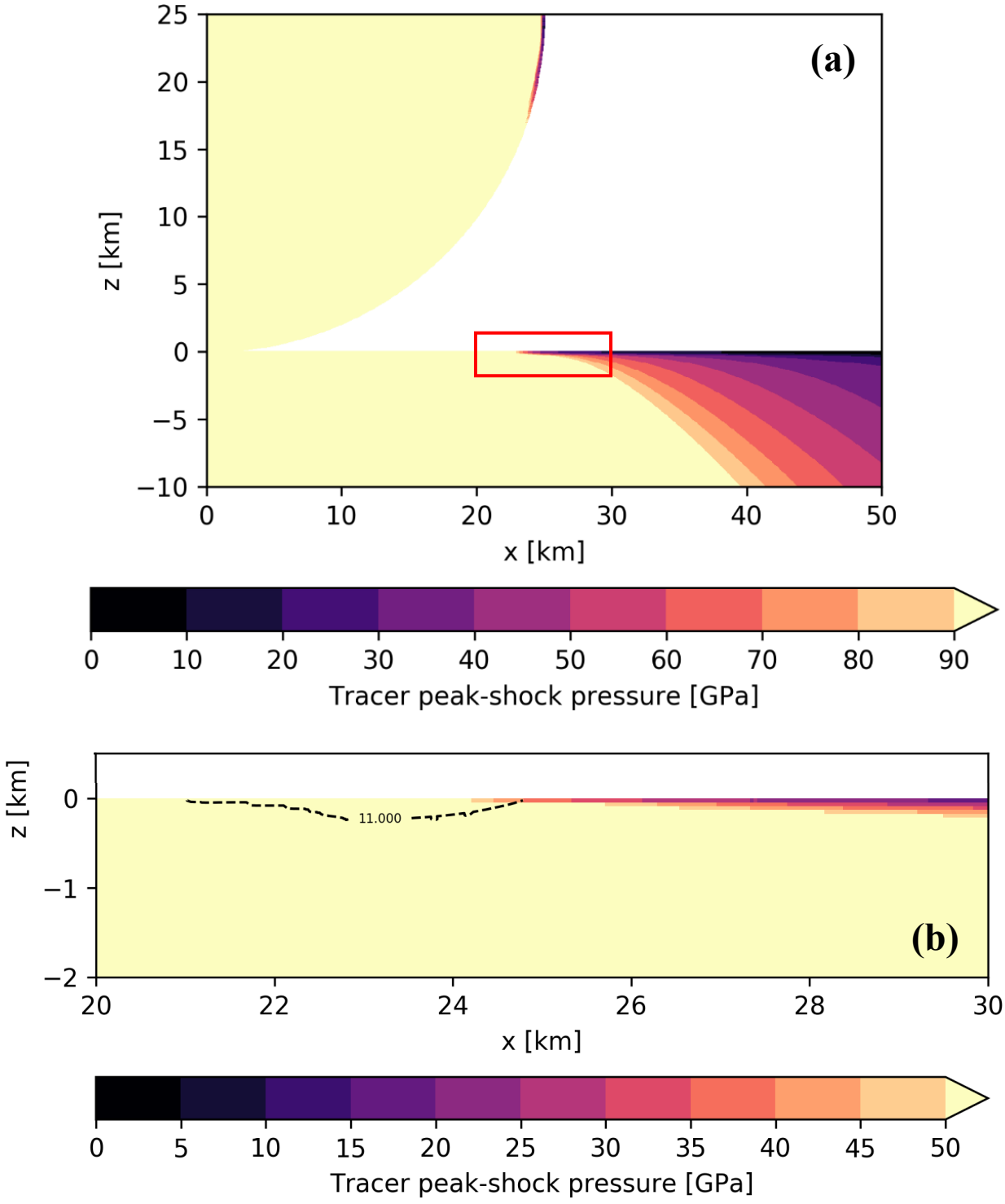

Figure 4.3: *Provenance plot of high-speed ejecta that experiences different peak shock pressures for a 2D simulation of a 50-km diameter impactor striking Earth with a speed of 20 km* $\mathbf{s^{-1}}$ *and resolution 600 cppr. The spallation zone from (a) is highlighted (red box) in (b) with lower peak pressures defined by the colour bar below. Black dashed line shows volume within which velocity reaches 11 km* $\mathbf{s^{-1}}$.

4.3.2 Three dimensional simulations

Results from the resolution test for the 3D simulations confirm that, in a typical large impact on Earth, some solid ejecta can reach escape velocity. In the highest resolution simulation (100 cppr) for a projectile with velocity 20 km s^{-1} and angle 45°, the total mass of material ejected faster than escape velocity M_{ej} (>11.2 km s^{-1}) as a fraction of impactor mass (M_i) is 5.5% (Figure 4.4). Ejected material that can still be considered solid (i.e., that experiences pressures lower than a nominal critical pressure for melting of 50 GPa) amounts to a mass fraction (M_{ej}/M_i) of 0.13%. The mass of escaping ejecta is consistent with estimates made by Armstrong *et al.* (2002) using analytical ejecta mass-velocity scaling relationships and hence support their predictions of the efficiency of Earth-Moon transfer. Armstrong (2010) showed that direct transfer of ejecta from Earth to the Moon, which was the most efficient transfer mechanism during the LHB, has an efficiency of ~1×10^{-4} and requires ejection speeds between ~10.9 and 11.2 km s^{-1}. Armstrong (2002, 2010) calculated the transfer efficiency by taking the number of particles that impacted the lunar surface and dividing by the total number of simulated particles ejected from the Earth during the simulation. According to the simulations, a total ejecta mass of approximately 4×10^{-3} projectile masses is ejected at speeds within this range (Figure 4.4b). This suggests that the mass flux of terrestrial meteorites to the Moon was approximately 4×10^{-7} times the mass flux of large impactors striking Earth during the LHB, consistent with previous estimates (Armstrong, *et al.* 2002; Armstrong, 2010). Building on the assumption of transfer efficiency from Armstrong *et al.* (2002) and Armstrong (2010), an ejection velocity of 11 km s^{-1} is used as a threshold for escaping material to reach the lunar surface.

Figure 4.4 also shows that high spatial resolution is necessary to resolve the low-shock, high velocity escaping ejecta. While the mass of solid escaping ejecta is well resolved at 100 cppr, simulations with a resolution of 40 cppr are unable to resolve any solid escaping ejecta. This explains the discrepancy between the ejecta mass-velocity scaling relationships used by Armstrong (2010) and the results of low(er) resolution simulations of the Chicxulub impact (Artemieva and Morgan, 2009). Low-shock material ejected fast enough to escape Earth originates from very close to the surface of the target, in close proximity to the impact site (Figure 4.5). This is the so-called interference zone (highlighted in Figure 4.5b) where interaction between the shock and release waves generates very steep pressure gradients but shields the ejected material from high pressure (Melosh, 1984). The minimum shock pressure experienced by ejected meteorites in the 100 cppr (250 m cell size) simulation is ~30 GPa for a mass of material equivalent to 10^{-6} M_i, however even at this high resolution the simulation is not fully resolved at the lowest shock pressures (Figure 4.4a) and the cell size is much

larger than the expected size of individual meteorites. It is therefore likely that a small volume of even lower shock ejecta not resolved in the simulations will reach escape velocity and may be transferred to the Moon.

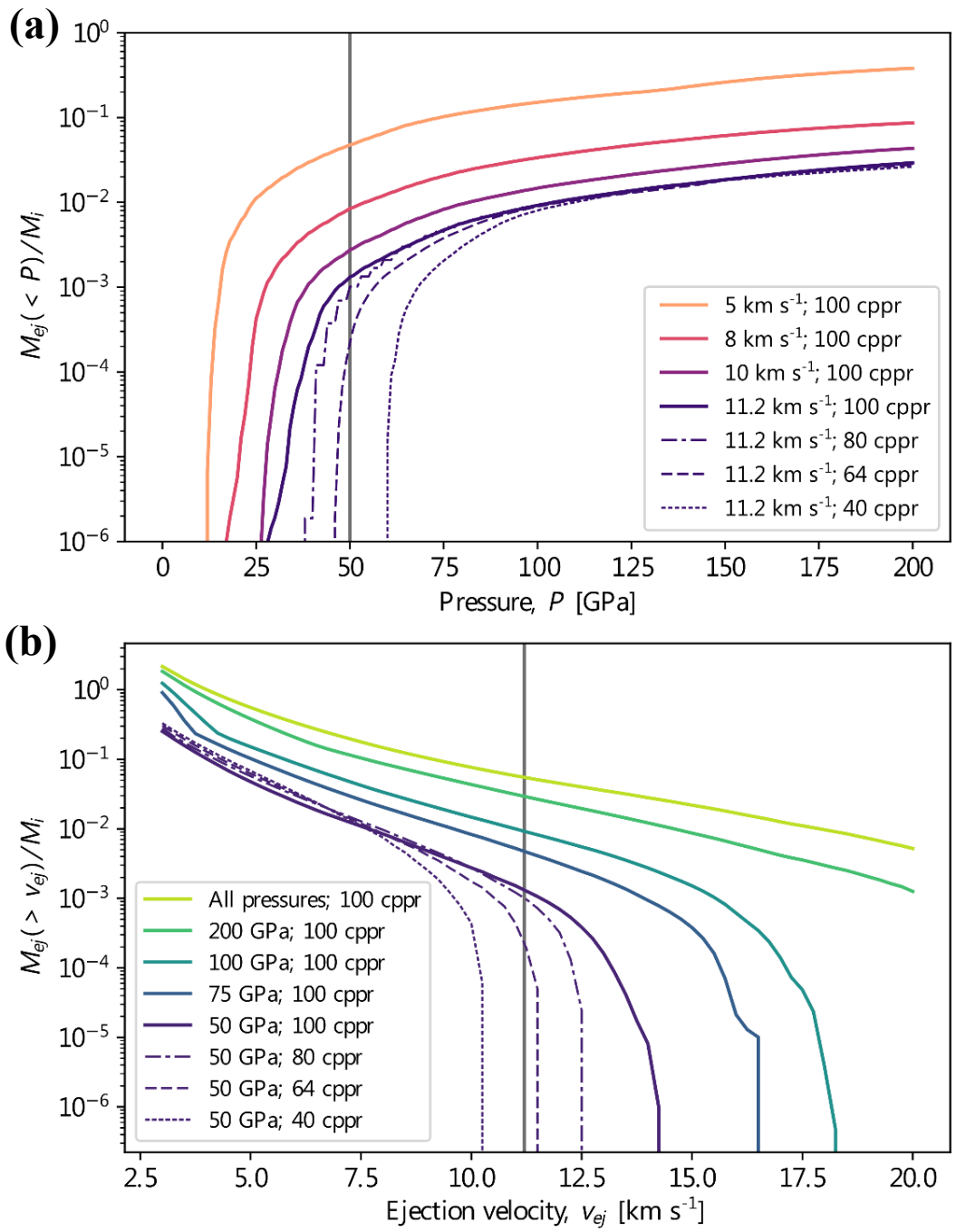

Figure 4.4: *Resolution test. The cumulative mass of target material ejected (M_{ej}) as fraction of impactor mass (M_i) shown as a function of shock pressure for different ejection speeds (a) and as a function of ejection speed for different shock levels (b). The influence of spatial resolution is shown for the solid ejecta (P <50 GPa) that escapes Earth (v_{ej} >11.2 km* $\mathbf{s^{-1}}$*).*

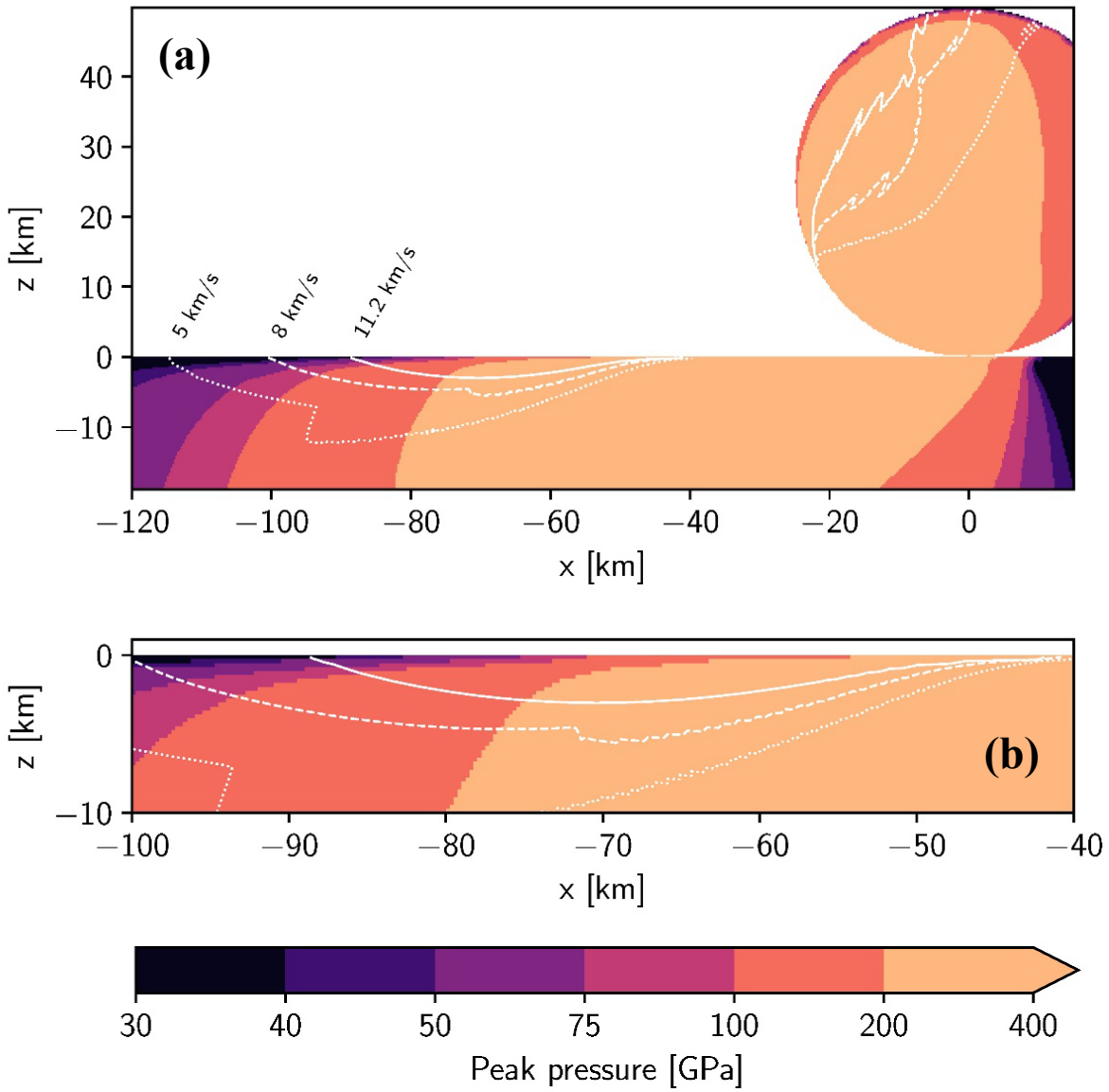

Figure 4.5: *Provenance plot of high-speed ejecta that experiences different peak shock pressures for a simulation of a 50-km diameter impactor striking Earth at 45° to the surface and with a speed of 20 km* $\mathbf{s^{-1}}$ *with resolution 100 cppr. The spallation zone from (a) is highlighted in (b). The direction of impact is from right to left. White contour lines display volumes of the target where different ejection velocities are reached.*

After investigating the influence of resolution and finding that the simulations required very high resolutions (100 cppr) to resolve the small mass of material experiencing high velocities and low pressures, subsequent scenarios involving varied impact velocity and angle were all run at 100 cppr. Beginning with the established impact velocity of 20 km s^{-1}, the impact angle was varied to consider 30°, 45°, and 60° (relative to the horizontal target surface). From this point forwards, the scenarios are referred to by the impact velocity (v) and angle (a) of the projectile and are labelled as such on the related figures. For example, the simulation where the projectile travels at 20 km s^{-1} into the target at an angle of 30° will be referred to as simulation v20_a30.

Increasing the angle of impact to 60°, closer to a vertical impact (90°) like those in the presented in the 2D simulations, resulted in an increase in the minimum pressure experienced by escaping ejecta. In fact, pressures exceeded 50 GPa and it is likely that all of the escaping material melted or vaporised after ejection. For pressures up to 150 GPa, the total mass of material being ejected at velocities >11 km s^{-1} was lower for this scenario (~4×10^{-3} M_i) versus scenarios with the same impact velocity but lower impact angles (45°: ~2×10^{-2} M_i, 30°: ~3×10^{-2} M_i) illustrated by Figure 4.6. Results from the simulation with impact velocity and angle of 20 km s^{-1} and 30° (v20_a30, Figure 4.6) resulted in the lowest pressures experienced for the 20 km s^{-1} velocity scenarios. An equivalent mass of 10^{-5} M_i experienced pressures equal to or less than 10 GPa, low enough to meet the requirements for being considered low-shock material that could harbour identifiable biomarker material after ejection. The majority of this material was ejected from an area very close to the target surface, between 100 and 125 km downrange from the point of impact (Figure 4.9). Material above the black dashed line in Figure 4.9 is ejected at velocities >11 km s^{-1} and Figure 4.9b highlights the location of the lowest pressure target material ejected above this velocity threshold. Pressure decreases significantly from 90 km to 125 km at the top surface, down from over 100 GPa to less than 10 GPa. Material ejected from depth experiences progressively higher pressures, associated with the path of the projectile as it entered the target at 30° and influenced the direction of the pressure waves that propagated through the target as a result.

Increasing impact velocity to 30 km s^{-1} to represent faster projectiles such as short-period comets (and potentially particularly fast asteroids) resulted in lower minimum peak pressures experienced for escaping ejecta in all three impact angles considered compared to their slower counterparts. This is likely due to low-pressure ejecta being located further from the impact site, but with enough energy transferred from the faster projectile to the target, the distant material was propelled fast enough to escape. Impacting at an angle of 30° again provides the lowest pressures for escaping ejecta, as low as 3 GPa for a mass of 10^{-5} M_i of target material. This material is the most likely to be the source region of terrestrial

ejecta that could transport biomarkers or evidence of organic material from the early Earth to the Moon. Such low pressures after ejection would be suitable for the survival of many amino acids, organic hydrocarbons, and some larger biomarkers which will be discussed in further detail in the next chapter. The provenance of such ejecta is highlighted in Figure 4.10.

Similar to the previous scenario at 20 km s^{-1}, the majority of low-pressure ejecta is located ~120 km from the point of impact (Figure 4.10b). The zone for where material can be ejected >11 km s^{-1} is larger and extends further downrange from the impact site, with escaping ejecta found over 140 km downrange (highlighted by the black, dashed contours on Figure 4.10a & 4.10b). Increasing the impact angle through 45° and 60° displays the same trend shown in Figure 4.7 as the 20 km s^{-1} impact velocity simulations in Figure 4.6, where less oblique impacts produce a reduced mass of escaping material overall. However, Figure 4.7 highlights how 30 km s^{-1} impacts at 45° and 60° display very similar trends in their plots for mass ejected versus pressure experienced. The initial trend of lower masses experiencing lower pressures continues with these results. There is ~10^{-2} to ~10^{-4} M_i of escaping material reaching a convergence at ~40 GPa for v30_a45 and ~50 GPa for v30_a60, where the plots essentially become vertical when trending toward zero.

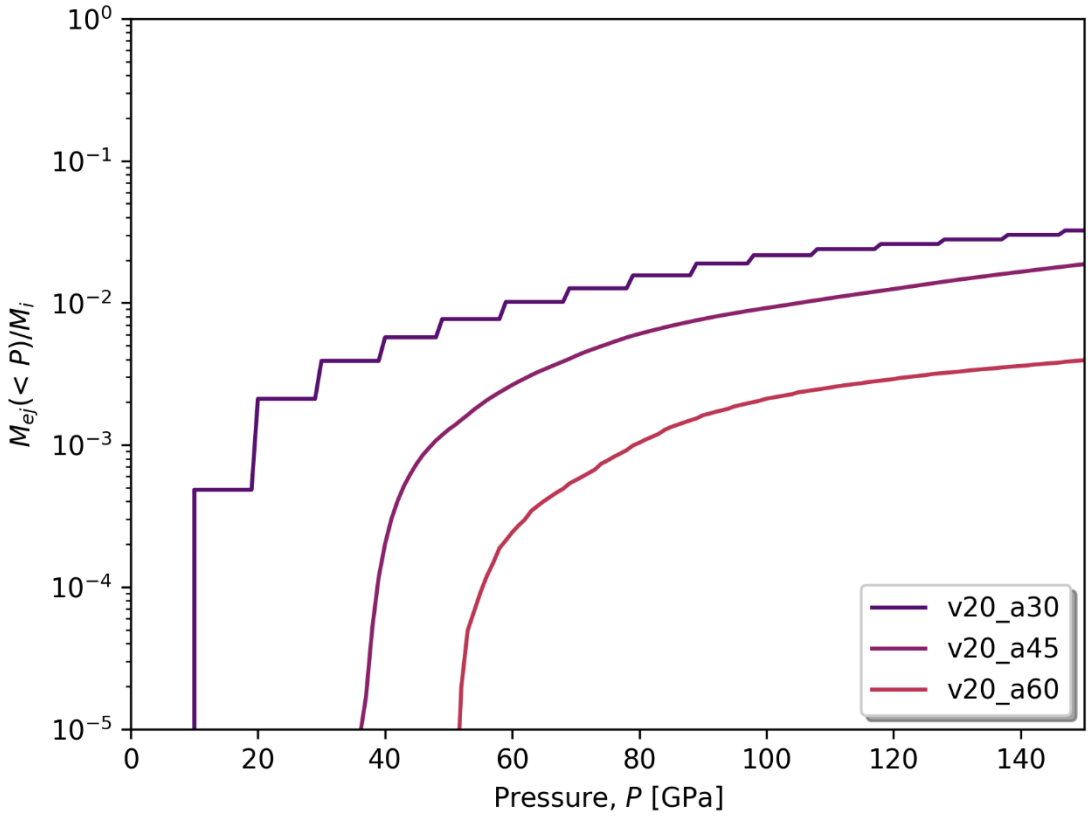

Figure 4.6: *The cumulative mass of target material ejected (M_{ej}) as fraction of impactor mass (M_i) shown as a function of shock pressure for different impact angles (30°-60°) for impacts with a velocity of 20 km* $\mathbf{s^{-1}}$.

Impacts at 55 km s^{-1} seem to converge in terms of the total mass of escaping ejecta at pressures up to 150 GPa, with masses equivalent to ~2–4×10^{-2} M_i for all three impact angles (Figure 4.8). Impacting at an angle of 30° results in pressures <10 GPa, but higher than the 30 km s^{-1} impact for the same angle. Impact angles of 45° and 60° follow the same trend as before, with higher pressures experienced by the escaping ejecta than at 30°. Once again, the 30° impact is the only scenario where material is able to escape the Earth and results in low enough shock pressures to remain viable for biomarker survival. When comparing all of the scenarios, it is clear that the impact angle has a greatest influence on the mass of low-pressure, high-speed ejecta when compared to impact velocity. An impact angle of 30° and velocity of 30 km s^{-1} produces the lowest pressure material for any scenario, 3 GPa, for a resolvable mass of ~10^{-5} M_i. Whilst the 30° impacts at 30 and 55 km s^{-1} produce ejecta with lower minimum peak pressures than the 20 km s^{-1} scenario, they produce lower masses of high-speed ejecta experiencing pressures suitable for biomarker survival (<10 GPa). Scenario v55_a30 only produces ~10^{-5} M_i of escaping ejecta with peak pressures <20 GPa, whilst scenarios v30_a30 and v20_a30 produce ~10^{-4} M_i and ~5×10^{-4} M_i at <10 GPa, respectively. Based on peak pressures alone, increasing the velocity for a given projectile at an impact angle of 30° results in a decrease in the mass of material viable for biomarker transfer from Earth to the Moon. The mass of viable material decreases by 5 times from 20 km s^{-1} to 30 km s^{-1} and by over an order of magnitude from 20 km s^{-1} to 55 km s^{-1}.

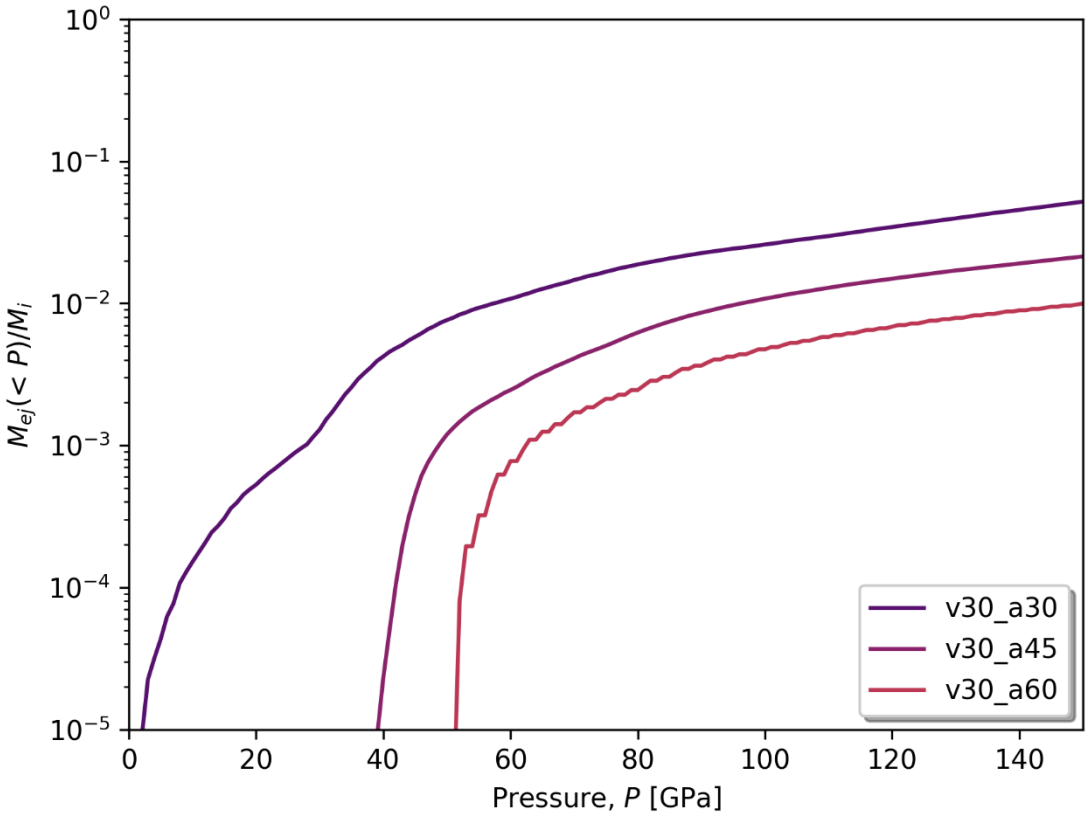

Figure 4.7: *The cumulative mass of target material ejected (M_{ej}) as fraction of impactor mass (M_i) shown as a function of shock pressure for different impact angles (30°-60°) for impacts with a velocity of 30 km* $\mathbf{s^{-1}}$.

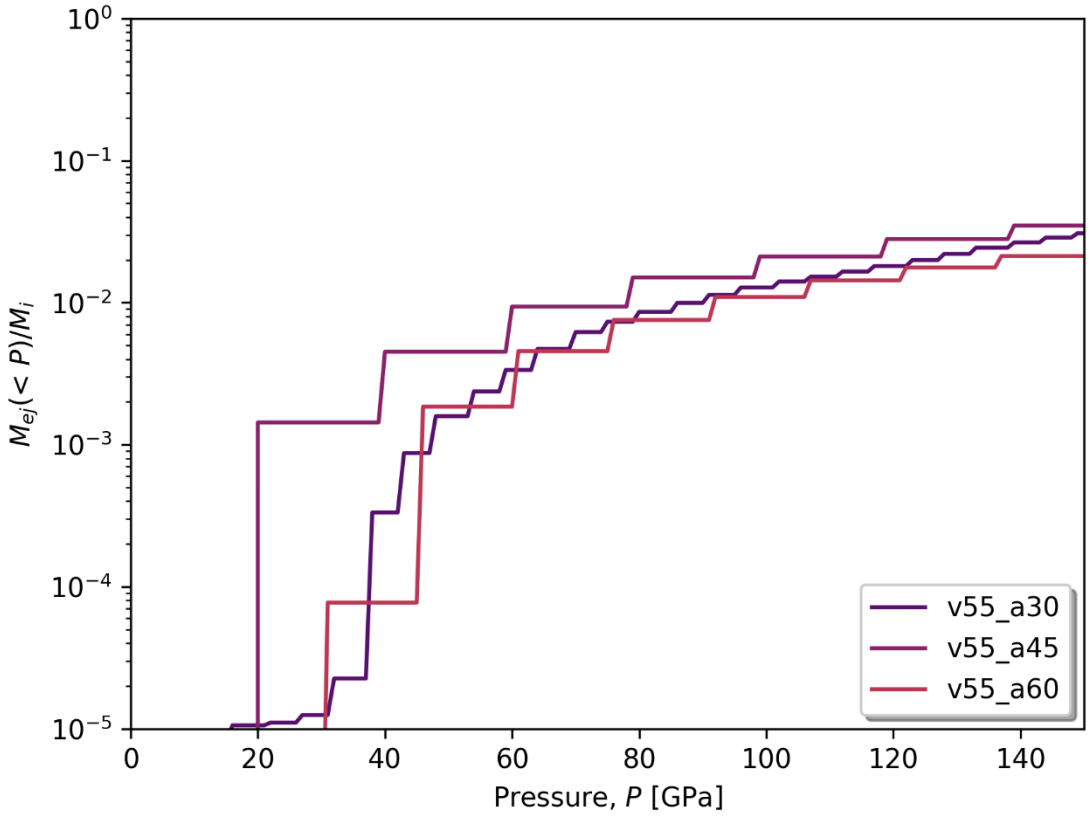

Figure 4.8: *The cumulative mass of target material ejected (M_{ej}) as fraction of impactor mass (M_i) shown as a function of shock pressure for different impact angles (30°-60°) for impacts with a velocity of 55 km* $\mathbf{s^{-1}}$.

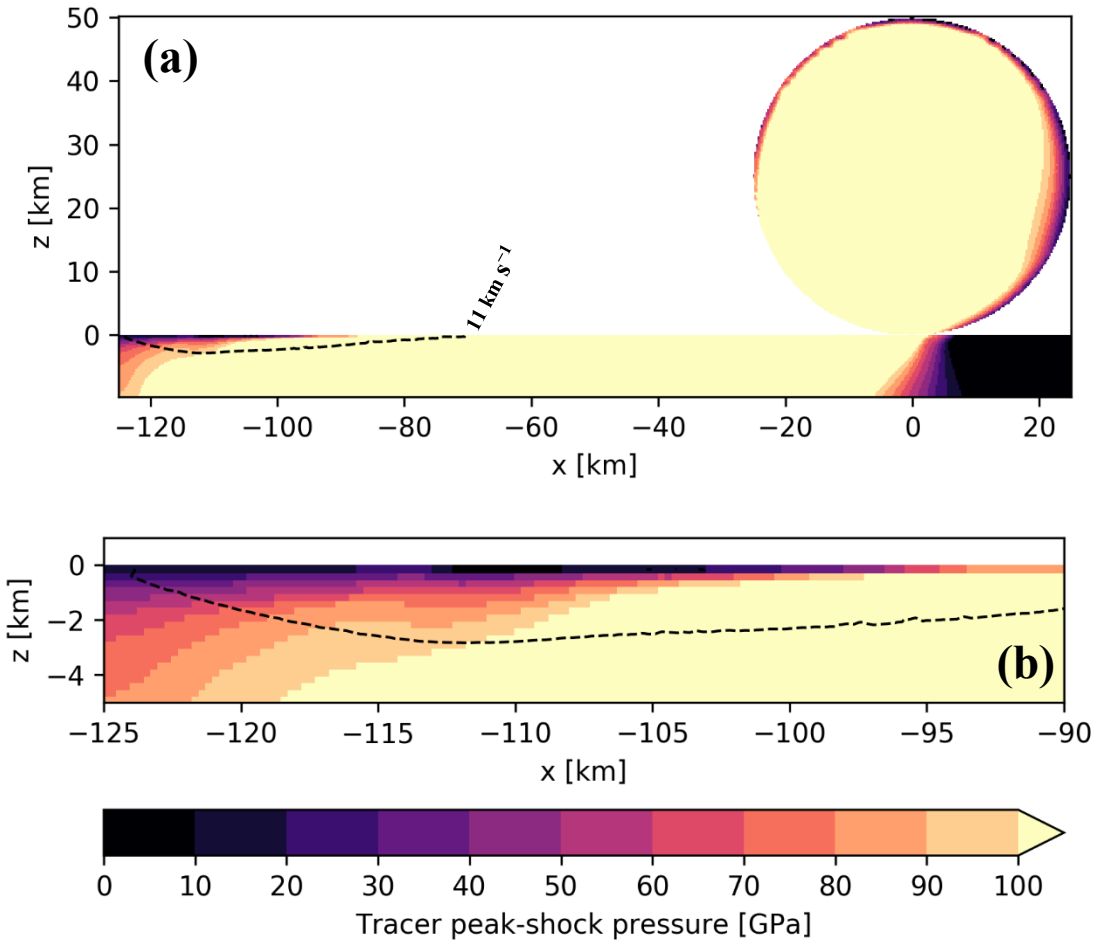

Figure 4.9: *Provenance plot of high-speed ejecta that experiences different peak shock pressures for a simulation of a 50-km diameter impactor striking Earth at 30° to the surface and with a speed of 20 km* $\mathbf{s^{-1}}$ *with resolution 100 cppr. The spallation zone from (a) is highlighted in (b). The direction of impact is from right to left. Black dashed line shows volume within which velocity reaches 11 km* $\mathbf{s^{-1}}$.

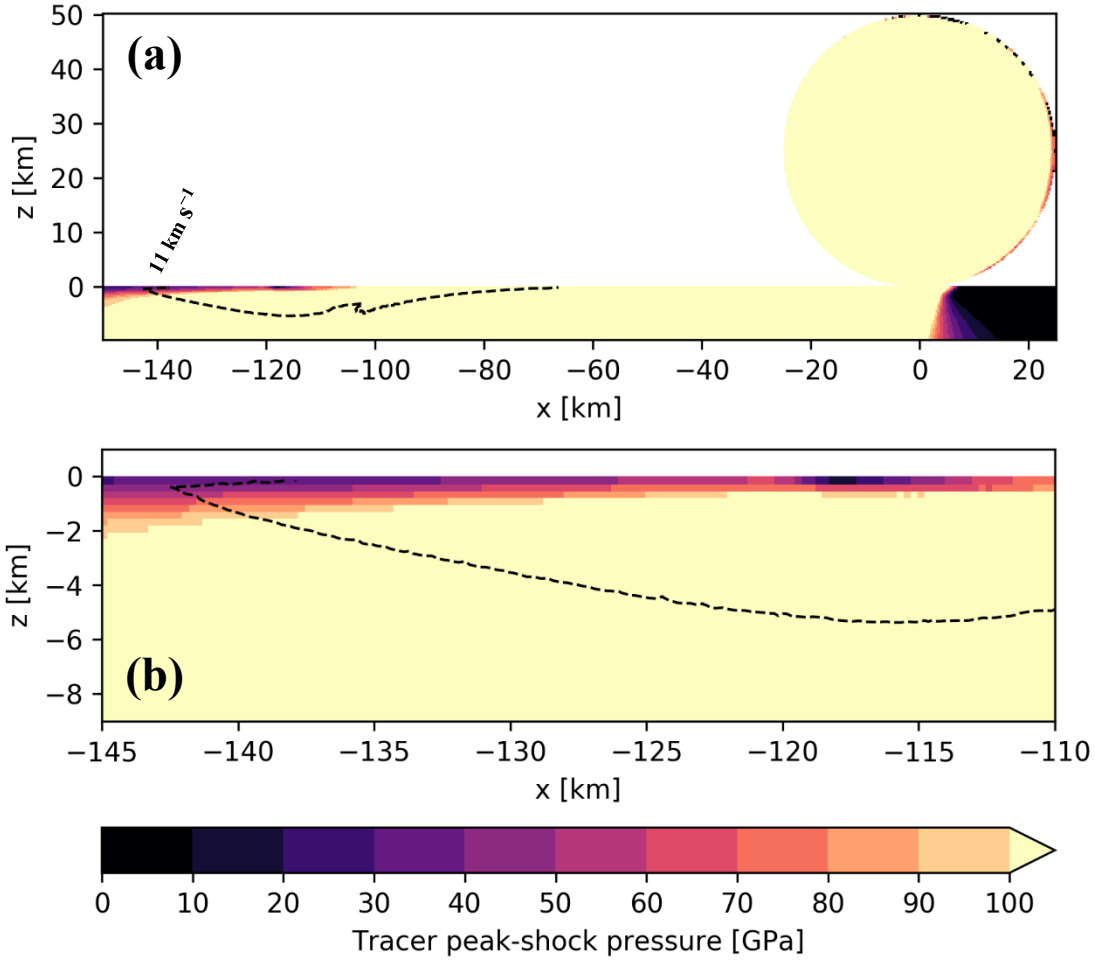

Figure 4.10: *Provenance plot of high-speed ejecta that experiences different peak shock pressures for a simulation of a 50-km diameter impactor striking Earth at 30° to the surface and with a speed of 30 km* $\mathbf{s^{-1}}$ *with resolution 100 cppr. The spallation zone from (a) is highlighted in (b). The direction of impact is from right to left. Black dashed line shows volume within which velocity reaches 11 km* $\mathbf{s^{-1}}$.

4.3.3 Temperature regimes in low-pressure ejecta

Now that we have investigated the pressure of escaping material and determined that it is possible to launch material from Earth that could contain surviving biomarkers, we need to also consider the temperatures experienced by the ejected low-pressure material. Some biomarkers, especially long-chain amino acids (Bertrand *et al.*, 2009), can survive near instantaneous bursts of high pressures and remain intact (or intact enough to be recognised as biological material), but can rapidly disintegrate under sustained temperatures as a result of the increased pressures. Therefore, there is the need to consider the temperature history of the ejected material and compare that to the likelihood of survival for entrained biological markers. For this, the best-case scenarios for a significant mass of ejecting low-pressure material was evaluated in terms of the temperatures experienced over the course of the ejection process, until the end of the simulation. Only the material that experienced pressures lower than 10 GPa was considered for this investigation and therefore includes the scenarios with impact angles of 30° as these produced the only high-speed ejecta below this pressure threshold. Both the peak-shock temperature recorded at any time in the simulation and the temperature experienced at the final timestep of the simulation were used to compare the extent of heating and the rate of cooling for each scenario.

Figure 4.11 displays results of the investigation, using the same format as the peak pressure plots shown previously, but for peak temperature (Figure 4.11a) and final temperature (Figure 4.11b) of the ejected material. Peak temperatures recorded by the ejecta are very high across all of the scenarios. A minimum peak temperature of ~5000 K is recorded in 10^{-6} M_i of ejecta in scenario v20_a30, rising to a maximum of ~14000 K. These temperatures rise further when considering faster impact velocities, with minimum peak temperatures of just over 10000 K for scenario v30_a30 and ~40000 K in scenario v55_a30 (Figure 4.11a). Despite this material recording maximum pressures of between 10–20 GPa at any point during the simulations, they appear to experience anomalously high temperatures compared to their relatively low shock pressures. However, these peak shock temperatures are only experienced for very short period of time, usually within one timestep (0.25 s); much like how maximum peak pressures are experienced by material near instantaneously as a pressure wave passes through the target material and then rapidly decreases as the pressure wave travels away from the point of impact. This “flash” of heat may not last long enough to fully melt or vaporise ejecta and the evidence for entrained biological material within. Therefore, it is important to consider the final recorded temperatures experienced by the low-pressure ejecta and these are recorded in the last timestep of the simulations (equivalent to 15 seconds of simulated time). Of course, the actual final temperature will be that of the ambient temperature surrounding the material once ejected. However, this is far beyond the length of time modelled in these simulations and would require an entirely new set of

dedicated modelling, far beyond the scope and capabilities of iSALE.

Results for the final recorded temperatures are shown in Figure 4.11b and display evidence for the rapid cooling of the ejecta compared to the peak temperatures recorded. Firstly, the final temperatures in scenario v55_a30 are still far too high to consider any surviving biomarker material, with minimum temperatures >6500 K still being recorded by the tracers within the ejecta. This material vaporised after ejection. Moving on to scenario v30_a30, final temperatures are significantly lower, with a minimum recorded temperature of ~700 K in a mass of $\sim 1.5 \times 10^{-6}$ M_i of ejecta. The majority of the material still remains at temperatures too high for the ejecta to remain solid, with a cumulative mass of $\sim 3 \times 10^{-6}$ M_i recording final temperatures <2000 K.

In terms of final temperatures, scenario v20_a30 provides the most likely conditions for the survival of biomarkers, despite recording higher minimum peak pressures than v30_a30. Temperatures reduce to a minimum of 250 K, recorded in a mass of $\sim 10^{-6}$ M_i, significantly lower than the minimum peak temperatures experienced and a dramatic reduction over the 15 seconds of simulated time. A large proportion of ejecta (cumulative mass of $\sim 10^{-5}$ M_i) also records final temperatures less than 1000 K. Combining this with the peak pressure data recorded by the same material, it is likely that a significant mass of material (between 10^{-6} and 10^{-5} M_i) experiences pressures and temperatures conducive to the survival of biomarkers. The parameters for this scenario, with an impact velocity of 20 km s^{-1} and angle of 30°, result in the only scenario where this is true for both pressure and temperature.

Whilst it may have seemed plausible for biomarkers to survive ejection from Earth in scenarios v30_a30 and v55_a30, recording significant masses of ejecta with relatively low peak pressures, the temperature data for both scenarios contradict this outcome. These results show that revealing the history of both the pressure and temperature regimes in the ejected material is critical to determining the survival of the relatively fragile entrained biological material. Previous studies investigating biomarker survival may have overestimated the mass of suitable material if only pressures were considered, and temperatures simply assumed to scale with peak pressure. Reasons for the unexpectedly high temperatures of the low-pressure, high-speed ejecta will be discussed in the next section, but is likely related to the relatively newly discovered process of 'post-shock acceleration'. Additionally, the clear favourability of low-pressure ejecta at more oblique impact angles may also be a consequence of 'post-shock acceleration' (Wakita *et al.*, 2019; Okamoto *et al.*, 2020). Sustained compression in the target produces a gradual acceleration with less shock, alongside higher acceleration efficiency in oblique impacts compared to vertical. However, shear deformation due to movement of the projectile through the target

produces additional heating for a wide area. This can lead to low shock pressures (<10 GPa) but significantly higher temperatures (>1000 K) due to the combined influences of shock and shear heating (Wakita *et al.*, 2019).

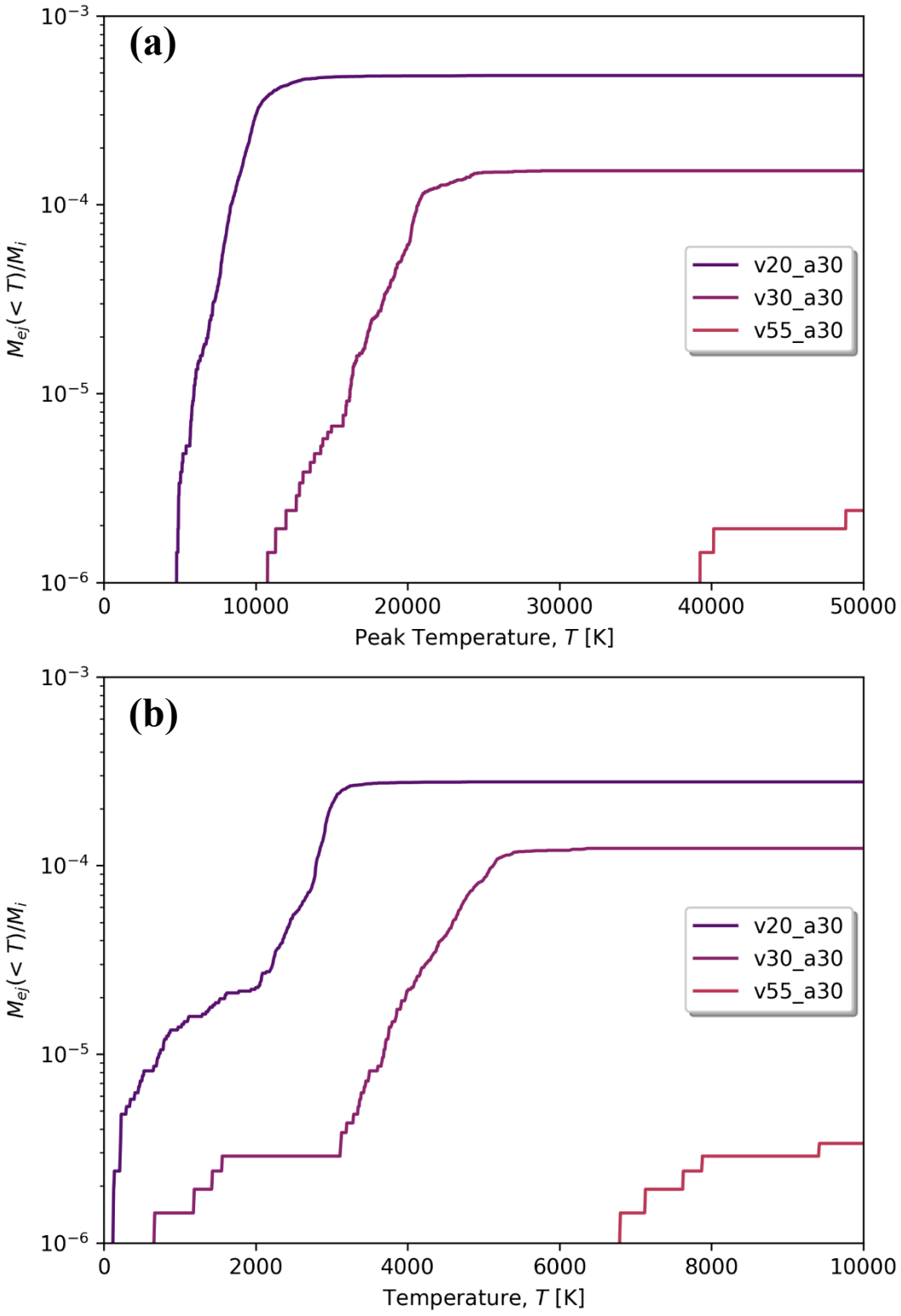

Figure 4.11: *The cumulative mass of target material ejected (M_{ej}) as fraction of impactor mass (M_i) that experiences pressures <10 GPa, shown as a function of (a) peak-shock temperature and (b) temperature at the final timestep of simulation (15 seconds post-impact) for different impact velocities (20, 30, & 55 km* $\mathbf{s^{-1}}$*) at an impact angle of 30°.*

4.4 Discussion

If pressure was the only threshold considered in these models as a barrier to surviving biomarkers after ejection, then multiple scenarios would have been considered to yield some mass of suitable material. Scenarios v20_a30, v30_a30, and v55_a30 all contained masses $>10^{-5}$ M_i of escaping ejecta with pressures <10 GPa. However, the extreme high temperatures experienced by the same ejecta restrict the suitability for material to contain survived biomarkers after ejection. Only scenario v20_a30 produced such ejecta that cooled fast enough to temperatures suitable for biomarker survival.

The extreme high temperatures recorded in part of the target material capable of escaping from Earth after a giant impact is somewhat contradictory to the expected outcome, especially when considering the low pressures experienced (<10 GPa). Usually, it is assumed that peak pressures can be used as a proxy for the survival of the material being examined and any entrained biological material within, with temperatures assumed to scale reasonably well with peak pressures. Therefore, many studies neglect to include temperature data at all when deciding the fate of the material and rely on peak pressures alone. Initially, a process called 'post-shock acceleration' potentially explained the high-temperature, low-pressure ejecta. First named 'late-stage acceleration', the process was discovered, and the term coined, by Kurosawa *et al.* (2018) during an investigation of high-speed ejecta near the point of impact. A suite of 2D, iSALE simulations and 3D, smooth particle hydrodynamic (SPH) numerical modelling scenarios were compared for a set of vertical impacts. They found that an unknown mechanism was accelerating some ejecta in the spallation zone to speeds faster than expected based on the impactor velocity and parameters relating to the target. This mechanism caused a pressure gradient to build from the root of the ejecta curtain, directed upward and outward from the target surface, adding to the acceleration of the ejecta. Later, a new study built upon this work (Okamoto *et al.*, 2020) and tested the influence of impact angle on the process of ejection and late-stage acceleration. In the work by Okamoto *et al.* (2020), simulations of both vertical and oblique impacts were considered and compared to experimental impacts of a similar nature. The original term of 'late-stage acceleration' was replaced with 'post-shock acceleration' to remove any misconceptions of when this process occurred in the terms of an impact. The term 'late-stage' has routinely been associated with the final processes of impact crater formation, such as modification and collapse of a crater, whereas the ejection of high-speed ejecta occurs relatively early in the impact process. Oblique impacts were revealed to greatly increase the mass of high-speed ejecta for a given scenario versus their vertical counterpart. The translational motion of the impacting projectiles parallel to the target in oblique impacts is likely to have

contributed to long-term, sustained acceleration at the root of the ejecta. It has been suggested by Wakita *et al.* (2019) that oblique impacts can generate ejecta with higher peak temperatures than a vertical impact at a given peak pressure. The area heated by the oblique nature of the impact is located close to the target surface and in a direction downrange of the projectile trajectory. The enhanced heating is likely the result of a combination between the shear strength of the material and the movement of ejecta after post-shock acceleration. Including material strength in the simulations allows for the calculation of shear heating within the ejecta, which can contribute a significant amount of heat in addition to the shock heating generated by the pressure wave from the impact. The influence of shear heating on impacting projectiles is discussed in detail in the next chapter when describing the pressure and temperatures regimes within terrestrial meteorites impacting the lunar surface.

However, the temperatures recorded for the simulations in this work are so high that it seems incompatible with the pressures, even with the assumption that late-stage acceleration and the associated shear heating contribute a significant amount of heating in low-shock material. It should therefore be noted that the high temperatures recorded may be an artefact of the simulation. This could be because of a number of factors. Firstly, it could be a symptom of the resolution of the simulations. The resolution tests (Figure 4.4) provide evidence of a lack of convergence for the high-speed (especially at or above escape velocity) and low-pressure ejecta, even at 100 cppr. Temperatures are significantly affected by the strength of material, whilst pressures remain relatively stable between hydrodynamic and strength-based modelling. Therefore, it may take higher resolution modelling to produce both accurate temperature and pressure regimes. Secondly, the problem may be the result of inaccuracies in the recording of tracer data. Tracer movement can become inaccurate at very high velocities and tracers can drift into areas away from the material they were originally meant to track. When recording peak temperatures, the highest temperature recorded by a tracer at any time in the simulation is saved. The peak temperature overwrites any others recorded during the simulation. Therefore, if the tracer drifted away from its original material, into an area with a particularly high temperature during the ejection process, this would inaccurately represent a much higher peak temperature history than the true temperature history of the tracer (and associated material). Lastly, it could be due to a bug in the code of iSALE3D itself. With more time, these results could be further investigated with additional modelling. However, due to the high computational power and time needed to simulate these impacts, there was not time during this work to repeat any of the large 3D simulations. Therefore, it is prudent to treat the temperature profiles of the ejected, low-pressure material with slight suspicion.

Simulating the ejection of low-pressure material from Earth requires a significant amount of time and computing

power. As a result, this requires the assumption or neglect of multiple parameters that may affect the mass of terrestrial material ejected in a real-world scenario. In addition to assumptions made, higher spatial resolution models could provide additional evidence for larger masses of low-pressure ejecta. The resolution tests show that 100 cells per projectile radius is not sufficient to resolve small fractions of low-shock, high-speed ejecta in some scenarios where the angle of impact is 45° or more (highlighted in the resolution test shown in Figure 4.4a). Whilst the results seem to have converged at higher pressures, the lowest pressures experienced by the ejecta consistently decreases with increasing resolution for masses of 10^{-5} M_i or less. This leaves room for continued reductions in peak pressure in the small volumes of material that do escape the Earth. Higher resolution modelling would be a considerable asset to future work, but is limited by computational resources, time, and limitation within iSALE itself with the number of tracers allowed to be tracked by a simulation. Next, some of the parameters expected to have the greatest effect on the results produced from the simulations in this chapter are explored to justify the assumptions made.

An atmosphere was not included in this suite of simulations. The inclusion of an atmosphere was deemed unnecessary due to the scale of the simulations, both in spatial resolution and the time it would have taken to consider the parameters required to model an accurate atmosphere for the time of the impact. Atmospheric deceleration and ablation of meteoroids entering an atmosphere have been studied in great detail for projectiles entering the Earth's atmosphere (e.g., Beech and Comte, 2018; Beech *et al.*, 2019). Equations describing this process have been modified to essentially reverse this process, calculating the effect an atmosphere may have on ejecta after launch from the Earth (Beech *et al.*, 2019). Generally, the consensus is that a giant impact (km scale projectiles) will greatly perturb an atmosphere from its normal state (Melosh and Vickery, 1989; Melosh, 1990; Newman *et al.*, 1999). The duration and scale of the perturbation is dependent on the energy of the impact, but for an impactor with size, velocity, and density of that simulated in this work, it is likely that the atmosphere would be greatly disrupted post-impact. According to Beech *et al.* (2019), using equations from Melosh (1990), an impactor that produces a crater on the order of 5-6 km in diameter will create a vapour plume large enough to burst through the Earth's atmosphere. Any scenario where the impactor is smaller than this will likely result in a relatively unperturbed atmosphere which would act as a filter for smaller ejected fragments, losing too much mass to ablation upon ejection. However, the 50 km diameter projectile modelled in this work is more than large enough to entirely disrupt the atmosphere it impacts into, likely creating a 'tunnel' for the escaping ejecta to travel to cis-lunar space relatively unaltered. Simulations by Beech *et al.* (2019) further suggest that multi-meter-sized (5 to 20-meter diameter) fragments will most likely reach cis-lunar space as a consequence of large terrestrial impact events. This is mostly due to the larger

fragments having a higher ballistic coefficient than the small fragments and are therefore able to travel through a greater volume of atmosphere (both perturbed and unperturbed) without losing so much mass that they become disrupted. As a result, a larger range of ejection angles (and therefore a wider range of distances for fragments to travel through the atmosphere) result in terrestrial material reaching space.

Targets with a weaker or lower density layer atop a stronger or denser layer may amplify the mass ejected at high-speed and has been demonstrated in numerical modelling studies for regolith layers on Mars (Elliott *et al.*, 2022). Comparison between an impact into a homogenous basalt layer and the same impact into a thin layer of dry tuff (equivalent to 2% of the impactor radius) overtop a basalt basement resulted in similar pressure regimes in the ejecting material. However, the more compressible overlying layer greatly enhanced ejection and increased the depth from which fast ejecta was launched. Incorporating a layer at least 500 m thick of weakly cemented and highly compressible material into the models produced for this chapter may enhance the mass of ejected material for launch into cis-lunar space. Weak layers included within a stronger target can also significantly affect the angle of ejection of the target material, with weaker material pulling apart from the stronger layers (Senft & Stewart, 2007). This allows the material to be ejected at a wider range of angles than the homogenous target. Although this affect is found to be reduced in complex crater formation compared to simple craters, the relative thickness of the layers against the size of the projectile will determine the level of impact on the ejecta. Similar ejecta distribution has been noted in numerical modelling investigating marine targets (Ormö *et al.*, 2002).

Depending on the timing of an impact over the course of geological history, the influence of a top layer consisting of water could also be explored to determine the effect on the mass of escaping, low-pressure, and low-temperature ejecta. The inclusion of water layers over stronger, geological material targets in some early numerical modelling work has demonstrated the suppression of pressures in the ejecta from the layers below the water, depending on the ratio between the impactor radius and depth of the body of water modelled (Bray *et al.*, 2022). However, the difference in scale between the models presented in this chapter and those in the work of Bray *et al.* (2022) is significant, kilometre-scale impactor to hundreds of metres, respectively. Additionally, the depth of the water layer was comparable to the size of the projectile and increased to over an order of magnitude larger than the projectile diameter in some scenarios. For the 50 km diameter impactors used in the simulations discussed in this chapter, a body of water with a depth of at least 50 km requires a deep ocean target and may be unlikely to provide escaping ejecta at such a scale. It may be required to consider small scale impactors at similar impact velocities to explore numerical simulations with a more reasonable water-topped target. This

will undoubtably produce a lower mass of escaping material per impact event, but would open the possibility for more frequent, smaller impact events over the course of geological time and therefore increase the probability of producing terrestrial meteorites.

4.5 Conclusions

This chapter demonstrates that high-resolution, 3D simulations of projectiles impacting Earth at 20, 30 and, 55 km s^{-1} with low impact angles (30°) can produce low-shock pressure material (<10 GPa) that is ejected at speeds fast enough (>11 km s^{-1}) to reach Moon-crossing orbits. However, when also considering the temperature history of this high-speed, low-pressure ejecta, only an impact with velocity 20 km s^{-1} results in material with low enough final temperatures (<1000 K in a mass of ~10^{-5} M_i) to potentially retain evidence of biological material. However, as discussed, this likely depends on the duration the material remains at elevated temperatures and the resulting rate of cooling. If this ejecta reached cis-lunar space relatively unaltered, due to the significant perturbation and thinning of the post-impact atmosphere, reached a Moon-crossing orbit, and landed on the Moon as terrestrial meteorites, it could provide a window to the Archean Earth's environment that we no longer have on Earth itself.

Impacting at angles of 45° to 90° can produce significant masses of escaping ejecta (>10^{-3} M_i) likely to remain solid, experiencing pressures lower than a nominal critical pressure for melting of 50 GPa. Whilst this material may not contain surviving evidence of biomarkers, once ejected and eventually landed on the Moon it would still be of significant scientific value if found, providing a geological record of the early Earth. The following chapters investigate the survival of a range materials impacting the lunar surface, including terrestrial meteorites. Future modelling work is needed to address some of the assumptions made during this study, including the improvement of spatial resolution, variation of target properties (weaker targets, layered targets, and oceans), and the explicit consideration of an atmosphere would be beneficial.

5 Assessing the survivability of biomarkers within terrestrial material impacting the lunar surface*

**This chapter is adapted from work published as a research paper:*
Halim, S. H., Crawford, I. A., Collins, G. S., Joy, K. H., Davison, T. M., 2021a. Assessing the survivability of biomarkers within terrestrial material impacting the lunar surface. Icarus, 354. doi:10.1016/j.icarus.2020.114026

5.1 Introduction

The lunar surface has been impacted by a multitude of hypervelocity projectiles over its lifetime, leading to the heavily cratered surface we see today. This rich impact history is exemplified by the Late Heavy Bombardment (LHB), an epoch circa 3.9 Gyr ago when the terrestrial planets are postulated to have experienced frequent large-scale impact bombardment (Stöffler *et al.*, 2006; Norman, 2009). Although it is still contentious whether or not the LHB occurred as a large spike of giant impacts at ~3.9 Ga (Turner *et al.*, 1973; Tera *et al.*, 1974; Cohen *et al.*, 2000; Gomes *et al.*, 2005), or as an initially very high impact rate which steadily decreased over time (Hartmann, 1975, 2003, 2019; Zellner, 2017), or as a hybrid of these possibilities (e.g., Turner, 1979; Marchi *et al.*, 2012; Morbidell *et al.*, 2012), it is undeniable that the early history of the Solar System prior to 3.5 Ga was dominated by a higher rate of large impacts than today (Xie *et al.*, 2020).

As discussed in the previous chapter, the mass of solid terrestrial material that experiences low shock pressures yet is ejected at greater than Earth's escape velocity is a matter of debate. The epoch of enhanced impact rates may have extended well beyond 3.9 Ga ago on the Earth, with basin-forming impacts possibly continuing until about 2.5 Ga (e.g. Bottke *et al.*, 2012; impact basins are impact structures >300 km in diameter). During this time, Earth would have experienced numerous, basin-forming, hypervelocity impacts (Marchi *et al.*, 2014), potentially ejecting terrestrial material at velocities great enough to surpass escape velocity and take up Moon-crossing orbits (Armstrong *et al.*, 2002; Beech *et al.*, 2019). This has led to the proposal that such ejecta could be preserved on the lunar surface as terrestrial meteorites (Armstrong *et al.*, 2002; Gutiérrez, 2002; Crawford *et al.*, 2008; Armstrong, 2010). In particular, Armstrong (2010) showed that the transfer efficiency of Earth-escaping ejecta from large terrestrial impacts to the Moon was 10^{-5} to 10^{-4} and concluded that in some regions of the lunar surface, as much as 510 kg km^{-2} of terrestrial material may have impacted since

3.9 Ga. This equates to a globally averaged concentration of terrestrial material in the regolith between 36 and 61 kg km^{-2}. Even higher rates of delivery of terrestrial material to the Moon would be expected before 3.9 Ga owing to the higher rate of basin-forming impacts on the Earth. The recent discovery of a possible terrestrial clast in Apollo sample 14321 by Bellucci *et al.* (2019) may provide physical evidence for terrestrial material surviving impact with the lunar surface, although this interpretation has now been questioned (Warren and Rubin, 2020; McIntosh *et al.*, 2022). However, new high-resolution 3D shock physics calculations presented in Chapter 4 show that in certain impact scenarios there is a fraction of the impactor mass that is ejected with both high speed and low pressure, confirming that low-shock impact ejection from Earth to the Moon is possible, if inefficient.

Assuming that terrestrial crustal materials can survive launch from Earth and subsequent impact with the lunar surface, the lack of an atmosphere, hydrological cycle, or plate tectonics enhance the likelihood that the Moon might preserve a record of early Earth contained within terrestrial meteorites (Joy *et al.*, 2016). These terrestrial meteorites could therefore provide a record of early biological evolution on Earth from a period that predates the earliest evidence of life on Earth itself. Suitable biological-markers (biomarkers) in such terrestrial meteorites would be complex molecular fossils derived from biochemicals of living organisms (Peters *et al.*, 2004), and conceivably even microfossils of early organisms. Terrestrial meteorites ejected later in Earth's history might possibly contain macrofossils of various kinds, although these would be of less interest as the Earth's own geological record has retained a good record of more recent times.

Although the lack of a lunar atmosphere makes for a less than soft landing for incoming projectiles, the low gravity and escape velocity means that a fraction of incoming projectiles will strike at relativity low impact velocities. Work by Armstrong *et al.* (2002) and Armstrong (2010) estimated the maximum velocity of a terrestrial meteorite landing on the lunar surface 3.9 Ga ago would have been ~5 km s^{-1}, and that >70% would impact with a vertical velocity component less than 2.5 km s^{-1} (owing to the high likelihood of oblique impacts). The fate of the projectile and survivability of organic material in impacts has been previously assessed by multiple studies. Rock projectile materials in numerically simulated hypervelocity impacts have been shown to survive impact with multiple simulated planetary bodies including Earth (Pierazzo and Melosh, 2000; Wells *et al.*, 2003; Potter and Collins, 2013; Beech *et al.*, 2019), the Moon (Bland *et al.*, 2008; Yue *et al.*, 2013), and Jupiter's Moon Europa (Pierazzo and Chyba, 2002). Earlier numerical models also indicate that volatiles and organic material within projectiles may survive impact with the Moon (e.g. Crawford *et al.*, 2008; Ong *et al.*, 2010; Svetsov and Shuvalov, 2015). Projectiles in laboratory-scale experiments can survive hypervelocity impacts with multiple target materials (Daly and Schultz, 2015; Wickham-Eade *et al.*, 2018), and organic constituents within such

projectiles have also been shown to survive (Mimura and Toyama, 2005; Parnell *et al.*, 2010; Meyer *et al.*, 2011; Burchell *et al.*, 2014a, 2014b, 2017). The median survival time for centimetre to meter scale rocky material on the surface of an airless body such as the Moon has been estimated to be between 40 to 80 Ma, with some surviving up to 300 Ma, depending on the material (Basilevsky *et al.*, 2013, 2015). Examples of surviving asteroidal material (see Joy *et al.*, 2016 for an overview) have been found in lunar samples from Apollo 11 (Goldstein *et al.*, 1970; McKay *et al.*, 1970; Quaid and Bunch, 1970), Apollo 12 (Wood *et al.*, 1971; Zolensky *et al.*, 1996; Joy *et al.*, 2020), and Apollo 16 (Jolliff *et al.*, 1993). Additionally, fragments of surviving material have been identified in lunar breccias, including a chondritic fragment found within lunar meteorite Pecora Escarpment 02007 (Day *et al.*, 2006; Liu *et al.*, 2009; Joy *et al.*, 2012), some younger Apollo 16 regolith breccias (Joy *et al.*, 2012), and as a micrometeorite from a stony asteroid source (potentially L or LL chondritic) identified in a Luna 16 soil (Deimdova *et al.*, 2022).

Previous modelling to assess the survival of terrestrial projectiles impacting the lunar surface was performed by Crawford *et al.* (2008) using the ANSYS AUTODYN software package. They considered 0.5 m wide, solid basalt and sandstone cubes as projectiles impacting an unconsolidated sand target layer at 2.5 km s^{-1} and 5 km s^{-1}, with impact angles between 20° and 90°. Here, this earlier work is built upon using the two-dimensional version of the multi-material, multi-rheology iSALE (impact-Simplified Arbitrary Lagrangian Eulerian) shock physics code (Amsden *et al.*, 1980; Collins *et al.*, 2004; Wünnemann *et al.*, 2006). Previously, specific peak pressure thresholds have been used as a proxy for survivability in a variety of materials, with peak temperature from shock heating assumed to correlate with peak pressure. Whilst shock heating may dominate for high-speed impacts that occur on Earth (minimum impact velocity of 11.2 km s^{-1}; e.g., Melosh, 1989), at lower impact velocities (<10 km s^{-1}), such as those associated with terrestrial meteorites impacting the Moon, shear heating may play an important or even dominant role in raising temperatures within the projectile (Kurosawa and Genda 2018). If this were the case, survivability of projectiles and their possible organic or hydrated mineral constituents would be less favourable than previously thought. Therefore, to fully understand and quantify 'survival' of a biomarker, both pressure and temperature must be considered, implying the need for a well understood strength model which can resolve both shock and shear heating.

In this chapter, survival of a molecular biomarker is defined using the method described by Pierazzo and Chyba (1999) where survival is assessed via the thermal degradation of amino acids, adopting a form of the Arrhenius equation and thermal degradation parameters unique to each biomarker. Larger microfossil biomarkers are also considered using

pressure and temperature survival thresholds based on their survival in metamorphosed Earth rocks for which the experienced peak pressures and temperatures have been determined.

5.2 Methods

5.2.1 iSALE modelling of terrestrial meteorite impacts on the Moon

This work used the iSALE–2D shock physics code (Wünnemann *et al.*, 2006), which is based on the SALE hydrocode solution algorithm (Amsden *et al.*, 1980). Multiple features were added to the original SALE code to simulate hypervelocity impacts, including an elasto-plastic constitutive model, fragmentation models, various equations of state (EoS), and multiple materials (Melosh *et al.*, 1992; Ivanov *et al.*, 1997). More recently, additions include a modified strength model (Collins *et al.*, 2004), a porosity compaction model (Wünnemann *et al.*, 2006; Collins *et al.*, 2011a) and a dilatancy model (Collins, 2014). iSALE has been benchmarked against other shock physics codes (Pierazzo *et al.*, 2008) and validated against experimental data from laboratory scale impacts (e.g., Pierazzo *et al.*, 2008; Davison *et al.*, 2011, Miljković *et al.*, 2012). Building upon previous modelling studies (Armstrong *et al.*, 2002; Armstrong 2010; Crawford *et al.*, 2008), the iSALE–2D shock physics code (Wünnemann *et al.*, 2006) was used to simulate vertical impacts of terrestrial meteorites into the lunar surface. The modelling approach followed previous projectile survivability studies using iSALE and other shock physics codes (e.g., Pierazzo and Melosh, 2000; Crawford *et al.*, 2008; Davison *et al.*, 2011, Potter and Collins, 2013), but considered impact scenarios relevant for impact of terrestrial meteorites on the Moon. The following section describes the justification for the choice of input parameters.

Terrestrial meteorites were modelled as 0.5 m diameter, sandstone, and limestone projectiles, vertically impacting a basalt target at 2.5 and 5 km s^{-1}. Sandstone and limestone materials were chosen to build upon the previous work of Crawford *et al.* (2008), investigating the survival of terrestrial meteorites using a different modelling software package. Projectile shape was varied between a sphere, oblate spheroid, and prolate spheroid. The two impact speeds considered in this work, 5 and 2.5 km s^{-1}, represent the highest impact speed as well as the most likely impact speed of terrestrial meteorites striking the lunar surface, estimated by Armstrong *et al.*, 2002 and Armstrong, 2010. Oblique impacts were not considered here; the effects of changing the angle of impact on the fate of the impactor have been well-documented by previous research (e.g., Pierazzo and Melosh, 2000; Crawford *et al.*, 2008; Davison *et al.*, 2011, Potter and Collins, 2013),

showing that the more oblique the impact, the lower the pressures experienced by the projectile. The vertical impact simulations presented here therefore represent a conservative estimate of surviving material at a given impact speed.

To investigate a range of possible sedimentary projectile materials and target types, porosity was varied in both the projectile and the target layer (Table 5.1). The basis for a 30% target porosity stems from Apollo samples with intra-granular porosities in lunar regolith of 21-32%, rising to 52% when including inter-granular porosities (Carrier *et al.*, 1991). An upper limit of 70% porosity was chosen based on the results of the Lunar Crater Observation and Sensing Satellite (LCROSS) impact which suggested a surface porosity of >70% in Cabeus crater (Schultz *et al.*, 2010); interestingly, Cabeus is geographically located in a region where terrestrial meteorites may be relatively common according to direct transfer models of terrestrial material to the Moon during giant impacts (Armstrong, 2010).

The solid components of the impactor and regolith were modelled using equation of state tables derived from the analytical equation of state package (ANEOS; Thompson and Lauson, 1972) with input parameters for quartz (sandstone; Melosh, 2007), calcite (limestone; Pierazzo *et al.*, 1998) and basalt (lunar surface; Pierazzo *et al.*, 2005), respectively. The maximum shock pressure in the projectile in these simulations ranged from 9 to 63 GPa, depending on projectile speed and target and material properties. This range coincides with the assumed pressure of the solid-solid phase transition in quartz (21 GPa) employed in the ANEOS equation of state (Melosh, 2007). As a consequence, a small volume of projectile material along the symmetry axis, in some impact scenarios, was driven into the mixed-phase state across the transition, which resulted in spuriously high temperatures recorded for this material. The quartz equation of state table was, therefore, modified for this specific study to remove the solid-solid phase transition, so that the high-pressure phase of quartz was not represented. While this removed the spurious temperatures within the projectile, the absence of any phase transition implies that temperatures associated with pressures exceeding ~20 GPa in this work are overestimated within the projectile material and therefore any conclusions made regarding biomarker survival should be deemed as conservative estimates.

Table 5.1: *Description of model set up parameters. The names given to the simulations indicate the material of the projectile, the extent to which the projectile and target are porous, and the impact velocity. For example, "S_30_0_5" represents a sandstone projectile (S), with 30% porosity (30), impacting a solid (0) target at 5 km* $\mathbf{s^{-1}}$ *(5).*

Simulation ID				**Projectile porosity**	**Target porosity**	**Projectile shape**
Sandstone		**Limestone**				
5 km s^{-1}	**2.5 km** s^{-1}	**5 km** s^{-1}	**2.5 km** s^{-1}			
S_0_0_5	S_0_0_2.5	L_0_0_5	L_0_0_2.5	0%	0%	Sphere
S_0_30_5	S_0_30_2.5	N/A	N/A	0%	30%	Sphere
S_0_50_5	S_0_50_2.5	N/A	N/A	0%	50%	Sphere
S_0_70_5	S_0_70_2.5	N/A	L_0_70_2.5	0%	70%	Sphere
S_10_0_5	S_10_0_2.5	N/A	N/A	10%	0%	Sphere
S_20_0_5	S_20_0_2.5	N/A	N/A	20%	0%	Sphere
S_30_0_5	S_30_0_2.5	N/A	N/A	30%	0%	Sphere
S_40_0_5	S_40_0_2.5	L_40_0_5	N/A	40%	0%	Sphere
Oblate_5	Oblate_2.5	N/A	N/A	0%	0%	Oblate spheroid
Prolate_5	Prolate_2.5	N/A	N/A	0%	0%	Prolate spheroid

The strength of the sandstone (projectile), limestone (projectile) and basalt (target) materials were modelled using the method described by Collins *et al.* (2004). Inclusion of this particular strength model in the projectile material allows for the heating of materials to be explicitly resolved via both shock and shear processes. Strength model parameters for the basalt target were taken from Miljković *et al.* (2013), representing a basaltic lunar crustal material (Table 5.2). The sandstone was represented with strength parameters taken from Winkler *et al.* (2018), representing a quartzite sandstone-like material. For the limestone impactor, parameters for the Collins strength model were taken from those used previously for a limestone material in a terrestrial impact simulation by Goldin *et al.* (2006). All of the limestone simulations used a spherical projectile shape model and the same porosity model parameters as those used in the sandstone projectiles.

To investigate the influence of projectile shape, various geometries of the projectile were considered, including spherical, oblate and prolate spheroids (1 m × 0.25 m, and 0.25 m × 1 m, respectively). An oblate spheroid describes a flattened spheroid, where the horizontal diameter (x), parallel to the target surface, is longer than the vertical diameter (y). Prolate spheroids are the opposite.

Table 5.2: *Thermal, strength, and damage input parameters for the impactor and target materials used in this numerical modelling work. Basalt target from Miljković et al. (2013), sandstone impactor from Winkler et al. (2018), and limestone impactor from Goldin et al. (2006).*

Parameter	Symbol (units)	Impactor (Quartz EoS)	Impactor (Calcite EoS)	Target (Basalt EoS)
Thermal				
Thermal softening coefficient	ξ	1.2	1.2	1.2
Melt temperature (p = 0)	T_m (K)	1600	1600	1393
Strength				
Poisson's ratio	ν	0.3	0.3	0.3
Intact cohesive strength	Y_{i0} (MPa)	97	50	20
Intact friction coefficient	μ_i	1.8	2	1.4
Intact strength limit	Y_{lim} (GPa)	1	0.65	2.5
Damaged cohesive strength	Y_{d0} (MPa)	0.00	0.005	0.01
Damaged friction coefficient	μ_d	0.7	0.4	0.6

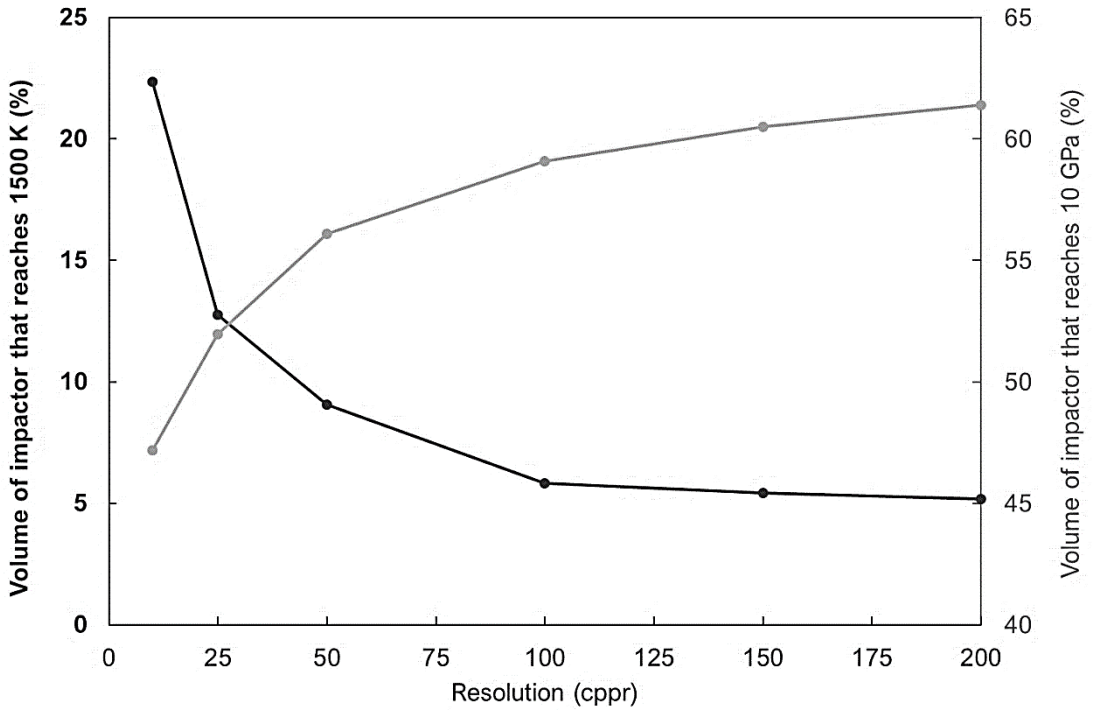

Figure 5.1: *Resolution study for simulation ID S_S_5, showing the volume (%) of the impactor which reaches a certain temperature (left y-axis) and pressure (right y-axis) at increasing amounts of cells per projectile radius (cppr).*

Tracer particles were used to track material located within each projectile cell at time zero. For each tracer, pressure and temperature at each time-step that was recorded, as well as the maximum peak pressure and temperature recorded over the entire simulation run. Simulations used lunar gravity (1.62 m s^{-2}) and a surface temperature of 273 K, within the range of expected temperatures for the lunar surface between the cold lunar night-time (140 K) and the hot lunar daytime (400 K). Simulations were run until the projectile material was released from high pressure; that is, until the shock wave in the projectile reflected off the back of the projectile and propagated back across the entire, deformed projectile (Melosh, 1989). Both peak and post-shock temperatures were determined for each tracer. Each simulation used 100 cells per projectile radius (cppr), improving on the 10 cells per projectile radius resolution adopted by Crawford *et al.* (2008). In order to check that this resolution was sufficient for the simulation results to approach convergence, model S_0_0_5 was replicated at 10, 25, 50, 100, 150 and 200 cells per projectile radius. From each simulation, the volume of the projectile that reached certain pressure and temperature values was derived in order to compare the variations across different resolutions; Figure 5.1 shows the results for a temperature of 1500 K and pressure of 20 GPa. Results of the resolution test found that pressures were underestimated, and temperatures overestimated, at lower resolutions. However, resolutions above 100 cells per projectile radius begin to show diminishing returns in terms of changes in the volume percentage for both pressure and temperature. For the volume of an impactor which experiences 1500 K and 20 GPa, the difference between 100 and 200 cells per projectile radius is 0.66% and 2.32 %, respectively. Therefore, a resolution of 100 cells per projectile radius was adopted as for simulations presented here as a compromise between accuracy and computational expense. An example input file describing the parameters for the global set-up of 2D simulations can be found in Appendix A3.

5.2.2 Material strength and shear heating in the projectile

During high-velocity impacts, some of the initial kinetic energy of the projectile is converted into internal energy (heat) of the projectile due to its sudden compression. For sufficiently high impact speeds the projectile material is heated dramatically at the point of contact and can melt or vaporise upon release from high pressure. Another heating mechanism during impact is the conversion of distortional energy to internal energy, known as shear heating, which has been largely overlooked in the history of numerical impact modelling (Kurosawa and Genda, 2018; Melosh and Ivanov, 2018). In high (>15 km s^{-1}) velocity impacts, the mass of material heated by shock heating exceeds the mass heated via shear heating and can reasonably be neglected. However, Quintana *et al.* (2015) identified that material strength is important for low-velocity

impacts, increasing melt and vapor generation, and Kurosawa and Genda (2018) concluded that additional shear heating was significant for impacts with velocities below 10 km s^{-1}. The additional heat reduced the impact-velocity thresholds for the onset of melting from 8 and 10 km s^{-1} in strengthless rocks, to 2 and 6 km s^{-1} when including strength, respectively.

Whilst Kurosawa and Genda (2018) considered the effect of shear heating in the target, its importance in projectile survivability has not been addressed as most previous studies of the fate of the projectile have assumed a strengthless impactor (e.g., Pierazzo and Melosh, 2000; Crawford *et al.*, 2008; Potter and Collins, 2013). For the work presented in this chapter, the influence of shear heating is quantified within the projectile material by comparing identical simulation scenarios with and without a strength model. A solid, spherical projectile was simulated impacting a solid target at 2.5 and 5 km s^{-1} to investigate the variation in shear heating at differing velocities. The same model parameters were used as described in Section 5.2.1, with the exclusion of the strength model in one set of simulations at both 2.5 and 5 km s^{-1}.

5.2.3 Biomarker selection

To quantify the survival of biomarkers within terrestrial meteorites, a set of organic materials was identified that may be contained within terrestrial rocks and that could potentially survive impact with the lunar surface once ejected from Earth. The organic materials chosen include examples of four amino acids and the molecule lignin (Table 5.3), where the latter is important in the formation of cell walls (Brebu and Vasile, 2010). Whilst amino acids and related biomarkers such as lignin are most likely to be preserved in terrestrial clays and mudstones, these materials were not modelled in the simulations. Instead, other terrestrial, sedimentary rocks were used, specifically sandstone and limestone. The main reason for this choice is that the iSALE material library does not contain a robust or well-tested clay-based equation of state, whereas the sandstone and limestone equivalents are very well tested and have been used many times previously for impact modelling. Additionally, mudstones and clay materials are mechanically very weak, likely to heavily deform and potentially destroy entrained biological material much more readily than the stronger sandstone and limestone. Sandstone and limestone are known to preserve an abundance of fossilised biological material and serve as adequate examples of potentially biomarker rich terrestrial meteorites. Following the method described by Pierazzo and Chyba (1999), biomarker survivability as a function of temperature was estimated using a modified version of the Arrhenius equation (Nelson, 1967):

$$dM = -M_{or} A e^{-E_a/RT(t)} dt \tag{5.1}$$

where:

M_{or} = mass of organic material (kg)

A = pre-exponential factor (s^{-1})

E_a = activation energy of organic molecule (kcal mol^{-1})

R = gas constant (kcal K^{-1} mol^{-1})

$T(t)$ = time dependant temperature (K)

dt = change in time (s)

Table 5.3: *Examples of organic materials that may be contained within terrestrial rocks, with thermal degradation parameters and decomposition/vaporisation temperatures based upon published experimental results.*

Biomarker	Thermal degradation parameters	Reference
Arginine	$A = 134\ s^{-1}$ $E_a = 8.79$ kcal mol^{-1}	Rodante, 1992
Valine	$A = 49\ s^{-1}$ $E_a = 6.7$ kcal mol^{-1}	Rodante, 1992
Glutamine	$A = 14.9\ s^{-1}$ $E_a = 5.9$ kcal mol^{-1}	Rodante, 1992
Tryptophan	$A = 8.2\ s^{-1}$ $E_a = 6.2$ kcal mol^{-1}	Rodante, 1992
Lignin	$A = 2.82\ s^{-1}$ $E_a = 6.0$ kcal mol^{-1}	Brebu and Vasile, 2010

Amino acid and lignin thermal decomposition is assumed to occur by a single reaction of the first order for their respective A and E_a values. This means the reaction proceeds at a rate that depends linearly on only one reactant concentration. This particular selection of amino acids and lignin were chosen for their range of thermal degradation parameters (Table 5.3) and other individual characteristics that make them interesting in terms of biomarker survival potential. Amino acids with alkyl groups (e.g., valine) can survive pressures up to ~28 GPa, with 1-4% of the initial mass

of amino acid surviving, and much larger percentages (up to 70%) beneath ~21 GPa (Bertrand, 2009). Tryptophan is a large, aromatic amino acid commonly synthesized by plants and microorganisms, whilst lignin is an even larger molecule crucial to the formation of cell walls. Both, if found in terrestrial meteorites, would indicate strong evidence of biological activity and hence their survival would be of incredible scientific value in landed meteoritic material on the lunar surface.

Cooling timescales for surviving projectile fragments can be bracketed by two end-member scenarios representing the slowest and fastest cooling times that can be realistically expected. The slowest cooling rate assumes the projectile survives impact as an unbroken sphere and is buried entirely in the insulating lunar regolith, thereby undergoing slow, conductive cooling. The fastest cooling rate refers to a smaller fragment which is ejected, lands on the surface regolith, and undergoes fast, radiative cooling to space. Regolith properties (including density, specific heat capacity, and thermal conductivity) were taken from Fagents *et al.* (2010) and combined with temperature data from the models to calculate the conductive heat transfer from projectile to regolith, with an assumed steady state heat conductivity and cooling of an isothermal sphere buried in a medium of known temperature (Lienhard and Lienhard, 2001). For radiative cooling, the equation for radiative cooling of an idealised sphere was used (Nave, 2017).

Table 5.4 shows examples of larger biomarkers in the form of microfossils and small fossilised remains. Using the thermal degradation method is not valid for these examples as they are composed of multiple molecules and therefore too complex to be estimated by the first-order approximation of the Arrhenius equation. Instead, the fossils have been chosen due to their survival in low-grade metamorphosed rocks (of known P-T conditions) for which the experienced peak pressures and temperatures have been determined (Bernard *et al.*, 2007; Laborda-López *et al.*, 2015; Shaw, 2019). It is important to note that these are not the maximum survival pressures and temperatures for each fossil itself, but the estimated maximum pressures and temperatures experienced by fossils shown to have survived. The maximum pressure experienced by the 300 μm lycophyte megaspores was constrained by the maximum silica content of phengites within the limestone sample (which had undergone metamorphism in the blueschist facies), used as a quantitative proxy to estimate peak pressure (Bernard *et al.*, 2007). Peak temperature (630 K) was constrained by the Fe-Mg exchange between Mg-carpholite and chloritoid, further supported by Raman spectroscopy of carbonaceous material (~633 K; Bernard *et al.*, 2007). Ammonites were found in a hornfels sample which experienced a minimum temperature of 800 K, estimated from the transition of pyrite to pyrrhotite and pressures of 0.02 GPa based on the depth of burial and density of materials above at the time of metamorphism (Shaw, 2019). Crinoids and some examples of cephalopods, among other fossil assemblages, were found in alpine marble and calc-silicate schist samples which survived temperatures of ~750 K and pressures ~0.2

GPa (Laborda-López *et al.*, 2015). Whilst it is not a likely outcome to find macroscopic fossils such as ammonites and crinoids in 3.9 Gyr Earth rocks, these macrofossils are used as examples of fossil survivability as a comparison to the molecular biomarkers.

Table 5.4: *Fossil and microfossil biomarkers that may be contained within terrestrial rocks with minimum survival pressures and temperatures based upon examples found in metamorphosed Earth rock samples.*

Biomarker	**Rock type**	**Minimum survival conditions based upon metamorphosed samples**		**Reference**
		Pressure (GPa)	**Temperature (K)**	
Ammonites	Hornfels	0.02	800	Shaw, 2019
Crinoids/Cephalopods	Graphitic marble and calc-silicate schist	0.2	750	Laborda-López *et al.*, 2015
Lycophyte megaspores	Limestone – blueschist facies	1.4	630	Bernard *et al.*, 2007

5.3 Results

5.3.1 The influence of material strength

The results of the meteorite survivability simulations show that at impact speeds of both 2.5 km s^{-1} and 5 km s^{-1} peak-shock temperatures are significantly higher across most of the projectile when projectile strength is accounted for, whilst peak pressure is almost unaffected (Figure 5.2). This is consistent with previous work that investigated shear heating in target materials (Quintana *et al.*, 2015; Kurosawa and Genda, 2018). Peak-shock pressures in the projectiles were approximately the same for the spherical projectile impacting a solid target at 2.5 and 5 km s^{-1}, with and without strength in the projectile. However, there is a marked difference in the peak temperatures experienced for the with strength vs. strengthless projectile in both the 2.5 km s^{-1} and 5 km s^{-1} scenarios (Figure 5.2). At 2.5 km s^{-1}, in the simulations with no strength, over 90% of the projectile volume experienced peak temperatures less than 400 K, whilst in the scenario with strength only 10% of the projectile experienced temperatures less than 400 K. At 5 km s^{-1}, a similar pattern was observed where over 90% of the strengthless projectile experienced temperatures less than 900 K, while only 15% of the projectile with strength experienced temperatures less than 900 K. The inclusion of both shear and shock heating is therefore crucial in considering the temperatures experienced by terrestrial meteorites striking the Moon at velocities less than 5 km s^{-1}.

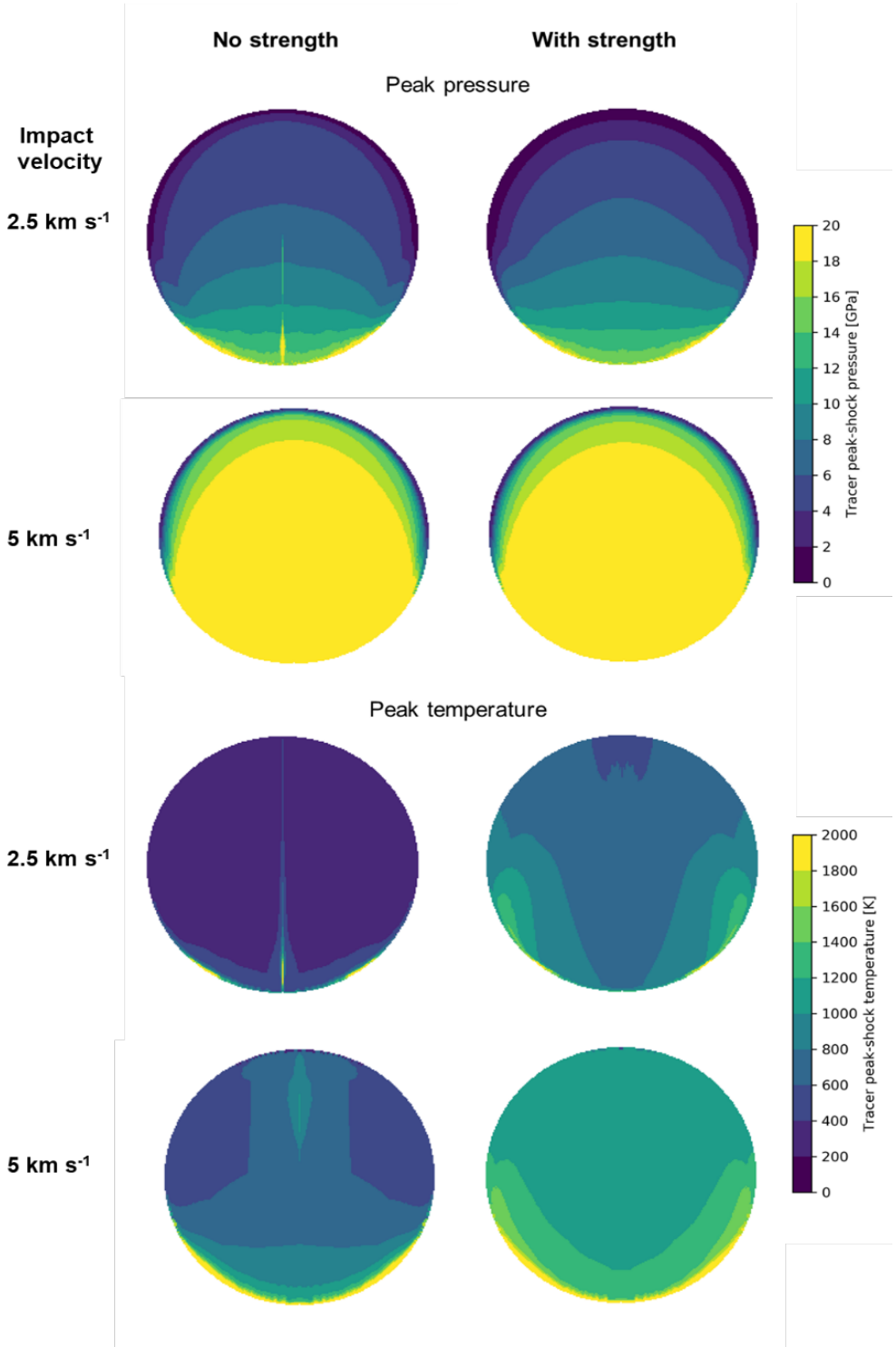

Figure 5.2: *Contour maps of peak pressure (top) and temperature (bottom) for solid projectiles impacting a solid target at 2.5 km* $\mathbf{s^{-1}}$ *and 5 km* $\mathbf{s^{-1}}$*. Left projectile maps used no strength model (hydrodynamic), right projectile maps used a rock strength model (Collins et al., 2004) which could explicitly resolve shock and shear heating. Projectile maps in this and all figures going forward show the state of the projectile volume mapped onto the original shape of the projectile before impact; it is not a representation of the final shape or distribution of the projectile mass.*

5.3.2 Influence of impactor velocity, shape, porosity, and composition

The simulations presented in this chapter demonstrate that terrestrial meteorites striking the Moon can experience large range of pressures and temperatures, depending on the impactor speed, composition, porosity, and shape, as well as the nature of the impacted target surface. Table 5.5 provides a summary of the mean pressure and temperatures recorded for each projectile in all of the scenarios considered. Full data files can be found in the electronic appendix, with filenames relating to Chapter 5 (i.e., "Ch5_Terrestrial_met_peak_shock_data").

Increasing the velocity of the projectile leads to greater peak-shock pressures and temperatures, regardless of the porosities of target or projectile, as expected (Figure 5.3). The influence of changing porosity within both the projectile (Figure 5.4) and target (Figure 5.5) was highly apparent from both 2.5 km s^{-1} and 5 km s^{-1} impact velocity scenarios. Increasing the porosity of the projectile from solid to 10% results in a decrease in the range of pressures experienced and in the average pressure across the projectile (Figure 5.4). For example, in the 5 km s^{-1} simulations, the solid projectile (0% porosity) and 10% porosity projectile experience average peak pressures of 23.4 and 21.9 GPa, respectively. At a higher projectile porosity of 40% a decrease in peak-pressures across the projectile is observed. This decrease in peak-pressures would be assumed to contribute to an overall lowering of the temperatures in the projectile, however the exact opposite is true. Temperatures in the projectiles are shown to increase significantly with increasing projectile porosity, likely caused by the heat generated by pore compaction.

An increase in the porosity of the target leads to a significant decrease in the peak pressures experienced by the projectile and as a result, peak and post-shock temperatures are decreased as well (Figure 5.5). Peak-shock pressures are similar to those found in previous work (Crawford *et al.*, 2008) across most combinations of projectile and target porosity, but most similar in the 30% porous target scenarios. This suggests that, in terms of impact properties, a 30-50% porous basalt layer is comparable to an unconsolidated sand target layer, like that used in the study of Crawford *et al.* (2008).

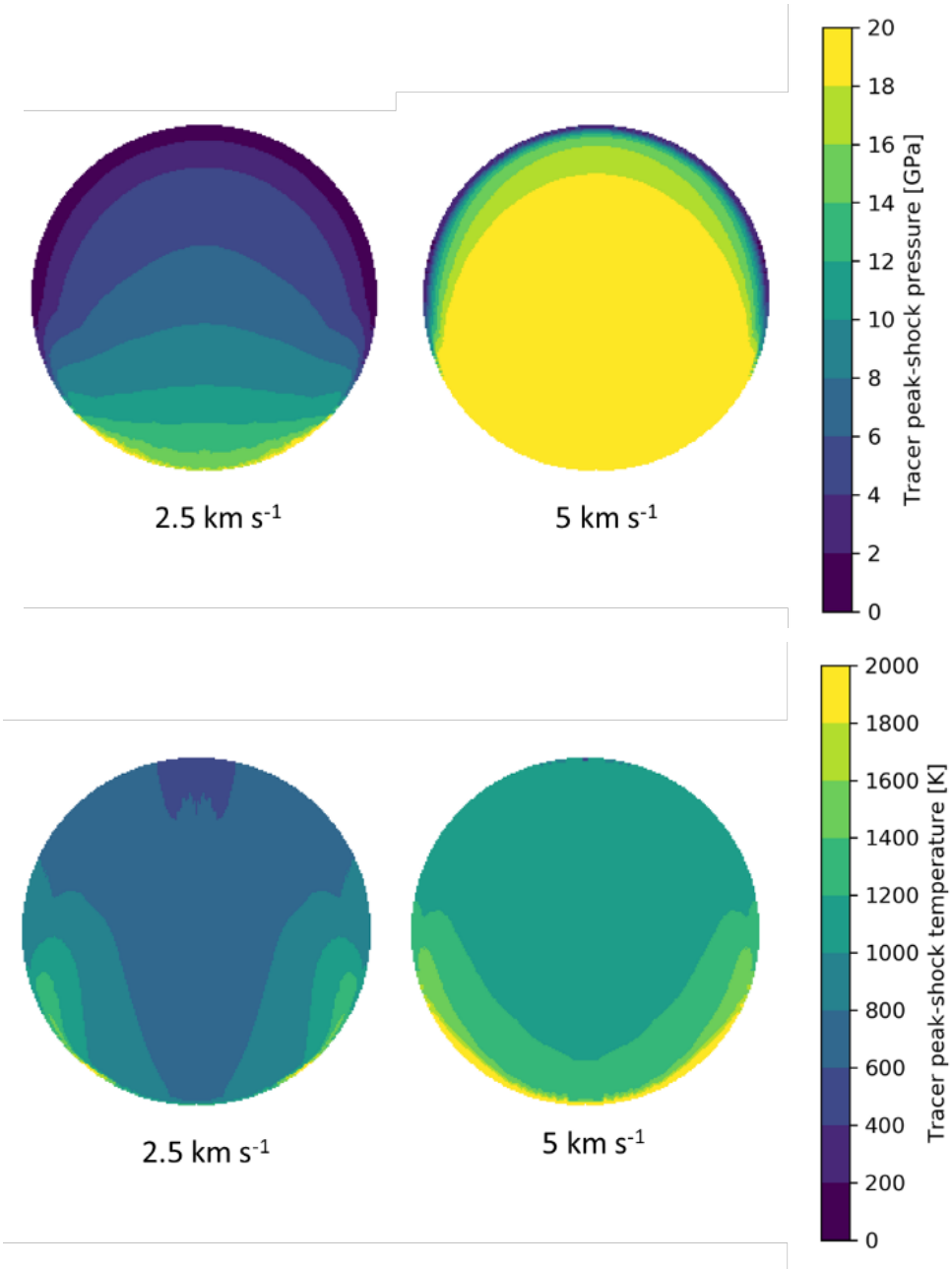

Figure 5.3: *Contour plots of peak-shock pressures (top) and peak-shock temperatures (bottom) in a solid sandstone projectile after impacting a solid basalt target at 2.5 and 5 km* s^{-1}.

Altering the shape model of the projectile from a sphere to a prolate or oblate spheroid significantly changed the pressure and temperature distributions across the projectile volume (Figures 5.6 and 5.7). In solid prolate projectiles impacting a solid target at 2.5 and 5 km s^{-1}, high peak pressures are concentrated in the initial impacting surface of the prolate projectiles at both impact velocities, when compared to their spherical counterparts at the same velocity. Over 90% of the lower velocity projectile experiences pressures less than 8 GPa, whilst the higher velocity projectile experiences pressures over 10 GPa in nearly 50% of the projectile volume. For prolate projectiles at both velocities simulated, the peak

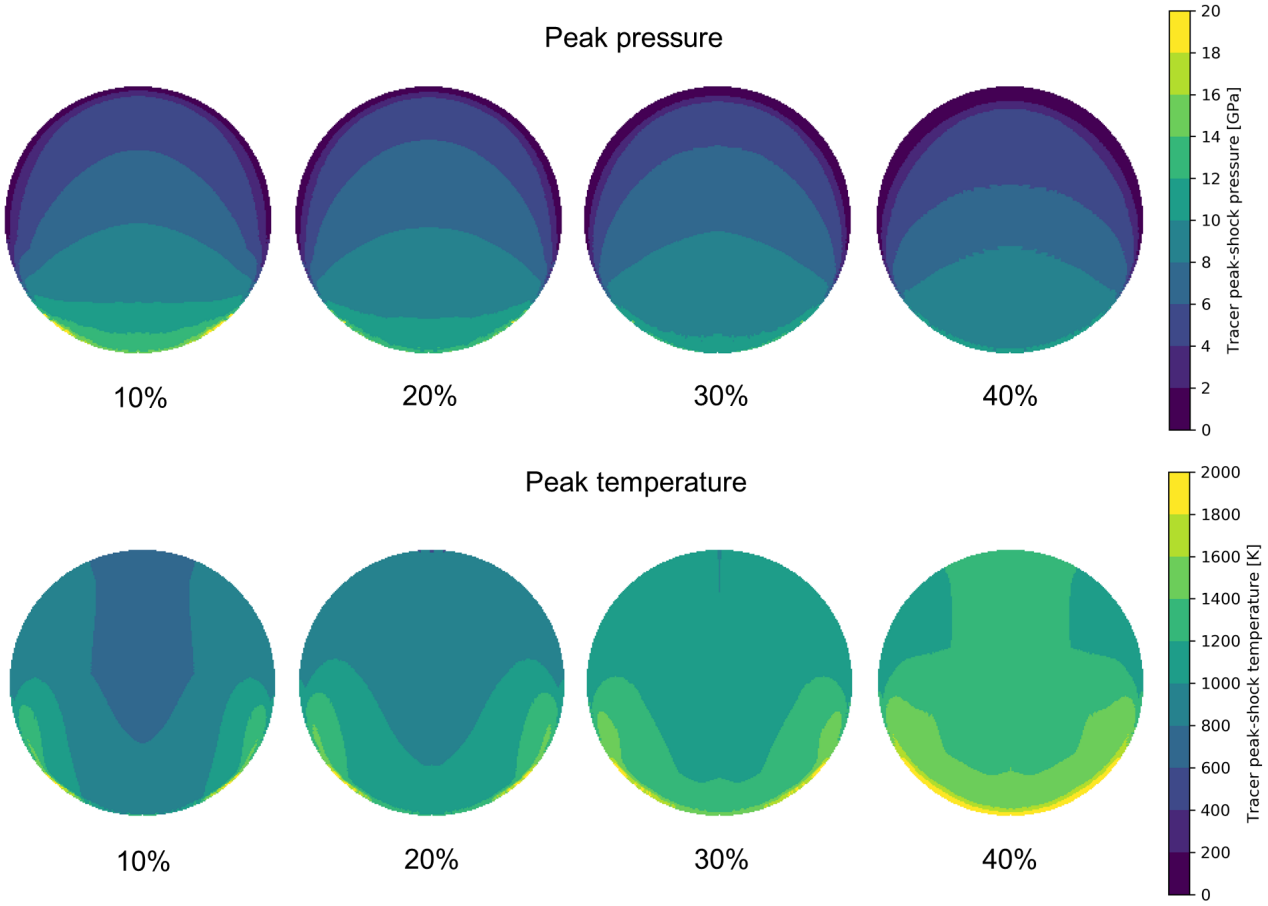

Figure 5.4: *Contour plots of peak-shock pressures (top) and peak-shock temperatures (bottom) in a sandstone projectile with varying porosity (10-40%) after impacting a solid basalt target at 2.5 km* s^{-1}.

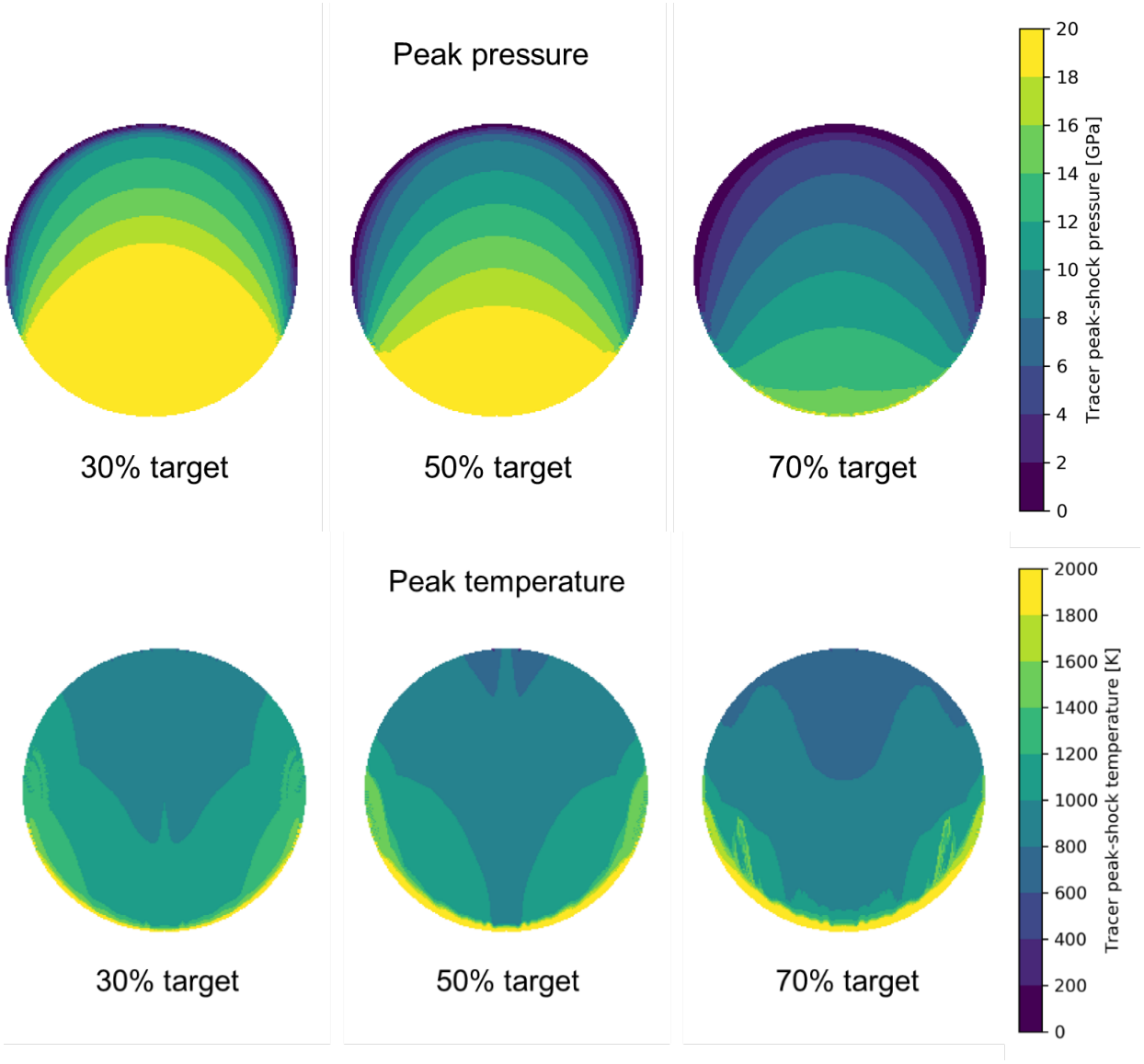

Figure 5.5: *Contour plots of peak-shock pressures (top) and peak-shock temperatures (bottom) in a solid sandstone projectile after impacting a basalt target with varying porosity (30-70%) at 5 km* s^{-1}.

temperatures are higher than in the respective spherical counterpart, across the entire projectile volume. Minimum temperatures at the back of both projectiles are ~400 K higher in the prolate projectile than in the spherical projectile and the distribution of the increased temperatures is concentrated in the centre rather than the edges of the projectiles. In the oblate projectiles, the opposite is seen, at least in the 2.5 km s^{-1} impact velocity projectile. Peak pressures are increased relative to the spherical and prolate models and, conversely, peak temperatures are reduced across most of the projectile volume when compared to the prolate shape model. Although the minimum temperature in the oblate projectile is higher than that in the spherical model, the bulk of the projectile never experiences temperatures above 800 K, with the exclusion of the outermost portions of the projectile. The temperature profiles more closely follow the pressure profiles across the prolate projectiles than in spherical or oblate projectiles.

For the sandstone projectiles, Figures 5.8 and 5.9 show the extremes of peak-shock pressure and temperature for the most and least favourable scenarios for biomarker survival in the simulation results, respectively. Pressure and temperature variations across the projectile are displayed using the information recorded by tracers in the projectile, mapped onto the original shape of the projectile. Any temperatures that display values less than 200 K (darkest blue in post-shock temperature plots of Figures 5.8 and 5.9) should be ignored as these represent tracers in material which has either gone into tension and become unphysical or has left the simulation boundaries via ejection. Figure 5.8 shows the result of a solid projectile impacting a 70% porous target at 2.5 km s^{-1}. Temperatures across the majority of the projectile do not exceed 600 K and remain at these temperatures for the duration of the simulation. Figure 5.9 shows the least favourable conditions for biomarker survival. In this case, peak temperatures exceed 2000 K and would prevent any substantial proportion of biomarker to survive across most of the projectile. However, post-shock temperatures decrease to less than 800 K away from the projectile centre, as can be seen in the post-shock tracer plot in Figure 5.9. This rapid decrease in temperature for a fraction of the projectile material over the course of the relatively short simulation (0.005 s) bodes well for biomarker survival.

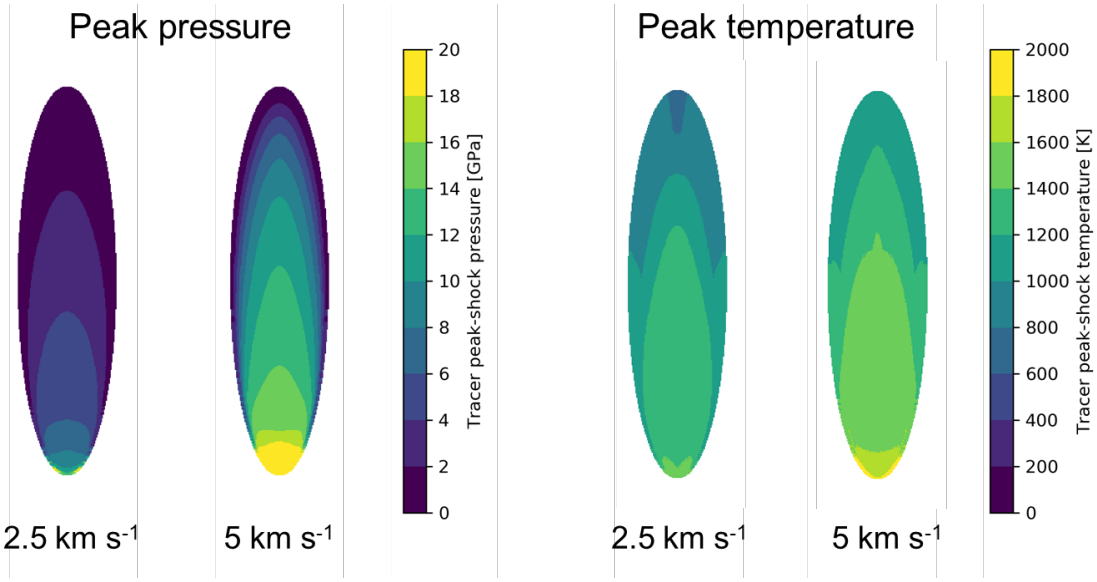

Figure 5.6: *Contour plots of peak-shock pressures (left) and peak-shock temperatures (right) in a prolate, solid sandstone projectile after impacting a solid basalt at 2.5 and 5 km* s^{-1}.

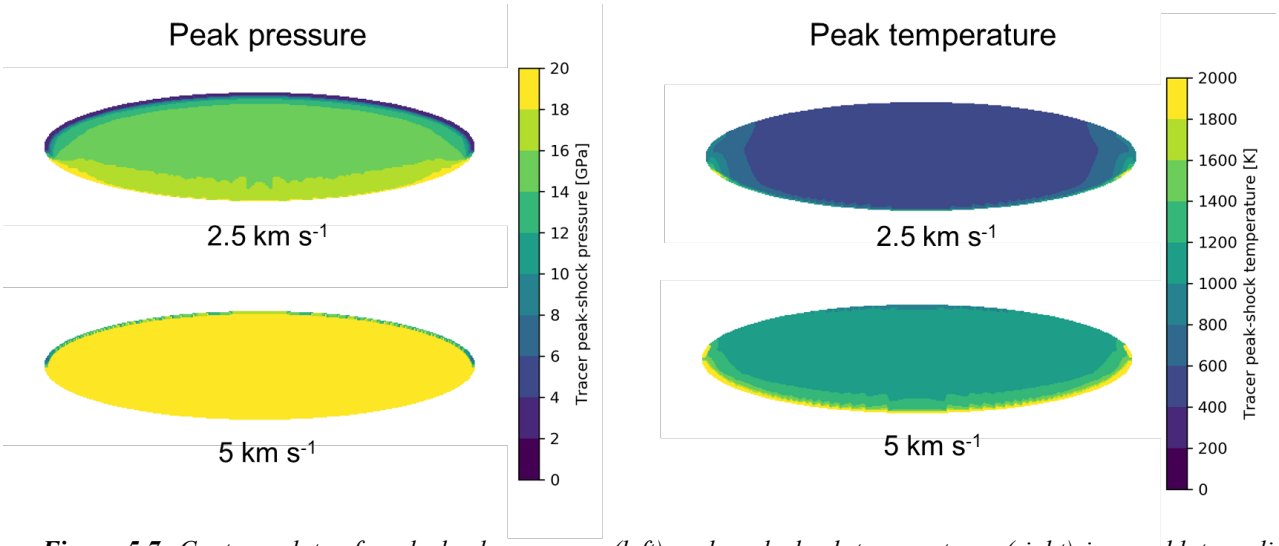

Figure 5.7: *Contour plots of peak-shock pressures (left) and peak-shock temperatures (right) in an oblate, solid sandstone projectile after impacting a solid basalt target at 2.5 and 5 km* s^{-1}.

Table 5.5: *Mean peak pressure and temperature results for each of the simulation scenarios. The names given to the simulations indicate the material of the projectile, the extent to which the projectile and target are porous, and the impact velocity. For example, "S_30_0_5" represents a sandstone projectile (S), with 30% porosity (30), impacting a solid (0) target at 5 km* $\mathbf{s^{-1}}$ *(5). Oblate and prolate scenarios feature solid, sandstone projectiles into a solid target.*

Simulation ID (2.5 km s^{-1}**)**	**Mean peak pressure (GPa)**	**Mean peak temperature (K)**	**Simulation ID (5 km** s^{-1}**)**	**Mean peak pressure (GPa)**	**Mean peak temperature (K)**
S_0_0_2.5	6.08	830	S_0_0_5	23.4	1210
S_0_30_2.5	4.24	745	S_0_30_5	16.2	1100
S_0_50_2.5	2.80	630	S_0_50_5	12.3	1050
S_0_70_2.5	1.67	485	S_0_70_5	7.27	990
S_10_0_2.5	6.55	895	S_10_0_5	21.9	1400
S_20_0_2.5	6.55	1015	S_20_0_5	20.6	1640
S_30_0_2.5	6.29	1150	S_30_0_5	19.3	1950
S_40_0_2.5	5.73	1290	S_40_0_5	18.1	2370
Prolate_2.5	2.45	1050	Prolate_5	8.56	1330
Oblate_2.5	14.7	565	Oblate_5	43.8	1200
L_0_0_2.5	6.62	660	L_0_0_5	23.5	1035
L_0_70_2.5	1.82	480	L_40_0_5	18.4	2290

Peak-shock pressures in the limestone projectiles were almost identical to those in the sandstone projectiles across all the simulations. However, peak, and post-shock temperatures were both reduced in the limestone projectiles relative to the sandstone projectiles, with the most noticeable difference in solid projectiles impacting solid targets at 2.5 km s^{-1} (Table 5.5 and Figure 5.8). The potential survivability of biomarkers is more favourable in the limestone projectiles shown in Figure 5.8 as temperatures are lower in the rear portion of the projectile by ~200 K, i.e., reduced from a maximum of 600 K to 400 K. This peak-temperature reduction translates to post-shock temperature, recorded at the final timestep (5 ms), with the surviving material experiencing maximum temperatures of 600 K across most of the projectile. This represents the most favourable conditions for biomarker survival. In the least favourable scenario for biomarker survival (Figure 5.9), peak-shock temperatures reach 2000 K and higher, however, the material temperatures have reduced below 1600 K by the time that post-shock temperatures are recorded (5 ms). Overall, across each of the limestone scenarios, the results show that the fraction of material in which biomarkers could potentially survive is increased compared to sandstone projectiles.

Whilst peak pressures for relevant models in this study are comparable with those obtained in previous work (Crawford *et al.*, 2008), the peak temperatures are higher than those predicted for strengthless material based on peak pressures alone owing to the effect of shear heating (Kurosawa and Genda, 2018). As a result, the peak-shock temperatures are higher than expected across all of the simulations compared to those predicted by shock heating alone. Peak-shock temperatures are observed to decrease with increasing target porosity and increase significantly with increasing projectile porosity, emphasising the need to consider both pressure and temperature in the assessment of biomarker survivability. Therefore, compared with previous work, these simulations indicate less favourable conditions for survivability of the projectile, especially for projectiles travelling at the maximum expected impact velocity of 5 km s^{-1} (Armstrong *et al.*, 2002; Armstrong, 2010). For otherwise identical simulations with an impact speed of 2.5 km s^{-1}, temperatures in the projectiles are much more favourable, experiencing temperatures that are on average ~500 K less than their 5 km s^{-1} counterparts. The potential for survival of all of the example organic molecules in terrestrial impactors is greatly increased for the lower velocity scenarios (i.e., 2.5 km s^{-1}), which would account for >70% of the terrestrial projectiles impacting the lunar surface at 3.9 Ga ago (Armstrong *et al.*, 2002).

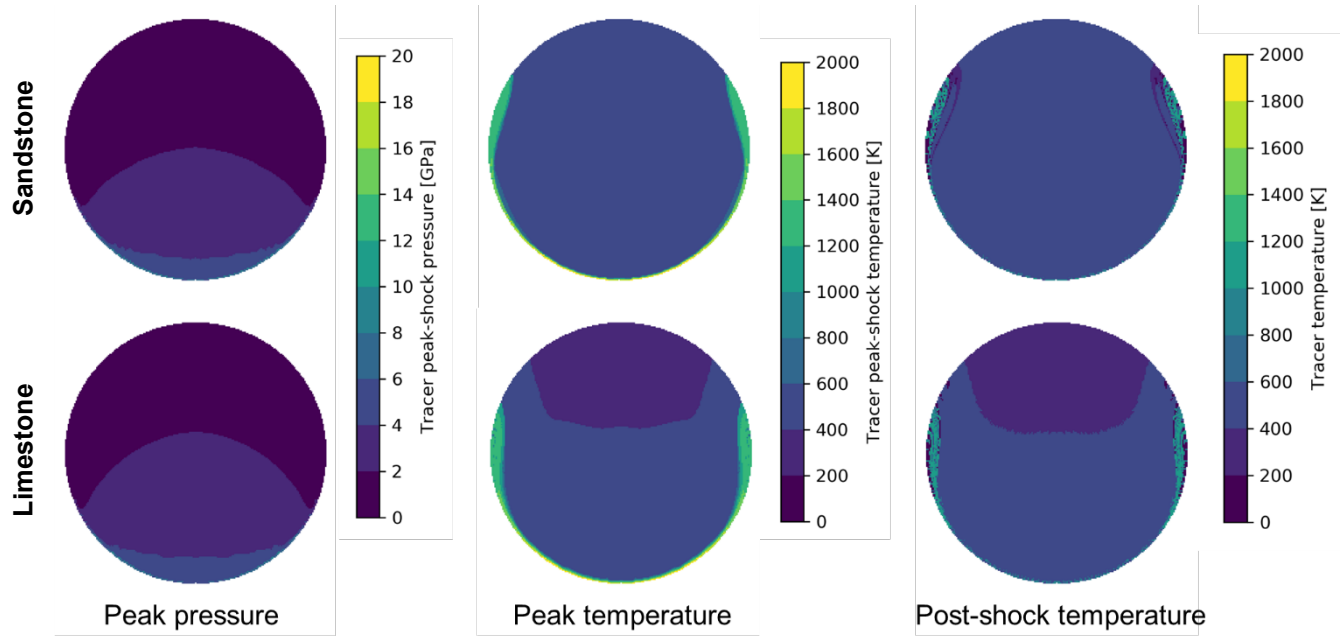

Figure 5.8: *Contour plots of comparing pressure and temperature regimes in sandstone (top) and limestone (bottom) projectiles. Both sets of plots are the result of a solid projectile impacting a 70% porous target at 2.5 km* s^{-1} *(most favourable for biomarker survival).*

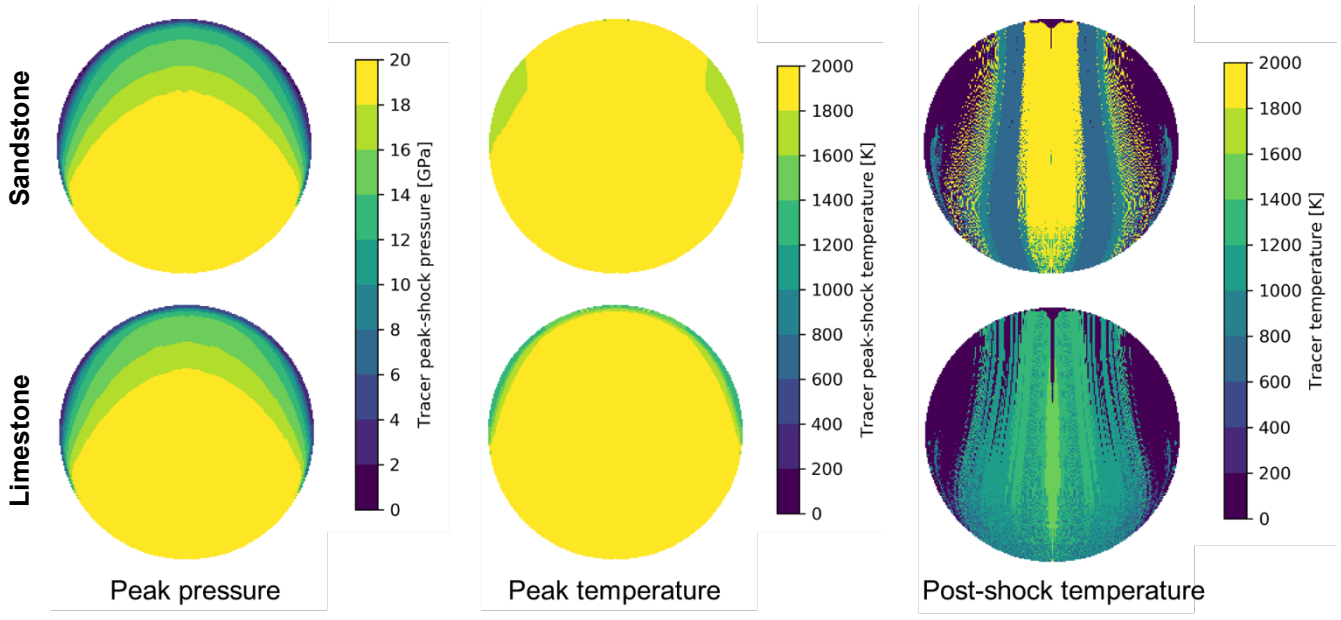

Figure 5.9: *Contour plots of comparing pressure and temperature regimes in sandstone (top) and limestone (bottom) projectiles. Both sets of plots are the result of a 40% porous projectile impacting a solid target at 5 km* s^{-1} *(least favourable for biomarker survival).*

5.3.3 Sandstone projectiles – molecule biomarker survival

In order to gauge biomarker survival beyond immediately post-impact, it is necessary to consider biomarker survival in the projectile fragments because, although the temperatures within the projectile fragments will only decrease with time, they may remain elevated for a sufficient time for biomarker degradation to occur. The post-shock temperatures taken from the final timestep of the simulations are used as the starting temperature and an estimate for the cooling of the projectile material is calculated over 100 seconds (methods detailed in Section 5.2.3). From these calculations, a sphere with diameter 0.5 m (representing the unbroken projectile) and initial temperature 1000 K will radiatively cool to 900 K in ~100 s and conductively cool to 900 K in ~4 days. This example demonstrates the importance of considering both the temperature of the surviving projectile (fragmented or otherwise), and also the location in which the material is cooling, as biomarkers will degrade much more significantly under prolonged elevated temperatures. Post-impact biomarker survival was conservatively estimated based on the degree of thermal degradation, calculated using the Arrhenius equation (Section 5.2.3). The assumption that the projectile remains unfragmented and completely buried in the regolith is unreasonable based on the deformation recorded in the simulations. Therefore, a fragment of ejecta is approximated as a 1 cm diameter sphere to compare the biomarker survival between radiatively cooling at the surface and conductively cooling whilst buried in regolith. Based upon these cooling timescale calculations, the best and worse-case scenarios can be determined for surviving biomarkers in the simulated projectiles (Figures 5.10-5.12).

The most favourable impact conditions for biomarker survival (illustrated in Figure 5.8) are combined with the most favourable (radiative) and least favourable (conductive) projectile cooling conditions in Figures 5.10a and 5.10b, respectively. All of the biomarkers survive in significant quantities in the best-case scenario (Figure 5.10a), with lignin, tryptophan and arginine having the highest surviving fractions after 100 seconds (69%, 41%, and 33% respectively). These fractions are likely to stay constant over time as the rate at which the biomarker is degrading after 100 s has plateaued. However, in the least-favourable projectile cooling conditions (Figure 5.10b) it can be seen that valine, glutamine and arginine have degraded to values less than 0.1%, with lignin and tryptophan rapidly degrading at a constant rate after 100 s of cooling. Results illustrated in Figures 5.10b, 5.11b, and 5.12b confirm that it is highly unlikely that the selected biomarkers will survive across any of the simulated impact conditions when subjected to conductive cooling times associated with burial in an insulating regolith. On the other hand, fractions of both lignin and tryptophan are shown to survive in the least favourable impact scenario simulated (Figure 5.9), especially if concentrated in an area away from the centre of the projectile (Figure 5.11a). Comparing the surviving percentage of a biomarker away from the centre of the

projectile with one at the centre leads to a decrease from 42% to 7% for lignin and 12% to 0.1% for tryptophan (Figures 5.11a and 5.12a).

Although largely neglected by previous studies regarding post-impact biomarker survival, the cooling timescales of surviving projectile fragments are important when considering the long-term thermal degradation of organic material. Even if the impact simulations imply pressures and temperatures compatible with the survival of significant proportions of organics immediately after the impact, depending on where the projectile fragments end up, and the size of the fragments, the cooling timescales to reach temperatures consistent with long-term survival may be on the order of days or weeks.

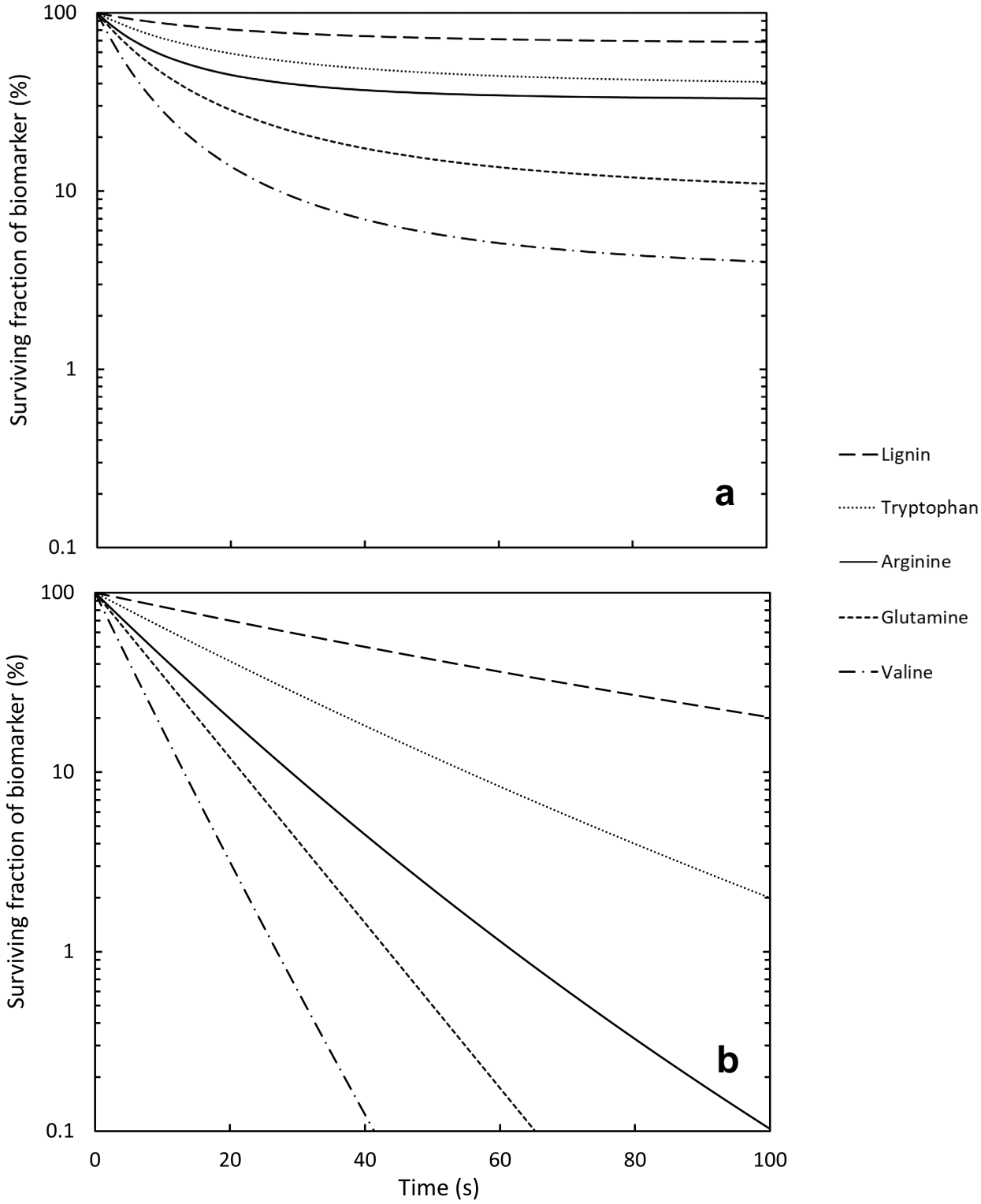

Figure 5.10: *Survival of selected biomarkers for a tracer that reaches a post-shock temperature of 600 K in the main body of the sandstone projectile shown in Figure 5.8. Survival has been extrapolated over a time period of 100 s, based on a 1 cm diameter sphere whilst a) radiatively cooling into space and, b) conductively cooling, buried in regolith.*

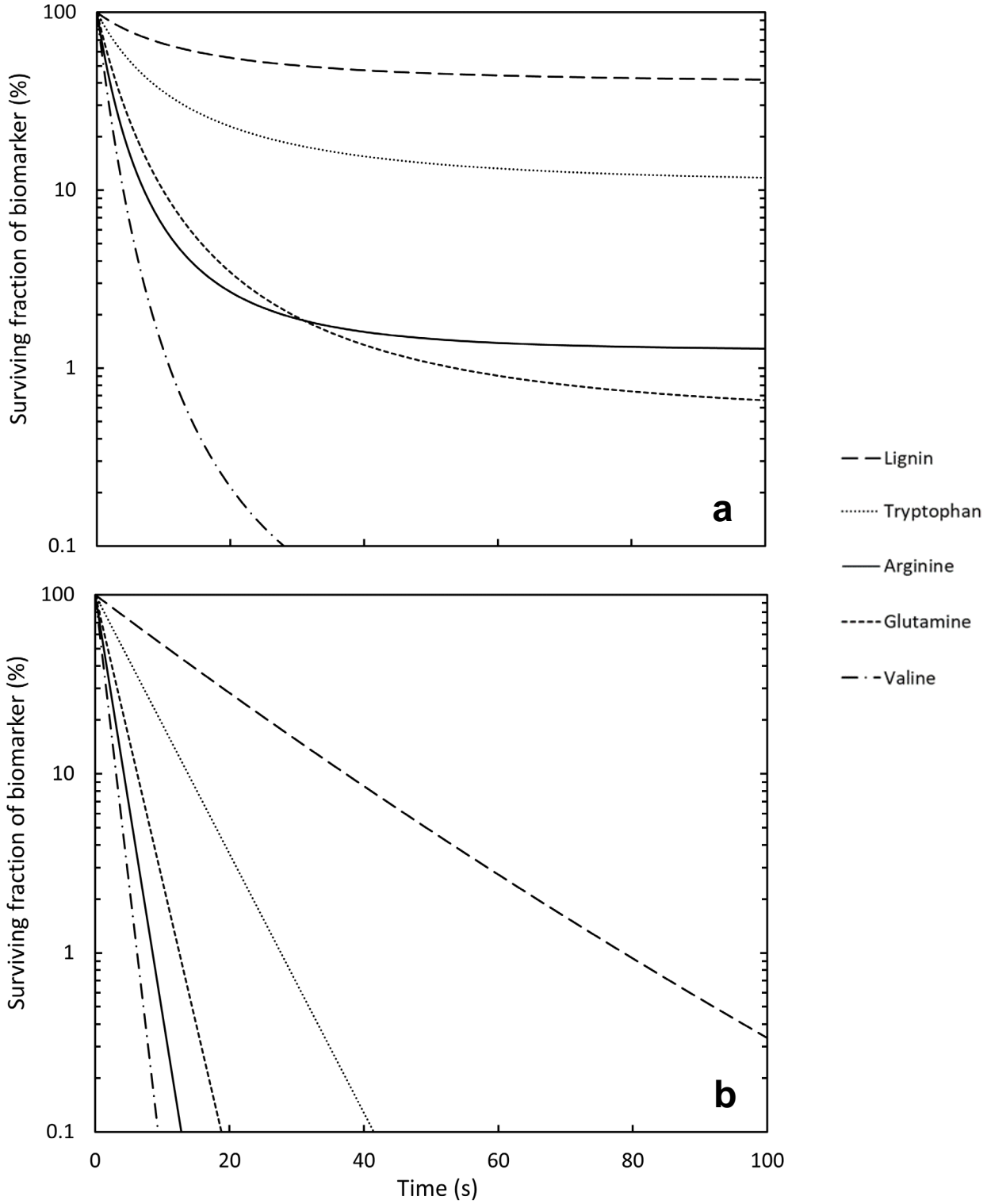

Figure 5.11: *Survival of selected biomarkers for a tracer that reaches a post-shock temperature of 800 K in part of the sandstone projectile shown in Figure 5.9. Survival has been extrapolated over a time period of 100 s, based on a 1 cm diameter sphere whilst a) radiatively cooling into space and, b) conductively cooling, buried in regolith.*

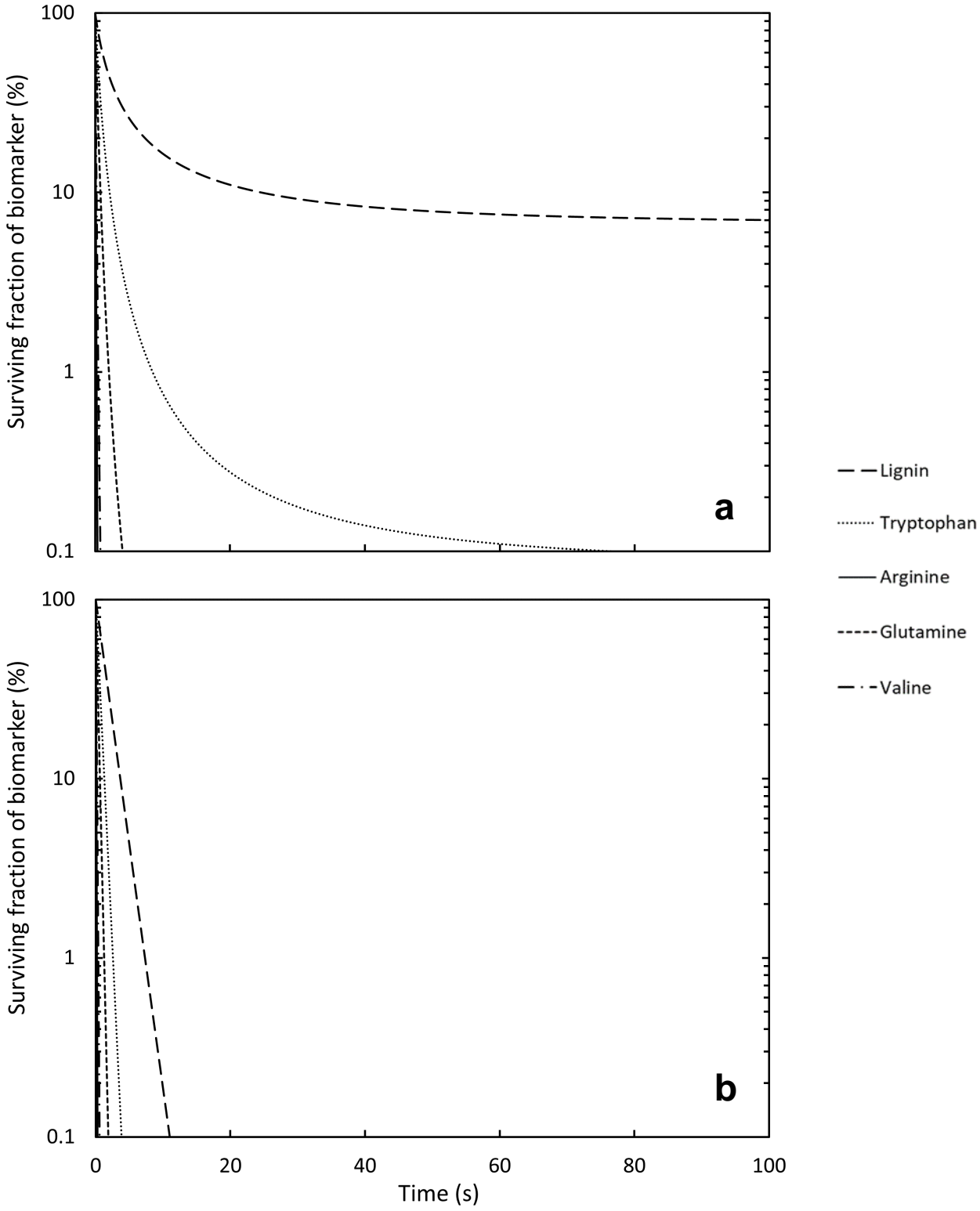

Figure 5.12: *Survival of selected biomarkers for a tracer that reaches a post-shock temperature of 2000 K in the main body of the sandstone projectile shown in Figure 5.9. Survival has been extrapolated over a time period of 100 s, based on a 1 cm diameter sphere whilst a) radiatively cooling into space and, b) conductively cooling, buried in regolith.*

5.3.4 Sandstone projectiles - fossil biomarker survival

All of the molecule biomarkers will survive to some degree in at least one of the impact scenarios, however, this is not the case for the conservative estimates of the fossil ammonite, crinoid, and cephalopod survival. For the sandstone projectiles, peak temperatures in six of the 2.5 km s^{-1} velocity impacts and two of the 5 km s^{-1} impacts are below the threshold for survival of ammonites, crinoids and cephalopods (Table 5.4), in at least part of the projectile. However, pressures in every permutation of simulation were too great for any significant proportion of the ammonite, crinoid and cephalopod fractions to survive, even in the most favourable conditions (Figure 5.8). The conservative survival pressure

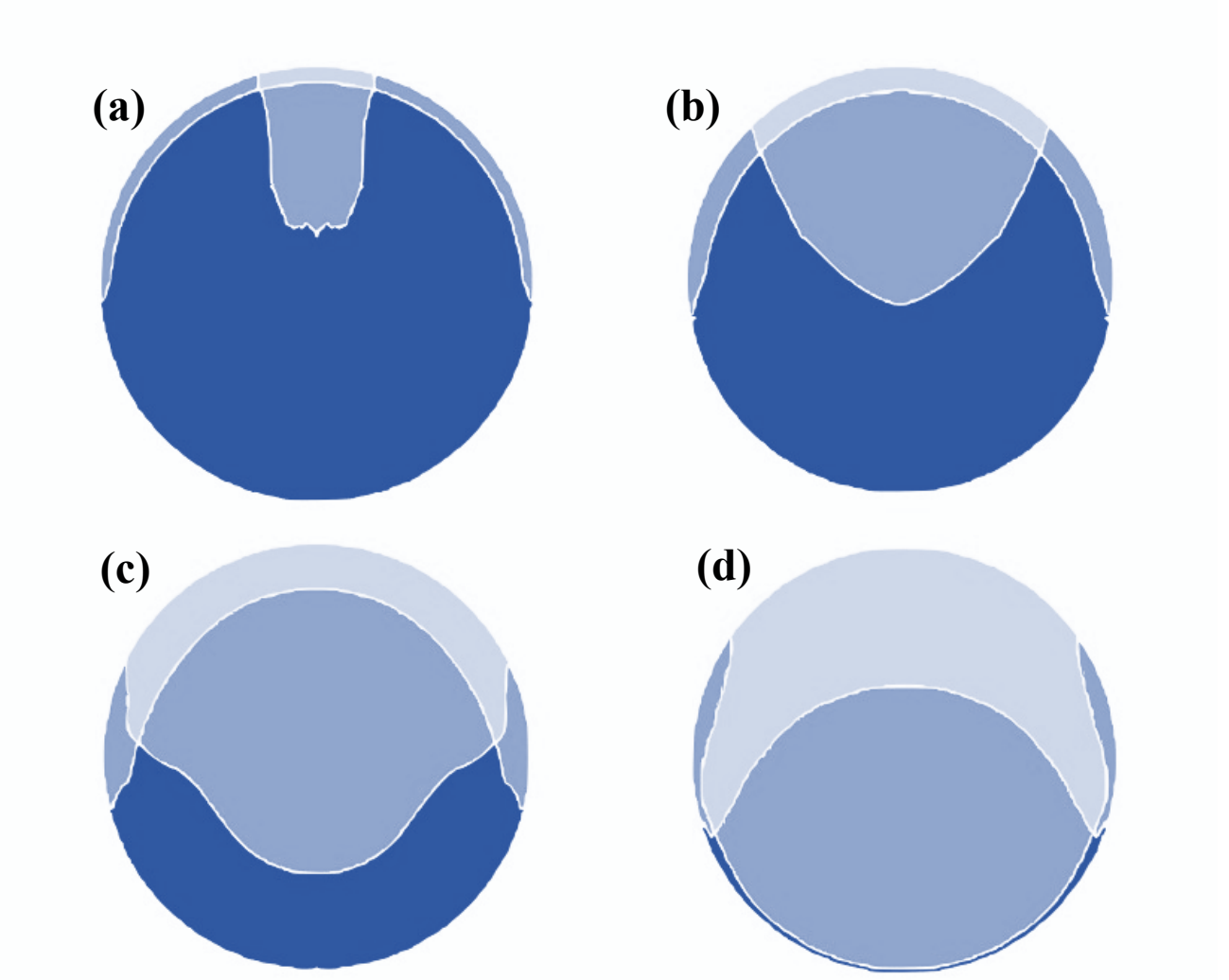

Figure 5.13: *Contour plots showing regions of the projectile where lycophyte megaspores are likely to survive after impact. Projectiles were all solid, impacting at 2.5 km* s^{-1} *into targets with varying porosity: a) 0% (solid), b) 30%, c) 50%, d) 70%. Lightest colour = both pressure and temperature favourable for survival, intermediate = pressure or temperature not favourable for survival, darkest = both pressure and temperature unfavourable for survival.*

estimates taken from metamorphosed ammonite and crinoid/cephalopod samples of 0.2 GPa and 0.02 GPa respectively, are too low for identifiable fragments to survive hypervelocity impacts, even when impacting highly porous, unconsolidated surfaces. Lycophyte megaspores have a higher-pressure threshold for survival, according to preservation in terrestrial metamorphic samples (Table 5.4, 1.4 GPa). All impacts with velocities of 5 km s^{-1} produced peak pressures across the projectile greater than the pressure threshold, whilst any projectiles that included porosity produced temperatures greater than the temperature threshold. Oblate and prolate projectiles also exceeded the pressure and temperature thresholds, respectively. Finally, scenarios with impact velocities of 2.5 km s^{-1} were considered, with solid projectiles impacting targets of varying porosity (Figure 5.13). Peak pressure and temperature regimes within these particular projectiles are favourable for the survival of lycophyte megaspores, with varying fractions of the projectiles being conducive to survival in each scenario. Increasing the porosity of the target has previously been shown to decrease both pressure and temperature across the impacting projectile. Therefore, in the scenarios shown in Figure 5.13, lycophyte megaspores would be expected to survive in a greater proportion of the projectile for increasing target porosity, especially towards the back of the projectile where pressures and temperatures are not as extreme. Note that in this case, consideration of cooling timescales of the post-impact projectile fragments can be neglected, as the survival temperatures are taken from samples which have undergone progressive heating and cooling over millions of years.

5.4 Discussion

5.4.1 External factors influencing biomarker survival

The results presented in this chapter highlight the need for consideration of both pressure and temperature in the determination of biomarker survival within projectiles that impact the lunar surface, and consideration of temperature is of particular importance when modelling materials with significant strength. Clearly, an important consideration for biomarker survival relates to the location of the biomarkers themselves within the projectile. Survival of organic material is not only dependant on the expected pressure and temperatures for a given volume of a projectile (extracted from tracers placed at set intervals within a simulation) but also where the organic material is concentrated within the projectile. The most obvious area for an enhanced probability of survival is as far from the point of contact with the target surface as possible, where pressures and temperatures are at a minimum (Pierazzo and Chyba, 1999; Pierazzo and Melosh, 2000; Potter and Collins, 2013). There are clear limitations and assumptions when using model tracer information to inform

survivability, as the simulations cannot consider the potentially heterogeneous nature of a terrestrial meteorite. For example, if organic material was situated within a pore space at the time of impact, then pore collapse will introduce an additional heating component to the usual shock heating process and pressure will be rapidly applied (Wünnemann *et al.*, 2008; Jutzi *et al.*, 2008; Güldemeister *et al.*, 2013) directly to the area where the organic material is located. However, if organic material was surrounded by a dense material within the matrix or contained within a diaplectic glass as an endogenic melt fragment, the chances of survival upon impact with the lunar surface may be increased (Bland *et al.*, 2014; Davison *et al.*, 2016). More specific consequences for biomarker survivability based upon the heterogeneous nature of polymict geological samples could be explored in future research using mesoscale modelling.

Results in this chapter have concentrated on the thermal degradation of biomarkers over time based on the decomposition of amino acids and lignin. However, it should be noted that amino acids can sublimate under reduced pressures, potentially escaping as whole amino acids before the degrading at high temperatures. For example, in a study by Glavin and Bada (2001), heating the CM-type Murchison meteorite above ~425 K led to the sublimation of glycine, but was recovered as recondensed molecules in a colder area of the experimental apparatus. All other amino acids in the original sample were destroyed during the experiment when heated to ~825 K. Whether this provides a pathway towards significant loss of amino acids due to sublimating into space or a higher yield of surviving, recondensed amino acids trapped in a meteorite would heavily depend on the location of biomarkers within terrestrial meteorites as they are heated. If certain amino acids could sublimate away from hot areas in the impacting terrestrial meteorites and recondense on the grains of cooler lunar regolith, this may provide a higher yield of identifiable biomarkers on the lunar surface after impact.

Additionally, it is important to consider the setting where a terrestrial meteorite may land on the lunar surface. Not only will the projectile state and material constrain the pressures and temperatures experienced post-impact, but the target material itself will heavily influence biomarker survivability (Jutzi *et al.*, 2008; Daly and Schultz, 2013; Bruck Syal and Schultz, 2015; Avdellidou *et al.*, 2016) as shown in the various target porosities modelled in this work. Here, a porous basalt target has been modelled, broadly representative of the lunar regolith, but what if the terrestrial material impacted a permanently shadowed region (PSR) at the lunar poles? In that case, the role of trapped volatiles would have to be considered in the prospective target (e.g., Watson *et al.*, 1961; Arnold, 1979; Haruyama *et al.*, 2008; Spudis *et al.*, 2008; Zuber *et al.*, 2012). For example, the very low (~40 K; Paige *et al.*, 2010) temperatures experienced by the PSRs would increase the long-term cooling rate of impactor material due to more effective conductive heat-loss. Moreover, the presence of ice in the target layer may enhance projectile survivability: an interstitial regolith-ice mixed target may lead to projectile

material experiencing a dissipation of energy over a greater distance into the target (Avdellidou *et al.*, 2016), which would be beneficial to biomarker survival. Further simulations including interstitially mixed and layered regolith-ice ice targets would be needed to address this question.

Organic material within landed terrestrial meteorites on the lunar surface would be subjected to multiple types of radiation over time. These include the solar wind, energetic solar particles, and more rare galactic cosmic rays. The solar wind provides a constant barrage of relatively low energy particles (mostly protons) across the lunar surface. Over geological time, this would degrade any organic molecules exposed but could not penetrate any further than a few micrometres into terrestrial meteorites (Matthewman *et al.,* 2016). Energetic solar particles from solar events and galactic cosmic rays from rays from Solar System could penetrate further into the lunar regolith (cm to several m), however would influence material on the lunar surface much less frequently than the solar wind. Therefore, despite retaining higher temperatures over longer timescales and therefore degrading organic molecules more efficiently, buried material would be more likely to survive solar radiation and more energetic events.

Finally, a note on the changing conditions on the Moon itself over a geological timescale. If the Moon had a thin (~10 mbar) atmosphere at the time of peak mare volcanism (~3.8 Ga, just after the LHB on the Moon but at a time when giant impacts may have been continuing on the Earth) as argued by Needham and Kring (2017), the survival of terrestrial meteorites on the Moon would be potentially enhanced. Atmospheric deceleration prior to impact would allow for slower impact velocities into the lunar surface and, depending on the composition of the atmosphere, could protect the biomarkers within from incoming radiation (at least in the relative, geological short-term). Incorporating an atmospheric component to the modelling work would be an interesting topic for future investigation. On the other hand, impacting into a surface that is experiencing some of the most active volcanism over the planetary body's lifetime could lead to the loss of a large proportion of the projectile. Consider the sustained high temperatures of lava and the consequence of a biomarker rich projectile impacting into and remaining within close proximity to for prolonged periods of time. Many impactors and their constituents from the early Earth may have been lost in these more violent lunar environments, in stark contrast to the "quiet" lunar surface we have come to recognise today.

5.4.2 Detecting terrestrial material on the lunar surface

Even when modelling results indicate that biomarkers within terrestrial material would survive impacts into the lunar surface, detecting and identifying the surviving material is a challenging prospect (see discussion by Crawford *et al.*,

2008). Survival time of metre-sized boulders on the lunar surface can vary between 10s to 100s of millions of years (Basilevsky *et al.*, 2013), eventually succumbing to destruction primarily by subsequent impacts and diurnal thermal cycling as a secondary process (Basilevsky *et al.*, 2015). Therefore, if left exposed on the lunar surface, the most abundant and scientifically relevant terrestrial examples from the LHB ~3.9 Ga ago would have been destroyed long ago. On the other hand, rapid burial of terrestrial meteorites by crater and basin ejecta, and/or by mare basalt flows, could have potentially provided protection for this material (e.g., Crawford and Joy, 2014; Joy *et al.*, 2016). Indeed, recent experimental work (Matthewman *et al.*, 2015, 2016) suggests that burial in lunar regolith will help preserve a range of potential organic molecules. Later exhumation by impact gardening of the lunar regolith would then allow for buried terrestrial material to be present on or near the surface at present day, where it might be detected spectroscopically (see discussion by Crawford *et al.*, 2008 and Joy *et al.*, 2016). Preservation of terrestrial material would presumably be maximised if it remained buried, but in that case the most likely form of detecting it would be as chance discoveries in drill core samples of palaeoregolith deposits collected for other purposes (Crawford and Joy, 2014).

A technique that could be used to look for buried terrestrial material would be by investigating the subsurface using Ground Penetrating Radar (GPR). An instrument and technique routinely used on Earth, GPR offers an efficient and non-invasive method of identifying and characterising subsurface features. Whilst this technique may not be able to identify buried terrestrial material in particular, it could lead to the discovery of palaeoregolith, buried craters, and potentially buried impactors. This would be the starting point for identifying areas with buried meteoritic material. GPR detects electrical discontinuities in the shallow subsurface by generation, transmission, propagation, reflection, and reception of discrete pulses of high-frequency electromagnetic energy (Neal, 2004). The Apollo 17 Lunar Sounder Experiment (ALSE) was used to detect broad, subsurface geological features at multiple depths (Porcello *et al.*, 1974), corresponding to wavelengths of 5, 15, and 150 MHz (60, 20, and, 2 m resolutions, respectively). Additionally, the Lunar Radar Sounder (LRS) onboard the SELENE lunar orbiter explored the lunar subsurface on a much larger scale, with a detection depth >5 km and a resolution of 75 m (Ono *et al.*, 2008). The Lunar Penetrating Radar (LPR) instruments onboard the Chang'E-3 and Chang'E-4 spacecrafts have conducted recent exploration of the lunar subsurface as part of the Chinese Lunar Exploration Program (Fang *et al.*, 2014). The instrument was placed on the Yutu rover, part of the Chang'E-3 mission, and has revealed both the geological and compositional variation of the lunar subsurface (Ding *et al.*, 2020) during a traverse of the lunar nearside, in close proximity to the landing site and Ziwei crater. The subsurface of the lunar farside has been investigated by Chang'E-4, unveiling properties of the lunar regolith within the upper ~50 m, then compared with regolith thickness

and properties with Chang'E-3 (Li *et al.*, 2020; Dong *et al.*, 2021). The discovery of a ~84 m diameter buried crater using radar sounding evidence by the Yutu-2 rover at the Chang'E-4 landing site (Zhou *et al.*, 2021) adds further proof of the capabilities of such instruments on the Moon. The ability to detect exogenous blocks of material within palaeoregoliths beneath the lunar surface would greatly depend on the resolution of the GPR. The current operational limits of the LPR are ~80 m depth (60 MHz) with a resolution of ~2.8 m or ~50 m depth (300 MHz) with a resolution of 17.1 cm (Fang *et al.*, 2014; Ding *et al.*, 2017). Most recently, the Lunar Regolith Penetrating Radar (LRPR) onboard the Chang'E-5 lander (Lu *et al.*, 2016; Xiao *et al.*, 2019) has unveiled the hyperfine structure of the uppermost 2.5 m beneath the landing site, with a very high resolution of 5 cm (Su *et al.*, 2022). Centimetre-scale resolutions are conducive to detecting surviving terrestrial material, based on the likelihood of ejected material from Earth potentially escaping as metre-sized blocks (Wells *et al.*, 2003; Beech *et al.*, 2019). Impacting the lunar surface at low velocity, like those explored in Chapter 5 of this work, will likely limit the destruction of metre sized blocks of terrestrial material. Even at higher velocities, break-up of terrestrial meteorites after impact into smaller, centimetre sized fragments would still be detectable by high resolution GPR in the upper few metres of the regolith.

Combining GPR with other techniques capable of investigating the lunar subsurface would greatly improve the probability of detecting buried meteoritic material. Magnetic Induction Spectroscopy (MIS) and Distributed Acoustic Sounding (DAS) are two such methods that could be used in conjunction with GPR to improve the detection of volatiles and potentially organic material in the lunar subsurface (Schmitz *et al.*, 2022). A proposed prospecting mission to the lunar surface has suggested a network of scouting rovers with a central lander or rover to enable investigation via all three methods in the upper ~10 to 20 m of the subsurface. Magnetic induction spectrometers, each with electromagnetic receiver antennas, would be placed on multiple rovers and respond to the powerful electromagnetic transmitter on the lander. The preliminary mission concept is focused on prospecting the lunar surface for volatiles, most importantly water ice for use as a resource for future missions. The great interest in prospecting for subsurface volatiles is likely to enable the discovery of buried meteoritic material and may provide the chance to detect hydrated, organic material on the Moon in the near future. These subsurface investigations will be crucial for informing and guiding drilling operations for the collection of samples, either for *in situ* investigation on the Moon or return to Earth for more in-depth interpretation.

5.4.3 Comparing Earth–Moon to Mars–Phobos material transfer

A comparison can be made between the transfer of material from Earth to the Moon and from Mars to Phobos. Phobos is the larger of the two Martian moons (Phobos and Deimos), yet still only 27 km in diameter on the longest axis. With a short orbital period (<8 hours) and close proximity to Mars (on average, ~6000 km above the surface), it has been suggested that Phobos could be an excellent "collection plate" for Martian material after ejection (Chappaz *et al.*, 2013). The small moon could not only be directly struck by meteorites but also sweep through a cloud of particles ejected from a large impact and models suggest that the regolith could host up to ~250 ppm of Martian ejecta material (Ramsley and Head, 2013; Kurosawa *et al.*, 2019). Certain locations on the surface of Mars are considered to have been conducive to life at some period in the planet's history (Eigenbrode *et al.*, 2018) and it is reasonable to assume that such life (if it was able to develop) could have left behind biomarkers. A large impact, proximal to such a location, could eject biomarker laden material into an orbit that crosses that of Phobos and deposit material onto the surface. The upcoming Japan Aerospace Exploration Agency (JAXA) Martian Moons eXploration (MMX) mission (Kuramoto *et al.*, 2022) plans to collect samples from the surface of Phobos and could potentially return Martian biomarkers to Earth. Investigation into the likelihood for biomarkers to survive transfer from Mars to Phobos is, therefore, necessary before returned samples and *in situ* spacecraft data are analysed. Previous impact modelling has suggested that a small proportion of near-surface, Martian material can be ejected at high velocities, capable of reaching Phobos from Mars, and experience shock-pressures low enough to remain solid (Artemieva and Ivanov, 2004). Furthermore, recent preliminary modelling has suggested that temperatures remain low enough within martian material impacting Phobos at typical, expected velocities (<4.5 km s^{-1}) for biomarkers to remain viable (Morland *et al.*, 2021).

5.5 Conclusions

In this work, it has been demonstrated that a range of biomarkers within terrestrial meteorites have the potential to survive impact on the lunar surface. At the maximum impact velocity for terrestrial meteorites impacting the Moon (5 km s^{-1}) or less, peak temperatures across the projectile are significantly higher when projectile strength is accounted for compared with the strengthless scenario in which heating is caused exclusively by shock compression. This supports findings in previous studies in target materials (Kurosawa and Genda, 2018) and shows shear heating can have an important effect in projectile material. Comparison with previous work (Crawford *et al.*, 2008), which neglected shear heating, indicates reduced survivability in models with 5 km s^{-1} projectile velocity due to higher peak temperatures within the projectile. Temperatures near the contact zone reach those required for melting and vaporisation of the projectile itself, especially when a porous projectile impacts a solid target. Lower impact velocity (2.5 km s^{-1}), lower projectile porosity, and/or higher target porosity, increases the likelihood of survival for the projectile and any organic molecules within them. The most favourable conditions for survivability involve a solid projectile, impacting at low velocity (2.5 km s^{-1}) into a highly porous (50-70%) regolith. In this case, even lycophyte megaspores are expected to survive with little to no alteration based on their survival pressures and temperatures in metamorphosed samples. Results presented here show that this would be the case for both sandstone and limestone projectiles, with limestone having a somewhat greater potential for biomarker survival than sandstone.

Post-impact cooling timescales depends heavily on the final location and size of the surviving fragments. Small (cm-scale) fragments which are ejected and land on the lunar surface will cool quickly (seconds) by radiation, leading to the most favourable conditions for biomarker material. Lignin and tryptophan have been shown to survive well in these conditions across the range of impact scenarios simulated in this work. Buried projectile fragments will cool over much longer timescales (days) by conduction leading to conditions in which no biomarkers would survive, even in the most favourable impact scenarios simulated in this work. Larger (tens of cm to metre-scale) fragments will cool slower, regardless of the cooling process, leading to less favourable conditions for biomarker survival. After their initial cooling, the survival of biomarkers over a geological timescale (millions to billions of years) will be dependent on the subsequent burial of biomarker rich projectile fragments by ejecta from later impacts or lava flows. These will act as an insulating layer to protect the surviving biomarkers from fluctuating surface temperatures and cosmic radiation.

Given that most terrestrial meteorites currently residing on the Moon will have been launched from the Earth during the first billion years of Solar System history during a period of enhanced impact bombardment, they have the potential to provide astrobiologically important information on a period of Earth's early geological and biological evolution that Earth itself no longer retains. These conclusions imply that a search for terrestrial meteorites on the Moon should join the already long list of scientific reasons for resuming the exploration of the lunar surface (e.g., NRC, 2007; Crawford and Joy 2014; LEAG, 2016; Tartèse *et al.*, 2019).

6 Survival of carbonaceous chondrites impacting lunar surface and their use as future resources

6.1 Introduction

The surface of the Moon is increasingly becoming a prime target for the next step in human exploration, with an emphasis on developing approaches for in situ resource utilisation (ISRU) (e.g. Bridenstine, 2019; NASA 2020; ISECG, 2020). Whilst the lunar surface may potentially provide an abundance of extractable metals (Duke *et al.*, 2006; Schwandt *et al.*, 2012), water (Arnold, 1979, Feldman *et al.*, 2001; Anand, 2010; Sargeant *et al.*, 2020), and potential construction materials for lunar habitats (Cesaretti *et al.*, 2014), there is a lack of several key elements in sufficient quantities to facilitate a long-term, sustainable human presence on the Moon (Crawford, 2015; Crawford *et al.* in press). Fortunately, however, some of key element resources lacking in lunar materials may have been delivered to the lunar surface by impacting asteroids and comets. For example, localised concentrations of Fe, and related siderophile elements, could be found within surviving metallic meteorite material after impacting the lunar surface (Haskin *et al.*, 1993; Wingo, 2004; Yue *et al.*, 2013). It is, therefore, necessary to determine which materials/elements are needed to maintain a sustainable human presence on the Moon. Furthermore, identifying materials that are not native/abundant in the lunar crust and may be provided by external sources that survive impact with the surface is of critical importance. Carbon and nitrogen are two elements that do not feature prominently in the lunar crust, but which will be very important for the longevity of human missions to the lunar surface. Both elements are critically important for life support systems, including producing breathable air within habitats (like the nitrogen-based air within the International Space Station) and eventual plant-based oxygen production (utilising lunar-produced carbon dioxide). In the short term, carbon could be important for refuelling methalox-based spacecraft, such as the SpaceX Starship (Cannon, 2021). This would enable the use of the Moon as a launchpad into *cis*-lunar space and beyond, without the need for hauling large amounts of fuel from the large gravity well of Earth. In a future where substantial lunar infrastructure is in place, large masses of native carbon could be of great use to the production of radiation-tolerant electronic components (Kanhaiya *et al.*, 2021) and construction of long-duration lunar habitats (Rojdev *et al.*, 2014; Naito *et al.*, 2020). Nitrogen, in reactive form (e.g., NO_3, NH_4), is an essential mineral for the growth of almost all plant life (Stevens *et al.*, 2011) and would, therefore, be a necessary material to sustain long-term food production on the lunar surface (Wamelink *et al.*, 2014). Whether that production process involved hydroponics or ‘fixing’ lunar soils

(e.g., Paul *et al.*, 2022) with enough nitrogen to provide sufficient nutrients, transporting enough nitrogen or nitrogen-rich soil to the Moon from Earth would be costly, unsustainable, and overly dependent on Earth for a self-sufficient lunar base. These elements are found in many forms within carbonaceous chondrite (CC) meteorites (Sephton 2002; Pearson *et al.*, 2006; Chan *et al.*, 2016) and have potentially been delivered to the Moon via impact processes. The rich impact history of the Moon indicates that asteroids with CC-like compositions will have impacted the lunar surface over geological time (e.g., Joy *et al.*, 2012, 2016, 2020) and could, therefore, be a source of these key elements if they survive the impact. Even if the CC meteorites completely melt or vaporise, they still may contribute to the chemical coatings on mineral grains in and around the impact zone (Thomas-Keprta *et al.*, 2014).

Unless, or until, significant quantities of surviving meteoritic materials are retrieved from the lunar surface, experimental and numerical modelling are the best tools to probe the fate of projectiles during and immediately after impact. Projectile survivability is influenced by multiple factors including impact velocity (Melosh, 1989; Bland *et al.*, 2008, Kurosawa and Genda, 2018), projectile material (Daly and Schultz, 2013; Svetsov and Shuvalov, 2015; Wickham-Eade *et al.*, 2018), projectile porosity (Wünnemann *et al.*, 2008; Jutzi *et al.*, 2008; Güldemeister *et al.*, 2013), target porosity (Wünnemann *et al.*, 2006; Avdellidou *et al.*, 2016), target material (Christiansen *et al.*, 1993; Davison *et al.*, 2011; Burchell *et al.*, 2014a), and angle of impact (Pierazzo and Melosh, 2000; Davison *et al.*, 2011; Potter and Collins, 2013; Nishida *et al.*, 2019). Rock projectile materials in numerically simulated hypervelocity impacts have been shown to survive impact with multiple simulated planetary bodies including Earth (Pierazzo and Melosh, 2000; Wells *et al.*, 2003; Potter and Collins, 2013; Beech *et al.*, 2019), the Moon (Bland *et al.*, 2008; Yue *et al.*, 2013), and Europa (Pierazzo and Chyba, 2002). Earlier numerical models also indicate that volatiles and organic material within projectiles may survive impact with the Moon (e.g. Crawford *et al.*, 2008; Ong *et al.*, 2010; Svetsov and Shuvalov, 2015).

Projectiles in laboratory-scale experiments can survive hypervelocity impacts with a multitude of different target materials (Daly and Schultz, 2015; Wickham-Eade *et al.*, 2018). Additionally, organic constituents within such projectiles have also been shown to survive (Mimura and Toyama, 2005; Parnell *et al.*, 2010; Meyer *et al.*, 2011; Burchell *et al.*, 2014a, 2014b, 2017). Examples of surviving asteroidal material (see Joy *et al.*, 2016) have been found in lunar samples from Apollo 11 (Goldstein *et al.*, 1970; McKay *et al.*, 1970; Quaid and Bunch, 1970), Apollo 12 (Wood *et al.*, 1971; Zolensky *et al.*, 1996; Joy *et al.*, 2020), Apollo 16 (Jolliff *et al.*, 1993) and Luna 16 soils (Demidova *et al.*, 2022). Fragments of silicate meteoritic material have also been identified in lunar breccias, including a chondritic fragment within lunar meteorite Pecora Escarpment 02007 (Day *et al.*, 2006; Liu *et al.*, 2009; Joy *et al.*, 2012), and younger Apollo 16 regolith

breccias (Joy *et al.*, 2012). CC survival after impact can be directly studied using laboratory impact experiments, replicating the small-scale impact of a CC meteorite into an analogue of the lunar surface. Simulated meteoritic impacts can be used to investigate textural changes in CC samples due to impact induced shock pressures (e.g., Nakamura *et al.*, 2000), heating effects of the CCs matrix (e.g., Tomioka *et al.,* 2007), or even the fate of amino acids after impact (e.g., Bertrand *et al.,* 2009). However, these types of experimental impact simulations can only be performed on samples on the mm-scale and at impact velocities up to a realistic maximum of 10 km s^{-1}. Some experimental set-ups may be limited to vertical impacts as well, missing the opportunity to investigate oblique scenarios. Most importantly, in regard to resource utilisation, it is very difficult to compare the final resting place of projectile material after impact in an experimental set-up versus a large-scale (km) impact. This is where the benefits of numerical modelling are highlighted. Simulating a large CC impacting the lunar surface at any impact velocity or angle, whilst being able to track the material temperature, pressure, and position in 3D space during the simulation, provides something laboratory impacts currently cannot.

Even if meteoritic material survives impact with the lunar surface, it will immediately start to be degraded by micrometeorite impacts and other surface processes. The median survival time for centimetre to meter scale rocky material on the surface of an airless body (like the Moon) has been estimated to be between 40 and 80 Myr, with some surviving up to 300 Myr, depending on the material (Basilevsky *et al.*, 2013, 2015). This means that in order for landed projectile material to survive over long periods of time (i.e., millions or billions of years) after impact, the material must be protected from destructive processes at the surface. Rapid burial of meteorites by crater and basin ejecta, and/or by mare basalt flows, could potentially provide protection for meteoritic material (e.g., Crawford and Joy, 2014; Joy *et al.*, 2016). The most likely form of protection will come from a covering by regolith due to subsequent impacts. In mare regions, basaltic lava flows could further protect the material by creating an insulating layer overtop the ejecta (Crawford *et al.*, 2007; Fagents *et al.* 2010; Rumpf *et al.*, 2013; Joy *et al.*, 2016). However, in order to be used as resources or for samples with scientific value, these meteorites would need to be at least partially exhumed at a later date via impact gardening.

Whilst there has been plenty of investigation into the fragmentation of projectiles upon impact (e.g., Melosh *et al.*, 1992; Nagaoka *et al.*, 2013; Wickham-Eade, 2017; Nishida *et al.*, 2019), there is a lack of data on the concentration of surviving fragments proximal to the impact site. Work by Yue *et al.* (2013) suggest that projectile remnants may become concentrated in the central peaks of complex impact craters on the Moon, and Potter and Collins (2013) have investigated how large fragments of a meteorite have survived at the Morokweng crater on Earth. Fe-rich meteorites, both iron and stony-iron, that have partially survived collision with the lunar surface may provide high localised concentrations of native

Fe, and associated siderophile elements (Haskin *et al.*, 1993; Wingo, 2004). Additionally, Wieczorek *et al.* (2012) have interpreted prominent lunar magnetic anomalies as being due to surviving Fe-rich meteoritic debris. Further afield, Daly and Schultz (2016) suggested that craters at or above the equilibrium crater diameter on Vesta are able to preserve localised deposits of carbonaceous projectile material. Additionally, the fate of amino acids during meteoritic impacts have been simulated (Bertrand *et al.*, 2009) indicating some survival, with impact shock acting as a selective filter to the delivery of extra-terrestrial amino acids via CCs. With a similar high porosity and low-density regolith as the Moon, it is reasonable to assume the same could occur on the Moon when considering projectiles with lower impact velocities (<10 km s^{-1}).

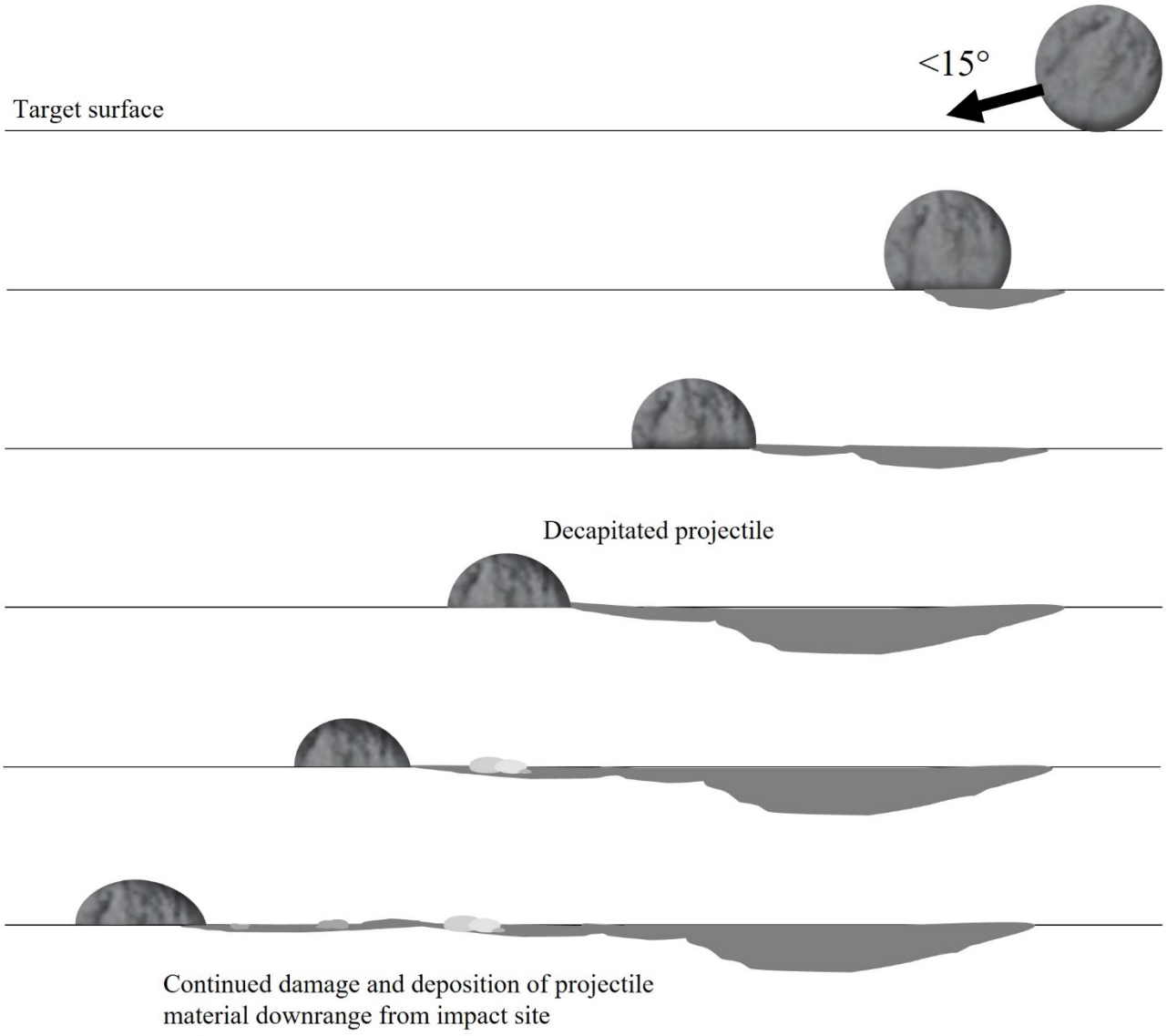

Figure 6.1: *Schematic diagram showing the process of projectile decapitation after a highly oblique impact. Several snapshots in the cratering process are shown for an impact angle less than 15°.*

In the context of specifically finding and using CC material as a resource for lunar surface operations, it is important to consider where the material remains concentrated post-impact. If the material survives (according to the pressure and temperature regimes recorded within the projectile), but is dispersed over a wide area after impact, it will be less economical to collect and use as a resource or even as an economically viable 'reserve'. However, if a significant amount of material is concentrated within a small area surrounding the impact site (e.g., within a few km), it could become an attractive resource and a potential location to establish a lunar outpost. Consider that a relatively small CC parent asteroid, 1 km in diameter, would have a mass on the order of 10^{11} to 10^{12} kg (depending on porosity, density, composition etc.) with C and N proportions reaching up to 6 and 0.6 wt.%, respectively (Pearson *et al.*, 2006). Even if only 10% of the original impactor mass does not exceed the vaporisation temperatures of C- and N-bearing molecules, and lands close to the impact site, there would still be ~10^{9} kg of C and ~10^{8} kg of N as potential resources. Compare this to the calculated potential total abundance of C in all lunar polar ice deposits, ~10^{11} kg (Cannon, 2021), one large CC impactor may contribute a comparable amount of C, but within a much smaller area. Survived material concentrated within and in close proximity to the crater resulting from just one large impact would be much more accessible via robotic or crewed missions to the Moon. It is also possible that projectile material may survive in larger local concentrations far downrange of the contact site after a highly oblique impact (<15°), via a process called "projectile decapitation" (Figure 6.1). Both of these scenarios could occur anywhere across the lunar surface, potentially leading to more favourable conditions for resource extraction versus the permanently shadowed regions of polar ice deposits.

6.2 Methods

Investigation of both the temperature regimes and the location of CC material post-impact requires a suite of 3D impact models at a variety of impact angles and velocities. Here, the survival of carbon- and nitrogen-bearing molecules is considered using the iSALE (impact-SALE) multi-material, multi-rheology shock physics code (Wünnemann *et al.*, 2006). A combination of 2D and 3D modelling were used to determine the extent to which km-scale CC projectiles survive after impact with the lunar surface. High spatial resolution 2D simulations were used to determine accurate temperature and pressure regimes across the projectiles via a resolution test. Three dimensional simulations have been limited in terms of resolution compared to 2D (due to computational requirements), however, they do allow for the estimation of the concentration of the projectile material after impact at an angle. The results, particularly the peak temperature data, end

location of projectile material, and local concentrations of projectile material, were then analysed to determine the likely survival of carbon and nitrogen bearing molecules within CCs.

6.2.1 Evaluating and selecting a projectile material model

Due to the large computational time required (many days per simulation) to complete much of the 3D modelling, it was necessary to restrict the analysis to the most C and N rich objects that may have impacted the Moon over geological time, rather than using a unique material model for each group of CCs. For this reason, the CM and CI groups of CC meteorites are chosen, which contain up to 6 wt.% C within Alais and 0.6 wt.% N within Orgueil (both CI meteorites: Pearson *et al.*, 2006). CI and CM carbonaceous chondrites are used as the representative source for C- and N-bearing molecules, neglecting the contribution of other types of CCs (CV, CR, CB etc.). Both CM and CI consistently contain the highest proportion of C and N by wt.% within the samples investigated so far in the literature (see Alexander *et al.*, 1998, Sephton 2002, and Pearson *et al.*, 2006 for reviews of C and N in CCs). A range of abundances of C-bearing molecules found in the CM meteorite samples Murchison and Murray were used, as well as samples of the CI Orgueil meteorite. For N-bearing molecules, the average abundances found in samples of the CM meteorites Murchison and Murray were selected (Cronin & Moore, 1971; Bundy, 1989; Huss & Lewis, 1994; Russell *et al*., 1996; Sephton, 2002; Weiss *et al.*, 2018; NIOSH, 2019). These types of meteorites and their representative parent asteroids will, therefore, contribute the most C or N to the lunar surface upon impact.

In the simulations, the projectile is represented using a material model best approximating CC-like material from those available in the iSALE library. Parameters needed to model the projectile and target in 2D and 3D simulations were carefully selected to best represent the CC material and target surface. These included the composition, porosity, velocity, and angle of impact for the projectile and the composition, porosity, and number of layers in the target. Projectile compositions of a multitude of candidate materials have been selected from the available equation of state (EoS) library within iSALE and compared with experimental shock Hugoniot data for the composition of CM2 chondrites (Murchison) and ordinary chondrites (Bruderheim; Anderson and Ahrens, 1998). Based upon materials previously used during modelling work involving CCs and those that represent the best approximation of the bulk composition of CC materials, a set of equations of state were tested (Table 6.1). The Carbchon Tillotson EoS aims to represent solid CI/CM material but is not included in the original iSALE EoS library and was added as a part of this work using parameters defined by Herbold *et al.* (2015). The other five material models use a semi-analytical equation of state (ANEOS) (Thompson and Lauson,

1972). Figure 6.2 shows the response of the materials to shock for a solid projectile impacting a solid target, using combinations of shock pressure, particle velocity, and shockwave velocity (the data for this is available within the iSALE EoS library). Dunite behaves more like ordinary chondrites than CC material, plotting near or above that of the Bruderheim meteorite data, and far from the Murchison meteorite data (Fig. 6.2, solid red line). Similarly, basalt plots further from the CM2 data than other candidate materials (Fig. 6.2, solid light blue line). Therefore, dunite and basalt were discounted as potential representations of CC material. Quartz, serpentine, granite, and carbchon all plot in very similar positions on both figures (6.2a and 6.2b). Both serpentine and the CC Tillotson EoS, with the introduction of a porosity compaction model to represent 20% of the volume as pore space (based on the porosity for a typical CC meteorite, e.g., Consolmagno *et al.*, 2008), match well to the Murchison material data (Figure 6.3). Based upon this investigation of potential materials to best represent a generalised CC-like projectile, serpentine was chosen as the material to be used across the suite of 2D and 3D simulations. Choosing this material model over the similarly performing CC Tillotson EoS, despite the latter being specifically created to represent CM material, was based on a number of factors. Firstly, the serpentine ANEOS has been used in previous simulations representing carbonaceous material (Richardson *et al.*, 2005; Davison *et al.*, 2016; Wakita & Genda, 2019), whereas the CC Tillotson EoS has so far only been used by the original creators of the material model (Herbold *et al.*, 2015). Secondly, ANEOS provides a limited estimation of phase changes within materials and, as a result, can model the thermodynamic evolution of a material beyond the initial shock of the impact. This allows for the account of melting and vaporisation in the projectile, which is vitally important in the context of CC survival and the resource potential of the surviving material. Lastly, and possibly most importantly in the context of time management, using the CC Tillotson EoS with iSALE-3D caused many simulation scenarios to unexpectedly fail before completion. No such issues occurred when using the serpentine EoS. This is likely due to the relatively untested nature of the CC Tillotson EoS within iSALE, whereas the serpentine is already included within the iSALE library and has provided robust results in multiple studies using iSALE (Table 6.1).

Table 6.1: *Equations of state (EoS) available within the iSALE EoS library which were considered to represent CC-like material.*

Equation of state	Previous use in modelling work
Granite – ANEOS (Pierazzo *et al.*, 1997)	Multiple studies have used both in a variety of lunar impact simulations, but less so as CC-like material. (e.g., Crawford *et al.*, 2008; Potter, 2012; Kring *et al.*, 2016). Used here for comparison vs. more likely candidate materials.
Basalt – ANEOS (Pierazzo *et al.*, 2005)	
Quartz – ANEOS (Melosh, 2007)	Approximation for hydrated asteroid material impacting the Moon (Svetsov & Shuvalov, 2015).
Dunite – ANEOS (Benz *et al.*, 1989)	Simulation of CM-like impactor striking Vesta (Turrini *et al.*, 2014).
Serpentine – ANEOS (Brookshaw, 1998)	Hydrocode modelling as the surface of a CC-like asteroid (Richardson *et al.*, 2005) and as the hydrated core of planetesimal impacts (Wakita & Genda, 2019).
Carbchon – Tillotson (Herbold *et al.*, 2015)	Specifically created by Herbold *et al.* (2015) to represent CI/CM material.

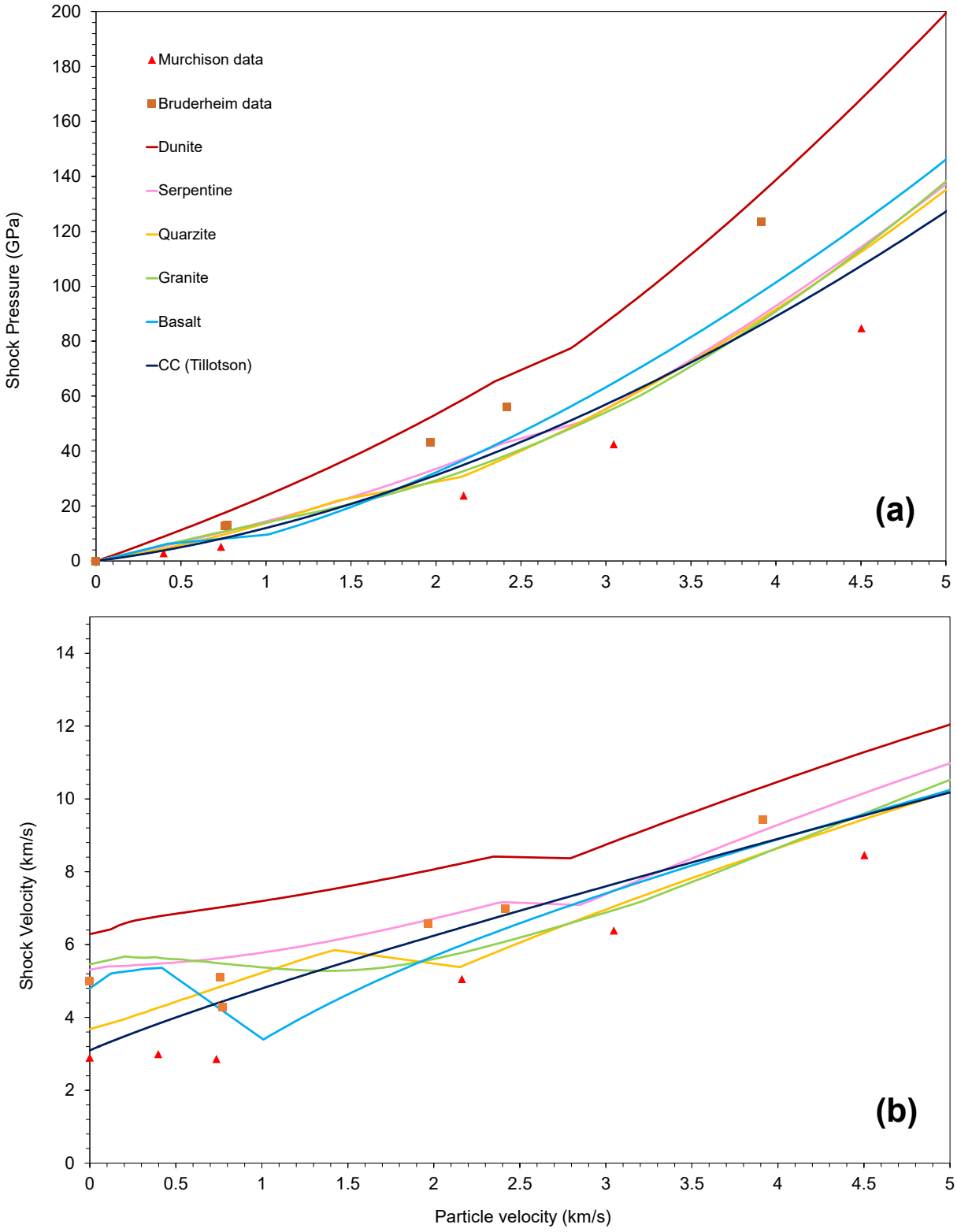

Figure 6.2: *A comparison of shock Hugoniot data for iSALE EoS data (dunite, serpentine, quartzite, granite, basalt, and CC material models) and experimental data for ordinary chondrites (Bruderheim) and CM carbonaceous chondrites (Murchison). Bruderheim and Murchison data taken from Anderson and Ahrens (1998). (a) Particle velocity vs. shock pressure, (b) particle velocity vs. shock velocity.*

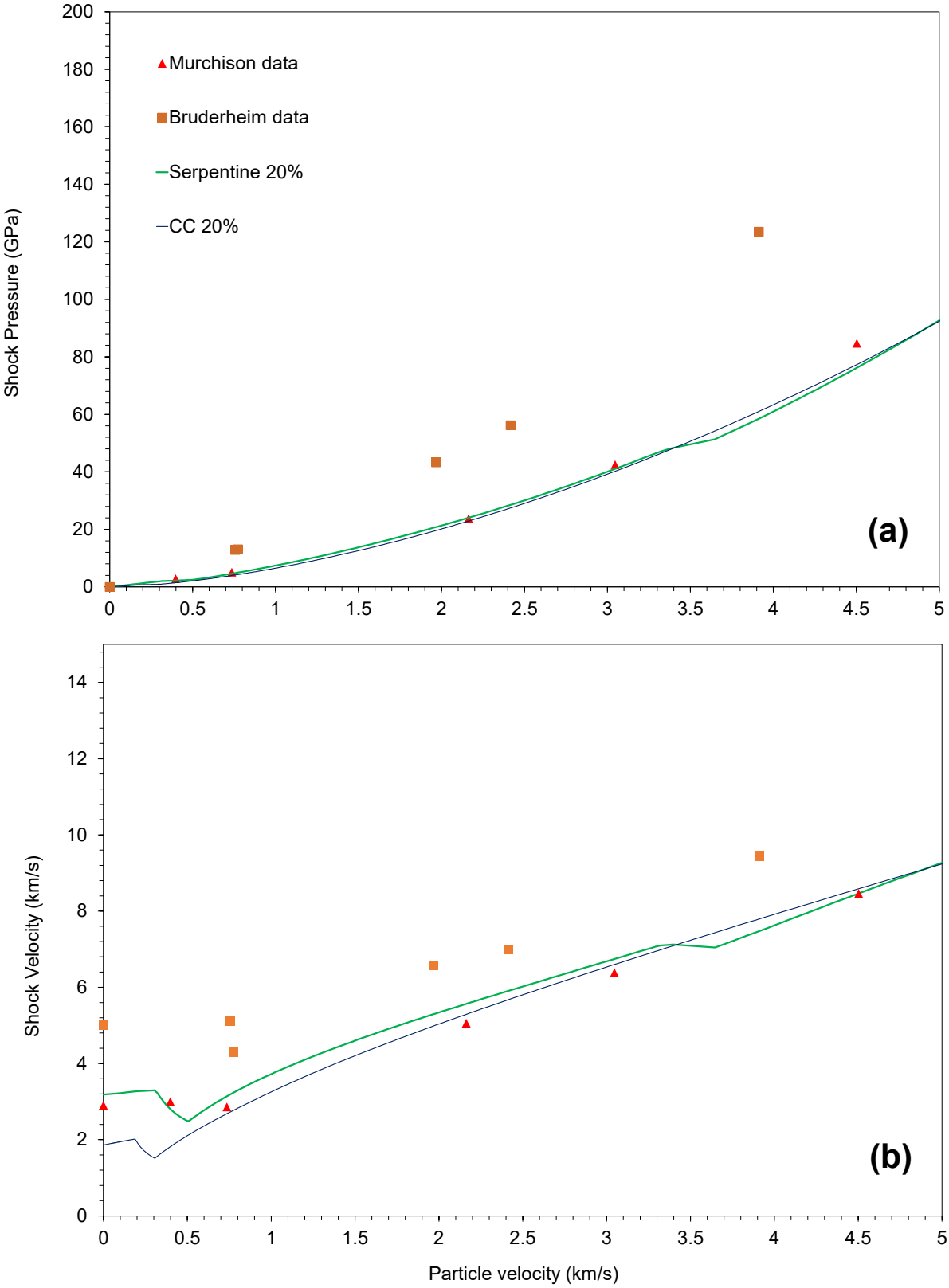

Figure 6.3: *A comparison of shock Hugoniot data for iSALE EoS (serpentine and CC, both including 20% porosity) and experimental data for ordinary chondrites (Bruderheim) and CM carbonaceous chondrites (Murchison). Bruderheim and Murchison data taken from Anderson and Ahrens (1998). (a) Particle velocity vs. shock pressure, (b) particle velocity vs. shock velocity.*

6.2.2 Simulation set-up – 2D

High spatial resolution, 2D simulations were used to determine accurate temperature and pressure regimes across the projectiles via a spatial resolution test. The spatial resolution of a simulation is based on the dimensions of the cells that make up the mesh geometry. Essentially, a simulation with a fixed impactor size and a smaller cell size means less averaging of variables recorded across a given area and is therefore deemed a higher resolution. The cell size is measured relative to the size of the projectile modelled, so a particular resolution can be described as the number of cells per projectile radius (CPPR). Each scenario was simulated at resolutions of 8, 16, 24, 32, 50, 100, and 200 CPPR and measured the volume of the projectile that experiences peak temperatures higher than the melt temperature of the serpentine projectile material (~2100 K; Brookshaw, 1998). Using iSALE-2D (Wünnemann *et al.*, 2006), a 1 km diameter, CC-like projectile was vertically impacted into a single-layer, lunar surface target at 5 km s^{-1}. The serpentine ANEOS EoS (Brookshaw, 1998) was used to represent the projectile and basalt ANEOS EoS (Pierazzo *et al.*, 2005) was used to represent the target. Strength parameters for the impactor (Table 6.2) were chosen by collating information from sources detailing the mechanical properties of carbonaceous asteroids and their associated simulants (Bruck Syal *et al.*, 2016; Davison *et al.*, 2016; Wakita and Genda, 2019; Avdellidou *et al.*, 2020). This provided an overview for the typical compressive and tensile strengths for carbonaceous chondrite-like material and therefore an informed choice could be made for the strength parameters of the impactor. Target strength parameters were taken from Miljković *et al.* (2013), the same as the basalt target represented in Chapter 5 (Table 5.2).

Typical average porosities were included in both the projectile (40%) and target (10%), based on average values for CC asteroid parent bodies (Veverka *et al.*, 1999; Britt *et al.*, 2002; Chesley *et al.*, 2014; Lauretta *et al.*, 2015; Sugita *et al.*, 2019) and the lunar highlands megaregolith (Wieczorek *et al.*, 2013). Figure 6.4 shows the results of this spatial resolution test, with the volume of material experiencing temperatures greater than that of the melt temperature decreasing with increasing resolution. At the highest resolution tested (200 cells per projectile radius) the results are close to converged, and it is likely that the volume of material reaching the melt temperature would only decrease slightly more for higher resolution simulations. Realistically, the time it takes to simulate these scenarios at high spatial resolution is too long (weeks per simulation) to be practically viable for a large suite of 3D simulations with variable impact velocities and angles. Therefore, when the final simulations were run at lower resolution, we assume that the temperatures recorded are somewhat overestimated compared to what they would be in a "real-world scenario" (converged with an essentially infinitely high resolution). For example, a simulation run at 16 cells per projectile radius would overestimate the volume

of projectile that reaches the melt temperature (2100 K) by ~70% when compared to an identical simulation at 200 cells per projectile radius. These results are particularly sensitive to spatial resolution because each cell represents a relatively small volume of the projectile.

Table 6.2: *Thermal, strength, and damage input parameters for the impactor and target materials used in this numerical modelling work. Serpentine melt temperature taken from the EoS for serpentine from Brookshaw (1998). Strength parameters are derived from previous experimental and numerical modelling of carbonaceous simulants (Avdellidou et al., 2020), asteroid impact modelling (Bruck Syal et al., 2016; Wakita and Genda, 2019), and carbonaceous material mesoscale modelling (Davison et al., 2016). Target strength parameters were taken from Miljković et al. (2013), simulating the lunar crust.*

Parameter	Symbol (units)	Impactor (Serpentine EoS)	Target (Basalt EoS)
Thermal			
Thermal softening coefficient	ξ	1.2	1.2
Melt temperature (p = 0)	T_m (K)	2171	1393
Strength			
Poisson's ratio	ν	0.25	0.3
Intact cohesive strength	Y_{i0} (MPa)	10	20
Intact friction coefficient	μ_i	1.2	1.4
Intact strength limit	Y_{lim} (GPa)	2	2.5
Damaged cohesive strength	Y_{d0} (MPa)	0.01	0.01
Damaged friction coefficient	μ_d	0.6	0.6

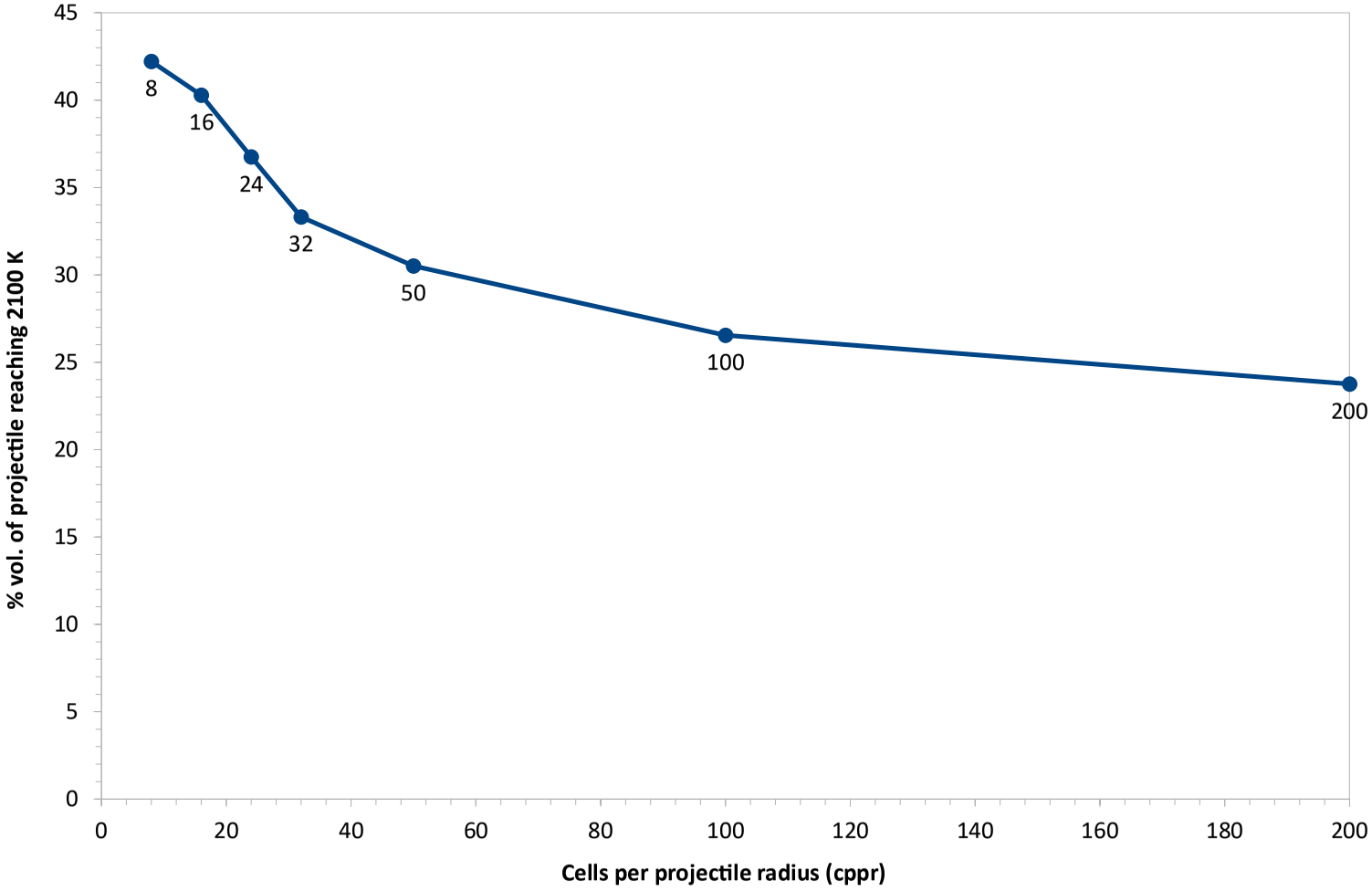

Figure 6.4: *Resolution study for the 2D, vertical impact described in the text, showing the volume (%) of the projectile which reaches a certain temperature (y-axis) at increasing amounts of cells per projectile radius (cppr). Points are labelled with the specific resolution (cppr, x-axis).*

6.2.3 Simulation set-up – 3D

Until recently, due to limitations in the code, target composition was constrained to be the same as the projectile in any 3D simulation. However, targets and projectiles can now be modelled using multiple materials in 3D, implemented using a new version of the iSALE code (Davison *et al.*, 2022). Therefore, simulation of separate equations of state for both the projectile and the target was possible. This allows for more accurate representation of the "real-world" materials for both the CC-like projectile and lunar surface target. Using iSALE-3D (Elbeshausen *et al.*, 2009; Elbeshausen and Wünnemann, 2011), simulations investigated the impact of a 1 km diameter, spherical, CC-like asteroid into a single-layer, basaltic lunar surface. The shape of the projectile may influence the decapitation process at lower velocities, as heating is limited mainly to the lower hemisphere of the projectile (Davison *et al.*, 2010). However, the simulations did not include any alternative projectile shapes in order to limit the computational time it would take to run multiple simulations with similar set-up parameters. Simulations were carried out on the Kathleen High-Performance Computing (HPC) Facility at University College London (Kathleen@UCL), designed for high performance, large-memory computer jobs. The simulations had resolutions of 16 cells per projectile radius, chosen as a compromise between calculation of temperatures in the projectile and the computational time taken to run each simulation. The ANEOS serpentine EoS (Brookshaw, 1998) was used to best approximate CM CC-material and the ANEOS basalt EoS (Pierazzo *et al.*, 2005) to represent the lunar surface. Initially, porosity was included in both projectile (40%) and target (10%), with porosities chosen based on average values for CC parent bodies (Veverka *et al.*, 1999; Britt *et al.*, 2002; Chesley *et al.*, 2014; Lauretta *et al.*, 2015; Sugita *et al.*, 2019) and the lunar megaregolith (Wieczorek *et al.*, 2013). The same thermal, strength, and damage parameters were used as in the 2D modelling, detailed in Table 6.2. Impact velocities of 5, 10, and 15 km s^{-1} were tested, with impact angles varied between 15 and 60º to the horizontal, at 15º increments (Table 6.3). Whilst the average impact velocity for asteroidal bodies striking the Moon has been calculated to be between 14 and 19.7 km s^{-1} (Chyba, 1991; Ivanov, 2001; Marchi *et al.*, 2009; Le Feuvre and Wieczorek, 2011), impacts at 5 and 10 km s^{-1} are possible and estimated to occur ~1% and ~5% of the time, respectively (Marchi *et al.*, 2009). It has been suggested that impacts with velocities between 5 and 10 km s^{-1} could make up to 26% of all Earth-crossing asteroid collisions with the Moon (Chyba, 1991). Lagrangian tracer particles were placed in each cell of the projectile to track temperature, pressure, velocity, and the location of the material over the course of the impact. A gravitational acceleration of 1.62 m s^{-12} was applied across the scenarios, consistent with that of the lunar surface. The simulations were run on the Kathleen HPC to a maximum simulated time of 25 seconds after impact, allowing the creation of the transient crater which, for most cases, had begun to reach a maximum volume.

6.2.4 Overcoming issues in 3D simulations

At the end of the simulation there was a large proportion of high-velocity, projectile ejecta still travelling away from the impact site. Due to the importance of the location of surviving projectile material in terms of suitability as an exploitable resource, the subsequent motion and emplacement on the Moon of this material was approximated using equations of ballistic motion. This was achieved by identifying the launch position and ejection velocity vector of each projectile tracer at some point before the end of the simulation and then applying constant acceleration formulae to approximate the time of flight and landing location. In theory, if the projectile material is moving ballistically before the end of the simulation, ballistic projection should produce the same results regardless of the time and position of "launch." However, as different parts of the projectile begin ballistic motion at different times, it is difficult to define a simple protocol for the moment of launch. In addition, tracer particles in the iSALE3D simulation can become separated from the material that they represent owing to errors in velocity interpolation and end up in a stationary void above the target. At this point, the tracer particle can no longer track its material and stops moving.

The optimised solution adopted in this work included multiple iterations of ballistic projection for different parts of the simulation (example script can be found in Appendix A6). Firstly, any projectile material with an upward motion crossing the elevation of the pre-impact surface ($z = 0$ m) was projected forward, using tracer particles to track when material crossed the defined threshold. The (x, y, z) coordinates for tracers were found before and after crossing the threshold and then combined with the three components of the material's velocity. These parameters were then used to find the time of flight of the ejecta to the point at which it returned to the lunar surface (assumed to be $z = 0$ m). This time of flight was combined with the original tracer position and the velocity at the time it crossed the threshold to calculate a final landing location on the lunar surface.

Secondly, any projectile material found within the transient crater, below the pre-impact surface, that experienced an upward motion by the end of the simulation was projected from the last point at which its velocity was defined. Due to the location of these tracers within the crater and the fact that the cratering process was incomplete by the end of the simulations, it is difficult to accurately predict where this particular set of tracers are likely to end up. These tracers may not have been moving ballistically at the time of projection. The exact size of the final crater is uncertain, and the velocity of this material may not propel any ejecta beyond the crater rim. Therefore, the material from within the crater was projected from the point at which the upwards velocity was at a maximum and projected back to the same height (z-axis value) from

which it was projected. This is likely a simplification of the reality and, therefore, the ballistically projected material is a best estimate of the final location.

Lastly, some projectile material was found downrange of the transient crater, had never experienced an upward motion, and was located beneath the pre-impact surface by the end of the simulation (especially in the 15° impacts). This is interpreted as projectile material that scours the lunar surface, and this material was plotted at its final location in the simulation. Any material that achieved a velocity greater than the escape velocity of the Moon (2.38 km s^{-1}) whilst experiencing an upward trajectory was removed from the calculations. Peak shock temperatures for the ballistically projected tracers were then compared to vaporization temperatures for known carbon and nitrogen bearing molecules in CCs (Table 6.4).

Table 6.3: *Names assigned to each of the 12 different scenarios covered by this suite of simulations by varying impact velocity and angle.*

	Velocity (km s^{-1})		
Angle (°)	5	10	15
15	a15_v5	a15_v10	a15_v15
30	a30_v5	a30_v10	a30_v15
45	a45_v5	a45_v10	a45_v15
60	a60_v5	a60_v10	a60_v15

Table 6.4: *Abundances of C-bearing materials found in a range of CM/CI meteorites (Murchison, Murray and Orgueil) and the average abundances of N-bearing molecules found in CM samples (Murchison and Murray). Associated vaporisation temperatures included for both C- and N-bearing molecules.*

Carbon type	**Abundance (wt.%)** [1-3]	**Vaporisation temperature (K)**	**Nitrogen type**	**Abundance (ppm)** [6]	**Vaporisation temperature (K)** [7]
Organic matter	0.6-2.3	550-750 [1]	Glycine	4.5	525
Carbonate	0.2 (Av.)	700-1000 [1]	Glutamic acid	2.3	700
Diamond	0.03-0.15	4000 [4]	Aspartic acid	1.7	600
Graphite	0.001-0.005	4000 [4]	Glutamine	1.1	850
Silicon carbide	0.001-0.009	3000 [5]			

[1] Huss & Lewis, 1994. [2] Russell *et al.*, 1996. [3] Sephton, 2002. [4] Bundy, 1989. [5] NIOSH, 2019. [6] Cronin & Moore, 1971.
[7] Weiss *et al.*, 2018.

6.3 Results

The melt temperature of the projectile material (serpentine), defined in Section 6.2 as ~2100 K (Brookshaw, 1998), is used as a conservative estimate for the survival of the hardiest C-bearing compounds (SiC/diamond/graphite). Assuming the computational cells in the projectile remain beneath this temperature, surviving material will remain (at least partly) solid and is more likely to remain *in situ* once landed after impact. This is not to say that C and N when subjected to these temperatures (either in projectile melt material or as vapour that recondenses) will not remain at the impact site, but there is less certainty as to where surviving material will come to rest with increased mobility as in liquid versus solid material. Surviving projectile material that experiences temperatures less than the melt temperature is compared with the vaporisation temperatures of the molecules in Table 6.4.

Different types of C-bearing molecules were chosen based on their abundance within a range of CI/CM meteorites (specifically samples from Murchison, Murray, and Orgueil) and the vaporisation temperature. Organic matter was chosen based on the relatively high abundance in the aforementioned CC samples (up to 2.3 wt.%), despite the relatively low vaporisation temperatures (550–750 K). Carbonates strike a compromise between abundance (an average 0.2 wt.%) and vaporisation temperature (700–1000 K). Despite abundances in the parts per million (ppm) range, carbon found in CCs as diamonds, graphite, and silicon carbide were chosen based on their resilience to high temperatures. Diamonds and silicon carbide, in particular, are known to withstand incredibly high pressures and have vaporisations temperatures up to 4000 K. Molecules chosen to investigate nitrogen survival were all amino acids found in CM samples Murchison and Murray. These are different from the amino acids considered in Chapter 5 (aside from glutamine) as they have been specifically picked for their known abundances in CC material recovered and investigated in samples. Glycine has a relatively high average abundance of 4.5 ppm, but a lower vaporisation temperature to the other amino caids chosen. Glutamine provides the N-bearing molecule with the highest resistance to temperature, with a vaporisation temperature of 850 K.

Amino acids can undergo thermal decomposition into constituent molecules at temperatures much lower than the vaporisation temperatures quoted in Table 6.4. Decarboxylation (the loss of CO_2 after heating) and deamination (the loss of an amino group, usually changing to ammonia NH_3) could lead to reduced masses of carbon and nitrogen in the CC material before reaching the quoted “vaporisation temperatures”. However, thermochemical experiments studying the thermal decomposition of multiple amino acids in temperatures up to 600 K showed no emission of CO_2 (Weiss *et al.*, 2018) and only some NH_3. In these experiments, glycine began decomposition at ~525 K, losing mass to gaseous products

(H_2O, NH_3, HCNO) above this temperature. Glutamic acid begins decomposition at ~475 K, but only undergoes a dehydration reaction producing H_2O and pyro-glutamic acid. No CO_2 or NH_3 production was detected, and the dehydrated glutamic acid has a well-known boiling point of ~700 K. Aspartic acid only loses H_2O during two stages of decomposition at ~500 K and ~525 K. The amino acid remains a powder up to ~575 K, therefore a conservative estimate of 600 K is used as the vaporisation temperature. Glutamine begins decomposition at ~460 K, where NH_3 is lost and γ-glutamylglutamine is produced. This reaction would potentially lose a quarter of the original nitrogen in the glutamine, however the γ-glutamylglutamine has a very high boiling point of ~860 K. Therefore, the vaporisation temperature quoted in Table 6.4 (850 K) could potentially lead to overestimates in the amount of nitrogen survived after a CC impact, but it is assumed that if the surrounding CC material does not melt or vaporise, the lost NH_3 will remain trapped in the CC material. This concludes the justification for the vaporisation temperatures used for amino acids in Table 6.4, by considering the purely thermochemical decomposition pathways experimentally verified by Weiss *et al.* (2018).

The proportion of C and N that is likely to be present in the remaining material is estimated in the particular simulation scenario and converted to a mass in kilograms, based on the original mass of the impactor. Any C and N bearing molecules that have experienced higher temperatures than their respective vaporisation temperature are assumed to be lost as a useful resource. However, this does lead to a potential underestimation of the amount of surviving C or N, because it neglects any material that may have recondensed after vaporisation. Also, this work predominantly uses the peak temperature reached within any cell in the projectile at any time during the simulation, which generally lasts for less than one timestep, 0.5 s. Whether the molecules are able to completely vaporise during that time is a question beyond the scope of iSALE and this study, so it is assumed that they do. Therefore, the definition of 'surviving' material containing C and N used here is inherently an underestimate.

Despite some of the projectile ejecta being ballistically projected many hundreds of kilometres away from the impact site (especially in the high velocity simulations), the projectile survival plots are restricted to 50 km downrange and 10 km either side of the impact point (Figures 6.5 and 6.6). This is to emphasise and focus on the material that concentrates in larger masses closer to the impact, rather than encompass all of the landed projectile material which may spread over thousands of square kilometres in less dense concentrations unsuitable and unviable in terms of resource potential. Additionally, the far-reaching ejecta inherently experiences very high velocities in order to reach a distant final location and therefore experiences high shock, resulting in peak temperatures exceeding that of the material melt temperature. Much of this distant ejecta is therefore unsuitable for carbon and nitrogen survival as a consequence.

The full set of data used to inform these results can be found in the electronic appendix under the filename "Ch6_CC_model_data".

6.3.1 Projectile survival – temperature and location

The majority of projectile material remains solid at low impact velocity (5 km s^{-1}) for any projectile impact angle. Similarly, 15º impacts allow for solid material survival at any velocity. All material melts or vaporises in the other scenarios (Table 6.5). Impacts with velocities >10 km s^{-1} and angles >30° do not yield any solid material. Figures 6.5 and 6.6 show the temperatures and location of projectile material on the lunar surface after impact, as seen from looking down over the surface (plan view), for the highlighted scenarios in Table 6.5. Figures 6.5a-c show the results for the scenarios with the most oblique impact angle (15°) at increasing velocities (5, 10, and 15 km s^{-1}, respectively). The only scenario where N-bearing molecules may survive in significant quantities is a15_v5 (Figure 6.5a). Approximately 16% of the original projectile mass experiences temperatures less than 700 K, suitable for the survival of most of the carbon species and many of the amino acids that contain nitrogen. In particular, glutamine and glutamic acid (with vaporisation temperatures of 850 K and 700 K, respectively) would both survive well, with little loss of carbon or nitrogen due to decomposition or vaporisation. Over 48% of the projectile material experiences temperatures <1000 K and ~85% of the material remains solid, with maximum peak temperatures of <2100 K at any time in the projectile. Some higher temperature material (peak temperatures >1500 K) is found closer to the impact site, spread in a triangle-like pattern, immediately downrange of the crater. A small amount of material does remain within the transient crater, but the temperatures exceed 2000 K and would, therefore, be unlikely to hold much resource value. Most projectile ejecta is deposited as part of the proximal ejecta blanket on the surrounding lunar surface. The material subject to the highest temperatures (2400 K) is not found within the crater itself, but rather many hundreds of km downrange of the impact site as a component within the distal ejecta.

Whilst these results indicate that some C- and N-bearing materials can remain as solid components after impact delivery, this is only one of the two key factors determining the usefulness of CC material as a resource. The second factor, location of surviving material, is equally important. In general, increasing the impact velocity or the impact angle leads to greater proportions of material landing outside of the crater. The vast majority of the surviving material suitable for the survival of nitrogen bearing molecules (<700 K, dark purple, Figure 6.5a) is found concentrated in a small area beginning ~20 km downrange of the original impact site. This zone of material extends to ~30 km downrange and is confined to a width of <6 km (dark "wedge" of material confined to ~3 km either side of y = 0, Figure 6.5a), and equates to being spread

over an area of ~60 km^2. Upon impact, some of the projectile material separates after initial contact with the lunar surface and travels further downrange with reduced velocity. This reduced velocity and "cushioning" of the projectile after impact has led to lower peak temperatures experienced by the material and a relatively quick deposition closer to the point of impact, compared to many of the more distant tracer particles. As previously described (Figure 6.1), this is a demonstration of projectile decapitation (Davison *et al.*, 2011), which produces a scenario from which a much more suitable "cache" of concentrated materials could be considered as a resource. The area of the projectile from which this decapitated material is sourced from is shown in Figure 6.7a, using a provenance plot of where the material lands after impact, superimposed on the initial projectile shape. The plots in Figure 6.7 display the final location of any projectile material at the particular x, z coordinates through the cross-section and so represent the general shape of the labelled zones. Figure 6.7a shows how the decapitated zone is sourced from the top of the projectile and extends down towards the middle of the projectile but does not reach the bottom. Additionally, with the initial site of impact being the lower left corner of the spherical projectile, the lower left face is dominated by material that is ejected beyond the area where decapitated material is deposited. This ejected projectile material, below the decapitated zone shown in Figure 6.7, impacts into the target immediately after contact and much of the material rebounds off and away from the transient crater. The small amount of material that remains within the transient crater during this scenario is concentrated at the lowest point at back of the projectile, far from the initial point of impact.

Figure 6.5b shows the results for scenario a15_v10, where the increased velocity has decreased the amount of surviving material subjected to low temperatures. A minimum temperature of 800 K is experienced by all of the projectile, with just ~3% of the original projectile volume experiencing temperatures <1000 K. These temperatures would potentially be suitable for the survival of some carbonate species and even glutamine, according to the vaporisation temperatures in Table 6.4. The more durable C-bearing molecules will likely survive in the majority of the landed projectile, with 58% of the material remaining solid. However, increasing the velocity along with such a low angle of impact has also caused the projectile material to spread over a larger area.

Table 6.5: *Percentage of 40% porous CC projectile material that remains solid after impact, based upon peak temperatures reached within the projectile at any time during the simulation. Green = solid material survival, orange = no solid material survival. Green scenarios are highlighted with projectile plots in Figures 6.5 and 6.6.*

Angle (°)	**Velocity (km s^{-1})**		
	5	10	15
15	85%	58%	21%
30	74%	0%	0%
45	65%	0%	0%
60	57%	0%	0%

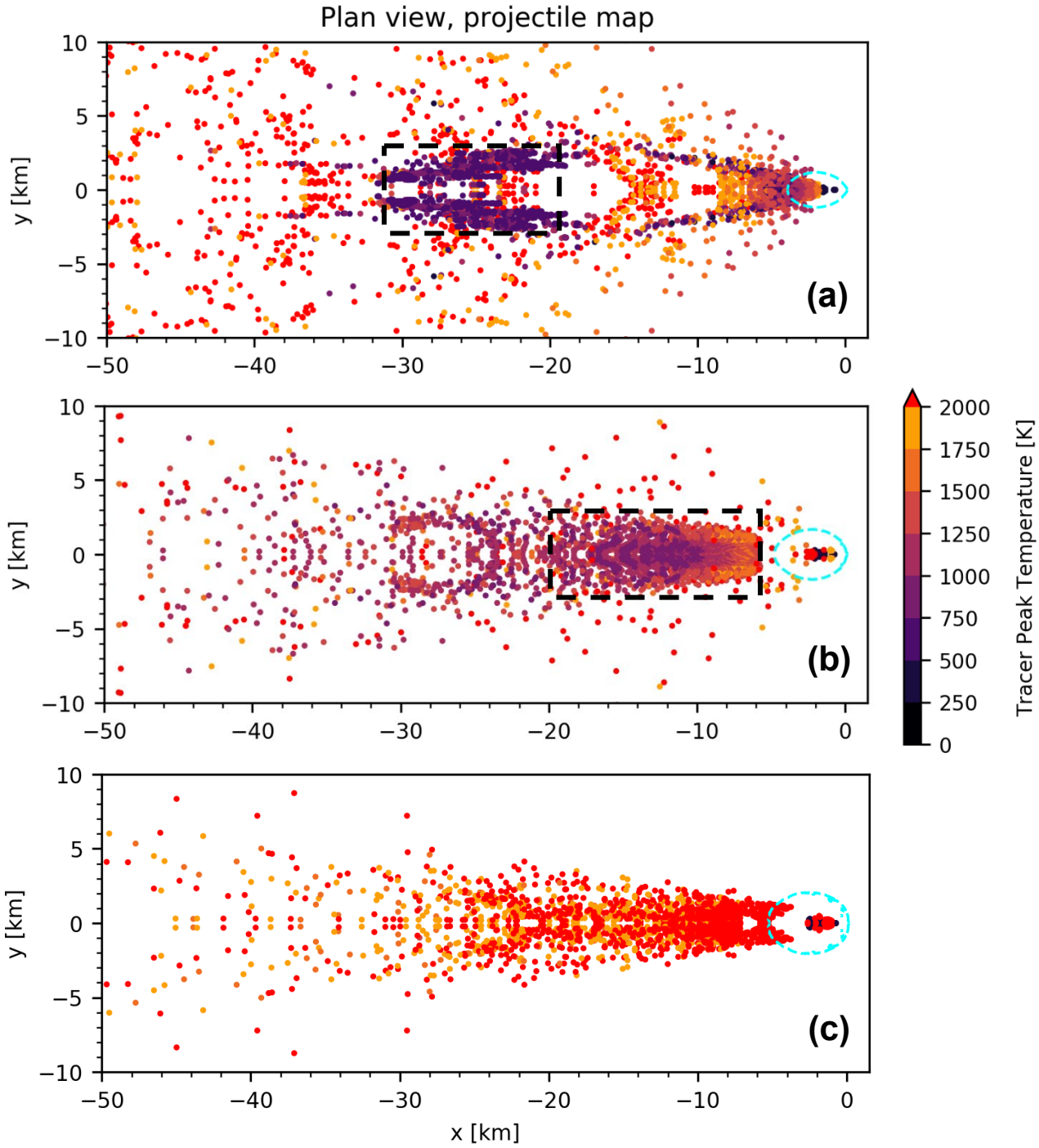

Figure 6.5: *Peak temperature and location plots of the fate of a 1 km diameter projectile (initial porosity = 40%) following impact on the lunar surface in scenarios (a) a15_v5, (b) a15_v10, and (c) a15_v15. Each tracer represents a cube of projectile material with an initial dimensions 31.25×31.25×31.25 m. Blue dashed line shows the approximate location of the transient crater rim. Direction of impact is from right to left, with the initial impact point located at [0,0]. Black dashed areas highlight the zones used for resource evaluation in Figures 6.8 and 6.9, and Table 6.7.*

Increasing the velocity further to 15 km s^{-1} (Figure 6.5c, a15_v15) results in minimum temperatures of ~1400 K and just ~21% of the projectile volume remaining solid after impact. This material is concentrated as a cone shape extending from the point of impact to ~30 km downrange, becoming sparser with distance from the impact. All of the amino acids considered would be vaporised in this scenario and the only C-bearing molecules to survive in significant quantities would be the most durable (SiC/graphite/diamond). Much of the melted material concentrates within 20 km downrange of the impact and overlaps lower temperature material (1500 K) in the area between 10 and 20 km downrange. This could cause impact melt to cover potentially viable solid material and make the process of finding and using said material more challenging from a resource perspective.

Less oblique impact angles lead to higher peak temperatures across a greater proportion of the projectile volume but concentrate much of the surviving projectile material within or directly surrounding the craters. Figure 6.6 demonstrates this effect, with the increase in impact angle (30º to 45 º to 60º) for the same impact velocity (5 km s^{-1}). At 30º (Figure 6.6a), temperatures reach a maximum of 2700 K, with almost three-quarters of the projectile remaining solid (Table 6.5). A small, but not insignificant, volume of the projectile records temperatures <1000 K (~1%). However, the majority (~50%) of the projectile experiences peak temperatures over 1800 K. Surviving projectile material is spread over a large area in both the x and y directions, however much of the mass is concentrated directly outside of the crater, especially compared to more oblique impacts at 15º. Ejecta deposition within the crater favours the downrange wall, with a lack of deposition behind the initial impact point. This is concurrent with combination of the impact velocity, direction, and angle, as the relatively slow impactor allows for material to be deposited within the crater without escaping. The comparison to the more oblique impact angle at the same velocity (simulation a15_v5, Figure 6.5a), shows the impact that an increase in 15° can have on the proportion of material that can remain within the crater.

Further increasing impact angle to 45º (Figure 6.6b), more material begins to concentrate within the crater, with minimum temperatures of 1600 K, and at 60º even less solid material survives. Figure 6.6c shows how the increase in impact angle decreases both the total amount of surviving, solid material (Table 6.5) and the amount of solid material outside of the crater. Increasing the impact angle in these simulations leads to the deposition of projectile material over a wider area of the target surface, particularly in the y-direction. Maintaining the same impact velocity (5 km s^{-1}) but increasing the impact angle steadily broadens the deposition pattern in the y-direction. Extending this angle to 45° and 60° further accentuates this trend, with projectile ejecta depositing further and further into the back of the transient crater, almost in-line with the initial impact site in Figure 6.6b and beyond in Figure 6.6c. Additionally, increasing the impact

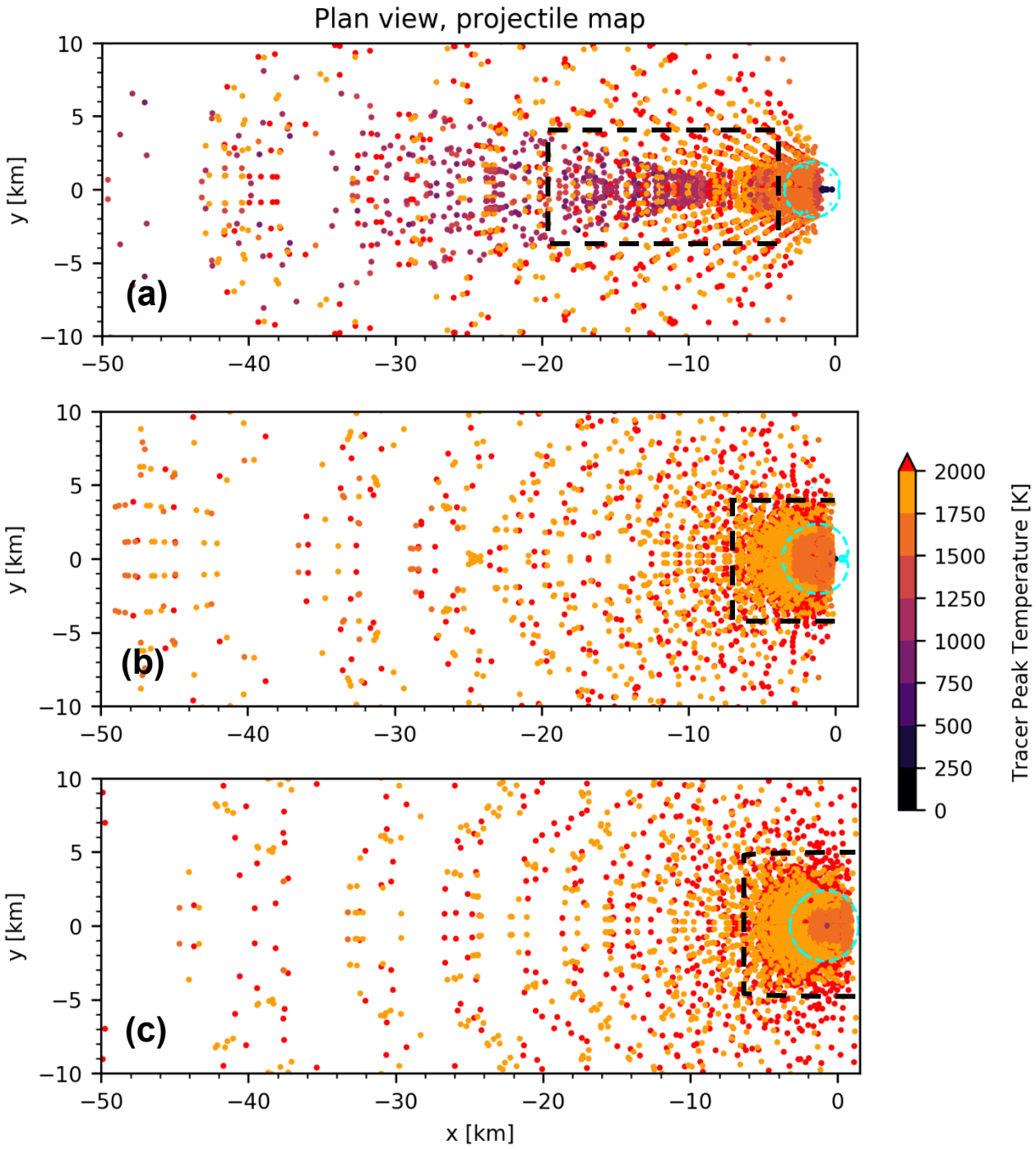

Figure 6.6: *Peak temperature and location plots of the fate of a 1 km diameter projectile (initial porosity = 40%) following impact on the lunar surface in scenarios (a) a30_v5, (b) a45_v5, and (c) a60_v5. Each tracer represents a cube of projectile material with an initial dimensions 31.25×31.25×31.25 m. Blue dashed line shows the approximate location of the transient crater rim. Direction of impact is from right to left, with the initial impact point located at [0,0]. Black dashed areas highlight the zones used for resource evaluation in Figures 6.10, 6.11, 6.12, and Table 6.7. The concentric nature of the ejecta deposition is likely due to the relatively low temporal and spatial resolution of the simulations (further explained in the text).*

angle leads to more sparse deposition in the x-direction, with a banded pattern forming in the least oblique impact scenarios. It is important to note that each of the tracers displayed in these figures is in reality a point representing a larger volume of material. This makes for precise measurement of temperatures and pressures, as well as useful estimation of the final location of the material the tracer represents. However, because the tracer data used to ballistically project material is only saved at every timestep (0.5 s), the tracer location is an averaged location for the material it initially represented, based on the velocity of the material at the launch position and time. As a result, bands of ejecta are produced as an artefact of the relatively low temporal resolution. Therefore, these bands with large gaps between tracers may actually represent areas of highly dispersed projectile material, where the gaps are not in fact empty but may have low concentrations of projectile mass. Scenarios with high masses of melted material may be particularly influenced by this process as the melted material is not likely to deposit as a single point but as a blanket of melt, whereas a piece of solid projectile is more likely to land at one specific point.

Provenance plots for the surviving projectile material displayed in Figures 6.6a–c are shown in Figures 6.7b–d, respectively. The transition away from decapitated projectile material towards the majority of the projectile volume remaining within the transient crater is clear. The angle of the zones where projectile ejecta meets crater-bound material relates well to the angle of impact, especially in scenarios a45_v5 (Figure 6.7c) and a60_v5 (Figure 6.7d).

The relative proportion of projectile material that (i) remains within the crater, (ii) is ejected beyond the crater rim, and (iii) escapes from the Moon are described for each scenario with surviving solid projectile material in Table 6.6.

Table 6.6: *Proportions of projectile volume in their respective final locations after impact for scenarios where solid material survived. Results are rounded to the nearest percent, apart from proportions <0.5% to avoid misrepresentation of a small amount of material that does in fact remain within the craters formed.*

Scenario	**Proportion of projectile material in final location**		
	Landed in crater	Landed ejecta	Escaped
a15_v5	<0.5%	96%	4%
a15_v10	<0.5%	52%	48%
a15_v15	<0.5%	29%	71%
a30_v5	9%	47%	44%
a45_v5	34%	56%	10%
a60_v5	51%	48%	1%

The proportion of material found within the transient crater by the end of the impact clearly increases with increasing impact angle. All of the scenarios with a 15° impact angle hardly retain any material within the transient crater: <1% of the original projectile volume in each velocity tested. In the scenario with the lowest impact velocity (5 km s^{-1}), the vast majority, 96%, of the projectile volume lands on the target surface, with 4% escaping. The combination of increased velocity with this very oblique impact angle leads to a significant increase in the amount of material expected to escape the lunar gravity, rising to 48% at 10 km s^{-1} and 71% at 15 km s^{-1}. This results in a reduction in the mass available as a potential resource as much of the projectile material, even if it remains solid, rebounds off the target and would either be ejected into orbit around the Moon or out into space. Orbiting material may lose energy and re-impact into the Moon at a later time, but it is impossible to say where that material would be found. The escape velocity of the Moon (2.38 km s^{-1}) is comparably much lower than the scenarios with impact velocities >10 km s^{-1}. In a vertical impact, the only component of the impact velocity would be in the negative z-direction, straight down into the target, which would likely lead to most of the projectile material to remain in the crater (given the trend of results in Table 6.6). With the very oblique, 15° impact angle, much of the impact velocity is not only concentrated in the negative z-direction, but also the negative x-direction. Therefore, much of the fast projectile material does not embed into the target and instead can skim off the target surface, translating much of the negative z-component of the velocity into a positive component, without changing the magnitude of the x-component to a significant degree. As escape velocity does not apply to a specific direction (there is no atmosphere on the Moon to travel through), any material with an x- or y- velocity component greater than 2.38 km s^{-1} and a positive z-velocity component of any value will escape to space and be lost. This is why we see the significant increase in the proportion of escaped material for the a15_v10 and a15_v15 scenarios, compared to the slower a15_v5.

Increasing the impact angle to 30° with a 5 km s^{-1} velocity results in 9% of the projectile within the crater, further increasing to 34% and 51% for the 45° and 60° impacts, respectively. The shift of the predominant component of velocity from the x-direction to the z-direction is very clear, with escaped material reducing from 44% at 30° to 1% at 60°. At an impact angle of 60°, landed projectile material concentrates relatively equally inside and outside the transient crater rim (51% and 48%, respectively). However, much of the material outside of the crater concentrates in the ejecta immediately surrounding the crater rim, as shown in Figure 6.6c. The scenarios with the greatest proportion of total landed material are a15_v5 and a60_v5 (over 96%), whilst scenario a15_v15 provides the least (30%).

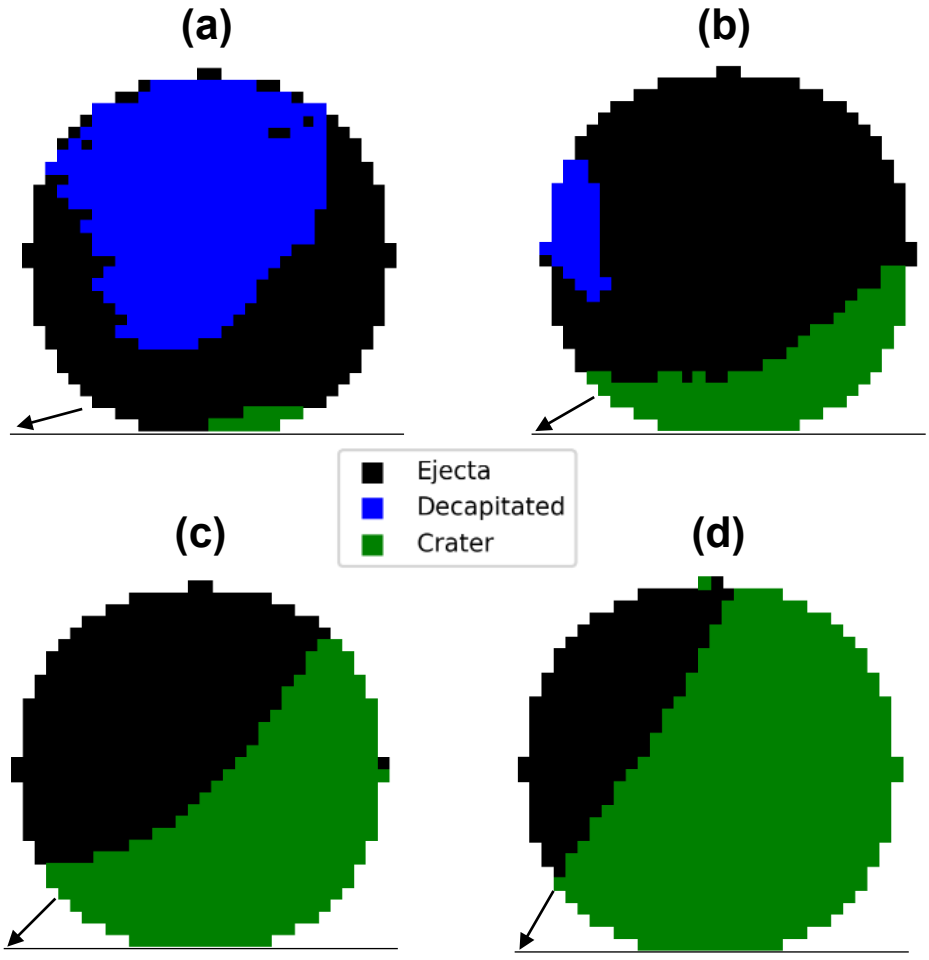

Figure 6.7: *Averaged provenance plots showing where different volumes of the projectile material are predicted to land by the end of the impact process for simulations (a) a15_v5, (b) a30_v5, (c) a45_v5, (d), a60_v5. These plots display the averaged final location when looking through the projectile and as such are not cross-sections along the y=0 axis. Black arrow represents impact angle and direction.*

6.3.2 Nitrogen and carbon survival

The following section specifically addresses the questions regarding the mass and location of viable material for C- and N-bearing molecules for the scenarios described in the previous section. These mass calculations are based on the mass of the 40% porous, 1 km diameter, serpentine material impactor used (~7.6×10^{11} kg) and therefore, only represent the masses for this particular impactor. The discussion on surviving carbon assumes all of the C-bearing phases respond to temperature in the same way, simplifying the calculations regarding surviving masses of carbon. In reality, organic C- (both soluble and insoluble) and inorganic C-bearing phases would be influenced by temperature in different ways, but this is beyond the scope of this work and would make an interesting topic for future work. Therefore, the calculated masses of surviving carbon should be taken as an estimate based on a simplification of the different phases of carbon.

The only scenario where N-bearing projectile material is both likely to survive based on the recorded peak temperatures and is confined to a reasonable area after impact is simulation a15_v5. This is the area highlighted in Figure 6.5a, where the dark purple data points (representing material recording temperatures <750 K) are concentrated, 20–30 km downrange of the transient crater. The material is referred to as the decapitated portion of the impactor. Figure 6.8 depicts the maximum temperatures reached within the total mass of material in this decapitated portion. Approximately 3×10^{10} kg of material in this region experiences temperatures suitable for the survival of glutamic acid (<700 K), with up to 7×10^{10} kg experiencing temperatures suitable for glutamine (<850 K). Organic carbon, the form of carbon with the highest wt.% in CCs (Table 6.4) is likely to survive in ~5×10^{10} kg of the decapitated projectile, with temperatures suitable for carbonate survival in ~8×10^{10} kg. Over 99% of this material in the decapitated projectile records peak temperatures less than the melt temperature of the material meaning it will likely remain in the area it lands and preserve most of the carbon originally found in this portion the CC impactor.

Figure 6.9 shows similar data for scenario a15_v10, focusing on the concentrated trail of ejecta from the edge of the transient crater rim extending to ~20 km downrange and ~3 km either side of the trajectory plane (y = 0). The total mass of material is approximately double that found in the decapitated projectile material in Figure 6.8. However, the lowest temperature experienced is >800 K and only 1.5×10^{10} kg of material records temperatures <1000 K, suitable for carbon survival in the form of carbonates and the more resilient carbon forms such as silicon carbide and graphite. The high proportion of escaped material and high temperatures recorded by tracers for scenario a15_v15 (highlighted in Figure 6.5c) leads to a distinct lack of resource viable material. Therefore, these results are neglected from further analysis.

Moving on to the less oblique impacts with surviving solid impactor material, Figure 6.10 highlights the resource potential of scenario a30_v5. At this point, and for the following scenarios with increasing impact angles, temperatures in areas where material concentrates into useful, resource viable areas become too high for amino acids to survive without considerable threat due to vaporisation. The lowest temperatures are found in the proximal ejecta, with ~2.2×10^{9} kg of material experiencing temperatures <1000 K and landing in the light purple cone of ejecta shown between ~10 and 20 km downrange of the impact site in Figure 6.6a. Including the material directly beyond the crater rim, ~4.8×10^{10} kg of impactor remains solid when deposited outside of the crater. For the proportion that remains within the crater this mass of solid material is reduced to ~4.2×10^{10} kg, most of which is concentrated on the downrange crater wall with very little beyond the middle of the crater floor. When proximal ejecta (<20 km downrange) and crater material are combined, this essentially concentrates ~9×10^{10} kg of solid, surviving projectile material into an area of <160 km^2. The total mass of material in each area at any temperature recorded is less in the crater than the proximal ejecta (6.4×10^{10} kg and 8.5×10^{10} kg, respectively).

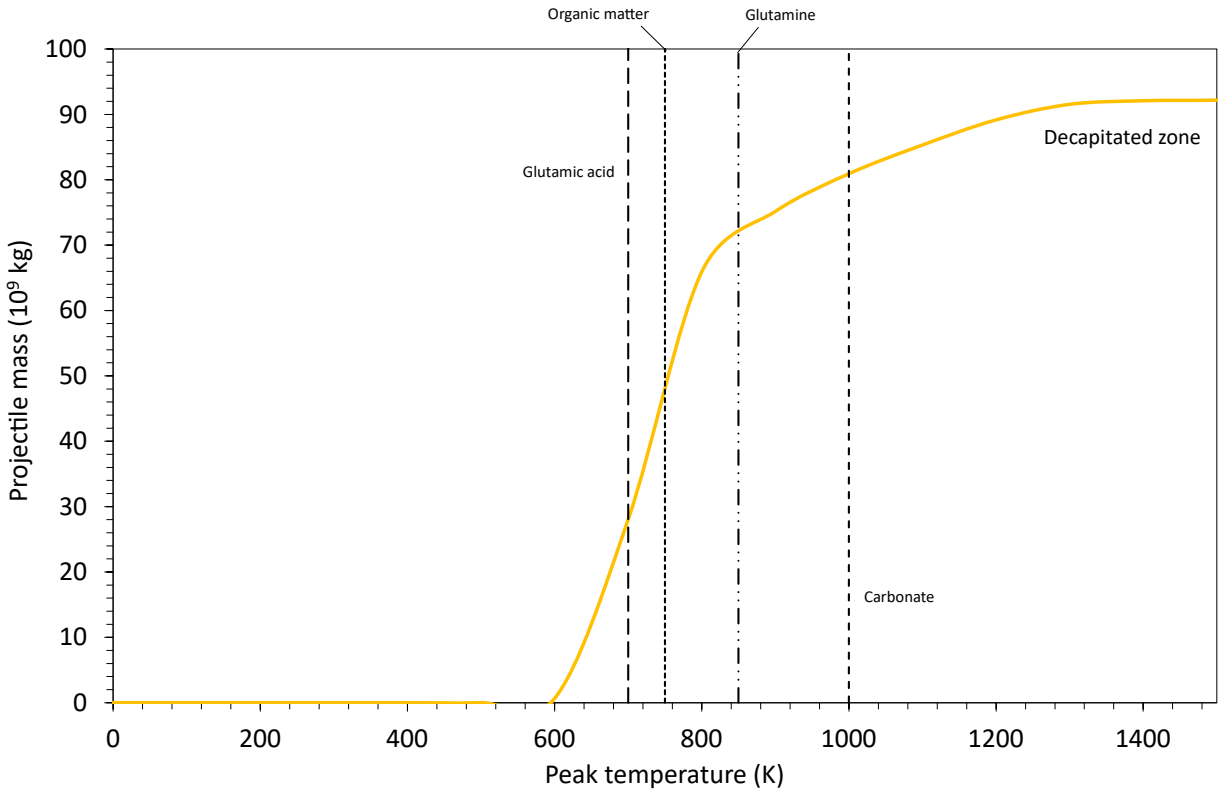

Figure 6.8: *Total mass of the decapitated portion of the projectile highlighted in Figure 6.5a, simulation a15_v5, plotted against the peak temperature recorded for a given cumulative mass. Vaporisation temperature thresholds for relevant molecules from Table 6.4 (references available within this table) are plotted with dashed lines and individually labelled.*

Transitioning from an impact angle of 30° to 45° has a significant effect on the proportion of material found inside and directly outside the crater (see Figure 6.11). The total mass of impactor remaining within the crater (~2.6×10^{11} kg) is significantly more than that which is found in the proximal ejecta (4.5×10^{10} kg), the area immediately surrounding the crater concentrated ~7 km downrange and ~4 km either side of the impact point (Figure 6.6b). Minimum temperatures within the crater are ~1600 K, lower than those in the proximal ejecta, ~1800 K. Clearly, any N-bearing amino acids or similar molecules are very unlikely to survive at these temperatures and the most likely C-bearing molecules remaining with any resource potential within these zones are silicon carbide, diamond, and graphite. Solid material comprises ~1.6×10^{11} kg in the crater and ~2.8×10^{10} kg in the proximal ejecta.

The trend is further exaggerated in the final simulation with surviving solid material, scenario a60_v5 (Figure 6.12). The increased impact angle further concentrates impactor material into the crater, with a total mass of ~3.9×10^{11} kg. Minimum temperatures are >1700 K and solid material within the crater comprises a mass of ~2.5×10^{11} kg. This is ~9×10^{10} kg more than in scenario a45_v5, concentrating a larger mass of material within the crater as a viable carbon resource. Outside of the crater rim, the proximal ejecta (describing material concentrated up to 6 km downrange and 5 km either side of the impact point in Figure 6.6c) experiences similar minimum peak temperatures, >1800 K and a solid component with a mass of ~4.1×10^{10} kg.

For a generalisation of the mass of carbon and nitrogen that might be found at the locations described above, Table 6.7 shows results based the masses of impactor at each location. For the total expected masses of surviving carbon and nitrogen, the mass of projectile material that experiences temperatures below the melt temperature (2100 K) is combined with average values for carbon and nitrogen abundances found in CI meteorites (6 and 0.6 wt.%, respectively) from Pearson *et al.* (2006). More conservative estimates of the total carbon and nitrogen are calculated for CM meteorites (using the same temperature threshold) to represent lower C- and N- bearing meteorite types (2.7 and 0.11 wt.%, respectively). These calculations assume that even if some carbon or nitrogen species vaporise because of the high temperatures, they do not escape the solid projectile material after impact or they all recondense fast enough to not be lost to space. Additionally, surviving masses for all of the individual molecules described in Table 6.7 are calculated based on the specific proportion and vaporisation temperature for each molecule. This will give an overview of the resource potential for each zone and the type of molecule that survives after impact.

Table 6.7: *Estimated masses of projectile material in their respective final locations after impact, for scenarios where solid material survived. Estimations for the total masses of C and N are calculated using the mass of surviving solid material experiencing temperatures <2100 K, the material melt temperature. This mass is multiplied by the average wt.% of C and N in CI and CM meteorites (Pearson et al., 2006). The vaporisation temperatures of individual C- and N-bearing molecules (taken from Table 6.4) are combined with the mass of material that remains below this temperature threshold at each location to find the surviving mass of each molecule.*

		Masses of carbon and nitrogen predicted to survive at each location (kg)												
Scenario	**Location**	**Total C in CI**	**Total C in CM**	**Total N in CI**	**Total N in CM**	**Organic matter**	**Carbonate**	**Diamond**	**Graphite**	**Silicon carbide**	**Glycine**	**Glutamic acid**	**Aspartic acid**	**Glutamine**
a15_v5	Decapitated zone	5.71×10^{9}	2.57×10^{9}	5.71×10^{8}	1.05×10^{8}	6.44×10^{8}	1.62×10^{8}	1.43×10^{8}	4.76×10^{6}	8.56×10^{6}	0	6.44×10^{4}	1.09×10^{3}	7.25×10^{4}
a15_v10	Decapitated zone	1.23×10^{10}	5.54×10^{9}	1.23×10^{9}	2.26×10^{8}	5.66×10^{7}	3.13×10^{7}	3.08×10^{8}	1.03×10^{7}	1.85×10^{7}	0	0	0	0
a30_v5	Crater	2.49×10^{9}	1.12×10^{9}	2.49×10^{8}	4.57×10^{7}	0	0	6.23×10^{7}	2.08×10^{6}	3.74×10^{6}	0	0	0	0
	Proximal ejecta	2.88×10^{9}	1.30×10^{9}	2.88×10^{8}	5.29×10^{7}	4.19×10^{6}	4.39×10^{6}	7.21×10^{7}	2.40×10^{6}	4.33×10^{6}	0	0	0	2.00×10^{2}
a45_v5	Crater	9.57×10^{9}	4.31×10^{9}	9.57×10^{8}	1.76×10^{8}	0	0	2.39×10^{8}	7.98×10^{6}	1.44×10^{7}	0	0	0	0
	Proximal ejecta	1.69×10^{9}	7.59×10^{8}	1.69×10^{8}	3.09×10^{7}	0	0	4.22×10^{7}	1.41×10^{6}	2.53×10^{6}	0	0	0	0
a60_v5	Crater	1.48×10^{10}	6.64×10^{9}	1.48×10^{9}	2.70×10^{8}	0	0	3.69×10^{8}	1.23×10^{7}	2.21×10^{7}	0	0	0	0
	Proximal ejecta	2.43×10^{9}	1.10×10^{9}	2.43×10^{8}	4.46×10^{7}	0	0	6.08×10^{7}	2.03×10^{6}	3.65×10^{6}	0	0	0	0

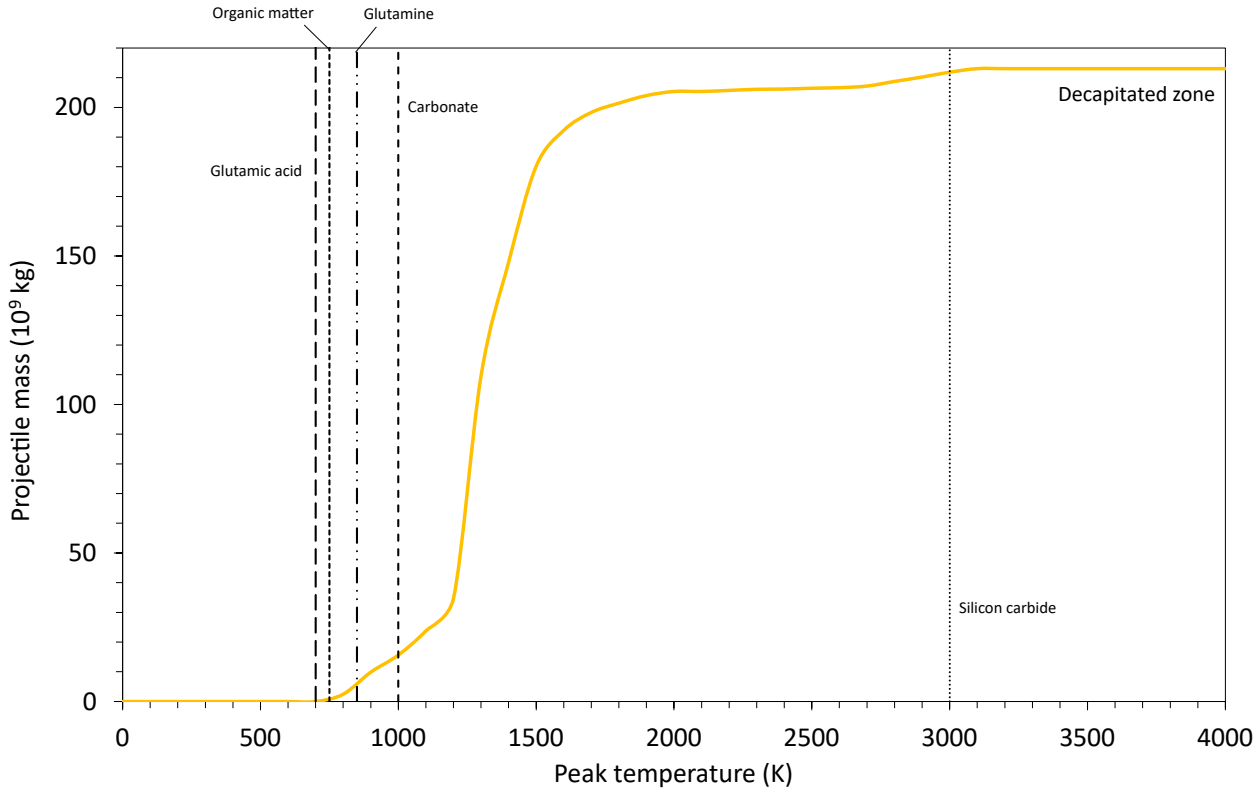

Figure 6.9: *Total mass of the projectile material landed directly downrange from simulation a15_v10 plotted against the peak temperature recorded for a given total mass. This plot represents material highlighted 20 km downrange and 3 km either side of the impact point in Figure 6.5b. Vaporisation temperature thresholds for relevant molecules from Table 6.4 are plotted with dashed lines and individually labelled.*

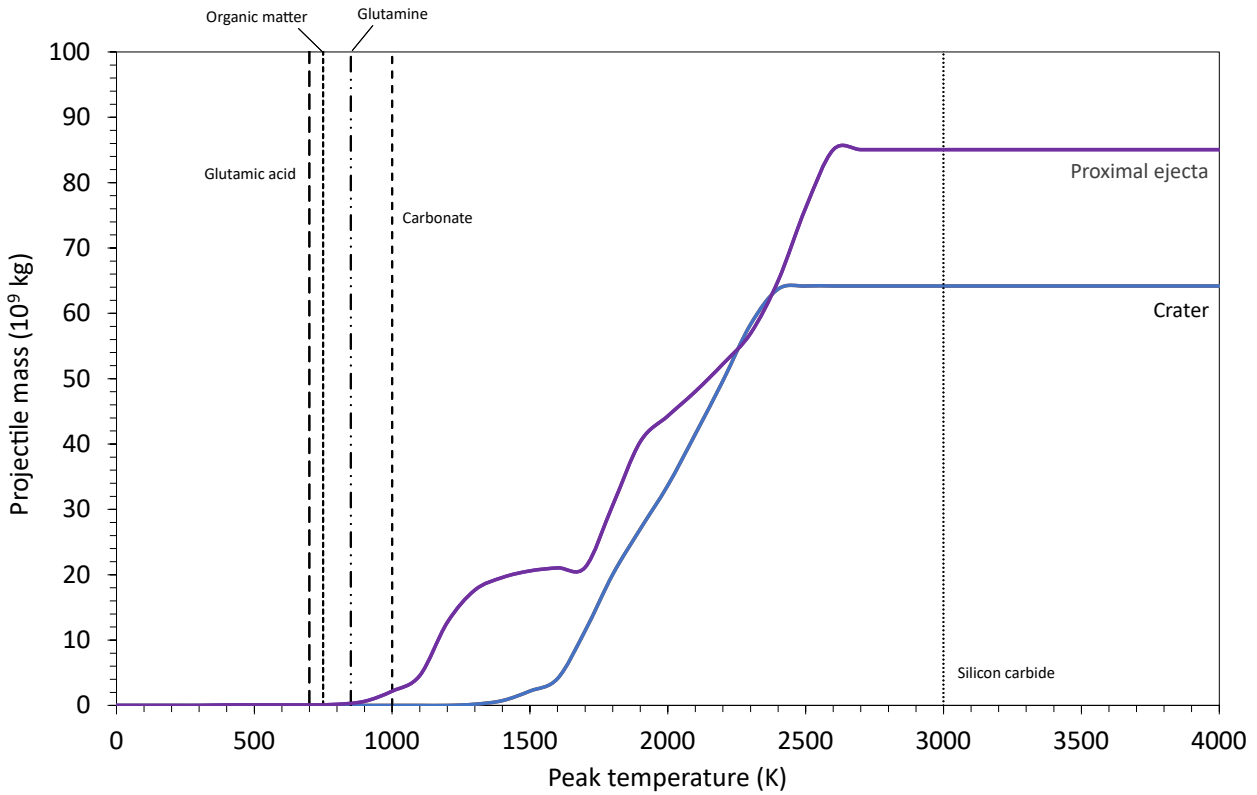

Figure 6.10: *Total mass of the projectile material landed in the proximal ejecta and crater from simulation a30_v5 plotted against the peak temperature recorded for a given total mass. The proximal ejecta describes material highlighted 20 km downrange and 4 km either side of the impact point in Figure 6.6a. Vaporisation temperature thresholds for relevant molecules from Table 6.4 are plotted with dashed lines and individually labelled.*

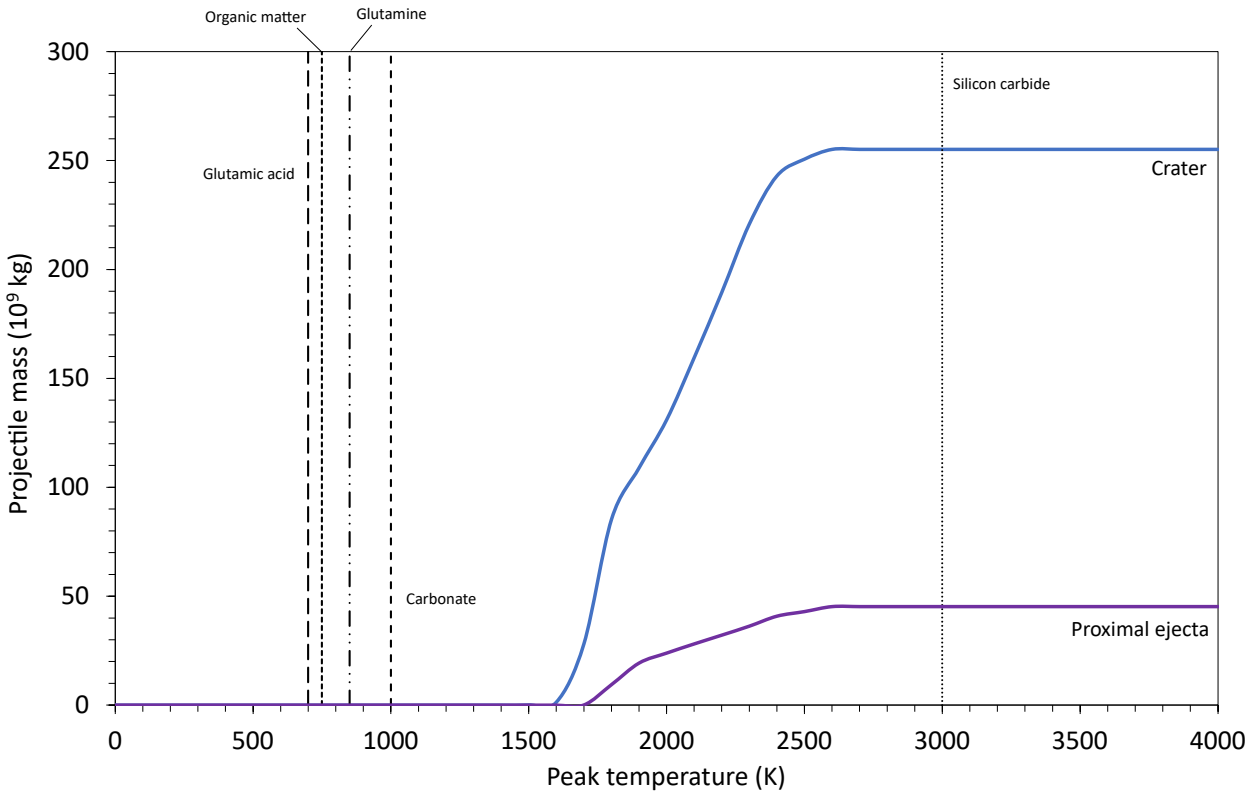

Figure 6.11: *Total mass of the projectile material landed in the proximal ejecta and crater from simulation a45_v5 plotted against the peak temperature recorded for a given total mass. The proximal ejecta describes material highlighted 7 km downrange and 4 km either side of the impact point in Figure 6.6b. Vaporisation temperature thresholds for relevant molecules from Table 6.4 are plotted with dashed lines and individually labelled.*

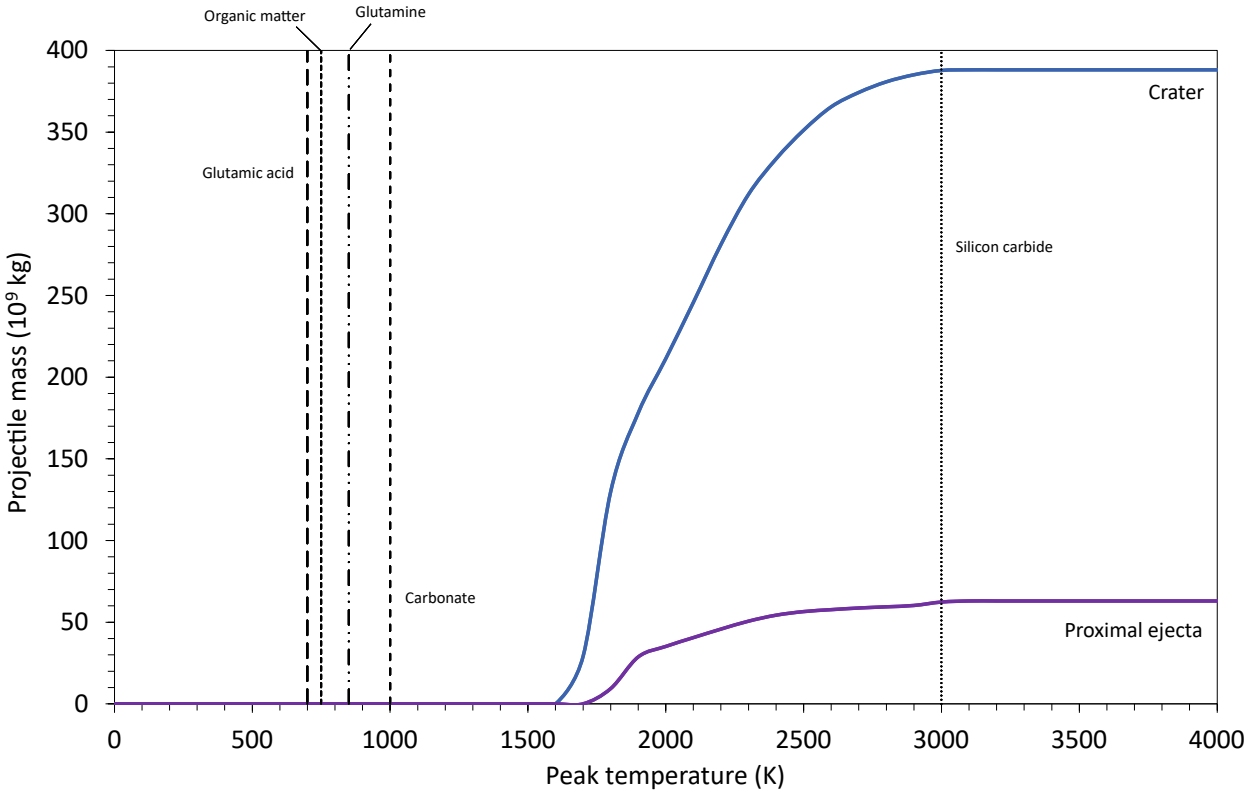

Figure 6.12: *Total mass of the projectile material landed in the proximal ejecta and crater from simulation a60_v5 plotted against the peak temperature recorded for a given total mass. The proximal ejecta describes material highlighted 6 km downrange and 5 km either side of the impact point in Figure 6.6c. Vaporisation temperature thresholds for relevant molecules from Table 6.4 are plotted with dashed lines and individually labelled.*

6.4 Discussion

The results show that low impact angle and velocity scenarios favour the survival of solid CC projectile material after impact with the lunar surface. Much of this material experiences maximum temperatures favourable for the retention of a variety of C- and N-bearing molecules found in CC meteorites and presumably their parent bodies. The following section discusses the mass of surviving carbon and nitrogen for particular impact scenarios, based on the relative proportions of the molecules typically found in a range of CC meteorites (Table 6.4).

6.4.1 Probability estimates for CC impacts into the Moon

The best-case scenario in terms of a high proportion of low temperature material is a15_v5. For the modelled 1 km diameter carbonaceous chondrite projectile, 86% of the original mass experiences temperatures low enough to remain solid throughout the impact, which equates to a mass of ~6.5×10^{11} kg. As mentioned in Section 6.2.2, peak temperatures are suitable for glutamic acid and glutamine to survive with little to no decomposition in ~16% of the projectile, a mass of ~1.2×10^{11} kg of CC material. This equates to ~2.8×10^{6} kg of glutamic acid and ~1.3×10^{6} kg of glutamine surviving after a single, CI-like projectile impacting of the many impacts that have occurred on the Moon. Of course, the true mass of these molecules remaining on the lunar surface is likely to be less, due to some material travelling fast enough to eject back off into space. The mass of these materials actually landing on the Moon and surviving in resource viable areas may be more like those shown in Table 6.7, 6.4×10^{4} kg for glutamic acid and 7.3×10^{4} kg for glutamine. Considering these are just two of the many varieties of N-bearing molecules within a range of CCs that could potentially impact the lunar surface, the mass of surviving material containing nitrogen is likely much higher. Even if particular molecules containing carbon and nitrogen do decompose or vaporise after impact, they may not be able to escape from the projectile. Preventing the devolatilization of carbonates by crystallisation during shock decompression has been suggested by Scott *et al.* (1997). Additionally, the survival of reactive carbon has been recorded in melt fragments from the Gardnos impact crater in Norway (Parnell and Lindgren, 2006). Using Gardnos melts as an analogue, Parnell and Lindgren (2006) suggest that carbon in parent bodies of CCs could survive devolatilization after impact by incorporation into silicate melts and also survive conversion into refractory or highly ordered forms of carbon. This indicates that carbon may resist degassing within silicate melts and could, therefore, be retained in elemental form. Moreover, vaporised molecules may recondense *in situ* after cooling and remain within the solid projectile material, not being allowed to escape into the lunar exosphere or to space

beyond. This hypothesis has been suggested to explain the apparent contrast between certain amino acids found in CC samples (e.g., Murchison) and those recorded as surviving in laboratory-based impact experiments (Bertrand *et al.*, 2009).

In order to discuss the mass of surviving N, let us consider an average proportion of N across a typical CI meteorite of 0.6 wt.% (Pearson *et al.*, 2006). If one suggests the minimum as material which experiences temperatures <700 K (16% of the original projectile volume) and the maximum as any material that remains solid (85%, assuming vaporised N-bearing molecules recondense and do not escape), then the amount of surviving N could be on the order of ~1×10^8 kg to ~5×10^8 kg. The likelihood of all of the nitrogen recondensing with no escape to space is unrealistic, even with little to no melting of the rock itself. Fracturing of the projectile after impact will expose molecules contained in pore spaces or incorporated into the rock itself and any N-bearing molecules near the surface at the point of impact will undoubtedly be lost. Therefore, it is more likely that the maximum amount of surviving nitrogen is closer to the ~1×10^8 kg estimated for this particular scenario and a minimum on the order of ~1×10^5 kg, if one only considers the total mass of nitrogen within the amino acids predicted to not decompose after impact (in this case glutamic acid, glutamine, and a small proportion of aspartic acid, Table 6.7).

Here, it can also be noted that the relatively low resolution of these simulations does lead to an underestimation in the amount of material suitable for nitrogen survival. There are two factors contributing to this underestimation: the overestimation of temperature at the current resolution compared to higher resolution simulations (Figure 6.4), and the limited number of modelled particle tracers tracking the projectile material over time. A higher number of tracers would allow for the tracking of smaller "packets" of material, which would then allow for more accurate temperature measurement. At the current resolution of 16 cells per projectile radius there are ~8250 tracers in the projectile. A minimum number of tracers must be used in order to reasonably represent the temperature experienced by a certain percentage of the projectile volume. In this case, 1% of the volume is represented by ~82 tracers, which is a reasonable number. If there was time to compute millions of tracers in the projectile then one may be able to consider much smaller percentages of surviving material, which would still translate to a considerable mass of material as the mass of the projectile is on the order of 10^{11} kg. Therefore, it is likely that at higher resolutions (better representing real-world impacts where resolution is essentially infinite) there would be higher volumes of low temperature projectile material and greater masses of surviving nitrogen and carbon.

This work has shown that many molecules routinely found in CCs that contain carbon and nitrogen can survive impact with the lunar surface given the right circumstances, such as low impact angle (<30°) and low impact velocity (<5

km s^{-1}) (Table 6.7). However, clearly it is important to assess the likelihood that these types of impact have occurred on the Moon. From the perspective of their use as a physical resource it is imperative that at least some of these impacts do occur in order for resource-rich CC material to be available. The probability (P_r) of a projectile impact into a target surface at an angle <θ (measured from the surface) can be determined via the empirical and theoretically well-established equation (Michikami *et al.*, 2017, adapted from Elbeshausen *et al.*, 2013 and Shoemaker, 1962):

$$P_r = 0.5(1-\cos(2\theta)) \quad (6.1)$$

Using this equation, we can determine that the probability of an oblique impact for any projectile at <15° is ~6.7%, where it is likely that a significant amount of low temperature material survives at low impact velocity. Conversely, the likelihood of a projectile impacting at a steeper angle is higher up to 45°, where surviving material mass is reduced but concentrated mainly in the crater formed. For an impact between 45-60°, the likelihood increases to ~25%. If the best-case scenario is considered for the survival of impacted material, there is also a need to determine the probability of such a projectile impacting the Moon at low velocity. Previously, it was shown that a significant proportion of projectile material survives at angles of 15° and impact velocities <15 km s^{-1} (42% to 100% of the original projectile mass, Table 6.5). Many assumptions about the proportion of projectiles impacting bodies in the inner Solar System are based on our understanding of the present-day structure of the asteroid belt. As a result, we cannot accurately consider what conditions were like in the very distant past, generally >3 billion years ago. However, based on present-day interpretations of the main belt and the inner Solar System, we can make estimates of impact rates and dynamics for the Moon over the last 3 billion years. The modelled distribution for simulated asteroidal impacts into the Moon provides an estimate of ~45% of the population striking the lunar surface at 15 km s^{-1} or less (Marchi *et al.*, 2009; Yue *et al.*, 2013). Combining this with the assumption that one third of all lunar impacts are produced by C-type asteroids (Shoemaker *et al.*, 1990), an approximate of the probability for both very oblique and more normal impacts into the Moon can be made. Impacts involving a CC parent body asteroid at <15 km s^{-1} and <15° impact angle occur ~1% of the time when considering all lunar impacts. Using the model cumulative size distributions of the number of impactors on the Moon with diameters >1 km (1×10^{-14} km^{-2} yr^{-1}; Marchi *et al.*, 2009), and the surface area of the Moon (3.794×10^{7} km^2), an estimate can be made for the number of impacts that have occurred over the last 3 billion years (3×10^{9} yr).

Impacts involving the specific combination of a CC parent body asteroid with a diameter >1 km, an impact angle <15°, and a velocity <15 km s^{-1}, culminates in a total of ~11 instances over the past ~3 billion years. This number should

be viewed as a minimum estimation for impacting bodies of a relatively large size (>1 km diameter) and would be significantly increased for smaller asteroids. In fact, decreasing the minimum diameter to 100 m would lead to an increase in the likelihood of impacts in this very specific set of scenarios by two orders of magnitude (over 1000 candidate impacts over 3 Ga). Of course, this comes with the caveat that the mass of impacting material would be decreased for each impact. Still, a 100 m diameter impactor could provide a projectile mass on the order of 10^8–10^9 kg (depending on the porosity, exact mineralogical composition etc.) to the lunar surface and, in favourable impact scenarios, could add thousands of kilograms of resource viable carbon and nitrogen to the lunar regolith. Larger impacts will obviously bring more carbonaceous material to the lunar surface but will be less frequent and also involve higher kinetic energy due to increased mass for the same impact velocities. Increasing kinetic energy will increase the shock pressure experienced by the projectile, especially at the leading edge, and will inevitably lead to higher temperatures. Whilst the size of the projectile will affect the mass and volume of the material surviving a given impact, the fraction of material surviving is likely to remain similar (e.g., Potter and Collins, 2013).

6.4.2 Detection of surviving CC meteoritic material

Determining whether surviving CC material can be used as resources for future missions is only the first step to realising their full potential. The next step will be determining the most appropriate techniques that may be used to search for the presence of caches of surviving impactor material on the lunar surface (e.g., see discussion in Joy *et al.* 2016). As a first point of investigation, consider the types of impacts that provided the highest mass of low temperature material to the lunar surface in the simulations. Highly oblique impacts (<15°) at low velocity (5 km s^{-1}) are the only scenarios where N bearing compounds can survive in significant quantities after impact (Table 6.7). Therefore, if you were searching explicitly for surviving nitrogen, a survey of craters that show evidence for a highly oblique angle of impact would narrow down the number of potential areas to search. These craters would be elliptical, with crater rims elongated in the direction of impact, with multiple smaller, secondary craters and damage downrange from the larger, original impact crater. Multiple cratering experiments and numerical models have shown that the ellipticity of a crater increases dramatically with decreasing impact angle after impact angles fall below a specific threshold (Bottke *et al.*, 2000; Collins *et al.*, 2011b; Elbeshausen *et al.*, 2013; Michikami *et al.*, 2017). This threshold angle is a function of cratering efficiency, estimated to be 15–20° on the Moon, with ~5% of all craters on the Moon (with diameters >1 km) being defined as elliptical (Bottke *et al.*, 2000). The low velocity of the impact would create a relatively shallow crater, with less energy available for target

material excavation. Highly elliptical cratering is much more likely to occur at low velocities on the Moon, with probabilities for elliptical crater formation of just a few percent when impacting at average velocities of ~15–20 km s^{-1} (Michikami *et al.*, 2017). Therefore, it is likely that elliptical craters on the Moon were formed under conditions suitable for C and N survival if they were created by a CC projectile. These areas would be the best place to start for the identification of resources on the Moon and could be the "test bed" for the remote sensing techniques required to distinguish CC material from the native lunar material.

Here, it has been demonstrated that C-bearing compounds survive in significantly more impact scenarios than N-bearing, due to their resilience to higher temperatures. However, many of the scenarios included angles of impact higher than the estimated threshold for elliptical crater formation on the Moon. This would mean the majority of the craters formed in these scenarios would likely be indistinguishable from other impacts by crater morphology alone. It would mean a much larger range of impact craters would have to be examined to find surviving CC material. Based upon the models described in this work, much of the surviving CC material (up to 50% of the original projectile mass) would be concentrated within the crater. If the impact conditions are suitable, increased amounts of minerals associated with surviving CC projectiles may be concentrated within the central peak of the impact crater, similar to the mechanism suggested by Yue *et al.* (2013). The threshold crater diameter for the transition from simple to complex craters (where central peaks begin to form) is ~15 km for the Moon. This would therefore require slightly larger impactor diameters than those investigated in this work, especially at the lower velocity range (<10 km s^{-1}) where carbon and nitrogen are more likely to survive in larger masses. As a first point of investigation, one could search for enhanced spectral signatures of many of the minerals discussed in the following paragraph. Whilst the bulk of central peaks are likely composed of rebounded crustal material from depth, some hydrated carbonaceous material may concentrate in the central peaks of large craters whose impacts were likely capable of delivering a sizeable quantity of carbon and nitrogen.

Many studies have focused on the detection and location of dark material on the asteroid Vesta (Reddy *et al.*, 2012a, 2012b; McCord *et al.*, 2012; De Sanctis *et al.*, 2012, Prettyman *et al.*, 2012). NASA's spacecraft Dawn, which orbited Vesta from 16th July 2011 to 5th September 2012 (Rayman, 2020), acquired images using its Framing Cameras (FCs; Reddy *et al.*, 2012a) and were subsequently analysed to reveal the heterogenous nature of the asteroid's surface. Dark material has predominantly been associated with areas around and inside impact craters (Reddy *et al.*, 2012b; McCord *et al.*, 2012) and has therefore been linked with the delivery of exogenous dark projectile material, such as carbonaceous chondrites. The detection of hydrated minerals (those bearing hydroxyl, OH) on localised dark material (De Sanctis *et al.*,

2012) by the VIR imaging spectrometer (De Sanctis *et al.*, 2010; Russell *et al.*, 2012) on board Dawn has lent further evidence to the idea that carbonaceous impactors have provided a projectile component to the Vestan regolith. Furthermore, investigation using spectral analysis suggests that the darkest material is associated with the richest OH signatures, in favour of a CC origin (Palomba *et al.*, 2014). Whilst this may not be directly related to the retainment and detection of C and N itself, it may be a good starting place for finding CC material from orbit on the lunar surface. Both experimental (Daly & Schultz, 2015) and modelling impact scenarios (Turrini *et al.*, 2014; 2016) at typical Vestan impact velocities (<5 km s^{-1}) have shown that CC-like projectiles can survive and be retained within the regolith in proportions significant enough to explain dark material around impact craters on Vesta. A comparison between the survival of CC material on the Moon and on Vesta can be made given the similarity of the bodies, especially the lack of atmosphere, low gravitational acceleration, and relatively high-porosity and low-density regolith of the targets. However, impact velocities on Vesta are significantly lower than those on the Moon (av. ~5 km s^{-1} and ~15 km s^{-1}, respectively), with more than 95% of impacts into Vesta occurring at velocities slower than 10 km s^{-1} (O'brien *et al.*, 2011; Marchi *et al.*, 2014). From modelling work exclusively investigating Vestan impacts (Turrini *et al.*, 2014; 2016) and from the results of the impact modelling in this work, it is clear that the lower average velocities experienced by projectiles hitting Vesta would greatly increase the proportion of surviving CC material vs. impactors hitting the Moon. Impacting at 5 km s^{-1} at any angle between 15° and 60° allows for a large proportion of the material to survive without any melting (a range between 76-100%) but increasing the velocity to 10 km s^{-1} or more leads to a significant decrease in surviving material, down to none at all. The lower average velocity of impacting projectiles for Vesta is likely the key parameter for survival of large amounts of carbonaceous material, which leads to relatively simple detection of material in and around craters on the surface.

Building on the evidence of surviving CC material on Vesta, the first obvious place to look for similar material on the lunar surface would be in close proximity to craters displaying dark ejecta material. Dark-haloed craters (DHCs) have been identified on the Moon (Salisbury *et al.*, 1968; Kaydash *et al.*, 2014; Kaur *et al.*, 2015), accompanied by multiple theories on the origins of their formation. Originally, many of the features from DHCs were attributed to lunar volcanism (Salisbury *et al.*, 1968; Schultz & Spudis, 1983), with dark material originating from transient pyroclastic volcanic events or excavation of buried ancient mare layers. More recent interpretations of DHCs consider mineralogical differences between the dark material and the surrounding regolith (Kaur *et al.*, 2015), or simply a difference in surface roughness or maturity (Kaydash *et al.*, 2014). Additionally, the dark haloes around a number of impact generated DHCs have been observed to at least partially consist of impact melt deposits (Hawke and Head, 1977; Bell & Hawke, 1984). Mineralogical

analyses using the Moon Mineralogical Mapper (M^3; Pieters *et al.*, 2009a) onboard Chandrayaan-1 (Pieters *et al.*, 2009b) have found that some DHC material is rich in olivine (Kaur *et al.*, 2015). The presence of olivine has been attributed to either excavation of olivine-rich cryptomare or a subsurface mafic pluton. Spectral analysis of DHCs has yet to uncover any association with hydrated minerals, in stark contrast to those found in dark material on Vesta. We clearly do not see the same type of dark material around many craters on the lunar surface and have definitely not detected large amounts of highly concentrated hydrated material (OH) in dark regions. It is possible that the Moon has experienced ancient impacts that have left similar evidence to that seen on Vesta today, but has since been obscured or covered by one of the many geological surface processes in the history of the Moon (volcanism, impact ejecta, Moonquakes). Additionally, Vesta's proximity to the asteroid belt provides ample opportunity for impacts with bodies rich in carbonaceous material in a variety of sizes and at a range of velocities, many likely to be much slower than those experienced by similar bodies impacting the Moon. Probably the combination of low impact velocities (<5 km s^{-1}) and the amount of CC-like material available in close proximity to Vesta has led to more recent impacts that are better preserved than ancient impacts of a similar nature on the Moon.

Additional methods of detection could include a search for phyllosilicates, which can be found in CCs and expected to be found in C-type asteroids but are essentially non-existent on the Moon. Spectral analysis from an orbiting spacecraft in the near-infrared portion of the electromagnetic spectrum could potentially identify phyllosilicates. Analysing continuum slopes in near-infrared spectra has been used previously (Ostrowski *et al.*, 2010) to identify and compare spectra of phyllosilicates on C-type asteroids to known phyllosilicates and CC samples. The same process could be used for targeted areas on the Moon, investigating in and around craters and comparing to known phyllosilicate spectra. The spatial resolution of the imaging spectrometer would need to be fine enough for targeting m-scale materials over km-scale craters and projectile material perhaps metres in size. M^3 was capable of targeted spectral analysis with a spatial resolution of 70 m and covered the relevant portion of the electromagnetic spectrum (Green *et al.*, 2011), making the instrument a potentially viable choice for this kind of investigation when considering large impacts (>1 km diameter projectiles). Finding evidence for surviving material after smaller CC impacts (closer to 100 m projectile diameters) would require a finer spatial resolution to identify smaller fragments. An evolution of M^3 is planned to investigate lunar volatiles and minerals in high resolution on the Lunar Trailblazer Mission (Ehlmann *et al.*, 2022). The High-resolution Volatiles and Minerals Moon Mapper (HVM^3) is planned to be a pushbroom, shortwave infrared imaging spectrometer onboard the mission. The 0.6–3.6 μm spectral range is suited for the detection of volatiles to map OH, bound H_2O, and water ice. Improvements from the

M^3 system predict a 50–90 m $pixel^{-1}$ spatial sampling resolution when observing from a ~100 km orbit. The HVM^3 instrument will be complemented by the Lunar Thermal Mapper (LTM), a pushbroom, multichannel imaging thermal radiometer. LTM will have a spatial resolution of 40–70 m, capable of simultaneously mapping temperature (110-400 K), physical properties, and composition of water-bearing areas in HVM^3 pixels. These instruments may be able to detect hydrated clay minerals and associated features in smaller craters, detecting the remnants of survived carbonaceous chondrite material.

6.5 Conclusions

This chapter has presented the results for a suite of simulations, investigating the survival of CC material after impact with the lunar surface. In this case, survival is defined as material experiencing temperatures under a specific threshold, most importantly the material melt temperature (~2100 K). Additionally, survival of individual C- and N-bearing molecules after impact is deemed by their specific vaporisation temperatures (Table 6.4). The only scenario in which significant amounts (16% of the original mass) of nitrogen-bearing compounds survive is at the lowest impact velocity (5 km s^{-1}) and angle (15º). Impacts with velocities >10 km s^{-1} and angles >30° do not yield any significant amount of solid material. However, particularly resilient carbon compounds (SiC/graphite/diamond) may still survive. Highly oblique impacts (15°) may lead to large concentrations of low-temperature (~3×10^{10} kg) projectile material downrange of the crater, depending on the impact velocity. This material may be the most useful from a resource perspective, as it is likely to contain abundant C and N-bearing compounds within a small area away from the impact site. It is likely that the material that concentrates downrange after oblique impacts would be found on flatter terrain, which could be much easier to access and traverse than a crater for both robotic and human missions. There is a trade-off between the mass and local concentrations of surviving material with varying impact angle, which is key from a resource perspective. A lower limit of ~11 suitable impact events over the last 3 Gyr are estimated to produce sizeable deposits of surviving CC projectiles. Each impact is capable of producing masses of N-bearing deposits on the order of ~10^8 kg and C-bearing material ~10^9–10^{10} kg, concentrated within in an area suitable for resource exploration (<60 km^2). This number of suitable impacts would rise significantly for impactors with smaller diameters but would lead to lower masses of suitable survived material for each impact. Producing deposits rich in only C-bearing molecules would allow for a larger range of candidate impact scenarios, especially at higher impact angles (>45º) with material concentrating immediately beyond the crater rim or inside the craters formed. Concentrating material within or directly nearby the crater itself may be easier to detect with remote sensing

techniques as the density of surviving material is likely to be higher than material that is ejected out and away from the impact zone. Higher spatial resolution spectral instruments will likely be needed to investigate candidate craters and to assess their potential from a resource perspective.

7 Discussion and conclusions

7.1 Scientific and commercial opportunities for meteoritic material on the Moon

Whilst the discovery of surviving impactor material on the Moon has been, and will continue to be, of great scientific value, it is likely that the commercial space sector would be especially interested in occurrences that are could be useful for future lunar missions and contribute to the development of lunar infrastructure. Meteorites with high concentrations of metals may be first on the list as an accessible and exploitable resource for metallic elements concentrated within small areas. Such areas have been suggested by Yue *et al.* (2013) where metallic material could be concentrated within craters and could potentially be detectable from orbit via associated magnetic anomalies (Wieczorek *et al.*, 2012).

The discovery of terrestrial meteorites, and any surviving entrained biomarkers within them, obviously provides a significant interest in terms of scientific value. They may record both geological and biological history no longer available on Earth and provide evidence for organic material transfer between planetary bodies and potentially lithopanspermia. However, they are unlikely to be of significant interest in an industrial or commercial setting. Additionally, the expected size of any terrestrial material making it to the lunar surface is perhaps 10s of metres at a maximum (Beech *et al.*, 2019), but more likely at the lower, metre-scale (Wells *et al.*, 2003; Armstrong, 2010). In order to retain any identifiable biomarkers over geological time, any surviving terrestrial material would have to be buried via one or multiple processes as discussed in previous chapters. Therefore, any hope for detecting such material from orbit is essentially impossible and robotic landers, rovers, or human missions to the Moon would probably be required. Currently there is no future mission planned that will focus solely on the detection and discovery of terrestrial material on the Moon. The best option for the near future is that instruments may be used by astronauts or robotic landers/rovers already planned to visit the lunar surface to facilitate the detection of terrestrial material. Whilst the long-term survival of meteoritic material requires burial, impact gardening will continuously bring previously buried material to the surface. If this occurs within the timescale that meter-sized boulders are estimated to survive on the lunar surface (median time: ~40–80 Ma, maximum time ~300 Ma; Basilevsky *et al.*, 2013), then at any given time some Earth meteorite material may be located at the surface and still contain compositional evidence of terrestrial origin. Fragments on the surface could be detected by astronaut-held or rover-mounted IR spectrometers, tuned to be sensitive to Earth-like mineralogy (e.g., Crawford *et al.*, 2008).

Surviving carbonaceous chondrites are likely to be of interest to both the scientific community and the commercial space sector. Whether they are discovered in small or large concentrations, investigating the mineralogy of surviving fragments and probing the temperature/pressure regimes experienced will provide insight into the history of carbonaceous chondrites. This is because the relatively inert and inactive lunar surface means that surviving material should be relatively unaltered from their original state in terms of atmospheric ablation, aqueous alteration, and any organic/biological contaminants (discounting the influence of impact processes). Indeed, remnants of carbonaceous chondrites on the lunar surface have been identified as a mm-scale fragment in an Apollo 12 sample (Zolensky *et al.*, 1996; Zolensky, 1997; Joy *et al.*, 2020). Analysis of this sample has been limited by the size of the fragment and it being the only sample of a carbonaceous meteorite on the Moon that we currently have. More recently, further evidence for carbonaceous material on the Moon has come from hyperspectral analysis of a 2 m diameter crater obtained by the Yutu-2 rover, a part of the Chinese Lunar Exploration Program mission Chang'E-4 (Yang *et al.*, 2021). Glassy material within the crater was spectrally distinct from the background regolith and contained 47 wt.% carbonaceous chondrite material, according to the spectra. Again, this is a small example of carbonaceous rich material on the Moon, potentially created via a secondary impact from a larger primary impact of carbonaceous body (Yang *et al.*, 2021). Creating interest for the commercial space sector hinges on the detection of much larger remnants of carbonaceous impactors, potentially using methods similar to those used on Vesta as part of the Dawn mission as described in Section 6.2.4. So far, there has been a lack of carbonaceous chondrite remnants directly observed on the lunar surface by remote sensing exploration, but new and improved instruments on future missions may remedy this current shortfall.

Setting up a lunar base to exploit the resource potential of a survived carbonaceous impactor will require similar considerations to those currently being suggested for other potential lunar resources. Carpenter *et al.* (2016) have stressed the importance of establishing the viability of a lunar resource from discovery to utilisation involving a number of steps. These include finding, characterising, and validating the required technologies to extract said resource, followed by demonstrating how the resource can be extracted and utilised for the intended purpose. Precursor missions by robotic landers or rovers to the lunar surface will be key to the prospecting stage of lunar resource utilisation, finding and characterising the potential resources. For the extraction and lunar volatiles, the south pole provides both topographically high locations which provide the illumination needed (Mazarico *et al.*, 2011; Speyerer and Robinson, 2013; Gläser *et al.*, 2014) and the probable presence of large volumes of volatiles in PSRs. Both of these factors are set to be investigated by the Volatiles Investigating Polar Exploration Rover (VIPER), a robotic exploration mission planned by NASA as part of

the Commercial Lunar Payload Services (CLPS) initiative (Colaprete *et al.*, 2019). Whilst polar ice deposits may contribute to the ISRU of carbon, with frozen deposits of CO_2 and CH_4, nitrogen is unlikely to be found. Similar precursor missions will need to be considered, planned, and carried out in order to fully explore any resources contributed by survived carbonaceous chondrite impactors.

7.2 Concluding remarks

In this thesis, a series of numerical simulations have been completed to address the aims and objectives set out in Chapter 1: the ejection of material from Earth (Objective 1), the survival biomarkers within terrestrial meteorites impacting the lunar surface (Objective 2), the survival of carbonaceous chondrites impacting the lunar surface (Objective 3). Additionally, post-processing, analysis, and interpretation of these numerical models has led to the determination of the location of surviving carbonaceous chondrite material relative to the crater formed during impact (addressing Objective 4). Reviews of proposed lunar mission concepts has also resulted in the consideration of surviving meteoritic material in terms of use for future lunar missions designed to make use of in situ materials (addressing Objective 5).

The main conclusions of this work are the following:

1) Terrestrial meteorites impacting the lunar surface at velocities <5 km s^{-1} can produce favourable conditions, in both pressure and temperature, for the survival of a number of biomarkers. Temperatures near the contact zone reach those required for melting and vaporisation of the projectile itself, especially when a porous projectile impacts a solid target. Lower impact velocity (2.5 km s^{-1}), lower projectile porosity, and/or higher target porosity, increases the likelihood of survival for the projectile and any organic molecules within them. The most favourable conditions for survivability involve a solid projectile, impacting at low velocity (2.5 km s^{-1}) into a highly porous (50-70%) regolith (Figure 5.8). In this case, the biomarker molecules lignin, tryptophan and arginine are shown to survive in significant proportions: 69%, 41%, and 33% of the original biomarker mass, respectively (see Figure 5.10). Lycophyte megaspore fossil biomarkers are also expected to survive, especially at the back of the projectile, with little to no alteration based on their survival pressures and temperatures in metamorphosed samples.

2) Long-term survivability of terrestrial meteorites and biomarkers entrained within them depends heavily on where the material lands and subsequent activity at the impact site over geological time. The cooling

timescales of surviving projectile fragments are important when considering the long-term thermal degradation of organic material. Even when simulations conclude pressures and temperatures are compatible with the survival of significant proportions of organics, much of the biomarker mass may become unrecognisable via thermal degradation. Depending on where the projectile fragments land, the size of the fragments, and the dominant cooling regime, the time it takes for projectile material to cool can vary considerably. The duration of cooling to reach temperatures consistent with long-term biomarker survival extends far beyond the initial shock due to impact.

3) Ejection from Earth is likely the toughest barrier to overcome for the survival of biomarkers in terrestrial meteorites en route to the lunar surface, not the impact into the Moon itself. Simulations with impact velocity and angle of 20 km s^{-1} and 30° resulted in a mass of 10^{-5} M_i of high-speed ejecta (>11 km s^{-1}) experiencing pressures equal to or less than 10 GPa (see Figure 4.6). This is low enough to meet the requirements for being considered low-shock material that could harbour identifiable biomarker material after ejection. Impacts with the same velocity but with an angle of 30° provided the lowest pressures for escaping ejecta, 3 GPa for a mass of 10^{-5} M_i of escaping target material (Figure 4.7). Increasing the impact angle to 45° and 60° at either of these velocities leads to minimum pressures for escaping ejecta of ~40 GPa and ~50 GPa; such material may remain solid (i.e., it experiences pressures lower than a nominal critical pressure for melting of 50 GPa) but is unlikely to be consistent with biomarker survival. For 45° and 60° impact angles, increasing impact velocity to 55 km s^{-1} leads to lower minimum pressures for escaping ejecta than 20 km s^{-1} and 30 km s^{-1} impact velocities (45°: ~20 GPa, 60°: ~30 GPa; Figure 4.8). This is likely due to the high velocity impactor (55 km s^{-1}) transferring sufficient velocity to target material further from the impact site, where it experiences lower pressures. When comparing all of the scenarios, impact angle has a greatest influence on the mass of low-pressure (<10 GPa), high-speed (> 11 km s^{-1}) ejecta. Temperatures are anomalously high compared to the pressures recorded. This may be a consequence of the process known as post-shock acceleration (Wakita *et al.*, 2019; Okamoto *et al.*, 2020), but high temperatures are also potentially an artefact resulting from the resolution of simulations or a defect in the iSALE code leading to inaccurate or unphysical results.

4) Carbonaceous chondrites are likely to have left a considerable amount of material on the lunar surface. Some impacts at low impact angle (<30°) and low impact velocity (<10 km s^{-1}) will retain many compounds rich

in both carbon and nitrogen. N-rich deposits will likely be located down range of the original impact site due to projectile decapitation. The distance of surviving material from the crater will depend on the impact velocity and angle but obvious projectile decapitation only occurs at impact angles less than 15°. In which case, the majority of the low-shock material (temperatures <700 K in ~16% of the original projectile volume) extends between 20 and 30 km downrange and <6 km each side of the point of impact (scenario a15_v5, Figure 6.5a); this is the only scenario where temperatures remain below that of amino acid vaporisation temperatures. Increasing the impact angle results in a greater proportion of the projectile material remaining within the crater (Figure 6.7). Scenarios a15_v5, a15_v10, and a30_v5 produce survived material with temperatures suitable for all carbon species (Table 6.7), within regions with resource potential. When assuming that all C- and N-bearing molecules survive in material experiencing temperatures less than the material melt temperature, scenario a60_v5 produces the largest masses of survived carbon and nitrogen: 1.48×10^{10} kg and 1.48×10^{9} kg, respectively (Table 6.7 & Figure 6.12); this material is concentrated within the crater. A lower limit of ~11 suitable impact events over the last 3 Gyr is estimated to produce sizeable deposits of surviving CC projectiles. Each impact is capable of producing masses of N-bearing deposits on the order of ~10^{8} kg and C-bearing material ~10^{9}–10^{10} kg, concentrated within areas suitable for resource exploration.

The simulations completed during this work demonstrate the potential for a variety of meteoritic material to survive impact with the lunar surface in a variety of scenarios. The next step will be to find such materials on the Moon. Finding these crashed impactors will provide a plethora of scientific knowledge as well as commercial opportunities for the future of space industry. The resource potential of materials which are useful for both commercialisation of space and the prolonged, sustainable, human presence on the Moon will be critical. Hopefully, we can begin to see the fruition of these ideas within the next phase of space exploration, including the Artemis missions and the boom of the commercial space sector.

7.3 Future work

With appropriate adjustments to the input parameters, much of this work could be applied to other planetary bodies, not just the Moon. There is the potential to evaluate the likelihood of finding new meteoritic material on a number of rocky and not-so rocky surfaces across the Solar System. Are Venusian or Mercurian meteorites ever likely to be found

here on Earth or beyond? Might we find terrestrial material on Mars, much like martian meteorites here on Earth? Could impact events facilitate the transfer of biological material to icy Moons like Europa or Ganymede? These questions might be answered in future work, potentially using numerical modelling that might be informed by the simulations presented in this thesis.

Much of the numerical modelling work presented in this thesis could be expanded to encompass a larger variety of parameters in addition to the current suite of scenarios. Additionally, laboratory-based impact experiments approximating some of the numerical simulations would be of great benefit, especially for the models simulating terrestrial meteorites impacting the Moon. The scale of the modelling for both the impact ejection from Earth (10s km projectile diameter) and carbonaceous chondrites impacting the Moon (~1 km projectile diameter) are too large to be represented to scale in any laboratory, but the centimetre sized fragments impacting the lunar surface may be more feasible to replicate. The following sections will detail scenarios which were planned to complement those presented in this work but could not be completed due to lack of time or unexpected circumstances, along with proposed work for the future to expand this work.

7.3.1 Earth ejection simulations

Firstly, high-speed ejecta that experiences low pressures, but also suspiciously high temperatures should be investigated further. This will require a suite of 3D simulations very similar to those produced for this thesis, but potentially with adaptations to the iSALE3D code itself or higher resolution. The highest resolution 3D simulations used in this work (100 cppr) already pushed the boundaries for the number of tracers allowed to be simulated by iSALE and increasing this further will likely take a substantial amount of time.

Simulations investigating the escape of ejecta from Earth included only a simplified, single-layer target, approximating the composition of the Earth's crust with a granite material model. Of course, this is an over-simplification of any surface that an impactor could hit on the Earth at any time in geological history However, with the time and computational power available it was deemed a necessary simplification in order to produce a suite of high-resolution simulations. With more time and perhaps access to higher powered computing clusters, there are many variations in the structure of both the target and impactor that would be beneficial to better understanding the ejection process. Beginning with the target, more accurately representing a range of geological materials would better inform the ejection process after impact into a range of potential, Earth-like scenarios. Within the current capabilities of iSALE3D, a maximum of three

materials can exist in the same cell (which includes the void where no materials are placed). Therefore, if the projectile material was kept the same as one of the layers of the target, another layer could be added composed of a different material. For example, to represent an impact into an ocean target, the top layer could be represented by an equation of state for water, overlaying a geological substrate with the same composition as the impactor, potentially basalt, sandstone, or granite. It would be very interesting to investigate how the depth of an ocean or shallow sea would influence the generation of high-velocity, low-pressure ejecta. Layers of weaker, unconsolidated geological materials (such as sediments or porous sedimentary rock) could also be added to the top of the simulation or interspersed within the consolidated rock.

Impactors of different diameters could be investigated in future to assess the influence of impactor size on the mass of target ejecta compared to the mass of the impactor. This is particularly important for the high-velocity, low-pressure ejecta during post-shock acceleration in the relatively small near-surface area where this ejecta has been shown to originate from. Additionally, changing the composition of the impactor to represent different types of asteroidal objects or potentially cometary objects would be a benefit. These could include dense, iron-rich impactors, which would require a smaller impactor size to represent the same mass as the granite material used in the work presented in Chapter 4. Another option, which was briefly mentioned in Chapter 4, would be to include ice in the impactor to represent cometary material, which would decrease the density of the impactor for a given diameter.

7.3.2 Terrestrial meteorite simulations

The scenarios for the terrestrial meteorite impacts on the Moon only included two-dimensional simulation set-ups. An obvious expansion to this work would be to investigate the survival of terrestrial meteorites during oblique impacts, using three-dimensional modelling. In order to maintain the level of reliability for recorded temperatures and pressures as the 2D models, the 3D models would need to be of comparable high resolution. This would require high computing power and sufficient computational time to complete, necessitating the use of high-powered, computing clusters, such as Kathleen at UCL. As mentioned in this thesis (particularly Chapter 6), shear heating contributes a significant component of the heating during impact and ejection. Investigating the additional shear heating contributed to a terrestrial meteorite during an oblique impact would be of great value when concerning the survival of temperature sensitive biomarkers.

A generalised target was used to represent the lunar surface (a basalt material model) during the terrestrial meteorite simulations. This target material could be expanded to include more specific locations on the lunar surface. For example, an anorthositic material model could be used to broadly represent the lunar highlands. However, the cm-scale

impactors used during these simulations allows for a wider range of potential targets than the more generalised targets required for km-scale impactors. There is the possibility that a terrestrial meteorite fragment could impact into a pre-existing crater, potentially one at either of the lunar poles where permanently shadowed regions are found. This could allow for impacts into an ice-regolith mixture, which can be represented by a mixed target in future numerical modelling.

7.3.3 Carbonaceous chondrite simulations

The material model for the carbonaceous chondrite survival scenarios was approximated using serpentine. Whilst a good estimation for a generalised carbonaceous chondrite-like impactor, the material model could be improved to represent different types of specific asteroid parent bodies. This would allow for better estimation of the surviving fractions of carbon- and nitrogen-based molecules by using the known proportions of studied samples (e.g., CI, CM, CO, CV Types). Again, similar to those suggested in subsection 7.3.2, the target material could also be altered to represent different specific areas of the lunar surface.

Due to size of the simulations and the time it took to run them in 3D, the current set of simulations discussed in Chapter 7 only extended to the point at which the transient crater reached a maximum volume. Expanding the simulations in terms of simulated time to the end of the crater formation could provide useful information of the crater morphology associated with the highest fraction of surviving projectile material at low temperature. Existing remote sensing datasets could then be used to search for similar crater morphologies on the lunar surface which are also likely to contain carbonaceous chondrite like material. These results could be used to make recommendations for future lunar missions designed to make *in situ* investigations of surviving asteroidal material on the Moon. This could also involve identifying specific landing sites where such materials may be expected to occur on the present surface or shallow sub-surface.

The results for the masses of surviving carbon after impact could be expanded to include the effect of temperature on different phases of carbon. Separating the chosen carbon molecules into organic and inorganic sources, and further separating organic carbon into soluble and insoluble sources, would provide more accurate information on the proportion of surviving carbon for particular temperature ranges. This may require an entirely new thermal model, separate to the impact modelling, to better understand the temperature variation over time for CC impacts on the lunar surface. iSALE would not be considered the best suited modelling tool to investigate such involved post-shock temperature variations.

7.3.4 Comparative experimental, laboratory-based modelling

Early in the commencement of this PhD project there was the possibility that comparative laboratory-based models could be used to complement the numerical simulations. These would likely have been carried out at the University of Kent, using the Light Gas Gun (LGG) at the Centre for Astrophysics and Planetary Science (Hibbert *et al.*, 2017). This work would have been similar to that already investigated for the survival of organic and fossilised material after impact (e.g. Parnell *et* al., 2010; Burchell *et al.*, 2014a; 2014b; 2017), but using the same (or similar as possible) biomarkers and impact parameters as those modelled in this thesis. However, the global COVID-19 pandemic prevented this and the project therefore remained numerically based. The capability of the LGG to fire projectiles up to 3 mm in diameter at velocities up to 7.5 km s^{-1} provides an excellent basis for modelling the impact of terrestrial meteorites into the lunar surface. Building upon previous work, projectiles would be doped with biomarkers, fired at comparable speeds to the numerical modelling, and recovered for investigation of the surviving biomarkers. Comparing these results to the pressure and temperature regimes predicted by the numerical modelling would be an excellent continuation and test the robustness of the results.

Bibliography

Abell, P.I., Eglinton, G., Maxwell, J.R., Pillinger, C.T., Hayes, J.M., 1970. Indigenous Lunar Methane and Ethane. *Nature 226,* 251–252. https://doi.org/10.1038/226251b0

Aléon J., Krot A. N., McKeegan K. D., 2002. Calcium-aluminum-rich inclusions and amoeboid olivine aggregates from the CR carbonaceous chondrites. *Meteoritics & Planet. Science 37*, 1729–1755.

Alexander, C. M. O'd., Russell, S. S., Arden, J. W., Ash, R. D., Grady, M. M., Pillinger, C. T., 1998. The origin of chondritic macromolecular organic matter: A carbon and nitrogen isotope study. *Meteoritics & Planetary Science 33*, 603–622. doi:10.1111/j.1945-5100.1998.tb01667.x#

Amsden, A., Ruppel, H., Hirt, C., 1980. SALE: a simplified ALE computer program for fluid flow at all speeds. LANL Rep., LA-8095.

Anand, M., 2010. Lunar Water: A Brief Review. *Earth, Moon, and Planets 107*, 65–73. https://doi.org/10.1007 s11038-010-9377-9

Anand, M., Crawford, I.A., Balat-Pichelin, M., Abanades, S., van Westrenen, W., Péraudeau, G., Jaumann, R., Seboldt, W., 2012. A brief review of chemical and mineralogical resources on the Moon and likely initial in situ resource utilization (ISRU) applications. *Planetary and Space Science 74*, 42–48. https://doi.org/10.1016/j.pss.2012.08.012

Anand, M., Barnes, J.J., Hallis, L.J., 2015. Lunar Geology, in: Lee, M.R., Leroux, H. (Eds.), Planetary Mineralogy. European Mineralogical Union, Mineralogical Society of Great Britain & Ireland.

Anderson, C. E., 1987. An overview of the theory of hydrocodes, *International Journal of Impact Engineering*, 5, 33–59.

Anderson, W. W., Ahrens, T. J., 1998. Shock wave equations of state of chondritic meteorites. *AIP Conference Proceedings* 429, 115. doi:10.1063/1.55475

Andert, T. P., Rosenblatt, P., Pätzold, M., Häusler, B., Dehant, V., Tyler, G. L., Marty, J. C., 2010. Precise mass determination and the nature of Phobos. *Geophysical Research Letters* 37. doi:10.1029/2009GL041829

Armstrong, J.C., 2010. Distribution of Impact Locations and Velocities of Earth Meteorites on the Moon. *Earth, Moon, and Planets 107*, 43–54. https://doi.org/10.1007 s11038-010-9355-2

Armstrong, J., Wells, L., Gonzalez, G., 2002. Rummaging through Earth's Attic for Remains of Ancient Life. *Icarus*, 160(1), 183-196.

Arnold, J. R., 1979. Ice in the lunar polar regions. *Journal of Geophysical Research* 84, 5659–5668.

Artemieva, N., Ivanov, B., 2004. Launch of martian meteorites in oblique impacts. *Icarus 171*, 84–101. https://doi.org/10.1016/j.icarus.2004.05.003

Artemieva, N. A., Morgan, J., 2009. Modeling the formation of the K–Pg boundary layer. *Icarus 201(2)*, 768-780. doi: 10.1016/j.icarus.2009.01.021

Avdellidou, C., Price, M., Delbo, M., Cole, M., 2016. Survival of the impactor during hypervelocity collisions – II. An analogue for high-porosity targets. *Monthly Notices of the Royal Astronomical Society*, 464(1), 734-738. doi: 10.1093/mnras stw2381

Avdellidou, C., Di Donna, A., Schultz, C., Harthong, B., Price, M.C., Peyroux, R., Britt, D., Cole, M., Delbo, M., 2020. Very weak carbonaceous asteroid simulants I: Mechanical properties and response to hypervelocity impacts. *Icarus 341*, 113648. https://doi.org/10.1016/j.icarus.2020.113648

Barber, S. J., Smith, P. H., Wright, I. P., Abernethy, F., Anand, M., Dewar, K. R., Hodges, M., Landsberg, P., Leese, M. R., Morgan, G. H., Morse, A. D., 2017. ProSPA: the science laboratory for the processing and analysis of lunar polar volatiles within PROSPECT. 48th Lunar and Planetary Science Conference, Abstract 2171.

Barnes, J., Kring, D., Tartèse, R., Franchi, I., Anand, M., Russell, S., 2016. An asteroidal origin for water in the Moon. *Nature Communications,* 7(1), . doi:10.1038/ncomms11684

Basilevsky, A., Head, J., Horz, F., 2013. Survival times of meter-sized boulders on the surface of the Moon. *Planetary & Space Science*, 89, 118-126.

Basilevsky, A., Head, J., Horz, F., Ramsley, K., 2015. Survival times of meter-sized rock boulders on the surface of airless bodies. *Planetary & Space Science*, 117, 312-328.

Becker, R. H., Clayton, R. N., Mayeda, T. K., 1976. Characterization of lunar nitrogen components. *Lunar and Planetary Science Conference Proceedings*, 7, 441-458.

Becker, R.H., Epstein, S., 1981. Carbon isotopic ratios in some low-δ^{15} N lunar breccias. *Proceedings from the Lunar and Planetary Science Conference 12*, 289-293.

Beech, M., Comte, M., 2018. The Chant Meteor Procession of 1913 – Towards a Descriptive Model. *American Journal of Astronomy and Astrophysics 6*, 31. https://doi.org/10.11648/j.ajaa.20180602.11

Beech, M., Comte, M., Coulson, I., 2019. The Production of Terrestrial Meteorites – Moon Accretion and Lithopanspermia. *American Journal of Astronomy and Astrophysics 7*. https://doi.org/10.11648/j.ajaa.20190701.11

Bell, J. F., Hawke, B. R., 1984. Lunar dark-haloed impact craters: origin and implications for early mare volcanism. *Journal of Geophysical Research 89*, 6899–6910.

Bellucci, J.J., Nemchin, A.A., Grange, M., Robinson, K.L., Collins, G., Whitehouse, M.J., Snape, J.F., Norman, M.D., Kring, D.A., 2019. Terrestrial-like zircon in a clast from an Apollo 14 breccia. *Earth and Planetary Science Letters 510*, 173–185. https://doi.org/10.1016/j.epsl.2019.01.010

Benz, W., Cameron, A. G. W., Melosh, H. J., 1989. The origin of the Moon and the single-impact hypothesis III. *Icarus 81*, 113–131. doi:10.1016/0019-1035(89)90129-2

Bernard, S., Benzerara, K., Beyssac, O., Menguy, N., Guyot, F., Brownjr, G., Goffe, B., 2007. Exceptional preservation of fossil plant spores in high-pressure metamorphic rocks. *Earth & Planetary Science Letters 262(1-2)*, 257-272. doi: 10.1016/j.epsl.2007.07.041

Bertrand, M., van der Gaast, S., Vilas, F., Hörz, F., Haynes, G., Chabin, A., Brack, A., Westall, F., 2009. The Fate of Amino Acids During Simulated Meteoritic Impact. *Astrobiology 9*, 943–951. https://doi.org/10.1089/ast.2008.0327

Besserer, J., Nimmo, F., Wieczorek, M.A., Weber, R.C., Kiefer, W.S., McGovern, P.J., Andrews-Hanna, J.C., Smith, D.E., Zuber, M.T., 2014. GRAIL gravity constraints on the vertical and lateral density structure of the lunar crust. *Geophysical Research Letters 41*, 5771–5777. https://doi.org/10.1002/2014gl060240

Bierson, C.J., Phillips, R.J., Nimmo, F., Besserer, J., Milbury, C., Keane, J.T., Soderblom, J.M., Zuber, M.T., 2016. Interactions between complex craters and the lunar crust: Analysis using GRAIL data. *Journal of Geophysical Research: Planets 121*, 1488–1497. https://doi.org/10.1002/2016je005090

Bischoff, A., Palme, H., Schultz, L., Weber, D., Weber, H., Spettel, B., 1993. Acfer 182 and paired samples, an iron-rich carbonaceous chondrite: Similarities with ALH85085 and relationship to CR chondrites. *Geochimica et Cosmochimica Acta 57*, 2631-2648. doi:10.1016/0016-7037(93)90422-s

Bland, P. A., Cressey, G., Menzies, O. N., 2004. Modal mineralogy of carbonaceous chondrites by X-ray diffraction and Mössbauer spectroscopy. *Meteoritics & Planetary Science 39*, 3–16.

Bland, P. A., Artemieva, N. A., Collins, G. S., Bottke, W. F., Bussey, D. B. J., Joy, K. H., 2008. Asteroids on the Moon: Projectile survival during low velocity impact. *Lunar & Planetary Science XXXIX,* Abstract #2045.

Bland, P.A., Collins, G.S., Davison, T.M., Abreu, N.M., Ciesla, F.J., Muxworthy, A.R., Moore, J., 2014. Pressure–temperature evolution of primordial solar system solids during impact-induced compaction. *Nature Communications 5.* https://doi.org/10.1038/ncomms6451

Boazman, S.J., Shah, J., Harish, Gawronska, A.J., Halim, S.H., Satyakumar, A.V., Gilmour, C.M., Bickel, V.T., Barrett, N., Kring, D.A., *Submitted.* The distribution and accessibility of geologic targets near the lunar south pole and potential Artemis Landing sites 001 and 004. *Planetary Science Journal*.

Botta, O., Glavin, D.P., Kminek, G., Bada, J.L., 2002. Relative Amino Acid Concentrations as a Signature for Parent Body Processes of Carbonaceous Chondrites. *Origins of Life and Evolution of the Biosphere 32*, 143–163. https://doi.org/10.1023/a:1016019425995

Bottke, W.F., Love, S.G., Tytell, D., Glotch, T., 2000. Interpreting the Elliptical Crater Populations on Mars, Venus, and the Moon. *Icarus 145*, 108–121. https://doi.org/10.1006/icar.1999.6323

Bottke, W.F., Vokrouhlický, D., Minton, D., Nesvorný, D., Morbidelli, A., Brasser, R., Simonson, B., Levison, H.F., 2012. An Archaean heavy bombardment from a destabilized extension of the asteroid belt. *Nature 485,* 78–81. https://doi.org/10.1038/nature10967

Bowling, T.J., Johnson, B.C., Wiggins, S.E., Walton, E.L., Melosh, H.J., Sharp, T.G., 2020. Dwell time at high pressure of meteorites during impact ejection from Mars. *Icarus 343*, 113689. https://doi.org/10.1016/j.icarus.2020.113689

Bray, V., 2009. Impact Crater Formation on the Icy Galilean Satellites. PhD Thesis. Department of Earth Science and Engineering, Imperial College London.

Bray, V.J., Hagerty, J.J., Collins, G.S., 2022. "False peak" creation in the Flynn Creek marine target impact crater. *Meteoritics & Planetary Science 57*, 1365–1386. https://doi.org/10.1111/maps.13822

Brebu, M., Vasile, C., 2010. Thermal degradation of lignin – A Review. *Cellulose Chemistry and Technology*. 44. 353-363.

Bridenstine, J., 2019. The scientific context for the exploration of the Moon. NASA Release, 19-022.

Brilliant, D. R., Franchi, I. A., Arden, J. W., Pillinger, C. T., 1992. An Interstellar Component in the Lunar Regolith. *Meteoritics*, 27(3), 206.

Britt, D., Consolmagno, G., 2000. The Porosity of Dark Meteorites and the Structure of Low-Albedo Asteroids. *Icarus 146*, 213-219. doi:10.1006/icar.2000.6374

Britt, D. T., Yeomans, D., Housen, K., Consolmagno, G., 2002. Asteroid density, porosity, and structure. In: Bottke W. F., Cellino, A., Paolicchi, P., Binzel, R. P. (Eds.), *Asteroids III*. University of Arizona Press, Tucson, pp. 485–500.

Brookshaw, L., 1998. An equation of state for serpentine. Technical Report, Working Paper Series SC-MC-9813, Faculty of Sciences, University of Southern Queensland.

Bruck Syal, M., Schultz, P.H., 2015. Impact delivery of water at the Moon and Mercury, 2015. *Lunar & Planetary Science XXXXVI*. Abstract #1680.

Bruck Syal, M., Michael Owen, J., Miller, P.L., 2016. Deflection by kinetic impact: Sensitivity to asteroid properties. *Icarus 269*, 50–61. https://doi.org/10.1016/j.icarus.2016.01.010

Bundy, F. P., 1989. Pressure-temperature phase diagram of elemental carbon. *Physica A: Statistical Mechanics and its Applications 156*, 169–178. doi:10.1016/0378-4371(89)90115-5

Burbine, T.H., 1998. Could G-class asteroids be the parent bodies of the CM chondrites? *Meteoritics & Planetary Science 33*, 253–258. https://doi.org/10.1111/j.1945-5100.1998.tb01630.x

Burchell, M., Bowden, S., Cole, M., Price, M., Parnell, J., 2014a. Survival of Organic Materials in Hypervelocity Impacts of Ice on Sand, Ice, and Water in the Laboratory. *Astrobiology 14(6*), 473-485.

Burchell, M., McDermott, K., Price, M., Yolland, L., 2014b. Survival of fossils under extreme shocks induced by hypervelocity impacts. *Philosophical Transactions of the Royal Society A: Mathematical, Physical and Engineering Sciences 372*, 20130190.

Burchell, M., Harriss, K., Price, M., Yolland, L., 2017. Survival of fossilised diatoms and forams in hypervelocity impacts with peak shock pressures in the 1–19 GPa range. *Icarus 290*, 81-88.

Buseck, P. R., Hua, X., 1993. Matrices of carbonaceous chondrite meteorites. *Annual Reviews in Earth & Planetary Science 21*, 255–305.

Cabot, S.H.C., Laughlin, G., 2020. Lunar Exploration as a Probe of Ancient Venus. *The Planetary Science Journal 1*, 66. https://doi.org/10.3847/psj/abbc18

Cannon, K.M., 2021. Accessible Carbon on the Moon. *Preprint, arXiv:2104.13521*. Available at: https://doi.org/10.48550/arXiv.2104.13521

Carrier III, W. D., Olhoeft, G. R., Mendell, W., 1991. Physical Properties of the Lunar Surface. In: G. H. Heiken, D. T. Vaniman, & B. M. French (Eds.), *Lunar Sourcebook, A User's Guide to the Moon*, 475-594. Cambridge University Press, Cambridge, U.K.

Carpenter, J., Fisackerly, R., Houdou, B., 2016. Establishing lunar resource viability. *Space Policy 37*, 52–57. https://doi.org/10.1016/j.spacepol.2016.07.002

Castillo-Rogez, J.C., 2011. Ceres - Neither a porous nor salty ball. *Icarus 215*, 599–602. doi:10.1016/j.icarus.2011.08.007

Cataldi, G., Brandeker, A., Thébault, P., Singer, K., Ahmed, E., de Vries, B.L., Neubeck, A., Olofsson, G., 2017. Searching for Biosignatures in Exoplanetary Impact Ejecta. *Astrobiology 17*, 721–746. https://doi.org/10.1089/ast.2015.1437

Cesaretti, G., Dini, E., De Kestelier, X., Colla, V., Pambaguian, L., 2014. Building components for an outpost on the Lunar soil by means of a novel 3D printing technology. *Acta Astronautica 93*, 430–450. https://doi.org/10.1016/j.actaastro.2013.07.034

Chan, Q.H.S., Chikaraishi, Y., Takano, Y., Ogawa, N.O., Ohkouchi, N., 2016. Amino acid compositions in heated carbonaceous chondrites and their compound-specific nitrogen isotopic ratios. *Earth, Planets and Space 68*. https://doi.org/10.1186 s40623-016-0382-8

Chang, S., Smith, J. W., Kaplan, I., Lawless, J., Kvenvolden, K. A., Ponnamperuma, C., 1970. Carbon compounds in lunar fines from Mare Tranquillitatis-IV. Evidence for oxides and carbides. *Proceedings from the Apollo 11 Lunar Science Conference,* 1857-1869.

Chappaz, L., Melosh, H.J., Vaquero, M., Howell, K.C., 2013. Transfer of Impact Ejecta Material from the Surface of Mars to Phobos and Deimos. *Astrobiology 13*, 963–980. https://doi.org/10.1089/ast.2012.0942

Chesley, S.R., Farnocchia, D., Nolan, M.C., Vokrouhlický, D., Chodas, P.W., Milani, A., Spoto, F., Rozitis, B., Benner, L.A.M., Bottke, W.F., Busch, M.W., Emery, J.P., Howell, E.S., Lauretta, D.S., Margot, J.-L., Taylor, P.A., 2014. Orbit and bulk density of the OSIRIS-REx target Asteroid (101955) Bennu. *Icarus 235*, 5–22. https://doi.org/10.1016/j.icarus.2014.02.020

Christiansen, E., Cykowski, E., Ortega, J., 1993. Highy oblique impacts into thick and thin targets. *International Journal of Impact Engineering, 14,* 157-168. doi:10.1016/0734-743x(93)90017-2

Chyba, C.F., 1991. Terrestrial mantle siderophiles and the lunar impact record. *Icarus 92,* 217–233. doi:10.1016/0019-1035(91)90047-w

Chyba, C. F., Owen, T. C., Ip, W. H., 1994. Impact Delivery of Volatiles and Organic Molecules to Earth, in *Hazards Due to Comets and Asteroids* (T. Gehrels, ed.), pp. 9–58, University of Arizona Press, Tucson.

Cohen, B. A., Swindle, T. D., Kring, D. A., 2000. Support for the Lunar Cataclysm Hypothesis from Lunar Meteorite Impact Melt Ages. *Science* 290(5497), 1754-1756.

Colaprete, A., Schultz, P., Heldmann, J., Wooden, D., Shirley, M., Ennico, K., Hermalyn, B., Marshall, W., Ricco, A., Elphic, R.C., Goldstein, D., Summy, D., Bart, G.D., Asphaug, E., Korycansky, D., Landis, D., Sollitt, L., 2010. Detection of Water in the LCROSS Ejecta Plume. *Science 330*, 463–468. https://doi.org/10.1126 science.1186986

Colaprete, A., Andrews, D., Bluethmann, W., Elphic, R.C., Bussey, B., Trimble, J., Zacny, K. and Captain, J.E., 2019. An overview of the volatiles investigating polar exploration rover (VIPER) mission. In: *AGU Fall Meeting Abstracts,* 2019, P34B-03.

Collins, G. S., 2002. An Introduction to Hydrocode Modeling,, Applied Modelling and Computation Group, Imperial College London. Available online at: http://citeseerx.ist.psu.edu/viewdoc/download?doi=10.1.1.515.4016&rep=rep1&type=pdf [Accessed 01/09/2022]

Collins, G. S., 2014. Numerical simulations of impact crater formation with dilatancy. *Journal of Geophysical Research: Planets 119*, 2600–2619. doi:10.1002/2014JE004708.

Collins, G. S., Melosh, H., Ivanov, B., 2004. Modeling damage and deformation in impact simulations. *Meteoritics & Planetary Science 39(2)*, 217-231.

Collins, G. S., Melosh, H. J., Wünnemann, K., 2011a. Improvements to the epsilon-alpha porous compaction model for simulating impacts into high-porosity Solar System objects. *International Journal of Impact Engineering 38,* 434-439.

Collins, G.S., Elbeshausen, D., Davison, T.M., Robbins, S.J., Hynek, B.M., 2011b. The size-frequency distribution of elliptical impact craters. *Earth and Planetary Science Letters 310*, 1–8. https://doi.org/10.1016/j.epsl.2011.07.023

Collins, G. S., Melosh, H. J., Osinski, G. R., 2012. The Impact-Cratering Process. *Elements 8*, 25-30. doi:10.2113/gselements.8.1.25

Collins, G.S., Patel, N., Davison, T.M., Rae, A.S.P., Morgan, J.V., Gulick, S.P.S., 2020. A steeply-inclined trajectory for the Chicxulub impact. *Nature Communications 11*. https://doi.org/10.1038 s41467-020-15269-x

Consolmagno, G., Britt, D., Macke, R., 2008. The significance of meteorite density and porosity. *Geochemistry 68*, 1-29. doi:10.1016/j.chemer.2008.01.003

Crawford, I. A., 2015. Lunar resources. *Progress in Physical Geography: Earth and Environment 39*, 137–167. doi:10.1177/0309133314567585

Crawford, I. A., Joy, K. H., 2014. Lunar exploration: opening a window into the history and evolution of the inner Solar System, *Philosophical Transactions of the Royal Society 372,* 20130315.

Crawford, I.A., Joy, K.H., Fagents, S.A., 2007. Full Moon exploration. *Astronomy & Geophysics 48*, 3.18–3.21. doi:10.1111/j.1468-4004.2007.48318.x

Crawford, I. A., Baldwin, E., Taylor, E., Bailey, J., Tsembelis, K., 2008. On the Survivability and Detectability of Terrestrial Meteorites on the Moon, *Astrobiology 8*, 242-252.

Cronin, J. R., Moore, C. B., 1971. Amino Acid Analyses of the Murchison, Murray, and Allende Carbonaceous Chondrites. *Science 172*, 1327–1329. doi:10.1126 science.172.3990.1327

Daly, R. T., Schultz, P. H., 2013. Experimental studies into the survival and state of the projectile. *Lunar & Planetary Science XXXXIV*. Abstract #2240.

Daly, R. T., Schultz, P. H., 2015. Predictions for impactor contamination on Ceres based on hypervelocity impact experiments. *Geophysical Research Letters 42(19)*, 7890-7898.

Daly, R., Schultz, P., 2016. Delivering a projectile component to the Vestan regolith. *Icarus 264*, 9-19. doi:10.1016/j.icarus.2015.08.034

Davison, T. M., Collins, G. S., Elbeshausen, D., Wünnemann, K., Kearsley, A., 2011. Numerical modeling of oblique hypervelocity impacts on strong ductile targets. *Meteoritics & Planetary Science 46(10)*, 1510-1524.

Davison, T. M., Collins, G. S., Bland, P. A., 2016. Mesoscale Modeling of Impact Compaction of Primitive Solar System Solids. *The Astrophysical Journal 821(1)*, 68. doi:10.3847/0004-637x/821/1/68

Davison, T. M., Baijal, N., Collins, G. S., 2022. High Resolution Oblique Impact Simulations of the Formation of the South Pole-Aitken Basin. *53rd Lunar and Planetary Science Conference*, Abstract #2444. Available at: https://www.hou.usra.edu/meetings/lpsc2022/pdf/2444.pdf

Day, J. M. D., Floss, C., Taylor, L. A., Anand, M., Patchen, A. D., 2006. *Geochimica et Cosmochimica Acta 70*, 5957–5989. doi:10.2113/gselements.8.1.25

De Carli, P.S., El Goresy, A., Xie, Z., Sharp, T.G., 2007. Ejection mechanisms for Martian meteorites. *AIP Conference Proceedings 955(1)*, 1371-1374. American Institute of Physics.

De Carli, P.S., 2013. Meteorites from Mars via a Natural Two-stage Gas Gun. *Procedia Engineering 58*, 570–573. https://doi.org/10.1016/j.proeng.2013.05.065

De Sanctis, M.C., Coradini, A., Ammannito, E., Filacchione, G., Capria, M.T., Fonte, S., Magni, G., Barbis, A., Bini, A., Dami, M., Ficai-Veltroni, I., Preti, G., 2010. The VIR Spectrometer. *Space Science Reviews 163*, 329–369. https://doi.org/10.1007 s11214-010-9668-5

De Sanctis, M.C., Combe, J.-P., Ammannito, E., Palomba, E., Longobardo, A., McCord, T.B., Marchi, S., Capaccioni, F., Capria, M.T., Mittlefehldt, D.W., Pieters, C.M., Sunshine, J., Tosi, F., Zambon, F., Carraro, F., Fonte, S., Frigeri, A., Magni, G., Raymond, C.A., Russell, C.T., 2012. Detection Of Widespread Hydrated Materials on Vesta by the VIR Imaging Spectrometer on-board the Dawn Mission. *The Astrophysical Journal 758*, L36. https://doi.org/10.1088/2041-8205/758/2/l36

Demidova, S.I., Whitehouse, M.J., Merle, R., Nemchin, A.A., Kenny, G.G., Brandstätter, F., Ntaflos, Th., Dobryden, I., 2022. A micrometeorite from a stony asteroid identified in Luna 16 soil. *Nature Astronomy 6*, 560–567. https://doi.org/10.1038 s41550-022-01623-0

DesMarais, D.J., 1978. Carbon, nitrogen and sulfur in Apollo 15, 16 and 17 rocks. In *Lunar and Planetary Science Conference Proceedings 9*, 2451-2467.

DesMarais, D. J., Hayes, J.M., Meinschein, W. G., 1973. The distribution in lunar soil of carbon released by pyrolysis. *Proceedings from the Lunar Science Conference 4*, 1543-1558.

Desai, C. S., Saadatmanesh, H., Girdner, K., 1993. Development and mechanical properties of structural materials from lunar stimulants. In: *Resources of near-earth space*, 297–324. University of Arizona Press, Arizona.

Ding, C., Su, Y., Xing, S., Dai, S., Xiao, Y., Feng, J., Liu, D., Li, C., 2017. Numerical Simulations of the Lunar Penetrating Radar and Investigations of the Geological Structures of the Lunar Regolith Layer at the Chang'E 3 Landing Site. *International Journal of Antennas and Propagation 2017*, 1–11. https://doi.org/10.1155/2017/3013249

Ding, C., Xiao, Z., Su, Y., Zhao, J., Cui, J., 2020. Compositional variations along the route of Chang'e-3 Yutu rover revealed by the lunar penetrating radar. *Progress in Earth and Planetary Science 7*. https://doi.org/10.1186 s40645-020-00340-4

Dong, Z., Fang, G., Zhou, B., Zhao, D., Gao, Y., Ji, Y., 2021. Properties of Lunar Regolith on the Moon's Farside Unveiled by Chang'E-4 Lunar Penetrating Radar. *Journal of Geophysical Research: Planets 126.* https://doi.org/10.1029/2020je006564

Drucker, D.C., Prager, W., 1952. Soil Mechanics and Plastic Analysis on Limit Design. *Journal of applied Mathematics 10*, 157-165.

Duke, M.B., Blair, B.R., Diaz, J., 2003. Lunar resource utilization: Implications for commerce and exploration. *Advances in Space Research 31*, 2413–2419. https://doi.org/10.1016 s0273-1177(03)00550-7

Duke, M.B., Gaddis L.R., Taylor G.J., Schmitt, H.H., 2006. Development of the Moon. *Reviews in Mineralogy and Geochemistry 60*, 597–656.

Dunham, D.W., Dunham, J.B., Binzel, R.P., Evans, D.S., Freuh, M., Henry, G.W., A'Hearn, M.F., Schnurr, R.G., Betts, R., Haynes, H., Orcutt, R., Bowell, E., Wasserman, L.H., Nye, R.A., Giclas, H.L., Chapman, C.R., Dietz, R.D., Moncivais, C., Douglass, W.T., Parker, D.C., 1990. The size and shape of (2) Pallas from the 1983 occultation of 1 Vulpeculae. *The Astronomical Journal 99*, 1636. https://doi.org/10.1086/115446

Eckart, P., 1999. The lunar base handbook : an introduction to lunar base design, development, and operations. Mcgraw-Hill, New York.

Ehlmann, B. L., Klima, R. L., Bennett, C. L., Blaney, D., Bowles, N., Calcutt, S., Dickson, J., Donaldson Hanna, K., Edwards, C. S., Green, R., House, M. A., Klesh, A., McCaa, C., Miura, J., Pieters, C., Seybold, C., Thompson, D., Williamson, W., Wood, J., 2022. Lunar Trailblazer: A Pioneering Smallsat for Lunar Water and Lunar Geology. *53rd Lunar and Planetary Science Conference*, Abstract# 2316.

Ehrenfreund, P., Glavin, D.P., Botta, O., Cooper, G., Bada, J.L., 2001. Extraterrestrial amino acids in Orgueil and Ivuna: Tracing the parent body of CI type carbonaceous chondrites. *Proceedings of the National Academy of Sciences 98*, 2138–2141. https://doi.org/10.1073/pnas.051502898

Eigenbrode, J.L., Summons, R.E., Steele, A., Freissinet, C., Millan, M., Navarro-González, R., Sutter, B., McAdam, A.C., Franz, H.B., Glavin, D.P., Archer, P.D., Mahaffy, P.R., Conrad, P.G., Hurowitz, J.A., Grotzinger, J.P., Gupta, S., Ming, D.W., Sumner, D.Y., Szopa, C., Malespin, C., 2018. Organic matter preserved in 3-billion-year-old mudstones at Gale crater, Mars. *Science 360*, 1096–1101. doi:10.1126 science.aas9185

Elbeshausen, D., Wünnemann, K., 2011. iSALE-3D: A three-dimensional, multi- material, multi-rheology hydrocode and its applications to large scale geodynamic processes. *Proceedings of 11th Hypervelocity Impact Symposium 287,* 301.

Elbeshausen, D., Wünnemann, K., Collins, G. S., 2009. Scaling of oblique impacts in frictional targets: Implications for crater size and formation mechanisms. *Icarus 204*, 716-731. doi: 10.1016/j.icarus.2009.07.018

Elbeshausen, D., Wünnemann, K., Collins, G. S., 2013. The transition from circular to elliptical impact craters. *Journal of Geophysical Research: Planets 118*, 2295–2309. doi:10.1002/2013je004477

Ellery, A., 2020. Sustainable in-situ resource utilization on the moon. *Planetary and Space Science 184*, 104870. https://doi.org/10.1016/j.pss.2020.104870

Elliott, J.R., Melosh, H.J., Johnson, B.C., 2022. The role of target strength on the ejection of martian meteorites. *Icarus 375*, 114869. https://doi.org/10.1016/j.icarus.2021.114869

Epstein, S., Taylor, H.P., Jr., 1970. The concentration and isotopic composition of hydrogen, carbon and silicon in Apollo 11 lunar rocks and minerals. *Proceedings from the Apollo 11 Lunar Science Conference,* 1085-1096.

Epstein, S., Taylor, H.P., Jr., 1972. O^{18}/O^{16} Si^{30} si^{28} C^{13}/C^{12}, and D/H studies of Apollo 14 and 15 samples. *Proceedings from the Lunar Science Conference 3*, 1429-1454.

Fagents, S. A., Elise Rumpf, M., Crawford, I. A., Joy, K. H., 2010. Preservation potential of implanted solar wind volatiles in lunar paleoregolith deposits buried by lava flows. *Icarus 207,* 595–604. doi:10.1016/j.icarus.2009.11.033

Fang, G.-Y., Zhou, B., Ji, Y.-C., Zhang, Q.-Y., Shen, S.-X., Li, Y.-X., Guan, H.-F., Tang, C.-J., Gao, Y.-Z., Lu, W., Ye, S.-B., Han, H.-D., Zheng, J., Wang, S.-Z., 2014. Lunar Penetrating Radar onboard the Chang'e-3 mission. *Research in Astronomy and Astrophysics 14,* 1607–1622. https://doi.org/10.1088/1674-4527/14/12/009

Fegley, B., Swindle, T.D., 1993. Lunar volatiles: implications for lunar resource utilization. In: J. Lewis, M. S. Matthews, and M. L. Guerrieri, (Eds.), *Resources of Near-Earth Space,* 367-426. University of Arizona Press, Arizona, U.S..

Feldman, W.C., Barraclough, B.L., Maurice, S., Elphic, R.C., Lawrence, D.J., Thomsen, D.R., Binder, A.B., 1998. Major Compositional Units of the Moon: Lunar Prospector Thermal and Fast Neutrons. *Science 281*, 1489–1493. https://doi.org/10.1126 science.281.5382.1489

Feldman, W.C., Maurice, S., Lawrence, D.J., Little, R.C., Lawson, S.L., Gasnault, O., Wiens, R.C., Barraclough, B.L., Elphic, R.C., Prettyman, T.H., Steinberg, J.T., Binder, A.B., 2001. Evidence for water ice near the lunar poles. *Journal of Geophysical Research: Planets 106,* 23231–23251. https://doi.org/10.1029/2000je001444

Fray, D.J., Farthing, T.W., Chen, Z., 1999. Removal of Oxygen from Metal Oxides and Solid Solutions by Electrolysis in a Fused Salt. *International Patent*, WO/99/64638.

French, B., 1998. Traces of catastrophe. 1st ed. Houston, Texas, Lunar and Planetary Institute, 18-23.

Friedman, I., Gleason, J. D., Hardcastle, K. G., 1970. Water, hydrogen, deuterium, carbon and C^{13} content of selected lunar material. *Proceedings from the Apollo 11 Lunar Science Conference,* 1103-1109.

Friedman, I., O'Neil, J. R., Gleason, J. D., Hardcastle, K., 1971. The carbon and hydrogen content and isotopic composition of some Apollo 12 materials. *Proceedings from the Lunar Science Conference 2*, 1407-1415.

Friedman, I., Hardcastle, K. G., Gleason, J. D., 1972. Isotopic composition of carbon and hydrogen in some Apollo 14 and 15 samples, In: J. W. Chamberlain and C. Watkins (Eds.), *The Apollo 15 Lunar Samples,* 302-306, Lunar and Planetary Institute, Houston, Texas.

Fritz, J., Greshake, A., Hecht, L., Stöffler, D., 2002. Shock metamorphism of Martian meteorites: New data from quantitative shock barometry. *33rd Lunar and Planetary Science Conference,* Abstract #1504.

Fritz, J.,, Greshake, A., Stöffler, D., 2004. Micro-Raman spectroscopy of plagioclase and maskelynite in Martian meteorites: Evidence of progressive shock metamorphism. *Antarctic Meteorites 28,* 10–11.

Fritz, J., Artemieva, N., Greshake, A., 2005. Ejection of Martian meteorites. *Meteoritics & Planetary Science 40*, 1393–1411. https://doi.org/10.1111/j.1945-5100.2005.tb00409.x

Fujita, K., Kurosawa, K., Genda, H., Hyodo, R., Matsuyama, S., Yamagishi, A., Mikouchi, T., Niihara, T., 2019. Assessment of the probability of microbial contamination for sample return from Martian moons I: Departure of microbes from Martian surface. *Life Sciences in Space Research 23*, 73–84. https://doi.org/10.1016/j.lssr.2019.07.009

Funkhouser, J. G., Schaeffer, O. A., Bogard, D. D., Zahringer, J., 1970. Gas analysis of the lunar surface. *Proceedings from the Apollo 11 Lunar Science Conference*, 1111-1116.

Füri, E., Marty, B., 2015. Nitrogen isotope variations in the Solar System. *Nature Geoscience 8*, 515–522. https://doi.org/10.1038/ngeo2451

Gawronska, A.J., Barrett, N., Boazman, S.J., Gilmour, C.M., Halim, S.H., Harish, McCanaan, K., Satyakumar, A.V., Shah, J., Meyer, H.M., Kring, D.A., 2020. Geologic context and potential EVA targets at the lunar south pole. *Advances in Space Research 66,* 1247-1264. https://doi.org/10.1016/j.asr.2020.05.035

Gibson, E.K., 1977. Volatile elements, carbon, nitrogen, sulfur, sodium, potassium and rubidium in the lunar regolith. *Physics and Chemistry of the Earth 10*, 57–62. https://doi.org/10.1016/0079-1946(77)90006-4

Gibson, E. K., Moore, G. W., 1973. Carbon and sulfur distributions and abundances in lunar fines. *Proceedings from the Lunar Science Conference 4,* 1577-1586.

Gingold, R. A., Monaghan, J. J., 1977. 'Smoothed particle hydrodynamics – Theory and application to non-spherical stars'. *Monthly Notices of the Royal Astronomical Society 181,* 375–389.

Gläser, P., Scholten, F., De Rosa, D., Figuera, R.M., Oberst, J., Mazarico, E., Neumann, G.A., Robinson, M.S., 2014. Illumination conditions at the lunar south pole using high resolution digital terrain models from LOLA. *Icarus 243*, 78–90. https://doi.org/10.1016/j.icarus.2014.08.013.

Glavin, D. P., Bada, J. L., 2001. Survival of amino acids in micrometeorites during atmospheric entry. *Astrobiology 1*, 259–269. https://doi.org/10.1089/15311070152757456

Goldin, T., Wünnemann, K., Melosh, H., Collins, G., 2006. Hydrocode modeling of the Sierra Madera impact structure. *Meteoritics & Planetary Science 41(12)*, 1947-1958. doi: 10.1111/j.1945-5100.2006.tb00462.x

Goldstein, J. I., Henderson, E. P., Yakowitz, H., 1970. Investigation of lunar metal particles. *Geochimica et Cosmochimica Acta Supplement*, Volume 1. Proceedings of the Apollo 11 Lunar Science Conference, Houston, TX. *Volume 1: Mineralogy and Petrology*. Edited by A. A. Levinson. New York: Pergammon Press, 1970., 499-512.

Gomes, R., Levison, H., Tsiganis, K., Morbidelli, A., 2005. Origin of the cataclysmic Late Heavy Bombardment period of the terrestrial planets. *Nature 435(7041)*, 466-469.

Grady, D.E., Kipp, M.E., 1980. Continuum modelling of explosive fracture in oil shale. *International Journal of Rock Mechanics and Mining Sciences & Geomechanics Abstracts 17*, 147–157. https://doi.org/10.1016/0148-9062(80)91361-3

Green, R.O., Pieters, C., Mouroulis, P., Eastwood, M., Boardman, J., Glavich, T., Isaacson, P., Annadurai, M., Besse, S., Barr, D., Buratti, B., Cate, D., Chatterjee, A., Clark, R., Cheek, L., Combe, J., Dhingra, D., Essandoh, V., Geier, S., Goswami, J.N., 2011. The Moon Mineralogy Mapper (M3) imaging spectrometer for lunar science: Instrument description, calibration, on-orbit measurements, science data calibration and on-orbit validation. *Journal of Geophysical Research 116*. https://doi.org/10.1029/2011je003797

Güldemeister, N., Wünnemann, K., Durr, N., Hiermaier, S., 2013. Propagation of impact-induced shock waves in porous sandstone using mesoscale modeling. *Meteoritics & Planetary Science 48*, 115-133. doi:10.1111/j.1945-5100.2012.01430.x

Gutiérrez, J. L., 2002. Terrene meteorites in the Moon: their relevance for the study of the origin of life in the Earth. *ESA SP-518*, 187-191.

Halim, S.H., Crawford, I.A., Collins, G.S., Joy, K.H., Davison, T.M**.,** 2021a. Assessing the Survivability of Biomarkers within Terrestrial Material Impacting the Lunar Surface. *Icarus 354*, 114026. https://doi.org/10.1016/j.icarus.2020.114026

Halim, S.H., Barrett, N., Boazman, S.J., Gawronska, A.J., Gilmour, C.M., Harish, McCanaan, K., Satyakumar, A.V., Shah, J., Kring, D.A., 2021b. Numerical Modeling of the Formation of Shackleton Crater at the Lunar South Pole. *Icarus 354*, 113992. https://doi.org/10.1016/j.icarus.2020.113992

Halim, S.H., Crawford, I.A., Collins, G.S., Joy, K.H., Davison, T.M., *In Prep*. Modelling the survival of carbonaceous chondrites impacting the lunar surface as a potential resource.

Hanuš, J., Viikinkoski, M., Marchis, F., Ďurech, J., Kaasalainen, M., Delbo', M., Herald, D., Frappa, E., Hayamizu, T., Kerr, S., Preston, S., Timerson, B., Dunham, D., Talbot, J., 2017. Volumes and bulk densities of forty asteroids from ADAM shape modeling. *Astronomy & Astrophysics 601*, A114. https://doi.org/10.1051/0004-6361/201629956

Hapke, B., Sato, H., 2016. The porosity of the upper lunar regolith. *Icarus 273*, 75–83. https://doi.org/10.1016/j.icarus.2015.10.031

Harland, D.M., 1999. Exploring The Moon : The Apollo Expeditions. Springer, New York.

Hartmann, W., 1975. Lunar "cataclysm": A misconception?. *Icarus 24(2)*, 181-187.

Hartmann, W., 2003. Megaregolith evolution and cratering cataclysm models-Lunar cataclysm as a misconception (28 years later). *Meteoritics & Planetary Science 38(4)*, 579-593.

Hartmann, W., 2019. History of the Terminal Cataclysm Paradigm: Epistemology of a Planetary Bombardment That Never (?) Happened. *Geosciences 9(7)*, 285. doi:10.3390/geosciences9070285

Haruyama, J., Ohtake, M., Matsunaga, T., Morota, T., Honda, C., Yokota, Y., 2008. Lack of exposed ice inside lunar south pole Shackleton crater. *Science 322(5903)*, 938–939. doi:10.1126 science.1164020

Haskin, L. A., and Warren, P. H. 1991. Chemistry. In: G. H. Heiken, D. T. Vaniman, & B. M. French (Eds.), *Lunar Sourcebook, A User's Guide to the Moon*, 357-474. Cambridge University Press, Cambridge, U.K..

Haskin, L. A., Colson, R. O., Vaniman, D. T., Gillett, S. L., 1993. A geochemical assessment of possible lunar ore formation. In: Lewis, J., Matthews, M. S., Guerrieri, M. L., (eds) *Resources of Near Earth Space*. Tucson: Tucson University Press, 17–50.

Hawke, B.R., Head, J.W., 1977. Impact melt on lunar crater rims. In: Roddy, D.J., Pepin, R.B., Merrill, R.B. (Eds.), Impact and Explosion Cratering. Pergamon, New York, pp. 815–841.

Head, J.N., Melosh, H.J., Ivanov, B.A., 2002. Martian Meteorite Launch: High-Speed Ejecta from Small Craters. *Science 298*, 1752–1756. https://doi.org/10.1126 science.1077483

Heiken, G. H., Vaniman, D. T., French B. M., 1991. Lunar sourcebook - A user's guide to the moon. Cambridge University Press, Cambridge, U.K.. Available online at: https://www.lpi.usra.edu/publications/books/lunar_sourcebook

Herbold, E. B., Owen, J. M., Swift, D. C., Miller, P. L., 2015. Simulations of defense strategies for Bennu: Material characterization and impulse delivery, *Procedia Engineering*. 173–180. doi:10.1016/j.proeng.2015.04.024

Herd, C., Blinova, A., Simkus, D., Huang, Y., Tarozo, R., Alexander, C., Gyngard, F., Nittler, L., Cody, G., Fogel, M., Kebukawa, Y., Kilcoyne, A., Hilts, R., Slater, G., Glavin, D., Dworkin, J., Callahan, M., Elsila, J., De Gregorio, B., Stroud, R., 2011. Origin and Evolution of Prebiotic Organic Matter As Inferred from the Tagish Lake Meteorite. *Science 332*, 1304-1307. doi:10.1126 science.1203290

Herrmann, W., 1969. Constitutive equation for the dynamic compaction of ductile porous materials. *Journal of Applied Physics 40(6)*, 2490–2499.

Hibbert, R., Cole, M.J., Price, M.C., Burchell, M.J., 2017. The Hypervelocity Impact Facility at the University of Kent: Recent Upgrades and Specialized Capabilities. *Procedia Engineering 204*, 208–214. doi:10.1016/j.proeng.2017.09.775

Hiroi, T., Pieters, C.M., Zolensky, M.E., Lipschutz, M.E., 1993. Evidence of Thermal Metamorphism on the C, G, B, and F Asteroids. *Science 261*, 1016–1018. https://doi.org/10.1126 science.261.5124.1016

Hiroi, T., Zolensky, M.E., Pieters, C.M., 2001. The Tagish Lake Meteorite: A Possible Sample from a D-Type Asteroid. *Science 293*, 2234–2236. https://doi.org/10.1126 science.1063734

Hodges, R.R., 1973. Helium and hydrogen in the lunar atmosphere. *Journal of Geophysical Research 78*, 8055–8064. https://doi.org/10.1029/ja078i034p08055

Hodges, R.R., 2016. Methane in the lunar exosphere: Implications for solar wind carbon escape. *Geophysical Research Letters 43*, 6742–6748. https://doi.org/10.1002/2016gl068994

Honniball, C.I., Lucey, P.G., Li, S., Shenoy, S., Orlando, T.M., Hibbitts, C.A., Hurley, D.M., Farrell, W.M., 2021. Molecular water detected on the sunlit Moon by SOFIA. *Nature Astronomy 5*, 1–7. https://doi.org/10.1038 s41550-020-01222-x

Hörz, F., Grieve, R., Heiken, G., Spudis, P., Binder, A., 1991. Lunar Surface Processes. In: G. H. Heiken, D. T. Vaniman, & B. M. French (Eds.), *Lunar Sourcebook, A User's Guide to the Moon*, 61–120. Cambridge University Press, Cambridge, U.K.

Hossner, L.R., Allen, E.R., 1989. Nutrient Availability and Element Toxicity in Lunar-Derived Soils. *Lunar Base Agriculture: Soils for Plant Growth*, 85-92.

Huss, G. R., Lewis, R. S., 1994. Noble gases in presolar diamonds I: Three distinct components and their implications for diamond origins. *Meteoritics 29*, 791–810. doi:10.1111/j.1945-5100.1994.tb01094.x

Hyodo, R., Genda, H., 2020. Escape and Accretion by Cratering Impacts: Formulation of Scaling Relations for High-speed Ejecta. *The Astrophysical Journal 898*, 30. https://doi.org/10.3847/1538-4357/ab9897

International Space Exploration Coordination Group (ISECG), 2020. Global Exploration Roadmap: Lunar Surface Exploration Scenario Update. National Aeronautics and Space Administration Headquarters, Washington, DC 20546-0001. Available at: http://www.globalspaceexploration.org

Ivanov, B. A., 2001. Mars/Moon Cratering Rate Ratio Estimates. *Space Science Reviews 96*, 87–104. doi:10.1023/a:1011941121102

Ivanov, B. A., Deniem, D., Neukum, G., 1997. Implementation of dynamic strength models into 2D hydrocodes: Applications for atmospheric breakup and impact cratering. *International Journal of Impact Engineering 20*, 411-430.

Izquierdo, K., Sori, M.M., Soderblom, J.M., Johnson, B.C., Wiggins, S.E., 2021. Lunar Megaregolith Structure Revealed by GRAIL Gravity Data. *Geophysical Research Letters 48*. https://doi.org/10.1029/2021gl095978

Jenniskens, P., Damer, B., Norkus, R., Pilorz, S., Nott, J., Grigsby, B., Adams, C., Blair, B.R., 2015. SHEPHERD: A Concept for Gentle Asteroid Retrieval with a Gas-Filled Enclosure. *New Space 3,* 36–43. https://doi.org/10.1089 space.2014.0024

Johnson, B. C., Bowling, T. J., and Melosh, H. J., 2014. Jetting during vertical impacts 49 of spherical projectiles. *Icarus 238*, 13-22. doi:10.1016/j.icarus.2014.05.003.

Johnson, B. C., Minton, D. A., Melosh, H. J., and Zuber, M. T., 2015, Impact jetting as the origin of chondrules. *Nature 517*, 339-341.

Johnson, G. R., Cook, W. H., 1985. Fracture characteristics of three metals subjected to various strains, strain rates, temperatures and pressures. *Engineering Fracture Mechanics 21 (1)*, 31–48.

Johnson, N.L., 1979. Handbook of Soviet lunar and planetary exploration. NASA STI/Recon Technical Report A 80, 24653.

Jolliff, B. L., Korotev, R. L., Haskin, L. A., 1993. An iridium-rich iron micrometeorite with silicate inclusions from the Moon. *Lunar & Planetary Science XXIV*, Abstract #1366.

Jolliff, B.L., Gillis, J.J., Haskin, L.A., Korotev, R.L., Wieczorek, M.A., 2000. Major lunar crustal terranes: Surface expressions and crust-mantle origins. *Journal of Geophysical Research: Planets 105*, 4197–4216. https://doi.org/10.1029/1999je001103

Joy, K.H., Arai, T., 2013. Lunar meteorites: new insights into the geological history of the Moon. *Astronomy & Geophysics 54,* 4.28–4.32. https://doi.org/10.1093/astrogeo/att121

Joy, K. H., Zolensky, M. E., Nagashima, K., Huss, G. R., McKay, D. S., Ross, D. S., Kring, D. A., 2012. Direct Detection of Projectile Relics from the End of the Lunar Basin–Forming Epoch. *Science 336*, 1426–1429. doi: 10.1126 sscience.1219633.

Joy, K. H., Crawford, I. A., Curran, N., Zolensky, M., Fagan, A., Kring, D. A., 2016. The Moon: An Archive of Small Body Migration in the Solar System. *Earth, Moon, & Planets 118(2-3)*, 133-158.

Joy, K. H., Tartèse, R., Messenger, S., Zolensky, M. E., Marrocchi, Y., Frank ,D. R., Kring D. A. 2020 The isotopic composition of volatiles in the unique Bench Crater carbonaceous chondrite impactor found in the Apollo 12 regolith. *Earth and Planetary Science Letters 540,* 116265 doi.org/10.1016/j.epsl.2020.116265

Jutzi, M., Benz, W., Michel, P., 2008. Numerical simulations of impacts involving porous bodies. *Icarus 198(1)*, 242-255. doi:10.1016/j.icarus.2008.06.013

Kallemeyn G. W., Wasson J. T., 1981. The compositional classification of chondrites: I. The carbonaceous chondrite groups. *Geochimica et Cosmochimica Acta 45*, 1217–1230.

Kallemeyn G. W., Wasson J. T., 1982. The compositional classification of chondrites: III. Ungrouped carbonaceous chondrites. *Geochimica et Cosmochimica Acta 46*, 2217–2228.

Kallemeyn, G. W., Rubin, A., Wasson, J. T., 1994. The compositional classification of chondrites: VI. The CR carbonaceous chondrite group. *Geochimica et Cosmochimica Acta 58*, 2873-2888. doi:10.1016/0016-7037(94)90121-x

Kanhaiya, P.S., Yu, A., Netzer, R., Kemp, W., Doyle, D., Shulaker, M.M., 2021. Carbon Nanotubes for Radiation-Tolerant Electronics. *ACS Nano 15*, 17310–17318. https://doi.org/10.1021/acsnano.1c04194

Kaplan, I. R., Petrowski, C., 1971. Carbon and sulfur isotope studies on Apollo 12 lunar samples. *Proceedings from the Lunar Science Conference 2*, 1397-1406.

Kaplan, I. R., Smith, J. W., Ruth, E., 1970. Carbon and sulfur concentration and isotopic composition in Apollo 11 lunar samples. *Proceedings from the Apollo 11 Lunar Science Conference*, 1317-1329.

Kaplan, I. R., Kerridge, J. F., Petrowski, C., 1976. Light element geochemistry of the Apollo 15 site. *Proceedings from the Lunar Science Conference 7*, 481-492.

Kaur, P., Chauhan, P., Rajawat, A.S., Kumar, A.S.K., 2015. Study of olivine-rich dark halo crater – Beaumont L in Mare Nectaris using high resolution remote sensing data. *Planetary and Space Science 109-110*, 92–105. https://doi.org/10.1016/j.pss.2015.02.001

Kaydash, V., Shkuratov, Y., Videen, G., 2014. Dark halos and rays of young lunar craters: A new insight into interpretation. *Icarus 231*, 22–33. https://doi.org/10.1016/j.icarus.2013.11.025

Keller, W. D., Huang, W. H., 1971. Response of Apollo 12 lunar dust to reagents simulative of those in the weathering environment of Earth. *Lunar and Planetary Science Conference Proceedings 2,* 973.

Kerridge, J.F., 1975. Solar Nitrogen: Evidence for a Secular Increase in the Ratio of Nitrogen-15 to Nitrogen-14*. Science 188*, 162–164. https://doi.org/10.1126 sscience.188.4184.162

Kerridge, J.F., 1993. Long-term compositional variation in solar corpuscular radiation: Evidence from nitrogen isotopes in the lunar regolith. *Reviews of Geophysics 31*, 423. https://doi.org/10.1029/93rg01953

Kieffer, S.W., 1977. Impact conditions required for formation of melt by jetting in silicates. In: Roddy, D.J., Pepin, R.O., Merrill, R.B. (Eds.), *Impact and Explosion Cratering*. Pergamon Press, pp. 751–769

Koga, T., Naraoka, H., 2017. A new family of extraterrestrial amino acids in the Murchison meteorite. Scientific Reports 7, *636.* doi:10.1038/s41598-017-00693-9.

Kring, D. A., Kramer, G. Y., Collins, G. S., Potter, R. W. K., Chandnani, M., 2016. Peak-ring structure and kinematics from a multi-disciplinary study of the Schrödinger impact basin. *Nature Communications 7.* doi:10.1038/ncomms13161

Krot A. N., Meibom A., Keil K., 2000. A clast of Bali-like oxidized CV3 material in the reduced CV3 chondrite breccia Vigarano. *Meteoritics & Planet. Science 35*, 817–827

Krot A. N., Meibom A., Weisberg M. K., Keil K., 2002. The CR chondrite clan: Implications for early Solar System processes. *Meteoritics & Planet. Sci*ence *37*, 1451–1490.

Kuiper, G. P., 1960. Orthographic Atlas of the Moon. University of Arizona Press. University of Arizona. Lunar and Planetary Laboratory.

Kuramoto, K., Kawakatsu, Y., Fujimoto, M., Araya, A., Barucci, M.A., Genda, H., Hirata, N., Ikeda, H., Imamura, T., Helbert, J., Kameda, S., Kobayashi, M., Kusano, H., Lawrence, D.J., Matsumoto, K., Michel, P., Miyamoto, H., Morota, T., Nakagawa, H., Nakamura, T., 2022. Martian moons exploration MMX: sample return mission to Phobos elucidating formation processes of habitable planets. *Earth, Planets and Space 74*. doi:10.1186 s40623-021-01545-7

Kurosawa, K., Genda, H., 2018. Effects of Friction and Plastic Deformation in Shock-Comminuted Damaged Rocks on Impact Heating. *Geophysical Research Letters 45*, 620–626. https://doi.org/10.1002/2017gl076285

Kurosawa, K., Nagaoka, Y., Senshu, H., Wada, K., Hasegawa, S., Sugita, S., and Matsui, T., 2015. Dynamics of hypervelocity jetting during oblique impacts of spherical projectiles investigated via ultrafast imaging. *Journal of Geophysical Research: Planets 120*, doi:10.1002/2014JE004730.

Kurosawa, K., Okamoto, T., Genda, H., 2018. Hydrocode modeling of the spallation process during hypervelocity impacts: Implications for the ejection of Martian meteorites. *Icarus 301*, 219–234. https://doi.org/10.1016/j.icarus.2017.09.015

Kurosawa, K., Genda, H., Hyodo, R., Yamagishi, A., Mikouchi, T., Niihara, T., Matsuyama, S., Fujita, K., 2019. Assessment of the probability of microbial contamination for sample return from Martian moons II: The fate of microbes on Martian moons. *Life Sciences in Space Research 23*, 85–100. https://doi.org/10.1016/j.lssr.2019.07.006

Laborda-López, C., Aguirre, J., Donovan, S., 2015. Surviving metamorphism: taphonomy of fossil assemblages in marble and calc-silicate schist. *Palaios 30(9),* 668-679. doi:10.2110/palo.2015.013

Lauretta, D.S., Bartels, A.E., Barucci, M.A., Bierhaus, E.B., Binzel, R.P., Bottke, W.F., Campins, H., Chesley, S.R., Clark, B.C., Clark, B.E., Cloutis, E.A., Connolly, H.C., Crombie, M.K., Delbó, M., Dworkin, J.P., Emery, J.P., Glavin, D.P., Hamilton, V.E., Hergenrother, C.W., Johnson, C.L., 2014. The OSIRIS-REx target asteroid (101955) Bennu: Constraints on its physical, geological, and dynamical nature from astronomical observations. *Meteoritics & Planetary Science 50*, 834–849. https://doi.org/10.1111/maps.12353

Le Feuvre, M., Wieczorek, M.A., 2011. Nonuniform cratering of the Moon and a revised crater chronology of the inner Solar System. *Icarus 214*, 1–20. doi:10.1016/j.icarus.2011.03.010

Li, C., Su, Y., Pettinelli, E., Xing, S., Ding, C., Liu, J., Ren, X., Lauro, S.E., Soldovieri, F., Zeng, X., Gao, X., Chen, W., Dai, S., Liu, D., Zhang, G., Zuo, W., Wen, W., Zhang, Z., Zhang, X., Zhang, H., 2020. The Moon's farside shallow subsurface structure unveiled by Chang'E-4 Lunar Penetrating Radar. *Science Advances 6*, 6898. https://doi.org/10.1126 sciadv.aay6898

Lienhard, J. H, Lienhard, J. H., 2001. A Heat Transfer Textbook, Third Edition, Phlogiston Press, Cambridge, Massachusetts, U.S.A. Available at: http://www.mie.uth.gr/labs/ltte/grk/pubs/ahtt.pdf

Liu, Y., Zhang, A., Taylor, L. A., 2009. Fragments of asteroids in lunar rocks. *72nd Annual Meteoritical Society Meeting*, Abstract #5434.

Lomax, B.A., Conti, M., Khan, N., Bennett, N.S., Ganin, A.Y., Symes, M.D., 2020. Proving the viability of an electrochemical process for the simultaneous extraction of oxygen and production of metal alloys from lunar regolith. *Planetary and Space Science 180*, 104748. https://doi.org/10.1016/j.pss.2019.104748

Lu, W., Ji, Y.C., Zhou, B., Fang, G.Y., 2016. Design of an array antenna system for Chang'E-5 LRPR. *16th International Conference on Ground Penetrating Radar (GPR)*. https://doi.org/10.1109/icgpr.2016.7572699

Lucey, P., Korotev, R.L., Gillis, J.J., Taylor, L.A., Lawrence, D., Campbell, B.A., Elphic, R., Feldman, B., Hood, L.L., Hunten, D., Mendillo, M., 2006. Understanding the lunar surface and space-Moon interactions. *Reviews in Mineralogy and Geochemistry 60(1)*, 83-219.

Lunar Exploration Analysis Group (LEAG), 2016. The Lunar Exploration Roadmap: Exploring the Moon in the 21st Century: Themes, Goals, Objectives, Investigations, and Priorities.

Lundborg, N., 1968. Strength of rock-like materials. *International Journal of Rock Mechanics and Mining Sciences 5(5)*, 427–454. doi:10.1016/0148-9062(68)90046-6

Luther, R., Zhu, M.-H., Collins, G., Wünnemann, K., 2018. Effect of target properties and impact velocity on ejection dynamics and ejecta deposition. *Meteoritics & Planetary Science 53,* 1705–1732. https://doi.org/10.1111/maps.13143

Luu, J., Jewitt, D., Cloutis, E., 1994. Near-Infrared Spectroscopy of Primitive Solar System Objects. *Icarus 109*, 133–144. https://doi.org/10.1006/icar.1994.1081

Macke, R., Consolmagno, G., Britt, D., 2011. Density, porosity, and magnetic susceptibility of carbonaceous chondrites. *Meteoritics & Planetary Science 46*, 1842-1862. doi:10.1111/j.1945-5100.2011.01298.x

Mandt, K.E., Mousis, O., Hurley, D., Bouquet, A., Retherford, K.D., Magaña, L.O., Luspay-Kuti, A., 2022. Exogenic origin for the volatiles sampled by the Lunar CRater Observation and Sensing Satellite impact. *Nature Communications 13, 642*. https://doi.org/10.1038 s41467-022-28289-6

Marchi, S., Mottola, S., Cremonese, G., Massironi, M., Martellato, E., 2009. A NEW CHRONOLOGY FOR THE MOON AND MERCURY. *The Astronomical Journal 137*, 4936–4948. doi:10.1088/0004-6256/137/6/4936

Marchi, S., Bottke, W., Kring, D. A., Morbidelli, A., 2012. The onset of the lunar cataclysm as recorded in its ancient crater populations. *Earth & Planetary Science Letters 325-326*, 27-38. doi:10.1016/j.epsl.2012.01.021

Marchi, S., Bottke, W. F., Elkins-Tanton, L. T., Bierhaus, M., Wuennemann, K., Morbidelli, A., Kring, D. A., 2014. Widespread mixing and burial of Earth's Hadean crust by asteroid impacts, *Nature 511*, 578-582. https://doi.org/10.1038/nature13539

Marshall, W., Shirley, M., Moratto, Z., Colaprete, A., Neumann, G., Smith, D., Hensley, S., Wilson, B., Slade, M., Kennedy, B., Gurrola, E., Harcke, L., 2011. Locating the LCROSS Impact Craters. *Space Science Reviews 167*, 71–92. https://doi.org/10.1007 s11214-011-9765-0

Mathew, K.J., Marti, K., 2001. Lunar nitrogen: indigenous signature and cosmic-ray production rate. *Earth and Planetary Science Letters 184*, 659–669. https://doi.org/10.1016 s0012-821x(00)00327-7

Matthewman, R., Court, R. W., Crawford, I. A., Jones, A. P., Joy, K. H., 2015. The Moon as a Recorder of Organic Evolution in the Early Solar System: A Lunar Regolith Analog Study*, Astrobiology 15*, 154-168.

Matthewman, R., Crawford, I. A., Jones, A. P., Joy, K. H., Sephton, M. A., 2016. Organic Matter Responses to Radiation under Lunar Conditions, *Astrobiology 16*, 900-912.

Mazarico, E., Neumann, G.A., Smith, D.E., Zuber, M.T., Torrence, M. H., 2011. Illumination conditions of the lunar polar regions using LOLA topography. *Icarus 211*, 1066–1081. https://doi.org/10.1016/j.icarus.2010.10.030.

McCauley, J.F., Wilhelms, D.E., 1971. Geological provinces of the near side of the moon. *Icarus 15*, 363–367. https://doi.org/10.1016/0019-1035(71)90114-x

McCord, T.B., Li, J.-Y. ., Combe, J.-P. ., McSween, H.Y., Jaumann, R., Reddy, V., Tosi, F., Williams, D.A., Blewett, D.T., Turrini, D., Palomba, E., Pieters, C.M., De Sanctis, M.C., Ammannito, E., Capria, M.T., Le Corre, L., Longobardo, A., Nathues, A., Mittlefehldt, D.W., Schröder, S.E., 2012. Dark material on Vesta from the infall of carbonaceous volatile-rich material. *Nature 491,* 83–86. https://doi.org/10.1038/nature11561

McDonnell, J.A.M., 2006. The Open University planetary impact facility: A compact two-stage light gas gun for all impact angles. *International Journal of Impact Engineering 33,* 410–418. doi:10.1016/j.ijimpeng.2006.09.038

McIntosh, E. C., Day, J. M. D., McCubbin, F. M., 2022. RE-EXAMINATION OF THE FELSITE CLAST WITHIN APOLLO SAMPLE 14321. *Lunar & Planetary Science LIII,* Abstract #1742.

McKay, D. S., Carter, J. L., Greenwood, W. R., 1970. *Science 171*, 479–480.

McKay D.S., Heikey G., Basu A., Blanford G., Simon S., Reedy R., French B.M., Papike J., 1991. The Lunar Regolith. In: G. H. Heiken, D. T. Vaniman, & B. M. French (Eds.), *Lunar Sourcebook, A User's Guide to the Moon*, 285–356. Cambridge University Press, Cambridge, U.K.

McKay, D.S., Carter, J.L., Boles, W.W., Allen, C.C., Allton, J.H., 1993. JSC-1: A New Lunar Regolith Simulant. NASA ADS 963.

McSween Jr., H. Y., 1977. On the nature and origin of isolated olivine grains in carbonaceous chondrites. *Geochim. Cosmochim. Acta 41*, 411–418.

McSween Jr., H.Y., 1979. Alteration in CM carbonaceous chondrites inferred from modal and chemical variations in matrix. *Geochim. Cosmochim. Acta 43*, 1761–1770.

Melosh, H.J., 1984. Impact ejection, spallation, and the origin of meteorites. *Icarus 59(2)*, 234–260. doi:10.1016/0019-1035(84)90026-5.

Melosh, H. J., 1985. Ejection of rock fragments from planetary bodies. *Geology 13(2)*, 144-148. doi: 10.1130/0091-7613(1985)13<144:EORFFP>2.0.CO;2

Melosh, H.J., 1989. Impact Cratering: A Geologic Process. Oxford University, Clarendon, Oxford.

Melosh., H. J., 1990. Vapor plumes: a neglected aspect of impact cratering. *Meteoritics 25*, 386.

Melosh, H.J., 2007. A hydrocode equation of state for SiO2. *Meteoritics & Planetary Science 42 (12),* 2079–2098. doi:10.1111/j.1945-5100.2007.tb01009.x.

Melosh, H.J., Ivanov, B., 2018. Slow Impacts on Strong Targets Bring on the Heat. *Geophysical Research Letters 45(6)*, 2597-2599. doi: 10.1002/2018gl077726

Melosh, H. J., Sonett, C. P., 1986. When worlds collide: Jetted vapor plumes and the Moon's origin, in Origin of the Moon. edited by Hartmann, W. K., Phillips, R. J., and Taylor, G. J., pp. 621–642, Lunar and Planetary Institute, Houston, Tex.

Melosh, H. J., 1988. The rocky road to panspermia. *Nature 332*, 687–688. https://doi.org/10.1038/332687a0

Melosh, H. J., Vickery, A. M., 1989. Impact erosion of the primordial atmosphere of Mars. *Nature 338*, 487-489.

Melosh, H.J., Ryan, E.V., Asphaug, E., 1992. Dynamic fragmentation in impacts: Hydrocode simulation of laboratory impacts. *Journal of Geophysical Research*, 97, 14735-14759.

Melosh, H. J., Johnson, B. C., and Bowling, T. J., 2017. Impact spall and fragmentation by near-surface stress wave interactions. *Lunar Planet. Science 48*, Abstract #2051.

Meyer, C., Fritz, J., Misgaiski, M., Stöffler, D., Artemieva, N.A., Hornemann, U., Moeller, R., De Vera, J.-P., Cockell, C., Horneck, G., Ott, S., Rabbow, E., 2011. Shock experiments in support of the Lithopanspermia theory: The influence of host rock composition, temperature, and shock pressure on the survival rate of endolithic and epilithic microorganisms. *Meteoritics & Planetary Science 46*, 701–718. https://doi.org/10.1111/j.1945-5100.2011.01184.x

Michikami, T., Hagermann, A., Morota, T., Haruyama, J., Hasegawa, S., 2017. Oblique impact cratering experiments in brittle targets: Implications for elliptical craters on the Moon. *Planetary and Space Science 135*, 27–36. doi:10.1016/j.pss.2016.11.004

Milbury, C., Johnson, B.C., Melosh, H.J., Collins, G.S., Blair, D.M., Soderblom, J.M., Nimmo, F., Bierson, C.J., Phillips, R.J., Zuber, M.T., 2015. Preimpact porosity controls the gravity signature of lunar craters. *Geophysical Research Letters 42*, 9711–9716. https://doi.org/10.1002/2015gl066198

Mileikowsky, C., Cucinotta, F. A., Wilson, J. W., Gladman, B., Horneck, G., Lindegren, L., Melosh, J., Rickman, H., Valtonen, M., Zheng, J. Q., 2000. Natural Transfer of Viable Microbes in Space: 1. From Mars to Earth and Earth to Mars. *Icarus 145(2)*, 391–427. https://doi.org/https://doi.org/10.1006/icar.1999.6317

Miljković, K., Collins, G.S., Patel, M.R., Chapman, D., Proud, W., 2012. High-velocity impacts in porous Solar System materials. *AIP Conference Proceedings 1426*, 871–874.

Miljković, K., Wieczorek, M.A., Collins, G.S., Laneuville, M., Neumann, G.A., Melosh, H.J., Solomon, S.C., Phillips, R.J., Smith, D.E., Zuber, M.T., 2013. Asymmetric Distribution of Lunar Impact Basins Caused by Variations in Target Properties. *Science 342*, 724–726. https://doi.org/10.1126 sscience.1243224

Mimura, K., Toyama, S., 2005. Behavior of polycyclic aromatic hydrocarbons at impact shock: Its implication for survival of organic materials delivered to the early Earth. *Geochimica et Cosmochimica Acta 69(1)*, 201-209.

Ming, D.W., Henninger, D.L., 1990. Lunar Base Agriculture: Soils for Plant Growth. *Soil Science 150*, 562. https://doi.org/10.1097/00010694-199008000-00012

Modzeleski, J. E., Modzeleski, V. E., Nagy, L. A., Nagy, B., Hamilton, P. B., McEwan, W. S., Urey, H. C., 1972. Carbon compounds in Apollo 15 lunar samples. In: *The Apollo 15 Lunar Samples*, Eds. J. W. Chamberlain and C. Watkins (Houston: Lunar and Planetary Inst.), 311-315.

Moorbath, S., 2001. A geochronological re-evaluation of claims for con-temporaneity of earliest life with major impacts. *Lunar & Planetary Science 32*, 1608.

Moore, C. B., Lewis, C. F., 1975. Total nitrogen contents of Apollo 15, 16, and 17 lunar fines samples. *Lunar Science VI*, 569-571.

Moore, C. B., Gibson, E. K., Larimer, J. W., Lewis, C. F., Nichiporuk, W., 1970. Total carbon and nitrogen abundances in Apollo 11 lunar samples and selected achondrites and basalts. *Proceedings from the Apollo 11 Lunar Science Conference*, 1375-1382.

Moore, C. B., Lewis, C. F., Larimer, J. W., Delles, F. M., Gooley, R. C., Nichiporuk, W., Gibson, E. K., 1971. Total carbon and nitrogen abundances in Apollo 12 lunar samples. *Proceedings from the Lunar Science Conference 2*, 1343-1350.

Moore, C. B., Lewis, C. F., Cripe, J., Delles, F. M., Kelly, W. R., 1972. Total carbon, nitrogen, and sulfur in Apollo 14 lunar samples *Proceedings from the Lunar Science Conference 3,* 2051-2058.

Moore, C. B., Lewis, C. F., Gibson, E. K., Jr., 1973. Total carbon contents of Apollo 15 and 16 lunar samples. *Proceedings from the Lunar Science Conference 4*, 1613-1623.

Moore, C. B., Lewis, C. F., Cripe, J. D., 1974. Total carbon and sulfur contents of Apollo 17 lunar samples. *Proceedings from the Lunar Science Conference 2*, 1897-1906.

Morbidelli, A., Marchi, S., Bottke, W. F., Kring, D. A., 2012. A sawtooth-like timeline for the first billion years of lunar bombardment, *Earth & Planetary Science Letters 355*, 144-151.

Morland, Z.S., Halim, S.H., Pearson, V.K., Patel, M.R., Green, S.F. Ramkissoon, N.K., 2021. Modelling Ejected Martian Biomarkers impacting Phobos. *52nd Lunar and Planetary Science Conference*. Abstract #1045.

Mortimer, J., Verchovsky, A.B., Anand, M., Gilmour, I., Pillinger, C.T., 2015. Simultaneous analysis of abundance and isotopic composition of nitrogen, carbon, and noble gases in lunar basalts: Insights into interior and surface processes on the Moon. *Icarus 255*, 3–17. https://doi.org/10.1016/j.icarus.2014.10.006

Mortimer, J., Verchovsky, A.B., Anand, M., 2016. Predominantly non-solar origin of nitrogen in lunar soils. *Geochimica et Cosmochimica Acta 193*, 36–53. https://doi.org/10.1016/j.gca.2016.08.006

Müller, O., Grallath, E., Tölg, G., 1976. Nitrogen in lunar igneous rocks. *Proceedings from the Lunar Science Conference 7*, 1615-1622.

Nagaoka, H., Takasawa, S., Nakamura, A., Sangen, K., 2013. Degree of impactor fragmentation under collision with a regolith surface-Laboratory impact experiments of rock projectiles. *Meteoritics & Planetary Science 49*, 69-79. doi:10.1111/maps.12126

Naito, M., Kodaira, S., Ogawara, R., Tobita, K., Someya, Y., Kusumoto, T., Kusano, H., Kitamura, H., Koike, M., Uchihori, Y., Yamanaka, M., Mikoshiba, R., Endo, T., Kiyono, N., Hagiwara, Y., Kodama, H., Matsuo, S., Takami, Y., Sato, T. and Orimo, S., 2020. Investigation of shielding material properties for effective space radiation protection. *Life Sciences in Space Research 26*, 69-76.

Nakamura, T., Tomeoka, K., Takaoka, N., Sekine, T., Takeda, H., 2000. Impact-Induced Textural Changes of CV Carbonaceous Chondrites: Experimental Reproduction. *Icarus 146*, 289–300. https://doi.org/10.1006/icar.2000.6385

National Aeronautics and Space Administration (NASA), 2020. Artemis Exploration Program Overview. Available online at: https://www.nasa.gov specials/artemis/

National Research Council (NRC), 2007. The Scientific Context for Exploration of the Moon, Final Report, National Academy Press, Washington, D. C..

Nave, R., 2017. Radiative Cooling Time. *Hyperphysics*, Georgia State University. Available at: http://hyperphysics.phy-astr.gsu.edu/hbase/thermo/cootime.html [Accessed 24/01/2020]

Neal, A., 2004. Ground-penetrating radar and its use in sedimentology: principles, problems and progress. *Earth-Science Reviews* 66, 261–330. https://doi.org/10.1016/j.earscirev.2004.01.004

Needham, D. H., Kring, D. A., 2017. Lunar volcanism produced a transient atmosphere around the ancient Moon, *Earth & Planetary Science Letters 478*, 175-178.

Nelson, J. B., 1967. Thermogravimetric analysis of ablating polymers to determine kinetic parameters describing mass loss due to thermal degradation. *NASA Technical Report*, 1-19. Hampton, VA: NASA Langley Research Center. ID: 19670013969.

Newman, W. I., Symbalisty, E. M. D., Arhens, T J., Jones, E. M., 1999. Impact erosion of planetary atmospheres: some surprising results. *Icarus 138*, 224-240.

Nishida, M., Hayashi, K., Toya, K., 2019. Influence of impact angle on size distribution of fragments in hypervelocity impacts. *International Journal of Impact Engineering 128*, 86-93. doi:10.1016/j.ijimpeng.2019.02.006

Norman, M. D., 2009. The lunar cataclysm: Reality or "mythconception". *Elements 5,* 23-28.

O'Brien, D. P., Sykes, M. V., Tricarico, P., 2011. Collision Probabilities and Impact Velocity Distributions for Vesta and Ceres. *42nd Lunar and Planetary Science Conference,* Abstract #2665.

Ohnaka, M., 1995. A shear failure strength law of rock in the brittle-plastic transition regime. *Geophysical Research Letters 22(1*), 25–28.

Ohtake, M., Haruyama, J., Matsunaga, T., Yokota, Y., Morota, T., Honda, C., 2008. Performance and scientific objectives of the SELENE (KAGUYA) Multiband Imager. Earth, *Planets and Space 60*, 257–264. https://doi.org/10.1186/bf03352789

Ohtake, M., Matsunaga, T., Yokota, Y., Yamamoto, S., Ogawa, Y., Morota, T., Honda, C., Haruyama, J., Kitazato, K., Takeda, H., Iwasaki, A., Nakamura, R., Hiroi, T., Kodama, S., Otake, H., 2010. Deriving the Absolute Reflectance of Lunar Surface Using SELENE (Kaguya) Multiband Imager Data. *Space Science Reviews 154*, 57–77. https://doi.org/10.1007 s11214-010-9689-0

Okamoto, T., Kurosawa, K., Genda, H., Matsui, T., 2020. Impact Ejecta Near the Impact Point Observed Using Ultra-high-Speed Imaging and SPH Simulations and a Comparison of the Two Methods. *Journal of Geophysical Research: Planets 125*. https://doi.org/10.1029/2019je005943

Ong, L., Asphaug, E., Korycansky, D. Coker, R., 2010. Volatile retention from cometary impacts on the Moon. *Icarus 207(2)*, 578-589.

Ono, T., Kumamoto, A., Yamaguchi, Y., Yamaji, A., Kobayashi, T., Kasahara, Y., Oya, H., 2008. Instrumentation and observation target of the Lunar Radar Sounder (LRS) experiment on-board the SELENE spacecraft. *Earth, Planets and Space 60*, 321–332. https://doi.org/10.1186/bf03352797

Ormö, J., Shuvalov, V.V., Lindström, M., 2002. Numerical modeling for target water depth estimation of marine-target impact craters. *Journal of Geophysical Research: Planets 107*, 3–13–9. https://doi.org/10.1029/2002je001865

Ostrowski, D.R., Gietzen, K., Lacy, C., Sears, D.W.G., 2010. An investigation of the presence and nature of phyllosilicates on the surfaces of C asteroids by an analysis of the continuum slopes in their near-infrared spectra. *Meteoritics & Planetary Science 45*, 615–637. https://doi.org/10.1111/j.1945-5100.2010.01047.x

Ozima, M., Seki, K., Terada, N., Miura, Y.N., Podosek, F.A., Shinagawa, H., 2005. Terrestrial nitrogen and noble gases in lunar soils. *Nature 436*, 655–659. https://doi.org/10.1038/nature03929

Paige, D.A., Foote, M.C., Greenhagen, B.T., Schofield, J.T., Calcutt, S., Vasavada, A.R., Preston, D.J., Taylor, F.W., Allen, C.C., Snook, K.J., Jakosky, B.M., Murray, B.C., Soderblom, L.A., Jau, B., Loring, S., Bulharowski, J., Bowles, N.E., Thomas, I.R., Sullivan, M.T., Avis, C., 2009. The Lunar Reconnaissance Orbiter Diviner Lunar Radiometer Experiment. *Space Science Reviews 150*, 125–160. https://doi.org/10.1007 s11214-009-9529-2

Palomba, E., Longobardo, A., De Sanctis, M.C., Zambon, F., Tosi, F., Ammannito, E., Capaccioni, F., Frigeri, A., Capria, M.T., Cloutis, E.A., Jaumann, R., Combe, J.-P., Raymond, C.A., Russell, C.T., 2014. Composition and mineralogy of dark material units on Vesta. *Icarus 240*, 58–72. https://doi.org/10.1016/j.icarus.2014.04.040

Parker, E.T., Chan, Q.H.S., Glavin, D.P., Dworkin, J.P., 2022. Non-protein amino acids identified in carbon-rich Hayabusa particles. *Meteoritics & Planetary Science 57*, 776–793. https://doi.org/10.1111/maps.13794

Parnell, J., Lindgren, P., 2006. Survival of reactive carbon through meteorite impact melting. *Geology 34*, 1029. https://doi.org/10.1130/g22731a.1

Parnell, J., Bowden, S., Lindgren, P., Burchell, M., Milner, D., Price, M., Baldwin, E.C., Crawford, I.A., 2010. The preservation of fossil biomarkers during meteorite impact events: Experimental evidence from biomarker-rich projectiles and target rocks. *Meteoritics & Planetary Science 45*, 1340–1358. https://doi.org/10.1111/j.1945-5100.2010.01100.x

Patel, M. R., Miljkovic, K., Ringrose, T. J., Leese, M. R., 2010. The Hypervelocity Impact Facility and Environmental Simulation at the Open University. In: *European Planetary Science Congress 2010*, 19-24 Sep 2010, Rome, Italy.

Paul, A.-L., Elardo, S.M., Ferl, R., 2022. Plants grown in Apollo lunar regolith present stress-associated transcriptomes that inform prospects for lunar exploration. *Communications Biology 5*, 1–9. https://doi.org/10.1038 s42003-022-03334-8

Pearson, V.K., Sephton, M.A., Franchi, I.A., Gibson, J.M., Gilmour, I., 2006. Carbon and nitrogen in carbonaceous chondrites: Elemental abundances and stable isotopic compositions. *Meteoritics & Planetary Science 41*, 1899–1918. https://doi.org/10.1111/j.1945-5100.2006.tb00459.x

Peters, K., Walters, C., Moldowan, J., 2004. The Biomarker Guide. Cambridge: Cambridge University Press. doi:10.1017/CBO9781107326040

Pierazzo, E., Chyba, C. F., 1999. Amino acid survival in large cometary impacts. *Meteoritics & Planetary Science 34*, 909–918. doi:10.1111/j.1945-5100.1999.tb01409.x

Pierazzo, E., Chyba, C., 2002. Cometary Delivery of Biogenic Elements to Europa. *Icarus 157(1)*, 120-127.

Pierazzo, E., Melosh, H. J., 2000. Hydrocode modeling of oblique impacts: The fate of the projectile. *Meteoritics & Planetary Science 35(1),* 117-130. doi:10.1111/j.1945-5100.2000.tb01979.x

Pierazzo, E., Vickery, A.M., Melosh, H.J., 1997. A Reevaluation of Impact Melt Production. *Icarus 127*, 408–423. https://doi.org/10.1006/icar.1997.5713

Pierazzo, E., Kring, D., Melosh, H., 1998. Hydrocode simulation of the Chicxulub impact event and the production of climatically active gases. *Journal of Geophysical Research: Planets 103(E12),* 28607-28625. doi: 10.1029/98je02496

Pierazzo, E., Artemieva, N. A., Ivanov, B. A., 2005. Starting conditions for hydrothermal systems underneath Martian craters: Hydrocode modeling. In *Large Meteorite Impacts III*, T. Kenkmann, F. Hörz, A. Deutsch, Eds. (Geological Society of America, Boulder, CO), 443–457.

Pierazzo, E., Artemieva, N., Asphaug, E., Baldwin, E.C., Cazamias, J., Coker, R., Collins, G.S., Crawford, D.A., Davison, T., Elbeshausen, D., Holsapple, K.A., Housen, K.R., Korycansky, D.G., Wünnemann, K., 2008. Validation of numerical codes for impact and explosion cratering: Impacts on strengthless and metal targets. *Meteoritics & Planetary Science 43*, 1917–1938. https://doi.org/10.1111/j.1945-5100.2008.tb00653.x

Pieters, C. M., Boardman, J., Buratti, B., Chatterjee, A., Clark, R., Glavich, T., Green, R., Head III, J., Isaacson, P., Malaret, E. and McCord, T., 2009a. The Moon mineralogy mapper (M^3) on chandrayaan-1. *Current Science*, 500–505.

Pieters, C.M., Goswami, J.N., Clark, R.N., Annadurai, M., Boardman, J., Buratti, B., Combe, J.-P. ., Dyar, M.D., Green, R., Head, J.W., Hibbitts, C., Hicks, M., Isaacson, P., Klima, R., Kramer, G., Kumar, S., Livo, E., Lundeen, S., Malaret, E., McCord, T., 2009b. Character and Spatial Distribution of OH/H2O on the Surface of the Moon Seen by M3 on Chandrayaan-1. *Science 326*, 568–572. https://doi.org/10.1126 sscience.1178658

Podolak, M., Prialnik, D., 1997. ^{26}Al and Liquid Water Environments in Comets, In: Comets and the Origin and Evolution of Life. (Eds) P. J., Thomas, C. F., Chyba, C. P., McKay, Springer, New York, pp. 259–272.

Polanskey, C.A., Ahrens, T.J., 1990. Impact spallation experiments: Fracture patterns and spall velocities. *Icarus 87*, 140–155. https://doi.org/10.1016/0019-1035(90)90025-5

Porcello, L.J., Jordan, R.L., Zelenka, J.S., Adams, G.F., Phillips, R.J., Brown, W.E., Ward, S.H., Jackson, P.L., 1974. The Apollo lunar sounder radar system. *Proceedings of the IEEE 62*, 769–783. https://doi.org/10.1109/proc.1974.9517

Potter, R. W. K., 2012. Numerical modelling of basin-scale impact crater formation, Ph. D. Thesis, Imperial College London, London, England.

Potter, R. W. K., Collins, G. S., 2013. Numerical modeling of asteroid survivability and possible scenarios for the Morokweng crater-forming impact. *Meteoritics & Planetary Science 48(5)*, 744-757.

Prettyman, T.H., Mittlefehldt, D.W., Yamashita, N., Lawrence, D.J., Beck, A.W., Feldman, W.C., McCoy, T.J., McSween, H.Y., Toplis, M.J., Titus, T.N., Tricarico, P., Reedy, R.C., Hendricks, J.S., Forni, O., Le Corre, L., Li, J.-Y., Mizzon, H., Reddy, V., Raymond, C.A., Russell, C.T., 2012. Elemental Mapping by Dawn Reveals Exogenic H in Vesta's Regolith. *Science 338*, 242–246. https://doi.org/10.1126 sscience.1225354

Qian, Y.Q., Xiao, L., Zhao, S.Y., Zhao, J.N., Huang, J., Flahaut, J., Martinot, M., Head, J.W., Hiesinger, H., Wang, G.X., 2018. Geology and Scientific Significance of the Rümker Region in Northern Oceanus Procellarum: China's Chang'E-5 Landing Region. *Journal of Geophysical Research: Planets 123*, 1407–1430. https://doi.org/10.1029/2018je005595

Qian, Y.Q., Xiao, L., Wang, Q., Head, J.W., Yang, R., Kang, Y., van der Bogert, C.H., Hiesinger, H., Lai, X., Wang, G., Pang, Y., Zhang, N., Yuan, Y., He, Q., Huang, J., Zhao, J., Wang, J., Zhao, S., 2021. China's Chang'e-5 landing site: Geology, stratigraphy, and provenance of materials. *Earth and Planetary Science Letters 561*, 116855. https://doi.org/10.1016/j.epsl.2021.116855

Quaide, W., Bunch, T., 1970. *Geochimica et Cosmochimica Acta Supplementary*, 1, 711–729.

Quintana, S., Crawford, D., Schultz, P., 2015. Analysis of Impact Melt and Vapor Production in CTH for Planetary Applications. *Procedia Engineering 103*, 499-506. doi: 10.1016/j.proeng.2015.04.065

Ramsley, K.R., Head, J.W., 2013. Mars impact ejecta in the regolith of Phobos: Bulk concentration and distribution. *Planetary and Space Science 87*, 115–129. https://doi.org/10.1016/j.pss.2013.09.005

Rayman, M.D., 2020. Lessons from the Dawn mission to Ceres and Vesta. *Acta Astronautica 176*, 233–237. https://doi.org/10.1016/j.actaastro.2020.06.023

Reddy, V., Nathues, A., Le Corre, L., Sierks, H., Li, J.-Y., Gaskell, R., McCoy, T., Beck, A.W., Schröder, S.E., Pieters, C.M., Becker, K.J., Buratti, B.J., Denevi, B., Blewett, D.T., Christensen, U., Gaffey, M.J., Gutierrez-Marques, P., Hicks, M., Keller, H.U., Maue, T., 2012a. Color and Albedo Heterogeneity of Vesta from Dawn. *Science 336*, 700–704. https://doi.org/10.1126 science.1219088

Reddy, V., Le Corre, L., O'Brien, D.P., Nathues, A., Cloutis, E.A., Durda, D.D., Bottke, W.F., Bhatt, M.U., Nesvorny, D., Buczkowski, D., Scully, J.E.C., Palmer, E.M., Sierks, H., Mann, P.J., Becker, K.J., Beck, A.W., Mittlefehldt, D., Li, J.-Y., Gaskell, R., Russell, C.T., 2012b. Delivery of dark material to Vesta via carbonaceous chondritic impacts. *Icarus 221*, 544–559. https://doi.org/10.1016/j.icarus.2012.08.011

Richardson, D.C., Leinhardt, Z.M., Melosh, H.J., Bottke, Jr., W.F., Asphaug, E., 2002. Gravitational Aggregates: Evidence and Evolution. In: W.F. Bottke Jr., A. Cellino, P. Paolicchi, and R.P. Binzel (Eds.), *Asteroids III*, 501–515. University of Arizona Press, Tucson.

Richardson, J. E., Melosh, H. J., Artemeiva, N. A., Pierazzo, E., 2005. Impact Cratering Theory and Modeling for the Deep Impact Mission: From Mission Planning to Data Analysis. *Space Science Reviews 117*, 241–267. doi:10.1007 s11214-005-3393-5

Rojdev, K., O'Rourke, M. J. E., Hill, C., Nutt, S., Atwell, W., 2014. Radiation effects on composites for long-duration lunar habitats. *Journal of Composite Materials 48(7),* 861–878. https://doi.org/10.1177/0021998313479416

Rubin, A., Trigo-Rodríguez, J., Huber, H., Wasson, J., 2007. Progressive aqueous alteration of CM carbonaceous chondrites. *Geochimica et Cosmochimica Acta 71*, 2361-2382. doi:10.1016/j.gca.2007.02.008

Rumpf, M. E., Fagents, S. A., Crawford, I. A., Joy, K. H., 2013. Numerical modeling of lava-regolith heat transfer on the Moon and implications for the preservation of implanted volatiles. *Journal of Geophysical Research: Planets 118*, 382–397. doi:10.1029/2012je004131

Russell, S. S., Arden, J. W., Pillinger, C. T., 1996. A carbon and nitrogen isotope study of diamond from primitive chondrites. *Meteoritics & Planetary Science 31*, 343–355. doi:10.1111/j.1945-5100.1996.tb02071.x

Russell, C.T., Raymond, C.A., Coradini, A., McSween, H.Y., Zuber, M.T., Nathues, A., De Sanctis, M.C., Jaumann, R., Konopliv, A.S., Preusker, F., Asmar, S.W., Park, R.S., Gaskell, R., Keller, H.U., Mottola, S., Roatsch, T., Scully, J.E.C., Smith, D.E., Tricarico, P., Toplis, M.J., 2012. Dawn at Vesta: Testing the Protoplanetary Paradigm. *Science 336*, 684–686. https://doi.org/10.1126 science.1219381

Sakai, H., Petrowski, C., Goldhaber, M. B., Kaplan, I. R., 1972. Distribution of carbon, sulfur and nitrogen in Apollo 14 and 15 material. *Lunar Science III*, 672–674.

Salisbury, J.W., Adler, J.E.M., Smalley, V.G., Ring, J., 1968. Dark-Haloed Craters on the Moon. *Monthly Notices of the Royal Astronomical Society 138*, 245–249. https://doi.org/10.1093/mnras/138.2.245

Samouhos, M., Tsakiridis, P., Iskander, M., Taxiarchou, M., Betsis, K., 2022. In-situ resource utilization: Ferrosilicon and SiC production from BP-1 lunar regolith simulant via carbothermal reduction. *Planetary and Space Science*, 105414. https://doi.org/10.1016/j.pss.2021.105414

Sargeant, H.M., Abernethy, F.A.J., Barber, S.J., Wright, I.P., Anand, M., Sheridan, S., Morse, A., 2020. Hydrogen reduction of ilmenite: Towards an in situ resource utilization demonstration on the surface of the Moon. *Planetary and Space Science 180*, 104751. https://doi.org/10.1016/j.pss.2019.104751

Schmitz, N. *et al.*, 2022. Concepts for a polar ice and volatiles prospecting mission in the context of ESA's EL3 program. *10th European Lunar Symposium*. Abstract available at: https:/ sservi.nasa.gov/els2022/program [Accessed 02/06/2022].

Schoenberg, R., Kamber, B.S., Collerson, K.D., Moorbath, S., 2002. Tungsten isotope evidence from ~3.8 Gyr metamorphosed sediments for early meteorite bombardment of the Earth. *Nature 418*, 403–405.

Schorghofer, N., Williams, J., Martinez-Camacho, J., Paige, D.A., Siegler, M.A., 2021. Carbon Dioxide Cold Traps on the Moon. *Geophysical Research Letters 48*. https://doi.org/10.1029/2021gl095533

Schultz, P.H., Spudis, P.D., 1983. Beginning and end of lunar mare volcanism. Nature 302, 233–236. https://doi.org/10.1038/302233a0

Schultz, P.H., Hermalyn, B., Colaprete, A., Ennico, K., Shirley, M., Marshall, W., 2010. The LCROSS Cratering Experiment. *Science 330(6003)*, 468-472.

Schwandt, C., Hamilton, J.A., Fray, D.J., Crawford, I.A., 2012. The production of oxygen and metal from lunar regolith. *Planetary and Space Science 74*, 49–56. https://doi.org/10.1016/j.pss.2012.06.011

Scott E.R.D., 1988. A new kind of primitive chondrite, Allan Hills 85085. *Earth & Planetary Science Letters 91*, 1–18.

Scott, E.R.D., Yamaguchi, A., Krot, A.N., 1997. Petrological evidence for shock melting of carbonates in the martian meteorite ALH84001. *Nature 387*, 377–379. doi:10.1038/387377a0

Sekine, T., Kobayashi, T., Nishio, M., Takahashi, E., 2008. Shock equation of state of basalt. *Earth Planets Space 60*, 999–1003. doi:10.1016/j.epsl.2015.07.008

Sekine, C., Sai, U., Hayashi, J., Kawamura, Y., Bauer, E., 2017. High-pressure Synthesis and Bulk Modulus of Non-centrosymmetric Superconductor Mo_3Al_2C. *Journal of Physics: Conference Series 950*, 042028. https://doi.org/10.1088/1742-6596/950/4/042028

Senft, L.E., Stewart, S.T., 2007. Modeling impact cratering in layered surfaces. *Journal of Geophysical Research 112*. https://doi.org/10.1029/2007je002894

Sephton, M.A., 2002. Organic compounds in carbonaceous meteorites. *Natural Product Reports 19*, 292–311. https://doi.org/10.1039/b103775g

Shaw, C., 2019. Metamorphic mineral assemblages in fossils in the contact metamorphic rocks of the Portrush Sill, Northern Ireland. *Lithos 338-339*, 99-110. doi:10.1016/j.lithos.2019.04.016

Shoemaker, E. M., 1962. Interpretation of lunar craters., in: Kopal, A. (Ed.), Physics and Astronomy of the Moon. Academic Press, New York., 283--351.

Shoemaker, E. M., Wolfe, R. F., Shoemaker, C. S., 1990. Asteroid and comet flux in the neighborhood of Earth. In *Geological Society of America Special Paper 247*, Global Catastrophes in Earth History: An Interdisciplinary Conference on Impacts, Volcanism, and Mass Mortality, ed. V. L. Sharpton & P. D. Ward, 155.

Shuvalov, V., 2011. Ejecta deposition after oblique impacts: An influence of impact scale. *Meteoritics & Planetary Science 46*, 1713–1718. https://doi.org/10.1111/j.1945-5100.2011.01259.x

Sibille, L., Carpenter, P., Schlagheck, R. French, R.A., 2006. Lunar regolith simulant materials: recommendations for standardization, production, and usage. *NASA Technical Report*, No. NASA/TP-2006-214605.

Speyerer, E.J., Robinson, M.S., 2013. Persistently illuminated regions at the lunar poles: Ideal sites for future exploration. *Icarus 222(1)*, 122–136. https://doi.org/10.1016/j.icarus.2012.10.010.

Spray, J.G., 2016. Lithification Mechanisms for Planetary Regoliths: The Glue that Binds. *Annual Review of Earth and Planetary Sciences 44*, 139–174. https://doi.org/10.1146/annurev-earth-060115-012203

Spudis, P.D., Bussey, B., Plescia, J., Josset, J., Beauvivre, S., 2008. Geology of Shackleton Crater and the south pole of the Moon. *Geophysical Research Letters 35 (14)*. doi:10.1029/2008GL034468

Spudis, P.D., Lavoie, A., 2010. Mission and implementation of an affordable lunar return, NASA Report, No. M11-0138.

Spudis, P.D., 2014. Moon First—Mine the Asteroids Later. Air & Space Magazine, Smithsonian. Available at: https://www.smithsonianmag.com/air-space-magazine/moon-firstmine-asteroids-later-180952272
[Accessed 01/08/2022)].

Stevens, C.J., Manning, P., van den Berg, L.J.L., de Graaf, M.C.C., Wamelink, G.W.W., Boxman, A.W., Bleeker, A., Vergeer, P., Arroniz-Crespo, M., Limpens, J., Lamers, L.P.M., Bobbink, R., Dorland, E., 2011. Ecosystem responses to reduced and oxidised nitrogen inputs in European terrestrial habitats. *Environmental Pollution 159*, 665–676. https://doi.org/10.1016/j.envpol.2010.12.008

Stöffler, D., Ryder, G., 2001. Stratigraphy and Isotope Ages of Lunar Geologic Units: Chronological Standard for the Inner Solar System. *Space Science Reviews 96*, 9–54. https://doi.org/10.1023/A:1011937020193

Stöffler, D., Ryder, G., Ivanov, B.A., Artemieva, N.A., Cintala, M.A., Grieve, R.A.F., 2006. Cratering History and Lunar Chronology. *Reviews in Mineralogical Geochemistry 60*, 519-596.

Su, Y., Wang, R., Deng, X., Zhang, Z., Zhou, J., Xiao, Z., Ding, C., Li, Y., Dai, S., Ren, X., Zeng, X., Gao, X., Liu, J., Liu, D., Liu, B., Zhou, B., Fang, G., Li, C., 2022. Hyperfine Structure of Regolith Unveiled by Chang'E-5 Lunar Regolith Penetrating Radar. *IEEE Transactions on Geoscience and Remote Sensing 60*, 1–14. https://doi.org/10.1109/tgrs.2022.3148200

Sugita, S., Honda, R., Morota, T., Kameda, S., Sawada, H., Tatsumi, E., Yamada, M., Honda, C., Yokota, Y., Kouyama, T., Sakatani, N., Ogawa, K., Suzuki, H., Okada, T., Namiki, N., Tanaka, S., Iijima, Y., Yoshioka, K., Hayakawa, M., Cho, Y., 2019. The geomorphology, color, and thermal properties of Ryugu: Implications for parent-body processes. *Science 364*. https://doi.org/10.1126 science.aaw0422

Svetsov, V., Shuvalov, V., 2015. Water delivery to the Moon by asteroidal and cometary impacts. *Planetary & Space Science 117*, 444-452.

Tartèse, R., Anand, M., Gattacceca, J., Joy, K.H., Mortimer, J.I., Pernet-Fisher, J.F., Russell, S., Snape, J.F., Weiss, B.P., 2019. Constraining the Evolutionary History of the Moon and the Inner Solar System: A Case for New Returned Lunar Samples. *Space Science Reviews 215*. https://doi.org/10.1007 s11214-019-0622-x

Taylor, L.A., Meek, T.T., 2005. Microwave Sintering of Lunar Soil: Properties, Theory, and Practice. *Journal of Aerospace Engineering 18*, 188–196. https://doi.org/10.1061/(asce)0893-1321(2005)18:3(188)

Tedesco, E.F., 1992. IRAS Minor Planet Survey (IMPS). VizieR On-line Data Catalog: II/190. Originally published in: Phillips Laboratory, Technical Report No. PL-TR-92-2049., Hanscom Air Force Base, MA.

Tera, F., Papanastassiou, D., Wasserburg, G., 1974. Isotopic evidence for a terminal lunar cataclysm. *Earth & Planetary Science Letters 22(1)*, 1-21.

The National Institute for Occupational Safety and Health (NIOSH), 2019. Centers for Disease Control and Prevention (CDC) - Pocket Guide to Chem. Hazards: Silicon carbide. Available online: https://www.cdc.gov/niosh/npg/npgd0555.html

Thiemens, M.H., Clayton, R.N., 1980. Ancient solar wind in lunar microbreccias. *Earth and Planetary Science Letters 47*, 34–42. https://doi.org/10.1016/0012-821x(80)90101-6

Thomas-Keprta, K .L., Clemett, S. J., Messenger, S., Ross, D. K., Le, L., Rahman, Z., McKay, D. S., Gibson Jr, E. K., Gonzalez, C. and Peabody, W., 2014. Organic matter on the Earth's Moon. *Geochimica et Cosmochimica Acta 134*, 1-15.

Thompson, S. L., Lauson, H. S., 1972. Improvements in the Chart-D Radiation Hydrodynamic Code III: Revised Analytical Equation of State: Sandia Laboratories Report SC-RR-71 0714, 119.

Tomioka, N., Tomeoka, K., Nakamura-Messenger, K., Sekine, T., 2007. Heating effects of the matrix of experimentally shocked Murchison CM chondrite: Comparison with micrometeorites. *Meteoritics & Planetary Science 42*, 19–30. https://doi.org/10.1111/j.1945-5100.2007.tb00214.x

Turkevich, A.L., 1973. Average chemical composition of the lunar surface. *The Moon 8*, 365–367. https://doi.org/10.1007/BF00581730

Turner, G., 1979. A Monte Carlo fragmentation model for the production of meteorites – implications for gas retention ages. *Lunar and Planetary Science Conference*, 10th, Houston, March 19–23, Proceedings, vol 2. Pergamon Press, New York, 1917–1941. (A80-23617 08-91)

Turner, G., Cadogan, P. H., Yonge, C. J., 1973. Argon selenochronology. In: Proceedings, 4th lunar science conference, Houston, 1889–1914.

Turrini, D., Combe, J.-P. ., McCord, T.B., Oklay, N., Vincent, J.-B. ., Prettyman, T.H., McSween, H.Y., Consolmagno, G.J., De Sanctis, M.C., Le Corre, L., Longobardo, A., Palomba, E., Russell, C.T., 2014. The contamination of the surface of Vesta by impacts and the delivery of the dark material. *Icarus 240*, 86–102. https://doi.org/10.1016/j.icarus.2014.02.021

Turrini, D., Svetsov, V., Consolmagno, G., Sirono, S., Pirani, S., 2016. Olivine on Vesta as exogenous contaminants brought by impacts: Constraints from modeling Vesta's collisional history and from impact simulations. *Icarus 280*, 328–339. https://doi.org/10.1016/j.icarus.2016.07.009

Udry, A., Howarth, G.H., Herd, C.D.K., Day, J.M.D., Lapen, T.J., Filiberto, J., 2020. What Martian Meteorites Reveal About the Interior and Surface of Mars. *Journal of Geophysical Research: Planets 125*. https://doi.org/10.1029/2020je006523

van Zuilen, M.A., Lepland, A., Arrhenius, G., 2002. Reassessing the evidence for the earliest traces of life. *Nature 418,* 627–630.

Veverka, J., Thomas, P., Harch, A., Clark, B., Bell, J.F., Carcich, B., Joseph, J., Murchie, S., Izenberg, N., Chapman, C., Merline, W., Malin, M., McFadden, L., Robinson, M., 1999. NEAR Encounter with Asteroid 253 Mathilde: Overview. *Icarus 140*, 3–16. https://doi.org/10.1006/icar.1999.6120

Vickery, A. M., 1993. The Theory of Jetting: Application to the Origin of Tektites, *Icarus 105*, 441–453.

Vickery, A.M., Melosh, H.J., 1987. The Large Crater Origin of SNC Meteorites. *Science 237*, 738–743. https://doi.org/10.1126 science.237.4816.738

von Mises, R., 1913. Mechanik der festen Körper im plastisch-deformablen Zustand. Nachrichten von der Gesellschaft der Wissenschaften zu Göttingen. *Mathematisch-Physikalische Klasse 1,* 582–592.

Wakita, S., Genda, H., 2019. Fates of hydrous materials during planetesimal collisions. *Icarus 328*, 58–68. doi:10.1016/j.icarus.2019.03.008

Wamelink, G.W.W., Frissel, J.Y., Krijnen, W.H.J., Verwoert, M.R., Goedhart, P.W., 2014. Can Plants Grow on Mars and the Moon: A Growth Experiment on Mars and Moon Soil Simulants. *PLoS ONE 9*, e103138. https://doi.org/10.1371/journal.pone.0103138

Warren, P. H., Rubin, A. E., 2020. Trace element and textural evidence favoring lunar, not terrestrial, origin of the mini-granite in Apollo sample 14321. *Icarus 347*, 113771. doi:10.1016/j.icarus.2020.113771

Watson, K., Murray, B. C., Brown, H., 1961. The behavior of volatiles on the lunar surface. *Journal of Geophysical Research 66*, 3033–3045.

Weisberg, M. K., Prinz, M., Clayton, R., Mayeda, T., 1993. The CR (Renazzo-type) carbonaceous chondrite group and its implications. *Geochimica et Cosmochimica Acta* 57, 1567-1586. doi:10.1016/0016-7037(93)90013-m

Weisberg M. K., Prinz M., Clayton R. N., Mayeda T. K., Sugiura N., Zashu S., Ebihara M., 2001. A new metal-rich chondrite grouplet. *Meteoritics & Planetary Science 36*, 401–418.

Weisberg, M. K., McCoy, T. J., Krot, A. N., 2006. Systematics and evaluation of meteorite classification. In: Lauretta, D.S., McSween, H.Y., Jr. (Eds.), Meteorites and the Early Solar System II. Univ. Arizona Press, Tucson, pp. 19–52.

Weiss, I. M., Muth, C., Drumm, R., Kirchner, H. O. K., 2018. Thermal decomposition of the amino acids glycine, cysteine, aspartic acid, asparagine, glutamic acid, glutamine, arginine and histidine. *BMC Biophysics 11*. doi:10.1186 s13628-018-0042-4

Weissman, P.R., 1997. Long-period Comets and the Oort Cloud. *Annals of the New York Academy of Sciences 822*, 67–95. https://doi.org/10.1111/j.1749-6632.1997.tb48335.x

Wells, L., Armstrong, J., Gonzalez, G., 2003. Reseeding of early earth by impacts of returning ejecta during the late heavy bombardment. *Icarus 162*, 38–46. https://doi.org/10.1016 s0019-1035(02)00077-5

Wilhelms, D.E., McCauley, J.F., 1971. Geologic map of the near side of the Moon. Washington, DC: US Geological Survey.

Whitaker, E.A., 1999. Mapping and naming the moon : a history of lunar cartography and nomenclature. Cambridge University Press, Cambridge.

Wickham-Eade, J., 2017. Fragmentation of Carbon-bearing Projectiles and the Effects on their Raman Spectra due to Hypervelocity Impacts, Ph.D. Thesis, University of Kent, Kent, England.

Wickham-Eade, J., Burchell, M., Price, M., Harriss, K., 2018. Hypervelocity impact fragmentation of basalt and shale projectiles. *Icarus 311*, 52-68.

Wieczorek, M.A., Weiss, B.P., Stewart, S.T., 2012. An Impactor Origin for Lunar Magnetic Anomalies. *Science 335*, 1212–1215. https://doi.org/10.1126 science.1214773

Wieczorek, M.A., Neumann, G.A., Nimmo, F., Kiefer, W.S., Taylor, G.J., Melosh, H.J., Phillips, R.J., Solomon, S.C., Andrews-Hanna, J.C., Asmar, S.W., Konopliv, A.S., Lemoine, F.G., Smith, D.E., Watkins, M.M., Williams, J.G., Zuber, M.T., 2013. The Crust of the Moon as Seen by GRAIL. *Science 339*, 671–675. https://doi.org/10.1126 science.1231530

Wieler, R., 2016. Do lunar and meteoritic archives record temporal variations in the composition of solar wind noble gases and nitrogen? A reassessment in the light of Genesis data. *Geochemistry 76*, 463–480. https://doi.org/10.1016/j.chemer.2016.06.001

Wieler, R., Humbert, F., Marty, B., 1999. Evidence for a predominantly non-solar origin of nitrogen in the lunar regolith revealed by single grain analyses. *Earth and Planetary Science Letters 167*, 47–60. https://doi.org/10.1016 s0012-821x(99)00012-6

Wiggins, S.E., Johnson, B.C., 2021. Solid Fragments Ejected by Lunar Hypervelocity Impacts. *52nd Lunar and Planetary Science Conference.* Abstract #2307.

Wiggins, S.E., Johnson, B.C., Bowling, T.J., Melosh, H.J., Silber, E.A., 2019. Impact Fragmentation and the Development of the Deep Lunar Megaregolith. *Journal of Geophysical Research: Planets 124*, 941–957. https://doi.org/10.1029/2018je005757

Wilhelms, D.E., 1993. To a rocky moon : a geologist's history of lunar exploration. University Of Arizona Press, Tucson.

Wingo, D., 2004. Moonrush: Improving life on Earth with the Moon's Resources. Burlington: Apogee Books.

Winkler, R., Luther, R., Poelchau, M.H., Wünnemann, K., Kenkmann, T., 2018. Subsurface deformation of experimental hypervelocity impacts in quartzite and marble targets. *Meteoritics & Planetary Science 53*, 1733–1755. https://doi.org/10.1111/maps.13080

Wood, J. A., Marvin, U. B., Reed, J. B., Taylor, G. J., Bower, J. F., Powell, B. N., Dickey, J. S., 1971. Mineralogy and petrology of the Apollo 12 lunar sample. *Smithsonian Astrophysics Observatory Special Report 333*, 177.

Worth, R.J., Sigurdsson, S., House, C.H., 2013. Seeding Life on the Moons of the Outer Planets via Lithopanspermia. *Astrobiology 13*, 1155–1165. https://doi.org/10.1089/ast.2013.1028

Wünnemann, K., Collins, G. S., Melosh, H., 2006. A strain-based porosity model for use in hydrocode simulations of impacts and implications for transient crater growth in porous targets. *Icarus 180(2)*, 514–527. doi:10.1016/j.icarus.2005.10.013.

Wünnemann, K., Collins, G. S., Osinski, G., 2008. Numerical modelling of impact melt production in porous rocks. *Earth & Planetary Science Letters 269(3-4)*, 530-539.

Xiao, Y., Su, Y., Dai, S., Feng, J., Xing, S., Ding, C., Li, C., 2019. Ground experiments of Chang'e-5 lunar regolith penetrating radar. *Advances in Space Research 63*, 3404–3419. https://doi.org/10.1016/j.asr.2019.02.001

Xie, M., Xiao, Z., Xu, L., Fa, W., Xu, A., 2020. Change in the Earth–Moon impactor population at about 3.5 billion years ago. *Nature Astronomy 5,* 128–133. https://doi.org/10.1038 s^{-1}41550-020-01241-8

Yamamoto, S., 2002. Measurement of Impact Ejecta from Regolith Targets in Oblique Impacts. *Icarus 158*, 87–97. https://doi.org/10.1006/icar.2002.6862

Yang, Y., Li, S., Zhu, M.-H., Liu, Y., Wu, B., Du, J., Fa, W., Xu, R., He, Z., Wang, C., Xue, B., Yang, J., Zou, Y., 2021. Impact remnants rich in carbonaceous chondrites detected on the Moon by the Chang'e-4 rover. *Nature Astronomy 6*, 207–213. https://doi.org/10.1038 s41550-021-01530-w

Yokota, S., Terada, K., Saito, Y., Kato, D., Asamura, K., Nishino, M.N., Shimizu, H., Takahashi, F., Shibuya, H., Matsushima, M., Tsunakawa, H., 2020. KAGUYA observation of global emissions of indigenous carbon ions from the Moon. *Science Advances 6.* https://doi.org/10.1126 sciadv.aba1050

Yue, Z., Johnson, B., Minton, D., Melosh, H., Di, K., Hu, W., Liu, Y., 2013. Projectile remnants in central peaks of lunar impact craters. *Nature Geoscience 6(6)*, 435-437.

Zellner, N. E. B., 2017. Cataclysm no more: New views on the timing and delivery of lunar impactors, *Origins of Life and Evolution of Biospheres 47*, 261-280.

Zhou, H., Feng, X., Ding, C., Dong, Z., Liu, C., Zhang, Y., Meng, Z., 2021. Yutu-2 Radar Sounding Evidence of a Buried Crater at Chang'E-4 Landing Site. *IEEE Transactions on Geoscience and Remote Sensing 60*, 1–19. https://doi.org/10.1109/tgrs.2021.3090528

Zolensky, M.E., 1997. Structural water in the Bench Crater chondrite returned from the Moon. *Meteoritics & Planetary Science 32,* 15–18. https://doi.org/10.1111/j.1945-5100.1997.tb01235.x

Zolensky, M. E., McSween, H. Y., 1988. Aqueous alteration. In: Kerridge, J. F., Matthews, M. S. (Eds*.), Meteorites and the Early Solar System*. University Arizona Press, Tucson, pp. 114–143.

Zolensky, M.E., Weisberg, M.K., Buchanan, P.C., Mittlefehldt, D.W., 1996. Mineralogy of carbonaceous chondrite clasts in HED achondrites and the Moon. *Meteoritics & Planetary Science 31*, 518–537. https://doi.org/10.1111/j.1945-5100.1996.tb02093.x

Zolensky, M.E., Nakamura, K., Gounelle, M., Mikouchi, T., Kasama, T., Tachikawa, O., Tonui, E., 2002. Mineralogy of Tagish Lake: An ungrouped type 2 carbonaceous chondrite. *Meteoritics & Planetary Science 37*, 737-761. doi:10.1111/j.1945-5100.2002.tb00852.x

Zolotov, M.Y., 2009. On the composition and differentiation of Ceres. *Icarus 204*, 183–193. doi:10.1016/j.icarus.2009.06.011

Zuber, M.T., Head, J.W., Smith, D.E., Neumann, G.A., Mazarico, E., Torrence, M.H., Aharonson, O., Tye, A.R., Fassett, C.I., Rosenburg, M.A., Melosh, H.J., 2012. Constraints on the volatile distribution within Shackleton crater at the lunar south pole. *Nature 486*, 378–381. https://doi.org/10.1038/nature11216

Appendix

Electronic appendix

The electronic appendix contains a catalogue of all of the set-up and ancillary data files used to create the simulations presented in this thesis. There is folder for each of the chapters, within which there is a detailed set of sub-folders containing all of the relevant files for both 2D and 3D modelling. The INFO folders contained within each separate model folder contain the input files “asteroid.inp” and “material.inp”. These input files detail the parameters used to set-up the respective model. Global input parameters (including grid dimensions, impact velocity, impact angle, cell size, resolution, etc.) can be found in asteroid.inp and material model parameters for both projectile and target (equation of state, strength, porosity, etc.) in material.inp. These files (.inp) can be downloaded and opened with any program capable of reading text-based formats.

Alongside the model data files are the data tables (in Excel format) produced to create many of the figures within the thesis. The files can be accessed using this link (Electronic Appendix) and include:

- **Ch4_2D_earth_esc_vel_resolution_tables**
  Results for the initial 2D resolution test for escaping ejecta after a simulated impact into the Earth, detailed in Chapter 4. The data tables and related graphs show the change in the mass of ejected material at different resolutions. The pressures of escaping ejecta are also shown.

- **Ch5_Arrhenius_equation_tables**
  Detailed spreadsheets calculating the effect of thermal degradation on biomarkers using the Arrhenius equation. Relates to the survival of biomarkers after impact with the lunar surface in Chapter 5.

- **Ch5_Terrestrial_met_peak_shock_data**
  Data tables of peak shock pressures and temperatures for terrestrial meteorites impacting the lunar surface (Chapter 5).

- **Ch5_Terrestrial_met_post_shock_data**
  Data tables for post shock temperatures of terrestrial meteorites impacting the lunar surface (Chapter 5).

- **Ch6_CC_model_data**
  Data tables relating to the peak shock temperatures and final locations of carbonaceous chondrites after impacting the lunar surface (Chapter 6).

A1: Example input file (asteroid.inp) detailing the parameters for the global set-up of 3D simulations detailed in Chapter 4.

```
#ISINP
------------------------------------------------------------------------
--- this is the new input file used by iSALE versions of v7.0 and higher
------------------------------------------------------------------------
--- lines beginning with '-' or '!' are treated as comments and not
--- further processed. The difference between the two comment lines
--- is, lines starting with '-' will appear also in the backup of this
--- input file and in the header of the jpeg-file, whereas lines
--- beginning with '!' are completely removed from these files.
------------------------------------------------------------------------
--- First 8 columns are reserved for short parameter identification  ---
--- (available abbreviations are found in the documentation)         ---
---                                                                  ---
--- The next 20 columns are reserved for parameter description!      ---
---                                                                  ---
------------------- General Model Info ---------------------------------
VERSION        __DO NOT MODIFY__              : 4.1
DIMENSION      dimension of input file        : 3
PATH           Data file path                 : ./
MODEL          Modelname                      : v20_a30_100cppr
DUMP           Restart Filename               : NONE
------------------- Mesh Geometry Parameters ---------------------------
GRIDH          horizontal cells               : 56          : 600         : 10
GRIDV          vertical cells                 : 50          : 240         : 0
GRIDD          depth cells                    : 0           : 120         : 20
GRIDEXT        ext. factor                    : 1.08d0
GRIDSPC        grid spacing                   : 250.D0
GRIDSPCM       max. grid spacing              : -20.D0
------------------- Global Setup Parameters ----------------------------
S_TYPE         setup type                     : DEFAULT
ALE_MODE       ALE modus                      : EULER
T_SURF         Surface temp                   : 293.D0
GRAV_V         gravity                        : 0.D0
GRAD_TYPE      gradient type                  : NONE
GRAD_DIM       gradient dimension             : 1
GRAD_OBJ       gradient in obj.               : 0
ROCUTOFF       density cutoff                 : 0.D0
------------------- Projectile Parameters ------------------------------
OBJNUM         number of proj.                : 1
PR_TRACE       collision tracers              : 0
OBJRESH        CPPR horizontal                : 100
OBJRESV        CPPR vertical                  : 100
OBJRESD        CPPR depth                     : 100
OBJVEL         object velocity                : -2.0D4
ANGLE          inc. angle (X-Z)               : 30.d0
ANGLE2         inc. angle (Y-Z)               : 0.D0
OBJMAT         object material                : granite
OBJTYPE        object type                    : SPHEROID
OBJTPROF       object temp prof               : CONDCONV
OBJENER        object energy                  : 0.D0
OBJTEMP        object temp                    : 293.D0
OBJOFF_H       object shift hor               : 200
OBJOFF_V       object shift ver               : 0
OBJOFF_D       object shift dpth              : 0
OBJDAM         object damage                  : 1.D0
------------------- Target Parameters ----------------------------------
LAYNUM         number of layers               : 1
LAYTYPE        layer type                     : 0
```

```
LAYPOS        layer position               : 90
LAYMAT        layer material               : granite
LAYTPROF      layer therm. prof            : CONDCONV
------------------- Time Parameters -----------------------------------
DT            initial time increment       : 5.0D-3
DTMAX         maximum timestep             : 1.D-2
TEND          end time                     : 1.501D1
DTSAVE        save interval                : 0.25D0
TDUMP         dump interval                : 1.d0
------------------- Boundary Conditions -------------------------------
BND_L         left                         : OUTFLOW
BND_R         right                        : OUTFLOW
BND_B         bottom                       : OUTFLOW
BND_T         top                          : OUTFLOW
BND_F         front                        : FREESLIP
BND_BK        back                         : OUTFLOW
------------------- Numerical Stability Parameters --------------------
AVIS          art. visc. linear            : 0.24D0
AVIS2         art. visc. quad.             : 1.2D0
ANC           alt. node coupl.             : 0.0D0
EPS_MIN       vol. frac. cutoff            : 1.D-6
------------------- Tracer Particle Parameters ------------------------
TR_QUAL       tracer quality               : 1
TR_SPCH       spacing horiz.               : -1.D0       : -1.D0       : -1.D0
TR_SPCV       spacing vertical             : -1.D0       : -1.D0       : -1.D0
TR_SPCD       spacing depth                : -1.D0       : -1.D0       : -1.D0
TR_VAR        add. tracer fiels            : #TrP-TrT-Trt-Trp-Tru-Trw-Trv#
------------------- Ac. Fluid. Parameters (read in read_material) ------
CVIB          c_vib                        : 0.1D0
TOFF          toff                         : 16.D0
VIB_MAX       Max. vib.vel.                : 200.D0
------------------- Data Saving Parameters -----------------------------
QUALITY       Compression rate             : -50
VARLIST       List of variables            : #Den-Pre-Tmp-Yld-Dam-VEL-Sie#
RANGE         write range                  : 1
RANGEH        write range hor.             : 0           : 0
RANGEV        write range ver.             : 0           : 0
RANGED        write range dpth             : 0           : 0
-------------------- Superflous later ---------------------------------
STRESS        calc_stress                  : 1
<<END
```

A2: Example input file (material.inp) detailing the parameters for the material set-up of 3D simulations detailed in Chapter 4.

```
#ISMAT
-------------------------------------------------------------------------------
MATNAME       Material name                : granite     : dunite_     : calcite
EOSNAME       EOS name                     : granit2     : dunite_     : calcite
EOSTYPE       EOS type                     : aneos       : aneos       : aneos
STRMOD        Strength model               : ROCK        : ROCK        : ROCK
DAMMOD        Damage model                 : IVANOV      : IVANOV      : IVANOV
ACFL          Acoustic fluidisation        : BLOCK       : BLOCK       : BLOCK
PORMOD        Porosity model               : NONE        : NONE        : NONE
THSOFT        Thermal softening            : OHNAKA      : OHNAKA      : OHNAKA
LDWEAK        Low density weakening        : POLY        : POLY        : POLY
-------------------------------------------------------------------------------
POIS          pois                         : 3.0000D-01  : 2.5000D-01  : 3.0000D-01
-------------------------------------------------------------------------------
TMELT0        tmelt0                       : 1.6730D+03  : 1.3730D+03  : 1.5000D+03
TFRAC         tfrac                        : 1.2000D+00  : 1.2000D+00  : 1.2000D+00
ASIMON        a_simon                      : 6.0000D+09  : 1.5200D+09  : 6.0000D+09
CSIMON        c_simon                      : 3.0000D+00  : 4.0500D+00  : 3.0000D+00
-------------------------------------------------------------------------------
YDAM0         ydam0 (ycoh)                 : 1.0000D+04  : 1.0000D+04  : 1.0000D+04
FRICDAM       fricdam                      : 6.0000D-01  : 6.0000D-01  : 4.0000D-01
YLIMDAM       ylimdam                      : 2.5000D+09  : 3.5000D+09  : 5.0000D+08
-------------------------------------------------------------------------------
YINT0         yint0                        : 1.0000D+07  : 1.0000D+07  : 5.0000D+06
FRICINT       fricint                      : 2.0000D+00  : 1.2000D+00  : 1.0000D+00
YLIMINT       ylimint                      : 2.5000D+09  : 3.5000D+09  : 5.0000D+08
-------------------------------------------------------------------------------
IVANOV_A      Damage parameter             : 1.0000D-04  : 1.0000D-04  : 1.0000D-04
IVANOV_B      Damage parameter             : 1.0000D-11  : 1.0000D-11  : 1.0000D-11
IVANOV_C      Damage parameter             : 3.0000D+08  : 3.0000D+08  : 3.0000D+08
-------------------------------------------------------------------------------
GAMETA        gam_eta                      : 7.5000D-03  : 7.5000D-03  : 0.0000D-03
GAMBETA       gam_beta                     : 1.0800D+02  : 1.0800D+02  : 0.0000D+02
-------------------------------------------------------------------------------
<<END
```

A3: Example input file (asteroid.inp) detailing the parameters for the global set-up of 2D simulations detailed in Chapter 5.

```
#ISINP
----------------------------------------------------------------------
--- this is the new input file used by iSALE versions of v7.0 and higher
----------------------------------------------------------------------
------------------- General Model Info --------------------------------
VERSION        __DO NOT MODIFY__             : 4.1
DIMENSION      dimension of input file       : 2
PATH           Data file path                : ./
MODEL          Modelname                     : a_proj_por10_2.5_nosol
------------------- Mesh Geometry Parameters --------------------------
GRIDH          horizontal cells              : 0           : 1000        : 100
GRIDV          vertical cells                : 100         : 1600        : 50
GRIDEXT        ext. factor                   : 1.05d0
GRIDSPC        grid spacing                  : 2.5D-03
CYL            Cylind. geometry              : 1.0D0
GRIDSPCM       max. grid spacing             : -20.D0
------------------- Global setup parameters ---------------------------
S_TYPE         setup type                    : DEFAULT
T_SURF         Surface temp                  : 273.D0
P_SURF         surface pressure              : 10.D0
GRAV_V         gravity                       : -1.62D0
------------------- Projectile ("Object") Parameters -------------------
OBJNUM         number of objects             : 1
OBJRESH        CPPR horizontal               : 100
OBJVEL         object velocity               : -2.5D3
OBJMAT         object material               : chondri
OBJTYPE        object type                   : SPHEROID
------------------- Target Parameters ---------------------------------
LAYNUM         layers number                 : 1
LAYPOS         layer position                : 875
LAYMAT         layer material                : lunar__
LAYTPROF       thermal profile               : CONST
------------------- Time Parameters -----------------------------------
DT             initial time increment        : 5.0D-5
DTMAX          maximum timestep              : 5.D-2
TEND           end time                      : 5.D-3
DTSAVE         save interval                 : 5.D-5
------------------- Boundary Condition Parameters ---------------------
-------------- 0=no slip,1=free slip, 2=cont.outflow ------------------
BND_L          left                          : FREESLIP
BND_R          right                         : OUTFLOW
BND_B          bottom                        : NOSLIP
BND_T          top                           : OUTFLOW
------------------- Numerical Stability Parameters --------------------
AVIS           art. visc. linear             : 0.2D0
AVIS2          art. visc. quad.              : 1.0D0
------------------- Tracer Particle Parameters ------------------------
--- if TR_SAVE == 1, only Trx and Try are automatically added to
--- the variable list. If additional variables shall be calculated
--- and stored, you have to set them in 'Tracer fields'.
-------- TR_NX/NY is the number of tracers in x/y-direction
-------  TR_DX/DY is the interval between tracers (usually the same as dx/dy)
TR_QUAL        integration qual.             : 1
TR_SPCH        tracer spacing X              : -1.D0       : -1.D0       : -1.D0
TR_SPCV        tracer spacing Y              : -1.D0       : -1.D0       : -1.D0
TR_VAR         add. tracer fiels             : #TrP-TrT-Trt-Trp#
------------------- Control parameters (global) -----------------------
STRESS         Consider stress               : 1
```

```
------------------- Data Saving Parameters ------------------------------
QUALITY       Compression rate              : -50
VARLIST       List of variables             : #Den-Tmp-Pre-Sie-Yld-YAc-Dam-VEL#
-----------------------------------------------------------------------------
<<END
```

A4: Example python script for creating ejecta provenance plots shown in Figures 4.9/4.10.

```
import pySALEPlot as psp
import matplotlib as mpl
import matplotlib.pylab as plt
import os
import numpy as np
from pylab import figure,arange,colorbar

# Create ouptut directory
dirname='TrP'
psp.mkdir_p(dirname)

# Open the datafile
m=psp.opendatfile('jdata.dat')

# Set the distance units to m
m.setScale('km')

# Tracer information is held in m.tru[u], for each tracer cloud, 'u'.
# You can print some information to the screen using:
#[m.tru[u].truInfo() for u in range(m.tracer_numu)]

trgrid = m.tracerGrid(spacing=(1,1),plane='xz')

# Read the first time step from the datafile for tracer positions
step=m.readStep(['Den','TrP'], 0)

# Read the final step from the datafile for tracer velocity/pressure
s2=m.readStep(['TrP','Tru','Trw','Trv'], m.nsteps-1)

# Set up a pylab figure
fig=figure()

# Set up the axes
ax=fig.add_subplot(111,aspect='equal',adjustable='box')

# Set the axis labels
ax.set_xlabel('x [km]')
ax.set_ylabel('z [km]')

# Set the axis limits
ax.set_xlim(m.xhires)
ax.set_ylim(m.zhires)

data = np.load('tracerdata.npz')
Tru = data['Tru']
Trw = data['Trw']
Trv = data['Trv']

vels = []

for i in range(0, m.nsteps-1, 1):

       # find vertical vel
       vel_vert = Trv[i, :]

       # Find magnitude of all three vel vectors using sqrt and sq functions
       vel_magnitude = np.sqrt(Tru[i, :]**2 + Trw[i, :]**2 + Trv[i, :]**2)
```

```
        #set to 0 if vertical velocity is pointing downwards
        vel_magn = np.zeros_like(vel_magnitude)
        vel_magn[vel_vert > 0] = vel_magnitude[vel_vert > 0]

        vels.append(vel_magn)

vel_max = np.maximum.reduce(vels)

# Define max
maxvalue=120#round(m.fmax[1]*1e-9, -1)

# Define the colour map
cmap=plt.cm.magma
# Extract all colours from cmap
cmaplist=[cmap(j) for j in range(cmap.N)]

# Create new cmap
cmap2=mpl.colors.LinearSegmentedColormap.from_list('Custom cmap', cmaplist, cmap.N)

# Define bins and normalize
bounds=range(0,maxvalue,10)
norm=mpl.colors.BoundaryNorm(bounds, cmap.N)

# Now, we'll set the tracer colours according to their temps,
# recorded in step.data[3] in this case.
q=ax.scatter(step.xmark[trgrid],step.zmark[trgrid],c=s2.data[0]
[trgrid]*1e-9,cmap=cmap2,vmin=0,vmax=maxvalue,s=1,linewidths=0,marker='s',norm=norm)

# Add a colorbar for the temp plot
cb=fig.colorbar(q, cmap=cmap2, norm=norm, spacing='proportional',
orientation='horizontal', extend='max', ticks=bounds, boundaries=bounds, format='%1i')
cb.set_label('Tracer peak-shock pressure [GPa]')

x=step.xmark[m.tru[1].start-1:m.tru[1].end]
y=step.zmark[m.tru[1].start-1:m.tru[1].end]
z=vel_max*1e-3
tri=ax.tricontour(x, y, z, levels=[11], colors='k', linewidths=1, linestyles='dashed')

cwd=str(os.getcwd())
name=str(cwd.split('Local_3D/')[1])
# Add title
fig.suptitle(name)

# Save the figure
fig.savefig(dirname+'/Xsection/'+name+'_contour_maxvel_v3.png'.format(i), dpi=300)
```

A5: Example python script for creating projectile pressure and temperature plots shown in Figures 5.2–5.9.

```
import pySALEPlot as psp
import matplotlib as mpl
import matplotlib.pylab as plt
import numpy as np
from pylab import figure,arange,colorbar

# Create ouptut directory
dirname='Projectile'
psp.mkdir_p(dirname)

# Open the datafile
model=psp.opendatfile('jdata.dat')

# Set the distance units to m
model.setScale('m')

# Tracer information is held in model.tru[u], for each tracer cloud, 'u'.
# You can print some information to the screen using:
[model.tru[u].truInfo() for u in range(model.tracer_numu)]

# Set up a pylab figure
fig=figure()
fig.subplots_adjust(left=0.000000000001)

# Clear the previous figure
fig.clf()
# Set up the axes
ax=fig.add_subplot(111,aspect='equal',adjustable='box')

# Set the axis labels
#ax.set_xlabel('r [m]')
#ax.set_ylabel('z [m]')

# Set the axis limits
ax.set_xlim([-0.3,0.3])
ax.set_ylim([-0.1,0.6])
ax.tick_params(labelcolor='w')
ax.axis('off')

# Read the first time step from the datafile for tracer positions
step=model.readStep(['Den','TrP'], 0)

# Read the last time step from the datafile for tracer temp at end
step2=model.readStep(['Den','TrP','TrT','Trt'], 100)

# Define max temperature
maxtemp=round(model.fmax[2], -2)

# Define the colour map
cmap=plt.cm.cool
# Extract all colours from cmap
cmaplist=[cmap(i) for i in range(cmap.N)]

# Create new cmap
cmap2=mpl.colors.LinearSegmentedColormap.from_list('Custom cmap', cmaplist, cmap.N)

# Define bins and normalize
bounds=np.linspace (0, maxtemp, 11)
```

```
norm=mpl.colors.BoundaryNorm(bounds, cmap.N)

# Now, we'll set the tracer colours according to their temps,
# recorded in step.data[3] in this case.
q=ax.scatter(step.xmark[model.tru[0].start:model.tru[0].end],step.ymark[model.tru[0].start
:model.tru[0].end],c=step2.data[2][model.tru[0].start:model.tru[0].end],cmap=cmap2,vmin=0,
vmax=maxtemp,s=7,linewidths=0,marker='.',norm=norm)
# Mirror the plot
q2=ax.scatter(-
step.xmark[model.tru[0].start:model.tru[0].end],step.ymark[model.tru[0].start:model.tru[0]
.end],c=step2.data[2][model.tru[0].start:model.tru[0].end],cmap=cmap2,vmin=0,vmax=maxtemp,
s=7,linewidths=0,marker='.',norm=norm)

# Add a colorbar for the temp plot
cb=fig.colorbar(q, cmap=cmap2, norm=norm, spacing='proportional', ticks=bounds,
boundaries=bounds, format='%1i')
cb.set_label('Tracer peak-shock temperature [K]')

# Add title

# Save the figure
fig.savefig('{}/PeakT.png'.format(dirname), dpi=300)
```

A6: Example python script for creating plots shown in Figures 6.5/6.6 and shock temperature tables used to inform Table 6.7.

```
import pySALEPlot as psp
import matplotlib.pylab as plt
import matplotlib as mpl
import matplotlib.ticker as ticker
import numpy as np
import os
from pylab import figure,arange,colorbar
from numpy import pi,zeros,arange,array,searchsorted,allclose,append
from matplotlib.ticker import AutoMinorLocator

# Create ouptut directory
dirname='Complete_proj'
psp.mkdir_p(dirname)

#Get info on model name or directory
cwd=str(os.getcwd())
name=str(cwd.split('Por40/')[1])

# Open the datafile
m=psp.opendatfile('jdata.dat')

m.tracerMassVol()

# Set the distance units to km
m.setScale('km')

# Save slice information to get just x and y coords at one z location
z0 = np.index_exp[:, :, 0]

# Find tracer masses
tracermass = m.tracerMass
impmass = m.tracerMass[m.tru[0].start-1:m.tru[0].end].sum()

# Find number of tracers in impactor
ntracers = m.tru[0].end

# Load all tracer positions/time for impactor into npz file (makes it quicker)
try:

       data = np.load('tracervel3D.npz')
       tracerxpos = data['tracerxpos']
       tracerypos = data['tracerypos']
       tracerzpos = data['tracerzpos']

except:

       tracerxpos = np.zeros((m.nsteps, ntracers))
       tracerypos = np.zeros((m.nsteps, ntracers))
       tracerzpos = np.zeros((m.nsteps, ntracers))
       time = []

       for i in range(m.nsteps):

              s = m.readStep('TrP', i)

              tracerzpos[i, :] = s.zmark[m.tru[0].start-1:m.tru[0].end]
              tracerypos[i, :] = s.ymark[m.tru[0].start-1:m.tru[0].end]
              tracerxpos[i, :] = s.xmark[m.tru[0].start-1:m.tru[0].end]
```

```
            time.append(s.time)

      time = np.array(time)
      np.savez('tracervel3D', tracerzpos=tracerzpos, tracerypos=tracerypos,
tracerxpos=tracerxpos, time=time)

# Load all tracer velocities for impactor into npz file (makes it quicker)
try:

      data = np.load('tracervels.npz')
      xvel = data['xvel']
      yvel = data['yvel']
      zvel = data['zvel']
      time = data['time']

except:

      xvel = np.zeros((m.nsteps, ntracers))
      yvel = np.zeros((m.nsteps, ntracers))
      zvel = np.zeros((m.nsteps, ntracers))
      time = []

      for i in range(m.nsteps):

            s = m.readStep(['Tru','Trv','Trw'], i)

            xvel[i, :] = s.Tru[m.tru[0].start-1:m.tru[0].end]
            yvel[i, :] = s.Trv[m.tru[0].start-1:m.tru[0].end]
            zvel[i, :] = s.Trw[m.tru[0].start-1:m.tru[0].end]
            time.append(s.time)

      time = np.array(time)
      np.savez('tracervels', xvel=xvel, yvel=yvel, zvel=zvel, time=time)

# Create lists of tr numbers, x pos and y pos for the following loops
over_z = np.empty(0,int)
under_z = np.empty(0,int)
decap_z = []
crater_z = []

tr_num = []
xmark = []
ymark = []
escape = []
cr_final = []
out_cr = []

cr_bal = np.empty(0,int)
cr_x = np.empty(0)
cr_y = np.empty(0)
xx = np.empty(0)
yy = np.empty(0)
xy_array = np.empty(0,int)

s=m.readStep('Den', m.nsteps-1)

# Find timesteps where tracer is above/below threshold
for i in range(ntracers):

      x = s.xmark[i]
      y = s.ymark[i]
      z = s.zmark[i]

      if z > 0:
```

```
                over_z = np.append(over_z, i)

        else:

                under_z = np.append(under_z, i)

                if 0.5 > x > -5 and y < 2:

                        crater_z.append(i)

                else:

                        decap_z.append(i)
                        xx = np.append(xx, s.xmark[i])
                        yy = np.append(yy, s.ymark[i])
                        xy_array = np.append(xy_array, i)

# Define height threshold for projecting ballistically
h = 0.00
# Find timesteps where tracer is above/below threshold
for i in over_z:

        # Skip first timestep (using range) to not include starting position
        x = tracerxpos[range(1,m.nsteps),i]
        y = tracerypos[range(1,m.nsteps),i]
        z = tracerzpos[range(1,m.nsteps),i]
        a = np.argwhere(z>h)

        if z[a].min()>z[a.min()]:

                # Find timesteps before (s1) threshold
                s1 = int(np.argwhere(z==z[a].min()))

        else:
                s1 = a.min()

        # Find xyz vel components when they cross height threshold

        xv = (xvel[range(1,m.nsteps),i])*1e-3
        yv = (yvel[range(1,m.nsteps),i])*1e-3
        zv = (zvel[range(1,m.nsteps),i])*1e-3

        # Remove tracers that escape due to vel
        if (-2.38<xv[s1]<2.38 and -2.38<yv[s1]<2.38 and zv[s1]<2.38) or (zv[s1]<0):

                # Use quadratic formula to find time of flight (t) for each tracer
                grav = -(0.5*1.62e-3)
                coeff = [grav, zv[s1], z[s1]]
                quad = np.roots(coeff)
                t = quad[quad>0]

                # Find projected distance by multiplying t by x and y velocities and adding
start point
                xproj = (x[s1])+(xv[s1]*t)
                yproj = (y[s1])+(yv[s1]*t)

                tr_num.append(i)
                xmark.append(xproj[0])
                ymark.append(yproj[0])

        else:
                escape.append(i)
```

```
s=m.readStep(['TrT','Trv','Tru','Trw'], m.nsteps-1)

# ballistically project frozen tracers from inside the crater using their z positions as
final landing height
for i in crater_z:

	# Skip first timestep (using range) to not include starting position
	xv2 = xvel[range(1,m.nsteps),i]*1e-3
	yv2 = yvel[range(1,m.nsteps),i]*1e-3
	zv2 = zvel[range(1,m.nsteps),i]*1e-3

	x2 = tracerxpos[range(1,m.nsteps),i]
	y2 = tracerypos[range(1,m.nsteps),i]
	z2 = tracerzpos[range(1,m.nsteps),i]

	# Find tracers that do not travel upwards at any time
	if zv2.max()<0.00:

		xx = np.append(xx, s.xmark[i])
		yy = np.append(yy, s.ymark[i])
		xy_array = np.append(xy_array, i)
		cr_final.append(i)

	else:

		a2 = int(np.argwhere(zv2==zv2.max()))

		# Remove tracers that escape due to vel
		if -2.38<xv2[a2]<2.38 and -2.38<yv2[a2]<2.38 and zv2[a2]<2.38:

			# Use quadratic formula to find time of flight (t) for each tracer
			grav = -(0.5*1.62e-3)
			coeff = [grav, zv2[a2], 0]
			quad = np.roots(coeff)
			t = quad[quad>0]

			# Find projected distance by multiplying t by x and y velocities and
adding start point
			xproj_2 = (x2[a2])+(xv2[a2]*t)
			yproj_2 = (y2[a2])+(yv2[a2]*t)

			tr_num.append(i)
			cr_bal = np.append(cr_bal, i)
			cr_x = np.append(cr_x, xproj_2[0])
			cr_y = np.append(cr_y, yproj_2[0])
			xmark.append(xproj_2[0])
			ymark.append(yproj_2[0])

		else:
			escape.append(i)

# Convert lists of tracer numbers, xpos, ypos to arrays to use in scatter plots

tr_array = np.asarray(tr_num)
xarray = np.asarray(xmark)
yarray = np.asarray(ymark)

# find tracers that remain in crater after ballistically projected or at end of iSALE run
for i in range(len(cr_bal)):

	if 0.5 > cr_x[i] > -5 and cr_y[i] < 2:

		cr_final.append(cr_bal[i])
```

```
	else:

		out_cr.append(cr_bal[i])

print 'Under_z0 = '+str(len(under_z))
print 'Over_z0 = '+str(len(over_z))
print 'Ballistically projected tracers = '+str(len(tr_array))
print 'Tracers in crater = '+str(len(cr_final))
print 'Escaped tracers = '+str(len(escape))

# write to text file
with open(dirname+'/Tr_info.txt', 'w') as f:

	f.write('Tracers ejected = '+str(len(over_z)))
	f.write('\n')
	f.write('Tracers decapitated = ' +str(len(decap_z)))
	f.write('\n')
	f.write('Tracers in crater = '+str(len(cr_final)))
	f.write('\n')
	f.write('Ballsitically projected tracers = '+str(len(tr_array)))
	f.write('\n')
	f.write('Escaped tracers = '+str(len(escape)))

# Set up a pylab figure
fig=figure()

# Clear the previous figure
fig.clf()

# Set up the axes
ax=fig.add_subplot(111,aspect='equal')

# Set the axis labels
ax.set_xlabel('x [km]', fontsize=8)
ax.set_ylabel('y [km]', fontsize=8)

# Set the axis limits
ax.set_xlim([-50,1.5])
ax.set_ylim([-10,10])

# Set axis tick label size
ax.tick_params(axis='both', which='major', labelsize=8)
ax.tick_params(axis='both', which='minor', labelsize=6)

ax.xaxis.set_minor_locator(AutoMinorLocator())
ax.yaxis.set_minor_locator(AutoMinorLocator())

# We can also search from the bottom of the mesh upwards by setting
# topdown=False (this is the default behaviour).
# Note, that if the step has already been read, you can save some time by
# passing the step instance instead of the timestep number
topography_dn = m.surfaceTopography(step=s, topdown=False)

maxtemp=2000

#Define a section of the colormap so it looks better
def truncate_colormap(cmap, minval=0.0, maxval=1.0, n=100):
	'''
	https:/ s^-1tackoverflow.com/a/18926541
	'''
	if isinstance(cmap, str):
		cmap = plt.get_cmap(cmap)
	new_cmap = mpl.colors.LinearSegmentedColormap.from_list(
		'trunc({n},{a:.2f},{b:.2f})'.format(n=cmap.name, a=minval, b=maxval),
```

```
            cmap(np.linspace(minval, maxval, n)))
        return new_cmap

cmap_base = 'inferno'
vmin, vmax = 0.0, 0.90
cmap2 = truncate_colormap(cmap_base, vmin, vmax)

#Anything over 2000 K is set to red
cmap2.set_over('red')
cmap2.set_under('white')

# Define bins and normalize
bounds=[0, 250, 500, 750, 1000, 1250, 1500, 1750, 2000, 2250]
norm=mpl.colors.BoundaryNorm(bounds, cmap2.N)

# Plot the ballistically projected material
q=ax.scatter(xarray,yarray,c=s.TrT[tr_array],cmap=cmap2,vmin=0,vmax=maxtemp,s=5,linewidths
=0, marker='o', norm=norm)
#mirror the plot
q2=ax.scatter(xarray,-
yarray,c=s.TrT[tr_array],cmap=cmap2,vmin=0,vmax=maxtemp,s=5,linewidths=0, marker='o',
norm=norm)

# Plot the iSALE material
q3=ax.scatter(xx,yy,c=s.TrT[xy_array],cmap=cmap2,vmin=0,vmax=maxtemp,s=5,linewidths=0,
marker='o', norm=norm)
#mirror the plot
q4=ax.scatter(xx,-yy,c=s.TrT[xy_array],cmap=cmap2,vmin=0,vmax=maxtemp,s=5,linewidths=0,
marker='o', norm=norm)

# Scale legend
#ax.legend(fontsize='small', markerscale=2)

# Plot contour of the transient crater
contour_locator = ticker.MultipleLocator(1)
ax.contour(m.xc[z0], m.yc[z0], topography_dn,
   locator=contour_locator,
   linewidths=1, colors='cyan', levels=[-.1])
ax.contour(m.xc[z0], -m.yc[z0], topography_dn,
   locator=contour_locator,
   linewidths=1, colors='cyan', levels=[-.1])


#Add a colorbar for the peak temp plot
cb=fig.colorbar(q4, shrink=0.52, cmap=cmap2, norm=norm, spacing='proportional',
ticks=bounds, extend='max', boundaries=bounds, format='%1i')
cb.set_label('Tracer Peak Temperature [K]', labelpad=10, size=8)
cb.ax.tick_params(labelsize=8)

# Add title
ax.set_title('Plan view, projectile map', fontsize=10)

# Save the figure
fig.savefig(dirname+'/'+name+'_proj_final.png'.format(i), dpi=300, bbox_inches='tight')

dirname2='Complete_shockT'
psp.mkdir_p(dirname2)

tnumu=m.tracer_numu

# ------------------------------------------------------------------
# First, find the tracer masses (and volumes) from the first timestep
# ------------------------------------------------------------------
```

```
# Note, if you didn't open the file with tracermassvol=True, you can
# always calculate the tracer masses and volumes using the
# model.tracerMassVol() function:
#m.tracerMassVol()

trvol = m.tracerVolume
trmas = m.tracerMass

# ------------------------------------------
# Now, loop over timesteps, and add up all the
# tracers with a given peak shock pressure
# ------------------------------------------

# Pressures we are interested in: (choose these based on your material)
temperatures=range(0,4001,100)

def writeOutput(line,outfile):
       print line
       outfile.write(line+'\n')

# Loop over time steps (here, every 1, but change this as you see fit)
for i in arange(m.nsteps**-1,m.nsteps,m.nsteps**-1):
       s=m.readStep('TrT',i)
       TrT = s.data[0]

       totalvol = zeros(len(temperatures))
       totalmas = zeros(len(temperatures))

       unitvol  = zeros((4,len(temperatures)))
       unitmas  = zeros((4,len(temperatures)))

       # Much faster way (gives same result):
       for t in range(len(temperatures)):
       # Make array of true/false for each tracer (whether its pressure meets the
threshold)
              tt = TrT >= temperatures[t]
              # Multiply that array by the volume and mass. "False" tracer masses and
volumes
              # are multiplied by zero, so don't count in the calculation of the sum
              totalvol[t]=sum(trvol*tt)
              totalmas[t]=sum(trmas*tt)

              x = [0,1,2,3]
              y = [cr_final, decap_z, tr_array.tolist(), escape]

              # Also do this for each tracer unit
              for n, p in zip(x, y):

                     unitvol[n,t]=sum(trvol[p]*tt[p])
                     unitmas[n,t]=sum(trmas[p]*tt[p])

       # Output to screen/file.
       f=open(dirname2+"ShockT-{:05d}_final.txt".format(i),'w')
       writeOutput("#For timestep {} ({:12.4e} secs)".format(i,s.time),f)
       writeOutput("#"+"-"*(39+26*4),f)

       objects = ['Crater','Decaptd','Projctd','Escaped']
       unitnames = ["{} Vol".format(nn) for nn in objects]
       unitnames.extend(["{} Mass".format(nn) for nn in objects])

       writeOutput(("#"+"{:>13s}"*(3+2*4)).format(
       "Temperature","Total vol","Total mass",*unitnames),f)
```

```
writeOutput("#"+"-"*(39+26*4),f)

for t in range(len(temperatures)):
       unitvalues = append(unitvol[:,t],unitmas[:,t])

       writeOutput((" "+" {:12.4e}"*(3+2*4)).format(
       temperatures[t],totalvol[t],totalmas[t],*unitvalues),f)

writeOutput("#"+"-"*(39+26*4),f)
f.close()
```